Total scattering studies of orbital disorder in strongly-correlated transition-metal oxides

Peter M. M. Thygesen

New College



A thesis submitted for the degree of

Doctor of Philosophy

Inorganic Chemistry Laboratory

University of Oxford

Trinity 2017

Total scattering studies of orbital disorder in strongly-correlated transition-metal oxides

Peter M. M. Thygesen, New College Trinity Term 2017

A thesis submitted for the degree of Doctor of Philosophy to the Division of Mathematics, Physical, and Life Sciences at the University of Oxford

Abstract

Transition metal oxides are a family of materials where the physical properties are determined by the strong interplay between orbitals, spins, and electron charge. This thesis aims to understand the local orbital ordering and its relation to the physical properties. Both neutron and X-ray total scattering data have been collected and analysed using a small box approach to obtain specific information about the orbital ordering and its relation to the physical properties within three canonical systems: the spin-glass material $Y_2Mo_2O_7$; the parent endmember compound, $LaMnO_3$, of the doped manganites showing colossal magneto resistance (CMR); and a related series of different compositions, namely $La_{1-x}Ca_xMnO_3$.

$Y_2Mo_2O_7$ consist of Jahn-Teller active Mo^{4+} ions which occupy corner-sharing tetrahedra in a frustrated pyrochlore lattice. In most pyrochlore oxides both frustration and positional disorder must be present to show spin-glass behaviour. In this thesis I present how the Mo^{4+} ions on each frustrated tetrahedron dimerise, leading to structural disorder on the Mo site large enough to drive the spin-glass state in $Y_2Mo_2O_7$.

$LaMnO_3$ undergoes a canonical orbital order/disorder transition at $\sim 750\,\mathrm{K}$ which is the same as the transition that precedes CMR itself in doped manganites. Here I find a discontinuity in local structure that indicates a fundamental change in the type of orbital arrangement at the transition. In the analysis of the transition I realise the difficulty of discriminating between local structure models when static and dynamic disorder are strongly coupled. Nevertheless, my data show a subtle but consistent preference for the anisotropic Potts model.

$La_{1-x}Ca_xMnO_3$ is of high interest because of its ability to show CMR. Here, I synthesised nine different sample compositions, using the citric gel method. I present a discontinuity in local structure as a function of composition similar to the observed orbital order/disorder transition in $LaMnO_3$. An extended study of the local structure of $La_{0.5}Ca_{0.5}MnO_3$ composition as a function of temperature is presented. This study indicates that there is a difference in the sample composition depending on which synthesis method used. However, the study shows that Goodenough's CO/OO model for the ground state of $La_{0.5}Ca_{0.5}MnO_3$ is too simplified and suggests that a different model may represent the low temperature state better.

Declaration of Authorship

This thesis is the result of my own work and where it draws on the work of others I acknowledge this at the appropriate points in the text. This thesis has not been submitted for a degree at this, or any other, institution.

Peter Thygesen

Acknowledgements

This work presented in this thesis would not have been possible without assistance and support from numerous people I have worked with and got to know during my time at Oxford. I would first and foremost like to thank Professor Andrew L. Goodwin for being such an inspirational and supportive supervisor. I have learned a lot from him and this thesis would not have taken place without him.

I would also like to thank those people I collaborated with during my DPhil. Professor Dave Keen, Dr. Matt Tucker, Dr. Karena Chapman, and Dr. Helen Playford gave much assistance with collecting and processing data for my thesis. I would also like to thank Professor Mike Hayward, Dr. Midori Patino, and Dr Ronghuan Zhang for their guidance in synthesising samples used in this work.
For specific parts of the project I would like to thank Joe for his help with the data collection, analysis, and putting the paper on $Y_2Mo_2O_7$ together (Chapter 3), Callum for helping out collecting data and for share his knowledge on total scattering, Josh for the I15 beam time we shared together, and Andy Chin for help performing SQUID measurements (Chapter 5). A special thanks to Sneha, Harry, Emily, Ali, and Hanna for proof-reading parts of this thesis. I would like to thank all the fantastic people I have been surrounded by during my time in Oxford. First I would like to thank the Goodwin group and ChemCryst members over the last four years. In particular I am thankful to Nick for all his help in the beginning of my DPhil., Mark for helping out with TOPAS refinements and general discussions on crystallography.

I would also like to thank Jerome "Jezza" Wicker for Wednesday football and pints as a good excuse to escape from thesis writing. Ines, Jasper, Matt, Paul, Andrew C, Hamish, Carl, Chloe, Mia, Arkadiy, Ali, Phil W, Phil M and numerous Part IIs; it has been a pleasure to work with and know you all.
Also, I would like to thank Simi and Scott for great weekends in London, my flatmates Josh and Ilsa for a fantastic year at city gate 12, and all the Danes in Oxford, it has been a pleasure to hang out with you all.

Finally I would like to thank Maria for her support and in particular keeping my mood up in the later stage of this thesis, and last but not least my family for their support throughout my DPhil. I would not have been able to finish this work without them.

For my parents

Contents

1 Introduction **1**

1.1 Jahn-Teller effects 2

1.2 Orbital order 8

1.3 Physical properties related to orbital ordering 17

1.4 Orbital disordered states 27

1.5 Overview of characterisation methods for ordered/disordered states . 30

1.6 Aim and structure of this thesis 42

2 Methods **45**

2.1 Introduction 45

2.2 Diffraction techniques 45

2.3 Total scattering 56

2.4 SQUID magnetometry 65

2.5 Monte Carlo simulations 66

3 Orbital dimer model for spin-glass formation in $Y_2Mo_2O_7$ **67**

3.1 Introduction 67

3.2 Background 67

3.3 Experimental 74

3.4 Results 77
3.5 Discussion 91
3.6 Conclusion 94

4 Local structure study of orbital disorder in $LaMnO_3$ 96

4.1 Introduction 96
4.2 Background 97
4.3 Experimental 103
4.4 Results and discussion 113
4.5 Future work and concluding remarks 128

5 Local structure study of the $La_{1-x}Ca_xMnO_3$ family 131

5.1 Introduction 131
5.2 Background 131
5.3 Experimental 138
5.4 Results and discussion 143
5.5 Future work and concluding remarks 168

6 Conclusion 172

Bibliography 175

Appendix A 190

A1 Obtained values from Rietveld refinement of
$Y_2Mo_2O_7$ 191

Appendix B 191

B1 Obtained values for Rietveld refinement of $LaMnO_3$ 192

B2 PDFGui fits of the three models examined across temperature of $LaMnO_3$ 195

Appendix C **195**

C1 Obtained values and plots from Rietveld refinements of $La_{1-x}Ca_xMnO_3$ 205

Publications **209**

Abbreviations

3SP	3-state Potts
2θ	scattering angle (diffraction)
CMR	colossal magnetoresistance
CO	charge order
CO/OD	charge order/Orbital disorder
CO/OO	charge order/Orbital order
EXAFS	extended X-ray absorption theory
FOJT	first order Jahn-Teller
HO	hidden order
JT	Jahn-Teller
K	Kelvin
MC	Monte Carlo
NMR	nuclear magnetic resonance
OO	orbital order
PDF	pair distribution function
PXRD	powder X-ray diffraction
RMC	reverse Monte Carlo
RSXS	resonant soft X-ray scattering
SG	spin-glass
SOJT	second order Jahn-Teller
SQUID	superconducting quantum interference device
RT	room temperature
XANES	X-ray absorption near-edge structure
ZFC/FC	zero-field cooling/field cooling

Chapter 1

Introduction

Many of the most exotic technological developments in the last sixty years have exploited the unusual physics of transition metal oxides. The functional properties obtained in transition metal oxides include magnetism,[1] superconductors,[2] batteries,[3] and multiferroicity.[4] The understanding of these properties has mainly been achieved by establishing structure – property relationships, which in turn allow for optimisation. This relationship is therefore of high interest and is often obtained from crystallography using diffraction theory.[5] Standard crystallographic techniques give information about the average structure of a material. However, when materials contain some degree of disorder the average structure may no longer represent the true atomic-scale arrangements and we do not gain the information related to the properties. Disorder has been observed in some transition metal oxides where it has been related to the strong correlation between magnetic spins, orbitals, lattice, and electron transport, which all couple to the d orbitals in these metals.[6] Not only are these materials scientifically interesting to investigate, but they also include functional properties of high relevance such as superconductivity,[7] frustrated magnetism,[8] colossal magnetoresistance,[9,10] and electrode materials.[11] The understanding of the local structure of disordered materials has therefore been a key problem in the field of solid-state chemistry.

This thesis aims to use combined neutron and X-ray total scattering techniques to analyse and model canonical systems where orbital order/disorder directly relates

to the physical properties of the material. The main focus is to understand how the orbitals order locally and how that affects other degrees of freedom in the materials. Through these studies I develop an overview of the use of total scattering methods in characterising orbital disorder, together with an appreciation of advantages of using combined neutron and X-ray data.

In this introduction I present the conceptual background for orbital ordering and provide examples where orbital ordering has a significant effect on the crystal structure and the related physical properties. I then summarise the different experimental methods available for characterising orbital order/disorder in materials.

1.1 Jahn-Teller effects

1.1.1 First-order Jahn-Teller distortions

Hermann Jahn and Edward Teller used a symmetry argument to demonstrate that a non-linear system in a degenerate energy state cannot be stable.[12] For a system to remove its degeneracy and for it to stabilise it will spontaneously undergo a geometrical bonding distortion, to lower the overall energy — this is what we today know as the first order Jahn-Teller effect (FOJT).[13] The degeneracy is a property of the valence electron configuration, which in transition metal oxides is the d electron configuration. The d electron orbitals can take five different shapes shown in Figure 1.1. From crystal field theory, the breaking of degeneracies of the electron orbital states are driven by the interaction between the metal and the ligands, $e.g$ if a d orbital material is located in an octahedral field with six coordinated ligands, the orbitals will split into two groups with the lower energy orbitals pointing inbetween the ligands

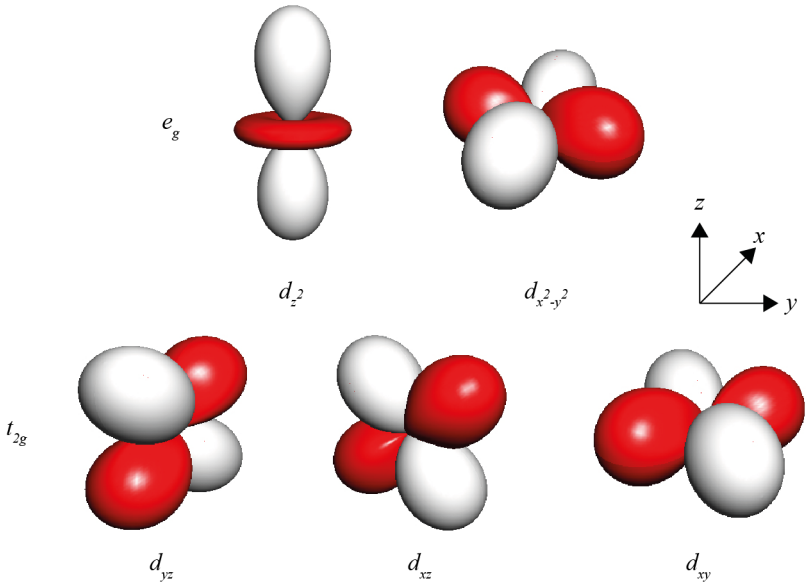


Figure 1.1: The five d orbital states in the octahedral crystal field. This five fold degeneracy is lifted to two e_g orbitals and three t_{2g} orbitals. The phase of the wave function for the different "clouds" is indicated by colour; white for positive and red for negative.

(d_{xy}, d_{xz}, and d_{yz}, called t_{2g} orbitals) and the higher energy orbitals pointing straight at the ligands (d_{z^2}, and $d_{x^2-y^2}$ called e_g orbitals) [Figure 1.2].[14] The electrons are distributed into these states according to Hund's rule where the low lying states are occupied by one electron, when these states are filled the occupation of a higher energy state or double occupation occur, all dependent on what is most energetically favoured.[15] In cases where both the d_{z^2}, and $d_{x^2-y^2}$ are partly occupied, the geometric bonding distortion can appear in a different configuration.[16] Van Vleck extended the JT theorem to ions in crystals. He derived the two e_g vibrational modes would remove the e-orbital degeneracy in an octahedral site.[17] Two of these modes are relevant for this thesis and correspond to orthorhombic and tetragonal deformations Q_2 and Q_3 displayed in Figure 1.3(a,b). Q_2 gives rise to three different bond lengths (two short, two medium, and two long) as a consequence of occupation of the d_{z^2} or $d_{x^2-y^2}$ states, while Q_3 gives rise to two different bond lengths (four short, and

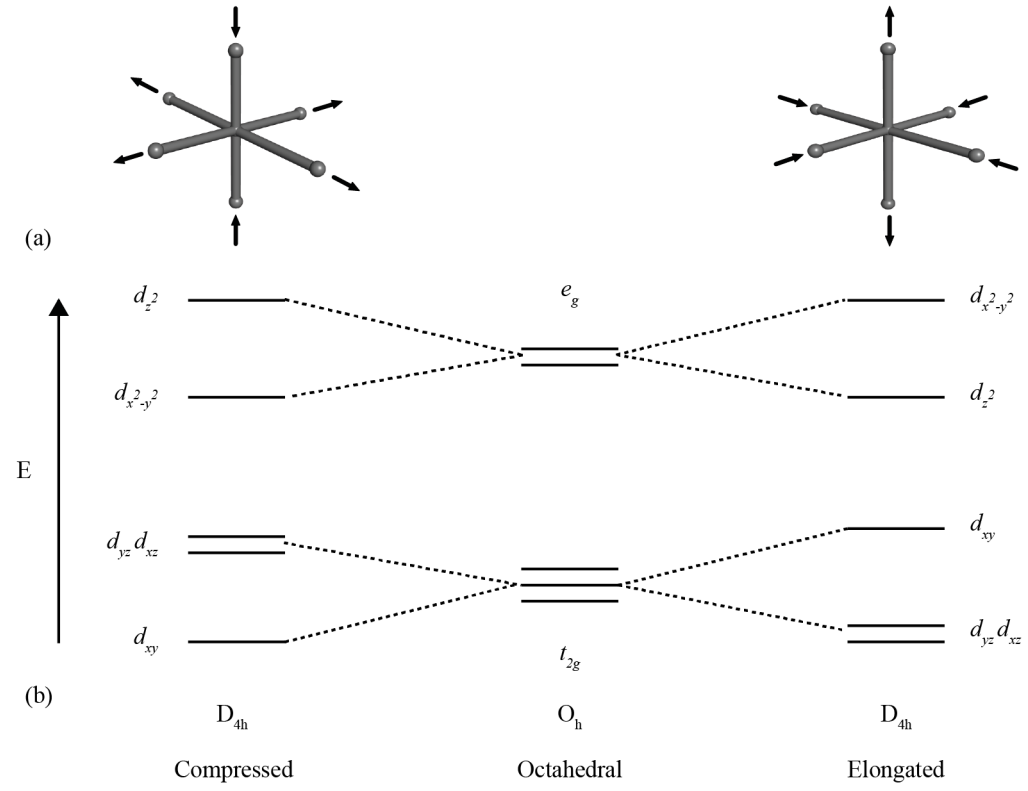


Figure 1.2: (a) Atomic models of the JT compressed and elongated octahedra from each of the orbital degrees of freedom by splitting the e_g state. (b) The energy states of Jahn-Teller distorted d orbitals in an octahedral configuration. The left and right side corresponds to the two orbital degrees of freedom generated from splitting the e_g state.

two long). The two states can be defined as: Q_2=2(l-s)/$\sqrt{2}$ and Q_3=2(2m-l-s)/$\sqrt{6}$, where l, m, and s stand for long, medium and short metal–ligand bond distances. These two states can also appear in a mixed state (Q_2/Q_3) — to determine which deformation that is dominant the average tilt angle of the metal-ligand octahedra can be calculated ϕ from tan(ϕ)= Q_2/Q_3.[18] The calculated ϕ value shows which state is dominant, *e.g* for material with ϕ =15°, using Figure 1.3(c) it is proved that Q_2 will be dominant.[19]

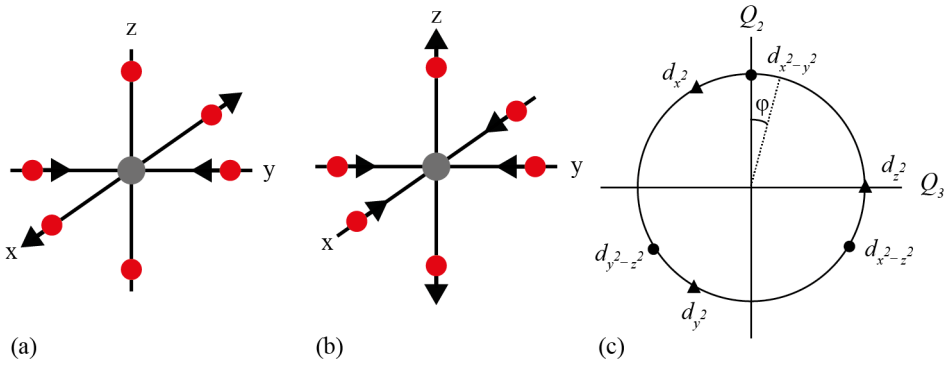


Figure 1.3: (a) Schematic view of the Q_2 deformation with two short, two medium and two long bonds. (b) Shows the Q_3 deformation with four short and two long bonds. (c) The Q_2 and Q_3 determined from the average tilt angle. The closed circles corresponds to the Q_2 state while triangles corresponds to Q_3 state. The dotted line shows a case where a mixed phase of Q_2/Q_3 occur, in this case the calculated ϕ=15° and shows that the phase is dominated by the Q_2 state.[19]

1.1.2 Collective Jahn-Teller distortions

The occupation of an electron in one of the two (Q_2,Q_3) states will either elongate or compress the octahedra due to the shape of the occupied orbital and give rise to variation of the metal–ligand bonds. The direction of the elongation in the octahedra is found to order throughout the material, leading to cooperative JT distortions. The arrangement of orbitals in these systems depends on both the geometry of the lattice and the cooperative JT distortion (the orientation of the elongation on one site affects the elongation orientation on the neighbour sites) and is also known as static JT deformation.[20] Lower concentrations of JT ions in a material can appear in doped systems, and locally cooperative dynamic JT deformations can occur for these systems.[21,22] The orderings of the orbitals are often coupled to the physical properties of materials, especially in the doped manganites where the ordering of the JT distortions are assumed to be related to the physical properties of this fam-

ily.[23–25]

The FOJT effect is mainly observed in metals where odd number of electrons occupy e_g orbitals. This situation includes the high spin Cr^{2+} (d^4), high spin Mn^{3+} (d^4), low spin Co^{2+} (d^7), and Cu^{2+} (d^9), with Cu^{2+} (d^9) to be the most common metal where JT distortion is observed.[13] The effect can also occur when there is a degeneracy in the t_{2g} orbitals. This situation occurs for the d^1 and d^2 metals such as V^{3+}, Ti^{3+}, Mo^{4+}, and Cr^{4+}. The splitting of the t_{2g} electron bands also generates geometric distortions of the local environment but the effect is slightly smaller than for splitting of the e_g levels.[26–28] The first order JT effect appears in a broad range of materials from coordination compounds of Cu^{2+}, which adopts a range of different stereochemistries dependent on the group of ligands bonded to the Cu^{2+},[29] to the stronger correlated transition metal oxide compounds,[30] which are the materials studied in this thesis.

1.1.3 Second-order Jahn-Teller distortions

An extension of the JT theory suggested that high-energy occupied orbitals can interact with low-energy unoccupied orbitals to cause a distortion—this is also known as the second order Jahn-Teller effect (SOJT).[31,32] This interaction causes the symmetry to break to allow the HOMO/LUMO to mix and leads to a very large distortion of the molecular geometry or even a complete dissociation can occur [Figure 1.4].[33]

The SOJT effect has been used to explain many structural shapes in materials such as the bending of the water molecule where the mixing of the bonding and anti bonding (HOMO/LUMO) is by symmetry allowed and generates the bending of the

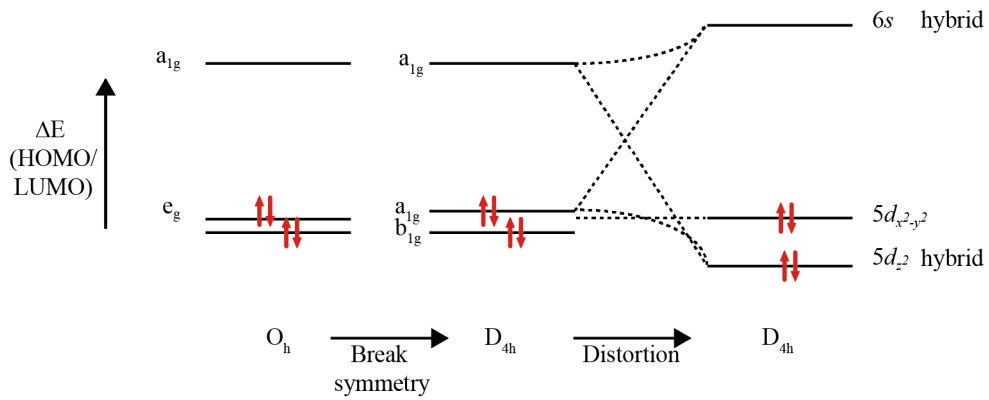


Figure 1.4: The crystal splitting diagram of a SOJT distortion in linear coordination of HgO is used as an example. With fully occupied *d*-orbitals the mixing of *d* and *s* orbitals appear and breaks the symmetry (SOJT) and a distortion of the unit cell appears.

molecule. In transition metal oxides, this is also a common effect causing symmetry lowering and is coupled to the physical properties such as the ferroelectricity in $BaTiO_3$ and $KNbO_3$.[34,35] The SOJT distortion is mostly common for main group ions,[32] and has not been the main focus of this thesis.

1.1.4 Experimental evidence for Jahn-Teller effect in materials

The JT effect can appear in materials in solution or in solid materials such as the six-coordinate copper complexes where the ligands consist of an organic molecule.[36] The variation in bonding geometries give rise to different vibrations and colours in metal complexes with JT effect.[13] The experimental evidence can therefore easily be observed from the variance in colours of metal compounds with different oxidation states. The most straight forward method to confirm the oxidation state of a metal in a material is from UV-Vis spectroscopy. The UV-Vis method collects a spectrum of different energies and the absorption is plotted against energy, the graph shows at

which energies a material absorbs the UV-Vis light. The certain energy at which the material absorbs the light is unique for each material and is related to the occupation of oxidation state of the metal. Experimentally the JT-distortion will be observed as a splitting of the absorbance band in the spectrum as a consequence of the reduction in symmetry which increases the number of energy bands.[14,37]

Another experimental method to observe the JT effect on a metal ion in a material is using crystallography. The JT effect is observed as a elongation or compression of the metal–ligand bonds. Furthermore, lowering of the symmetry in the local or average structure will appear as a consequence of the JT effect. To be able to observe these trends using diffraction, the JT distortion must be ordered. Some examples of materials where JT effect lowers the symmetry are presented in next section.

1.2 Orbital order

It is well known that orbital ordering in a crystal structure and its degrees of freedom play a key role in the properties of a material. Physical properties where this is the scenario are colossal magnetoresistance (CMR),[38] frustrated magnetism,[39] ferroelectricity,[40,41] and magnetoelectric coupling.[42] In all these cases, it is the existence and nature of correlations between local orbital states that gives rise to the relevant phenomena of interest. Long-range orbital ordering can assume many forms, but its nature is usually evident in crystallography *via* coupling between orbital occupancy/orientation and bond strain and this coupling results in long-range symmetry breaking in materials.[43]

Here, I exploit the relationship between orbitals and multipoles of different order: orbital ordered states correspond to different types of dipolar, quadrupolar, or oc-

topolar order. I focus on examples where the orbital ordering effects the long-range symmetry and the physical properties in materials.

Multipoles are already well-understood in chemistry and have already been used to describe magnetic spins where two magnetic states (+1,-1) appears,[44] or charge polarisation of a bond.[45] The s, p, d and f orbitals correspond to multipoles of different orders. A spherical s orbital can be described as a monopole, with its spherical form it does not have any degrees of freedom. p orbitals transform as dipoles, d orbitals as quadrupoles [Figure 1.1], and f orbitals as octopoles. These descriptions can be used to represent the orientation and ordering of the orbitals on the crystallographic lattice.

1.2.1 Dipolar order

A metal with partially–occupied p states can be thought of as a dipole with a stereochemically active lone pair in one end of the orbital while the other end bonds to ligands. A canonical example of a metal where the p orbital acts as a dipole are Pb^{2+} ions, where one end coordinates to the ligands while the other end has an active lone pair.[46] In two similar situations, lead acts in two different ways. First, in PbTe, lead does not have an active lone pair and the material crystallises in a high symmetry cubic cell with the Pb^{2+} ion occupying the centre of the unit cell with the Te^{2-} occupying the corners, forming an octahedron with equal distances to the Pb^{2+} ion [Figure 1.5(a)]. By substituting the Te^{2-} ions with O^{2-} ions, the band gap between the HOMO and LUMO orbitals decreases and Pb^{2+} undergoes a SOJT distortion.[47] As a consequence, the Pb^{2+} ions displace and break the symmetry from cubic to tetragonal with a stereochemically active lone pair pointing opposite the

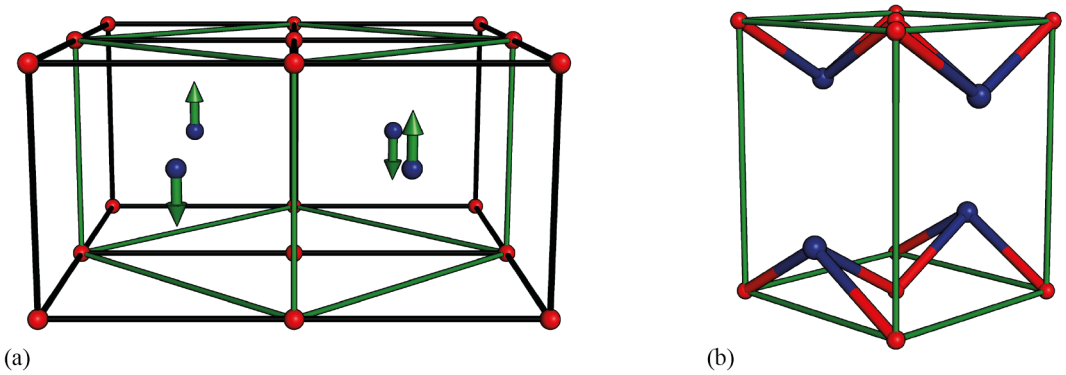


Figure 1.5: (a) a 2×2 box of the cubic structure of PbTe and (b) shows the lowered symmetry crystal structure of PbO. The green arrows represents SOJT displacement when the ligand is changed to oxygen. The green unit cell inside the PbTe cell shows the relation between the two structures.

ligand [Figure 1.5(b)]. The driving force for this displacement is the lowering of the energy in the filled antibonding Pb $6s$ orbitals, by mixing with the empty Pb $6p$ orbitals. This mixing is forbidden by symmetry in tetrahedral and octahedral coordination, so a distortion of the lattice is a consequence of stabilisation.[48–50] Cyanides also act as dipoles but instead of a lone pair they have an electric dipole moment, ordered through a structure.[51] Instead of a lone pair at one end the cyanide has a unpaired electron. A reorientation of the CN^- ions introduces disorder and causes symmetry changes. An example of that is in KCN, where the C and N ends act as poles and ordering of these are related to three transitions of the structure.[52] The material undergoes an order/disorder phase transition at 83 K of the dipole orientation of the CN^- ions which in the ordered state align in an antiferroelectric manner. The ordered state crystallises in orthorhombic $Pmmn$ cell where the CN^- ions all align parallel to each other in the ab plane and antiparallel in the adjacent $a-b$ planes [Figure 1.6].[53] At 168 K KCN reorientates into an orthorhombic structure

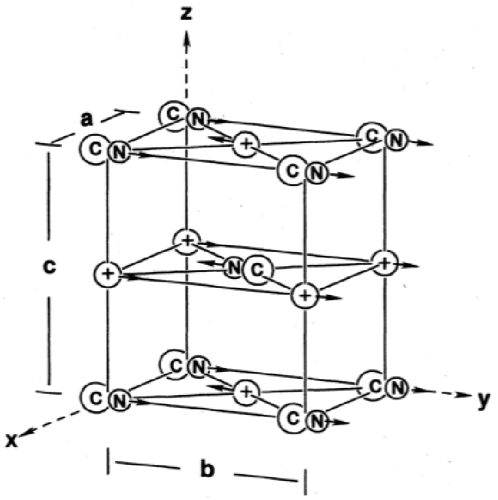


Figure 1.6: The KCN crystal structure at 83 K showing the electrically ordered structure with the CN^- ions are aligned parallel to each other in any given a-b plane. The figure is adapted from Ref. 55

with space group $Immm$ driven by the CN^- ions ordering along the b axis but with a random orientation of the C and N ends of the CN^-.[54] At room temperature (RT) the structure is pseudocubic with space group $Fm\bar{3}m$ with rapid reorientations of the CN^- ions which give an average spherical shape.[55] In the example presented here the orientation of the CN^- ions clearly drives the phase transitions across temperature in KCN.

1.2.2 Quadrupolar order

The d orbitals which consist of five electronic states, displayed in Figure 1.1, transform as quadrupoles. When occupying one of the d orbitals with an electron, the orbitals have quadrupolar symmetry and therefore have a quadrupolar moment at the centre of the orbital.[56] For the d orbitals, a FOJT effect often appears and the orientation of the JT elongation or compression in a crystal lattice has been described by John B. Goodenough.[24]

The nomenclature Goodenough used to describe antiferromagnetic spins on a cubic lattice was transferred on to describing the ordering of JT distortion of d orbitals.[24] The antiferromagnetic ordering of spins on a cubic lattice can appear in four different configurations, A-type, C-type, charge/orbital order (CE)-type, and G-type. In the A and C-type models, the spins are parallel to the z and y direction. C-type ordering is shown [Figure 1.7(a)]. The CE-type have layers of ferromagnetic ordering in the x, z direction and organises in an antiferromagnetic order in the y direction. In the G-type model, a spin is surrounded by opposite spins which alternates through the structure [Figure 1.7(b)]. By converting the spins into JT elongated orbitals the orbital order on a lattice can be described in a similar way. In orbital ordering it is only the C- and G-type that is relevant for crystal structures. In the C-type, the JT elongated axes are perpendicular to the z-direction, alternating parallel to the x and y axes [Figure 1.7(c)]. In the G-type, the JT elongation is always neighbouring a JT elongation pointing in the opposite direction [Figure 1.7(d)]. Once the ordering type is known, the orbital orientation of a single metal ion will dictate the orbital ordering of the lattice.[24]

Orbital order can have a large effect on material symmetry. The canonical example where long-range orbital ordering controls the symmetry is in $KCuF_3$.[57] To understand how the orbital ordering changes the symmetry we will look at the sister compound–the cubic perovskite system $KMnF_3$ where the B-site is occupied by octahedrally coordinated Mn^{2+} ions which are JT inactive located on the corners of the unit cell. In this system the structure is only slightly distorted from the unstable cubic perovskite structure itself.[58] In the main compound $KCuF_3$ the orbital ordering arises from the Cu^{2+} t^6e^3 d-electron configuration. The JT active Cu^{2+}

ions occupy the B-site, and the symmetry is lowered into a tetragonal unit cell with space group $I4/mcm$. The JT elongation on Cu^{2+} alternates along the x and y directions corresponding to a G-type ordering of the orbitals on the lattice throughout the structure [Figure 1.7(d)]. The long-range ordering of the orbitals couples to the bond strain. This coupling is the main reason for the long-range symmetry breaking that occurs in $KCuF_3$.[56,59]

Another canonical material containing orbital order is $LaMnO_3$, where the JT distortions arise from the degeneracy of the Mn^{3+} t^3e^1 d-electron configuration.[60]

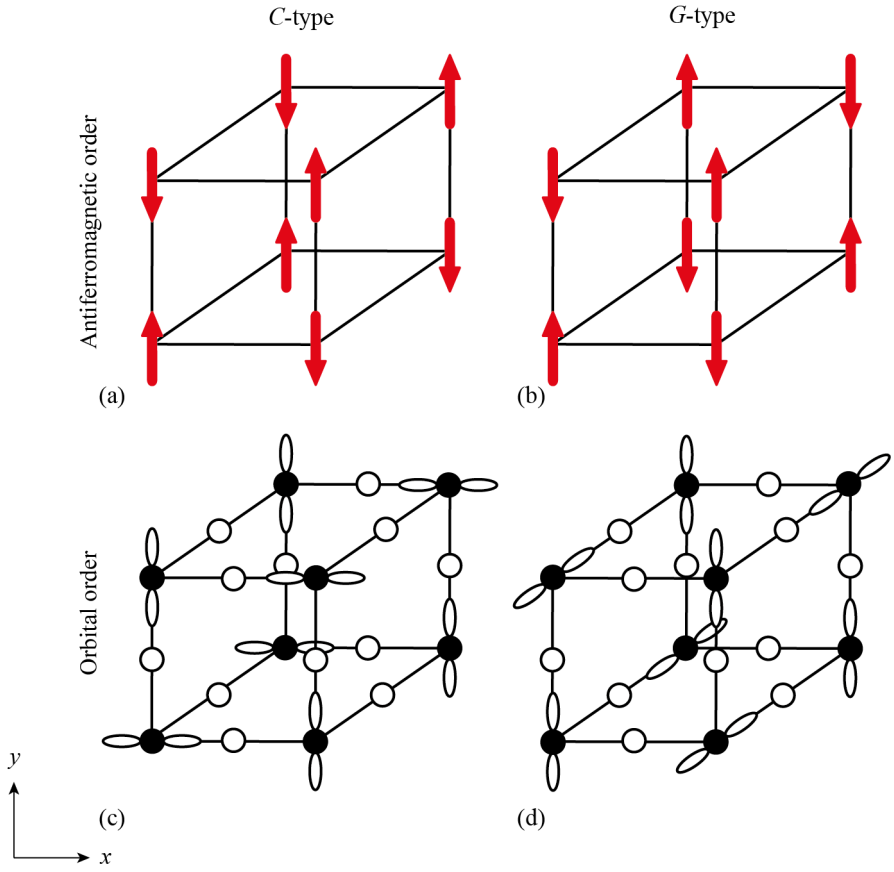


Figure 1.7: Schematic representation of the C-type and G-type orderings on a cubic lattice. (a,b) Show the C-type (a) and G-type (b) antiferromagnetic ordering. (c,d) demonstrate the C-type (c) and G-type (d) orbital ordering on a cubic lattice. The orbitals represent the elongated JT axes.[24]

This degeneracy is lifted by a JT distortion of the [MnO_6] coordination environment, which acts to couple Mn–O bond displacements with orbital occupancies, and hence structural and electronic degrees of freedom.[61] Crystallographic measurements of $LaMnO_3$ performed under ambient conditions indicate that these distortions (and hence orbital occupancies) are ordered throughout the crystal lattice, with a periodicity that coincides with that imposed by the octahedral tilt system.[62] This periodicity accounts for the orthorhombic *Pnma* symmetry of the orbital ordered phase as displayed in Figure 1.8(a). There is a single Mn environment (Wyckoff site 4*b*; site symmetry $\bar{1}$) and three symmetry-inequivalent pairs of Mn–O bonds: "long" (2.1 Å), "medium" (2.0 Å), and "short" (1.9 Å), corresponding to Q_2 deformation. The long and short bonds alternate within the (a, c) plane [Figure. 1.8(b)] to give a *C*-type orbital order arrangement.[63] In this case, the specific octahedral tilts present mean that the projection of the long bonds is slightly greater along a than c and so the difference in these two lattice parameters is related to the presence of orbital order. $LaMnO_3$ undergoes an orbital transition into a disordered state at 750 K and this orbital order/disorder transition is studied in detail in Chapter 4.

The JT orientation does not only depend on the metal ion: it can also be controlled by switching between ligands. In a traditional octahedral environment where a JT distortion occurs, the ligands coordinated to the metal are identical.[37] If the metal is coordinated to a mixture of different ligands the material will preferentially stabilise one of the JT orientations in terms of the crystal field strengths of the ligands.[64] This preference can be manipulated by adding various external pertubations to the system. In Ref 65, Halder *et al.* proved this by applying pressure to $CuF_2(H_2O)_2$(pyrazine) [Figure 1.9(a)]. At ambient pressure the JT active Cu^{2+} sta-

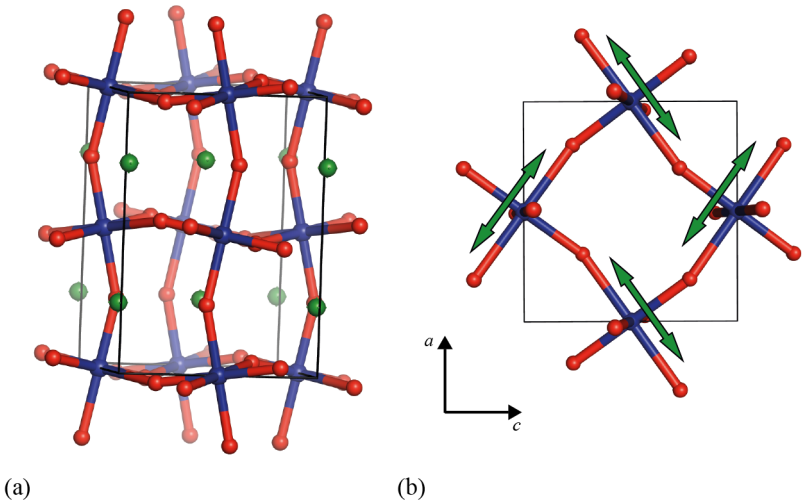


Figure 1.8: Structure and phase behaviour of $LaMnO_3$. (a) The ambient (O') structure consists of a framework of corner sharing MnO_6 octahedra (Mn atoms blue; O atoms red), with La atoms (green) occupying 12-coordinate extra framework sites. The presence of octahedral tilts confers orthorhombic *Pnma* symmetry; in this representation the b axis is vertical and the c axis approximately horizontal. (b) Axial JT distortions are arranged with the same periodicity as the octahedral tilts. Long Mn–O bonds (indicated by arrows) are confined within the (a, c) planes; this particular arrangement results in a small difference between a and c lattice.

bilises the system by elongating the bonds to the pyrazine nitrogens. As the pressure is increased to 0.9 GPa the JT axis switched to the oxygens and finally by further increase of the pressure to 3.1 GPa the JT distortions switch over to the flourine ligand.[65] This flipping of the JT distortion causes changes of the magnetic orbitals which were observed as a change in the magnetic properties from a two dimensional to a one-dimensional coupling.[65] These kinds of properties are relevant in designing materials that can act as sensors controlled by pressure variation.

1.2.3 Multipolar order

Just as p and d orbitals transform as dipoles and quadrupoles, respectively, the f orbitals can be described as high-order multipoles. In materials containing f-electrons, exchange interactions of the lanthanide or actinide magnetic moments

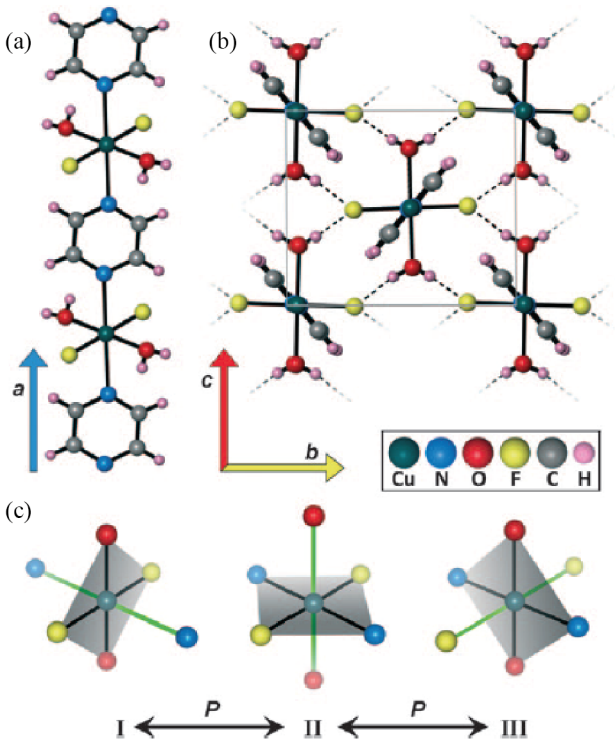


Figure 1.9: (a) An isolated $CuF_2(H_2O)_2$(pyrazine) along the a direction and (b) the 2D hydrogen bonding network in the bc plane in structure of $CuF_2(H_2O)_2(pyrazine)_2$. (c) The pressure induced switching of the JT-axis (green) of the $CuF_2O_2N_2$ octahedra. The figure is adapted from Ref. 65.

can generate long-range antiferromagnetic or ferromagnetic ordering at low temperatures, but it is also possible to generate multipolar ordering.[66] In Ref 67 Kung *et al.* used the phenomena of multipolar order to explain the hidden order (HO) phase in URu_2Si_2.[67] In hidden order materials, the order is of a type that cannot be directly probed by experimental techniques.[68] This appears in URu_2Si_2 which undergoes a second-order phase transition from a nonmagnetic to an electronically ordered state at $T_{HO} = 17.5\,K$ before it becomes superconducting below 1.5 K. The HO phase transition was described by chiral density waves of multipolar ordering, generated from the symmetry of the f orbitals of the uranium. They showed this experimentally by using polarisation-resolved Raman spectroscopy to specify the

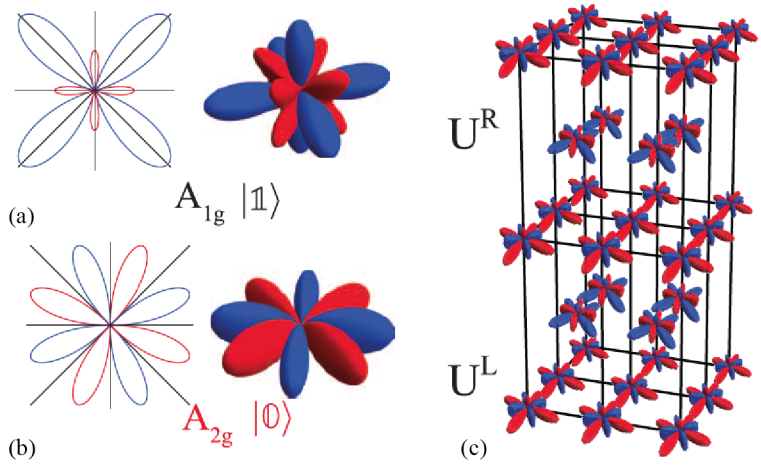


Figure 1.10: (a) The A_{1g} state which is symmetric in the vertical and diagonal reflections while (b) A_{2g} state is antisymmetric to these reflections. (c) Shows schematic the chirality density wave in the HO phase with the alternating occupation of the A_{1g} and A_{2g} states. The figure is adapted from Ref. 67

symmetry generated below and above the HO transition. The experimental analysis of the HO phase showed a split of the uranium ions into two different states (A_{1g} and A_{2g}) Figure 1.10(a,b). The two states which have different chirality density waves, alternate across the structure at the HO phase of URu_2Si_2 and explains the HO phase displayed in Figure 1.10(c).[67] This description of the electronic ordering emerged from the f electrons is a fairly new idea and is therefore expected to be relevant to other intermetallic compounds.

1.3 Physical properties related to orbital ordering

As presented in the previous section the orbital ordering affects the symmetry and shape of the structure. The orbitals are also strongly coupled to spin and electronic degrees of freedom in materials and are therefore directly related to many of their physical properties. In this section, I will present some examples where the physical properties in a material are directly related to the ordering of the valence orbitals.

1.3.1 Magnetism

Magnetic materials have a large effect on our daily life where they are used in refrigerators, furnaces, computers, and cell phones.[69] Magnetism is generated from the angular moment of the electron spin: when a material has an unpaired electron the spin angular moment generates a paramagnetic spin. These spins interact in different ways to generate a variety of ordering patterns that in turn give the material specific magnetic properties.[70–72]

The exchange interactions between unpaired spins achieved from the minimisation of electronic repulsion is the key in collective magnetism. In transition metal oxides the interactions between the metal ions are often mediated by a non-magnetic oxygen ion: this is the so-called superexchange interaction. The superexchange interaction depends on the degree of orbital overlap, which is a function of the metal–oxygen–metal angle—the overlap is strongest for a 180° bond angle and impossible for a 90° angle.[56] Orthogonal systems actually give rise to a parallel arrangement of spins as the loss of orbital overlap means that the electrostatic repulsions are minimised by parallel spins. These observations has been formalised by Goodenough-Kanamori-Anderson rules.[24,73,74]

In Ref. 75, Rao *et al.* examined the M–O–M angles to explain the ferromagnetism observed in $BiMnO_3$. They explained the ferromagnetism to be driven by orbital ordering of the Mn ions. The material crystallises in a monoclinic space group with $C2$ symmetry and JT active Mn^{3+} ions occupying the B-site.[76] By examining the Mn–O–Mn angles they observed that four of the superexchange pathways were ferromagnetic while the last two were antiferromagnetic. The four superexchange

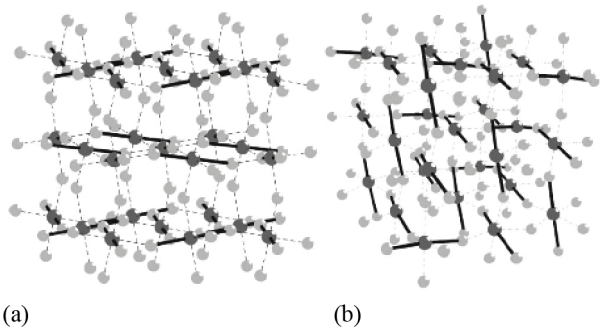


Figure 1.11: (a) The two dimensional *C*-type orbital ordering in $LaMnO_3$ compared to the three-dimensional orbital ordering in (b) $BiMnO_3$. The bold lines represents the JT-distortion in the MnO_6 octahedra. The figure is adapted from Ref. 75.

pathways are generated from orbital ordering that ensures half filled d_{z^2} orbitals pointing towards empty $d_{x^2-y^2}$ on the neighbouring manganese and generates a three dimensional orbital ordering [Figure 1.11(b)]. This is in good agreement with the Goodenough-Kanamori-Anderson rules where this type of orbital interaction is predicted to be strongly ferromagnetic when the M–O–M angles are close to 180° which explains the ferromagnetism in $BiMnO_3$. The last two pathways have empty $d_{x^2-y^2}$ orbitals pointing towards each other, this interaction is weakly antiferromagnetic which gives rise to a small frustration in the system but not enough to break the strong ferromagnetism.[75]

In YVO_3 the orbital ordering is also directly related to the magnetism. In YVO_3 the orbital ordering drives a preferred formation of magnetism and a rearrangement of the orbitals drives a change in the magnetic properties. At room temperature the material is paramagnetic, consisting of an orthorhombic unit cell with space group *Pbnm* with a local *G*-type orbital ordering on the V^{3+} d^2 ions.[77] When cooling the material to 200 K a phase transition to a monoclinic unit cell with $P2_1/a$ symmetry appears, in this phase the orbitals keep a *G*-type ordering (out-of-phase along

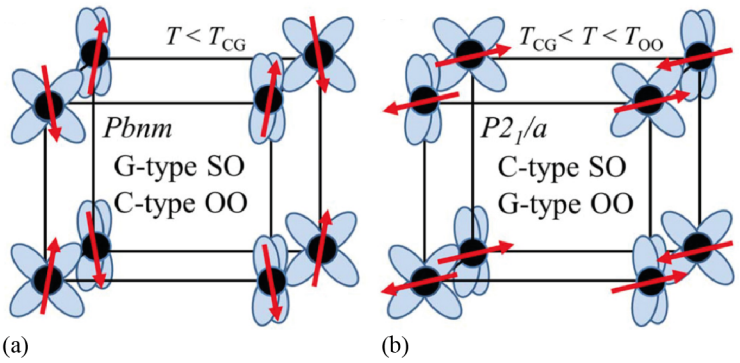


Figure 1.12: A schematic ordering of the vanadium orbitals with C-type ordering and G-type ordering in YVO_3. (a) Schematic presentation of the orbital and spin ordering of the phase below T < 77 K with C-type orbital ordering and G-type spin ordering. (b) The orbital and spin ordering of the phase 77 K < T < 200 K with G-type orbital ordering and C-type spin ordering. The figure is adapted from Ref. 77

the c-direction) but with a ferromagnetic C-type ordering of the magnetic spins, Figure 1.12(b).[78,79] At $T = 116$ K the spins align into a G-type antiferromagnetic ordering and at $T = 77$ K the structure changes into an orthorhombic unit cell with $Pbnm$ symmetry with the orbitals switched into a C-type ordering in phase along the c-direction Figure 1.12(a). These magnetic transitions are expected to be driven by the change in orbital ordering at each transition in YVO_3.[77,80]

1.3.2 Hybrid improper ferroelectricity from orbital order

Orbital ordering is also strongly correlated to the physical properties in molecular perovskites which have drawn a lot of attention within the last 10 years.[81,82] The molecular perovskite analogues have been interesting because of their ability to benefit from the properties of inorganic and organic building blocks from which they are constructed gives more structural flexibility. In their crystal structures, metal ions are connected by an organic linker, creating open frameworks.[83] The materials are relevant to gas adsorption and separation,[84] polymerisation,[85] hydrogen storage,[86]

magnetic ordering,[87] and can show extreme positive and negative thermal expansion.[88]

The use of molecular cations as links between the metal ions makes the metal–metal interaction much weaker (because of the larger separation in superexchange interaction) and it is possible to easily separate the strong correlations between orbitals, magnetism, and electron charge compared to the transition metal oxides. Furthermore, the use of a molecular cations gives rise to more complex multipolar degrees of freedom.

A subgroup of the molecular frameworks are the molecular perovskite analogues guanidinium transition metal formates with general formula $[C(NH_2)_3]M(HCOO)_3$. The structure of guanidinium transition metal formate is similar to the conventional perovskites but the oxygen linker is replaced by a formate ion ($HCOO^-$), and the A-site cavity is filled by a molecular guanidinium cation instead of metal cation.[89] By using a molecule as A-site cation, the number of degrees of freedom increases because the molecule can order in many different ways.[90]

In Ref 41, Stroppa *et al.* studied the hydrogen bonding between the guanidinium and the formates in $[C(NH_2)_3]Cu(HCOO)_3$. The ordering of guanidinium alone gives *Pnna* symmetry. They realised that the presence of Cu^{2+} JT order lowered the symmetry to $Pna2_1$. The JT local modes on the Cu^{2+} ion are nonpolar, and the correlated JT distortion breaks the inversion symmetry through the coupling to the formate ion which is hydrogen-bonded to the guanidinium, generating additional atomic displacement of the molecular cation group [Figure 1.13]. The displacement on the A-site then gives rise to small induced dipole moments which sum up to give a net component and therefore a ferroelectric polarisation. Furthermore, in this

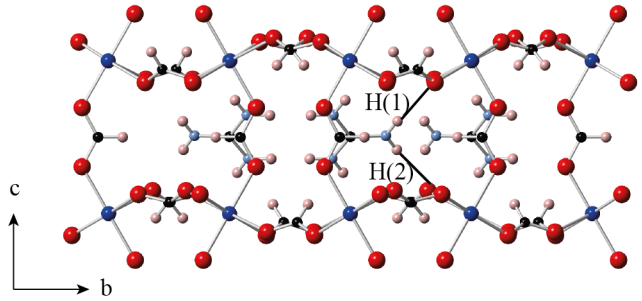


Figure 1.13: Coupling of the JT modes to A-site group arms through the hydrogen. Blue are the Cu ions, red O ions, black C ions, turquoise N ions, pale pink H ions, and the hydrogen bond is marked as a black line. The JT distortion controls the guanidinium orientation. The figure is reproduced from Ref 41.

copper formate the weak ferromagnetic component is coupled to the polarisation and they are mutually reversible, thus making the material a magnetoelectric multiferroic. The predicted polarisation is small but the rich variety of modifications in these materials can potentially develop new areas in the field of multiferroics.[41] Coupling between orbital order and bulk polarisation is also observed in some transition metal oxides. One of the most studied ferroelectric materials where the polarisation is linked to the ferroelectric transition is $BaTiO_3$.[35] The phase digram of $BaTiO_3$ consists of four different phases spanning cubic–tetragonal–orthorhombic–rhombohedral symmetries.[40] In the cubic phase the Ti^{4+} ion is located in the centre of the cube coordinating to six oxygens. The Ti^{4+} undergoes a SOJT distortion and displaces in a rhombohedral-like distortion with shortening of three bonds. In the cubic state that displacement affects the next neighbour to randomly distort in any direction not pointing toward the nearest neighbour and generates local disorder. When the system is cooled the energy barrier to this random nearest neighbour distortion becomes too high and the displacements start to order throughout the structure. When the material reaches the low temperature rhombohedral phase, the

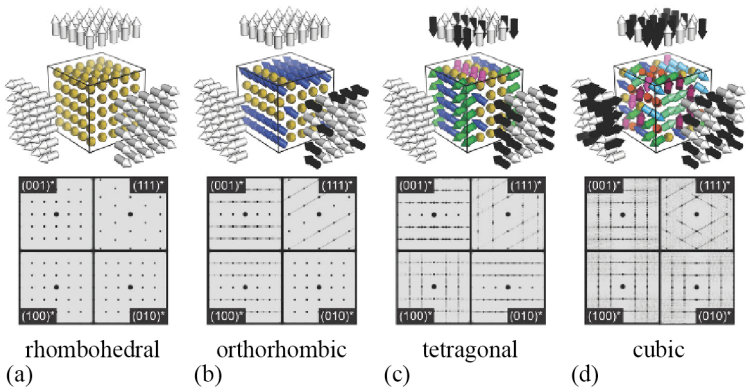


Figure 1.14: Representation of the ordering of the atomic displacement in the four phases of $BaTiO_3$. (a)–(d) is a part of the simulated MC configuration of the Ti displacement and underneath sections of the single crystal diffuse scattering pattern for each phase are shown. The black and white arrows shows the polarisation direction of each corresponding column of Ti centres. The figure is adapted from Ref. 40.

displacements are all ordered by pointing in the same direction [Figure 1.14].[40] The SOJT is here coupled to the polarisation of the Ti displacement which causes the ferroelectric phase transition.[34]

1.3.3 Colossal magnetoresistance

Perhaps one of the most studied families of the perovskites are the manganites.[10,91,92] This family of materials has a very complicated phase diagram, where strong couplings between orbital, spin, and charge gives rise to a broad variety of physical properties [Figure 1.15(a)].[93] The main reason this family of perovskites has been of scientific interest is because of the materials ability to show colossal magnetoresistance (CMR).[94] Magnetoresistance is a phenomena where a large change in electric resistance of a material appears when a magnetic field is applied [Figure 1.15(b)]. Not only is this phenomenon fascinating from a scientific point of view, but CMR is itself of great technological interest to magnetic storage and sensors.[25,95]

The main CMR compounds that have been studied have the composition $La_{1-x}A_x$

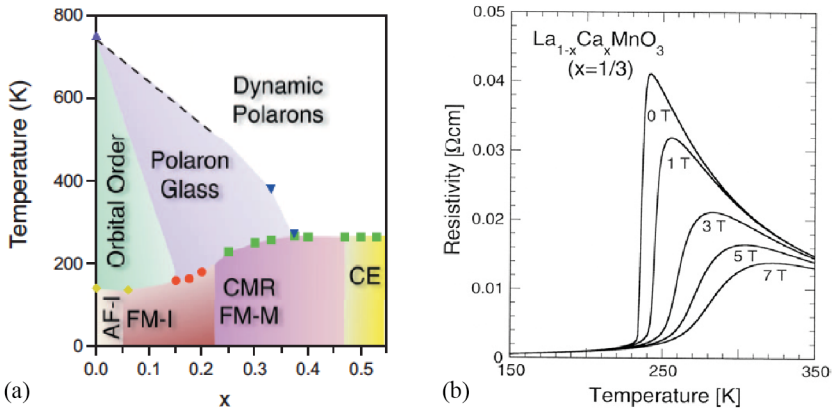


Figure 1.15: (a) Phase diagram of $La_{1-x}Ca_xMnO_3$ showing the different magnetic phases across composition. (b) When an applied magnetic field is added to $La_{1-x}Ca_xMnO_3$, the resistivity changes dramatically. The figures are adapted from Ref. 96,97.

MnO_3 (A=Ca, Sr, or Ba).[98–102] In these perovskite manganites the lattice, magnetism, orbital, and charge properties all rely on the Mn d electrons, where the number of electrons are related to the oxidation state on the A-site cation. The parent compound of this family is $LaMnO_3$ (see section 1.2.2) in which an orbital order/disorder transition occurs with temperature. This transition is the same that precedes the CMR itself within the doped manganites [Figure 1.15(a)].[103] Therefore, $LaMnO_3$ itself has been well investigated to understand how the orbitals arranges throughout the structure in the disordered phase.[104,105]

However, by doping the A-site with a metal with a lower oxidation state, the number of electrons in the d orbitals decreases and a mixed phase of JT-active Mn^{3+} and vacancies of JT-inactive Mn^{4+} ions appear.[106] The number of electrons in the d orbitals of $La_{1-x}A_xMnO_3$ can be determined by $4-x$, and by changing the concentration of x, a variety of different magnetic and structural phases can be accessed [Figure 1.15].[96]

From the phase diagram in Figure 1.15(a) it is clear that the doped manganites

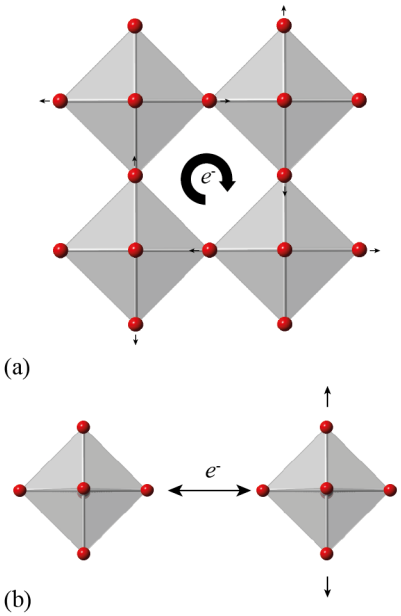


Figure 1.16: Comparison of (a) the polaron state and (b) the normal JT distortion. In the polaron state the e_g electron is shared over several MnO_6 octahedra, causing a small displacement on each octahedron, as compared to (b) the classic JT distortion, where the e_g electron is entirely localised on a single MnO_6 octahedron.

contain charge and orbital ordering in a variety of functional condensed phases.[103] By doping in a metal with lower oxidation state, three out of the $4 - x$ d electrons fill up the t_{2g} states while the location of the $1 - x$ electron occupying the e_g state has not been clear. The localisation of this e_g electron has been the subject of several experimental and theoretical studies.[107,108] It has been suggested that it goes into a linear combination of e_g orbitals and jumps between unoccupied e_g states on the manganese site. As a consequence of the electron delocalised over many atoms the MnO_6 octahedra will be less distorted compared to the end member but the distortion will be distributed over many atoms and generate a strong microscopic electron–phonon coupling, known as a polaron [Figure 1.16(a)].

In CMR materials it is expected that this electron–phonon coupling competes with double exchange interactions *via* the JT active Mn^{3+} ions. At the right doping

a transition from a ferromagnetic-metallic state with the e_g electron located in the conduction band into a inhomogeneous paramagnetic-insulating polaron state occurs on elevating the temperature [Figure 1.15(a)].[109,110] It has been suggested that this strong correlation generates the CMR state in the doped manganites.[93,94] Experimentally, this behaviour has been studied using several experimental methods. One study examined the Mn–O distances across temperature from Rietveld refinement and PDF analysis of neutron data at the composition x=0.22 where the metallic CMR state appears.[111] They did not observe any changes in the Mn–O distances across temperature using Rietveld refinement. Furthermore, the PDF analysis did not show any local JT distortions in the low temperature metallic phase with the e_g electron stabilised in the conduction band with no JT-distortion on the MnO_6 octahedra. As the material is heated and goes into the insulating state (polaron state) it was observed from the data that the MnO_6 octahedra start to distort. The authors analysed whether the state was a two-phase system consisting of distorted and undistorted MnO_6 octahedra or if a single phase appeared. They did not observe any phase separation; instead the MnO_6 octahedra had a smaller distortion amplitude compared to the end member ($LaMnO_3$) which is in good agreement with the suggested polaron state. No detailed picture of the structure in the polaron state was presented.

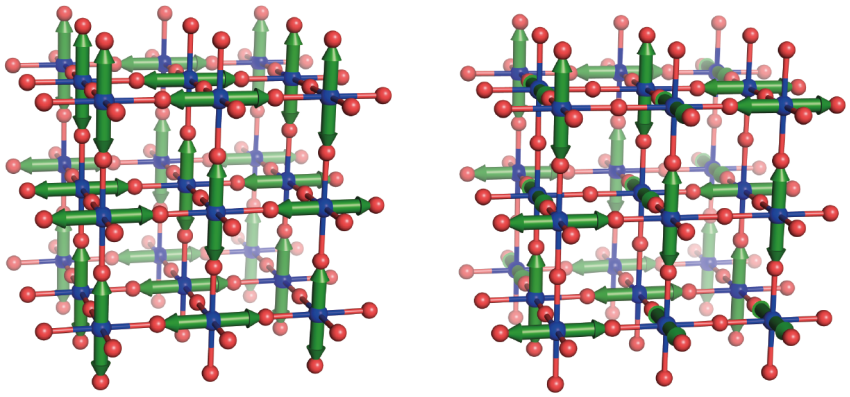
Nevertheless, this study did shed light on one of the main issues in the $La_{1-x}Ca_xMnO_3$ studies: namely, the absence of experimental evidence showing a clear picture of the polaron state and its relationship to CMR in these manganite perovskites.[103] In Chapter 5 of this thesis I study the local structure of $La_{1-x}A_xMnO_3$ across a broad range of compositions and temperature.

1.4 Orbital disordered states

In the previous section I introduced orbital ordering and the corresponding effect on crystal structure and relation to the physical properties. However, orbitals need not adopt an ordered arrangement. In orbital disordered states, long range order disappears, and this will reduce the strain on the lattice and the structure will normally shrink in a certain direction. As in the ordered state the orbital disordered state has an effect on the physical properties. For disordered arrangements one expects strong local coupling between neighbouring states, and, so one key problem is determining local orbital order and its effect on properties in a material. With the easy access to powerful computers the modelling of these disordered states has become more common. In this section I will present some of the most common ways to model orbital disorder related to this thesis.

1.4.1 3-state Potts model

Multiple studies have used a Potts model to analyse orbital disordered states in materials.[112,113] To understand the Potts model it is necessary first to understand the Ising model. The Ising model describes any system with binary degrees of freedom. It is often used to model magnetic materials in which strong anisotropy reduces spin degrees of freedom to "up" or "down" states, for example.[44] The Potts model is a generalisation of the Ising model to an arbitrary number of states. In 3-state Potts (3SP) model the components adopt any one of three possible states.[113] It is a natural model for JT active systems since the elongated axis aligns along one of the three axes (x, y or z) in a crystal lattice. However, this does not make the



(a) (b)

Figure 1.17: Orbital order/disorder on a cubic lattice, the green arrows shows the direction of the JT elongation. (a) C-type orbital ordering. (b) 3-state Potts model on a cubic lattice with JT elongation to be short range ordered but long range disordered.

alignment of orbitals entirely random: the interaction between two sites depends on both the JT elongation of these sites and the direction of the nearest neighbour bond between them. Perpendicular interactions are always favoured whereas parallel interactions are only allowed when the resulting elongated axes do not point directly at each other. These rules can be used to make a Hamiltonian to generate a model which exhibits short range order but long range disorder displayed in Figure 1.17(b). Unlike the ordered C and G type ordering, fixing a single orbital orientation on a metal ion does not determine the orbital orientation on each metal ion throughout the crystal lattice.

In Ref 114 Ahmed *et al*. used a 3-states Potts model to study the orbital disordered state in $LaMnO_3$. They reproduced the order parameter behaviour measured in resonant X-ray scattering experiments from an anisotropic 3SP model which describes a meaningfully local arrangement of the orbital disordered state in $LaMnO_3$.

1.4.2 Polaron glass

The electron–phonon coupling known as polarons as introduced in section 1.3.3 can also arrange in a static disordered state which is called polaron glass. In the phase diagram of $La_{1-x}Ca_xMnO_3$ the term polaron glass appears [Figure 1.15], and is a state where the polaron displacement is static with short-range correlations indicating a glasslike state. This state is very similar to the 3SP model described above but instead of being charge-ordered the electron is shared over several MnO_6 octahedra with a minor JT distortion. As the polaron glass turns into the dynamic polaron state the displacement becomes dynamic.[96]

A study of $La_{1-x}Ca_xMnO_3$ using inelastic scattering techniques observed that the ordering of the polarons in the paramagnetic state of $La_{0.7}Ca_{0.3}MnO_3$ only spanned a length scale of 1 nm and introduced the polaron glass state.[93,115] It is still an ongoing process to understand how the charge-ordering occurs in $La_{1-x}Ca_xMnO_3$.[116]

In Ref 117 Senn *et al.* used a highly structured small polaron to explain the Verwey structure (where changes in magnetic, electrical, and thermal properties appear) in the charge-ordered magnetite (Fe_3O_4). The material consists of JT-active Fe^{2+} and non-JT-active Fe^{3+} ions with the transition occurring at $T_V = 125\,K$.[118,119] The low-temperature structure is monoclinic with Cc symmetry in which Fe^{3+} occupies the tetrahedrally coordinated A site and a 1:1 order of Fe^{2+} and Fe^{3+} is expected to occupy the B-site. Senn *et al.* used single crystal diffraction to realise that an electron was shared over three Fe-sites, which they called a trimeron [Figure 1.18].[117] The trimeron causes atomic displacement and transfer of spin electron density, which explains the Verwey transition in Fe_3O_4.

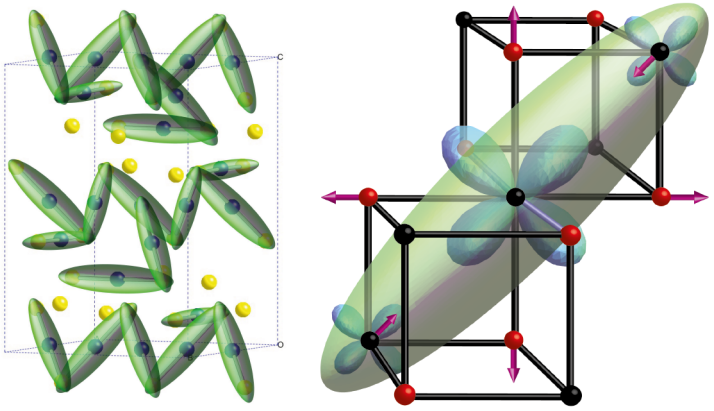


Figure 1.18: (a) Representation of the trimeron distribution (green ellipsoids) in the low temperature magnetic structure with Fe^{2+} (blue) and Fe^{3+} (yellow). Some Fe^{3+} sites do not participate in any trimerons. (b) The green ellipsoid shows the delocalisation of the shared electron from the central B-site across sites. The distortions associated with the trimeron ordering are indicated by purple arrows and the blue bonds indicate the shortening of the JT bonds. The figure is adapted from Ref 117.

1.5 Overview of characterisation methods for ordered/disordered states

Orbital order/disorder can be analysed directly or indirectly using different experimental techniques. Orbital disordered states are hard to analyse due to the lack of periodicity. Therefore is it often necessary to use several methods to get a picture of the arrangement of a orbital disordered state. In this section, I will present the most common ways to recognise orbital disorder.

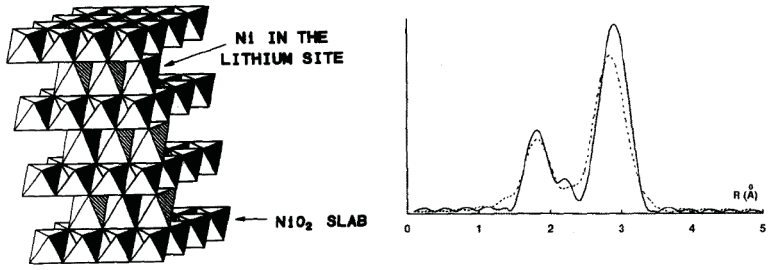
1.5.1 Spectroscopic techniques

X-ray Absorption Spectroscopy

Extended X-ray absorption fine structure (EXAFS) and X-ray absorption near edge structure (XANES) are both X-ray absorption spectroscopy (XAS) techniques and

have been used to probe JT distortions irrespective of the presence of orbital order. The XANES spectrum is the low energy XAS spectrum, and is related to the oxidation state and the coordination number, indirectly related to the JT-active metal ions. Also, the method can identify impurities or vacancies. At the higher end of the XAS spectrum is the EXAFS. The EXAFS signal gives information about the distance and number of neighbour atoms for a specific element in the material. This makes the method element specific which can be an advantage and a disadvantage. The method is a very strong tool in the analysis of amorphous and disordered materials because of the ability to look at the local structure of specific metal ions. The main drawback is the indirect analysis and the limited real-space resolution. Furthermore, the method normally only gives reliable data in the short range real space range (nearest neighbour).[120]

XAS was used to investigate the electrode material $LiNiO_2$ used in batteries. The material exists as a layered structure with Li and Ni cations alternating along the (111) planes. The material consist of trivalent nickel ions which are in the low spin state (t^6e^1) and are JT-active. The crystal structure consist of nickel ions sitting on divalent sites of NiO_2 sheets with edge-sharing NiO_6 octahedra in-between the NiO_2 sheets [Figure 1.19(a)].[121] The material exhibits a strong departure from stoichiometry and its true formula is $Li_{1-z}Ni_{1+z}O_2$. The extra nickel ions substitute the lithium leading to a structural 3D character. In order to maintain the charge neutrality nickel ions are in divalent site and are non-JT-active (t^6e^2). The JT effect was not observed from average structure analysis using X-ray diffraction, so the question was if the nickel ion actually swapped sites as the material got charged/discharged. An EXAFS study was performed to investigate the local nickel environment to con-



(a) (b)

Figure 1.19: (a) The crystal structure of $Li_{1-z}Ni_{1+z}O_2$ with the NiO_2 layers and JT active NiO_6 occupying the lithium sites. (b) Shows the Fourier transformed EXAFS data zoomed shows peaks associated to the Ni–O and Ni–Ni separations. The figures are adapted from Ref 121

firm that the nickel actually had divalent site occupation by observing JT-distortion in the octahedral coordinated nickel ions sitting in the lithium layer. A clear split of the Ni–O peak at $r \simeq 1.5 - 2.3$ Å was observed in the Fourier transformed data which confirmed the existence of JT-distortion on the divalent nickel ions [Figure 1.19(b)]. The reason why it was not observed in the average structure may have been the small amount of trivalent nickel ions which are stable in isotropic environment and can prevent macroscopic distortion. [121]

The XAS method was also used to investigate the spin-glass material $Y_2Mo_2O_7$ where atomic disorder on the Mo site was expected to explain the spin-glass state. [122] The XAS study clearly showed a variation in atomic distances between the Mo ions on the lattice [Figure 1.20]. [123] Although, this displacement for the individual Mo ion was not big enough to generate the spin-glass state in $Y_2Mo_2O_7$. In Chapter 3, I present an alternative model where the Mo ions dimerise to generate disorder that is sufficient to explain the spin-glass state in $Y_2Mo_2O_7$ and is in agreement with these EXAFS data.

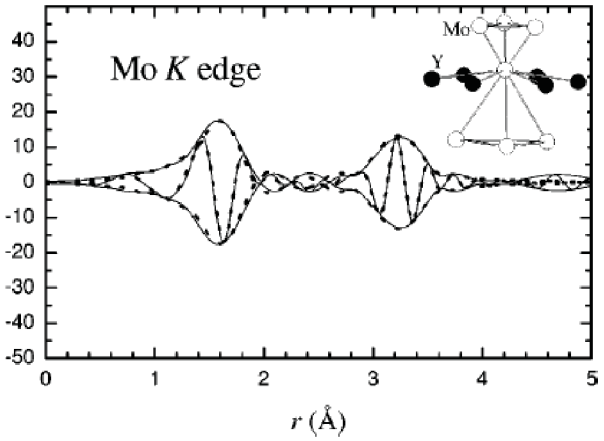


Figure 1.20: Plot of the Fourier transformed EXAFS data using Mo K-edge energy. The data clearly shows a broadening of the peaks associated with the Mo–O and Mo–Mo separations. The figure is adapted from Ref. 123.

Nuclear magnetic resonance

Nuclear magnetic resonance (NMR), is a technique used in a broad variety of subjects spanning biological organic chemistry to solid state chemistry.[124,125] NMR is also an element-specific method using a specific resonance frequency. In studies of solid-state materials, NMR makes it possible to characterise metal environments in materials at atomic dimensions.[125] Solid state NMR can be designed to measure the different sites in solid materials. Disorder on the sites in the material will be observed as a broad peak in the NMR spectrum. This is caused by the fact that NMR covers MHz regime while the vibrations in a solid occur over THz timescale, *e.g* for an orbital-disordered material the orbital orientation can switch direction faster than the method can measure.

The canonical orbital order/disorder transition in $LaMnO_3$ has been confirmed using ^{17}O and ^{139}La NMR measurements. The NMR study showed for the ordered state in the ^{17}O NMR spectra two distinguishable frequencies related to the O1

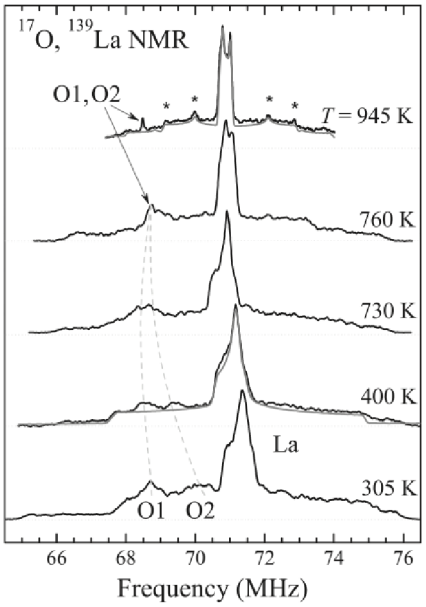


Figure 1.21: The ^{17}O and ^{139}La NMR. The O1 and O2 peaks are split in the ordered state while they merge into a single peak at the disordered states. Asterisks denote spinning sidebands. The figure is adapted from 126.

and O2 sites [Figure 1.21]. At the orbital order/disorder transition the frequencies related to the oxygens merged into a single peak related to a non-polarised e_g orbital occupation showing a clear disorder of the orbital ordering in the crystal structure.[126] The study was limited to only confirming the transition but did not give any suggestions to how the configuration was arranged in the disordered state. Another study used ^{47,49}Ti NMR to investigate the orbital ordering in $LaTiO_3$ and was carried out in Ref. 127, by Kiyama *et al*. $LaTiO_3$ has JT active Ti^{3+} ions generated from splitting the t_{2g} states which gives rise to small distortions. The material is a G-type antiferromagnet (AFM) showing AFM ordering by coupling along the Ti–O–Ti bonds with $T_N = 130\,\mathrm{K}$. It is surprising that the material is an AFM since it would be expected with an antiferro-orbital ordering the material would be ferromagnetic (FM). Because of the weak JT distortions the orbital ordering has not

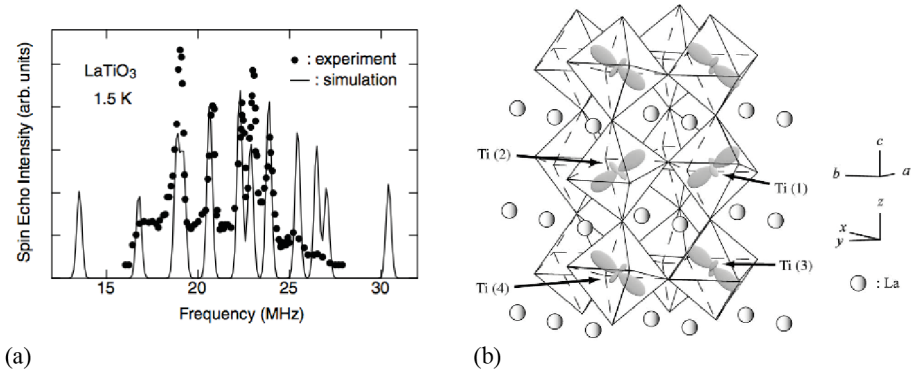


Figure 1.22: (a) Shows the simulated (solid lines) and experimental (solid circles) ^{47,49}Ti NMR spectra of $LaTiO_3$. The simulated data are made from the $1/\sqrt{3}(d_{xy}, d_{xz}$, and $d_{yz})$ model. (b) The crystal structure of $LaTiO_3$ with the expected orbital ordering from $1/\sqrt{3}(d_{xy}, d_{xz}$, and $d_{yz})$ model. The figures are adapted from Ref. 127.

been clear from experimental evidence. Two different models presenting the orbital arrangement from previous studies suggested that either an orbital liquid model appears or the orbitals order in a model expressed approximately by $1/\sqrt{3}(d_{xy}, d_{xz}$, and $d_{yz})$ [Figure 1.22(b)]. The ^{47,49}Ti NMR data were in good agreement with a calculated spectrum of the $1/\sqrt{3}(d_{xy}, d_{xz}$, and $d_{yz})$-like ordering [Figure 1.22(a)]. By calculating the energies and spin-exchange constants this model was in reasonable agreement with obtained data and explains the G-type antiferromagnetic state in $LaTiO_3$.[128]

1.5.2 Magnetic state measurement

Superconducting, quantum interference device

As mentioned above the orbital ordering is directly related to the magnetic state in materials. In the laboratory it is possible to measure the magnetic state of a material by using superconducting, quantum interference device (SQUID) analysis. In Ref. 60, Zhou *et al.* used SQUID analysis to measure the change in Weiss constants

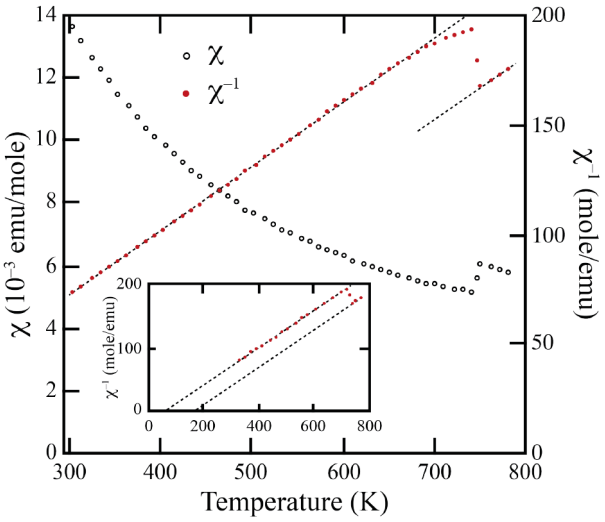


Figure 1.23: Magnetic susceptibility data $\chi(T)$ and $\chi^{-1}(T)$ for a single crystal sample of $LaMnO_3$ showing the transition at $T_{JT} = 750\,K$ and the change in magnetic behaviour. Adapted from Ref. 60.

below and above the orbital order/disorder transition in $LaMnO_3$. It is known that C-type orbital ordering has a direct effect on the electronic transport and magnetic properties of ambient $LaMnO_3$. For the ordered state $LaMnO_3$ is an insulator with strongly anisotropic magnetic interactions, which was evidenced by a Weiss constant $\theta = 52\,K$ that represents ferromagnetism within the (a, c) plane and antiferromagnetic interactions between adjacent (a, c) planes (*i.e.*, along b directly related to the C-type orbital ordering). When the sample was heated above the phase transition at $T_{JT} = 750\,K$, the Weiss constant switched to $\theta = 177\,K$ consistent with isotropic ferromagnetic interactions in the disordered state which is in good agreement with an orbital disordered state [Figure 1.23].[60,129]

1.5.3 Specific heat capacity

Specific heat capacity experiments are an easy way to investigate phase transitions in materials. The method is also indirectly sensitive to orbital order/disorder transi-

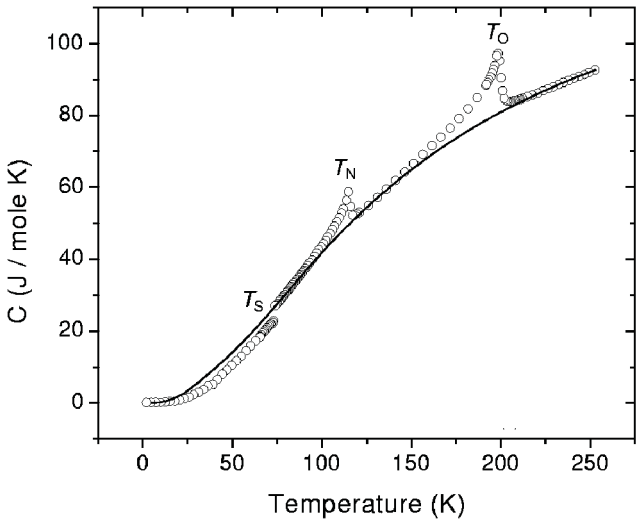


Figure 1.24: (a) Plot of the specific heat *vs* temperature for YVO_3. The anomalies corresponding to the three transitions between orbital ordering at (T_S) AFM ordering at (T_N) and the onset of local orbital ordering at (T_O). The figure is adapted from Ref. 79

tions and is an efficient way to clarify at which temperature the transitions appear. In Ref. 79, Blake *et al*. used specific heat measurements to confirm the temperatures where the reorientation of the orbitals in YVO_3 appeared. This was observed as a clear shift in the data at the three transitions from local orbital ordering to G-type orbital ordering and the final transition to C-type ordering [Figure 1.24]. The energy necessary for the reorientation of the orbitals and magnetic spins appears as absorption of energy in the specific heat diagram, [Figure. 1.24].[79]

1.5.4 Scattering techniques

Resonant scattering

The elastic resonant soft X-ray scattering (RSXS) method is a mixed spectroscopy and scattering technique which can provide information about the long range order of spins, charges, and orbitals in a material. The method uses X-rays to excites a core electron into a unoccupied state close to the Fermi level which creates a

intermediate state. This intermediate transition is very strongly dependent on the properties of the valence shell. The intermediate state decays back to its initial state and a photon with the same energy as the incoming energy will be re-emitted. This energy is kept fixed and the crystal is rotated along an axis and the difference in Bragg intensity is measured. The variation in intensity is related to the symmetry and is a unique method to obtain direct evidence for orbital ordering.[130]

In Ref. 131, Wilkins *et al.* used RSXS to study orbital ordering in the manganite oxide $La_{0.5}Sr_{1.5}MnO_4$. On cooling, $La_{0.5}Sr_{1.5}MnO_4$ undergoes a phase transition into a charge order/orbital order (CO/OO) state at $T_{CO} = 240\,K$.[132,133] The authors used energies near the manganese L_{III} and L_{II} edges directly related to the orbital ordering of the JT distortions on the Mn^{3+} ions to investigate this transition. On heating the sample from low temperatures, the peak related to orbital ordering disappeared at $T_{CO} = 240\,K$ [Figure 1.25(a)] suggesting onset of orbital disorder. This result suggests that the Jahn-Teller distortions in the ordered state of the Mn^{3+} ions coupled with a charge localisation cause large MnO_6 distortions. This distortion causes cooperative displacements of the Mn^{4+} ions to order in alternating layers with the Mn^{3+} ions to layer in-between. This is in good agreement with Goodenough's CO/OO model.[131]

The orbital order/disorder transition in $LaMnO_3$ was studied in Ref. 134, by Endoh *et al.*, using RSXS energies near the Mn K-absorption edge. The collected data showed Mn $3d$ orbital ordering up to $T_O = 780\,K$ where the reflection representing the ordering rapidly drops to zero indicating that the orbital ordering disappears [Figure 1.25(b)].[130,134] This observation also agrees with previous studies of the orbital order/disorder transition in $LaMnO_3$.[62,135]

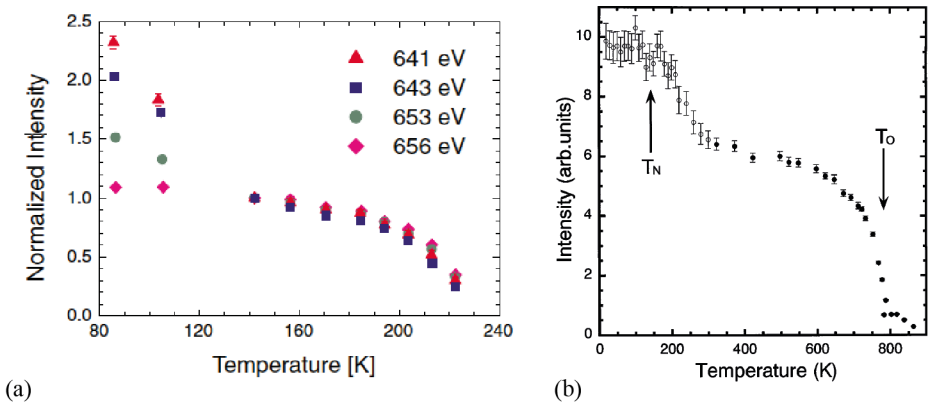


Figure 1.25: (a) Temperature dependence of the integrated intensity of the orbital order peak in $La_{0.5}Sr_{1.5}MnO_4$. The figure is adapted from Ref. 131. (b) Temperature dependence of the normalised intensity of the orbital ordering reflection in $LaMnO_3$, arrows indicating the antiferroemagnetic transition (T_N) and the orbital order/disorder transition T_O. The figure is adapted from Ref. 134.

1.5.5 Coherent elastic diffraction

Diffraction is probably the most used method to investigate crystalline materials. This method may be the principal method for characterise orbital order: bond lengths from the average structure show cooperative JT distortions. The diffraction technique has been used in several studies to investigate the orbital order/disorder transition by simply looking at how the average structure changes across a phase transition. In Ref. 136, Evans *et al.* used average structure investigation to understand the compositional dependence of molecular orientation and orbital order in $[C(NH_2)_3]Cu_xCd_{1-x}(HCOO)_3$. The authors doped the metal formate with JT-active Cu^{2+} ions and observed an orbital order/disorder transition and a multipolar reorientation transition as the composition varied. These transitions were attributed to a combination of size, charge distribution, and percolation effects. As the fraction of Cu^{2+} ions increased the strain effects enforced local coupling between orbital

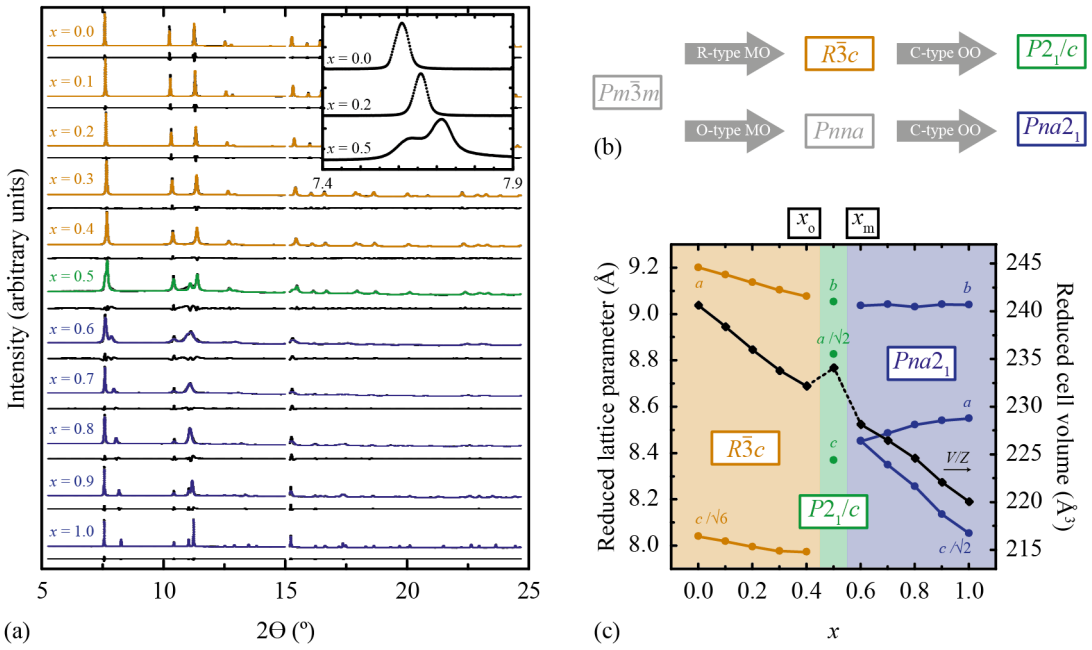


Figure 1.26: (a) X-ray diffraction patterns at RT for $[C(NH_2)_3]Cu_xCd_{1-x}(HCOO)_3$ across composition. The inset shows the splitting of a single reflection upon the transition. (b) the relationship between the three space groups identified. (c) Corresponds to the reduced lattice parameters across the series. The figure is adapted from Ref. 136.

orientations. At a certain composition these become long-range which was clearly observed as a transition into an intermediate state before it turned into the final ordered average structure observed in the diffraction data [Figure 1.26].[136]

Total scattering

One of the most studied JT active compounds investigated using total scattering analysis is the series of CMR perovskite manganites $La_{1-x}Ca_xMnO_3$. The end members and other compositions in the series have been studied using PDF measurements, with the main goal to address how the local structure changes as function of temperature or composition.[109–111,137–140] As introduced in section 1.3.3 by doping with Ca^{2+} the composition of JT-active Mn^{3+} and JT-inactive Mn^{4+} ions change, leading to a variation in local structure observed as a splitting of the Mn–O peak

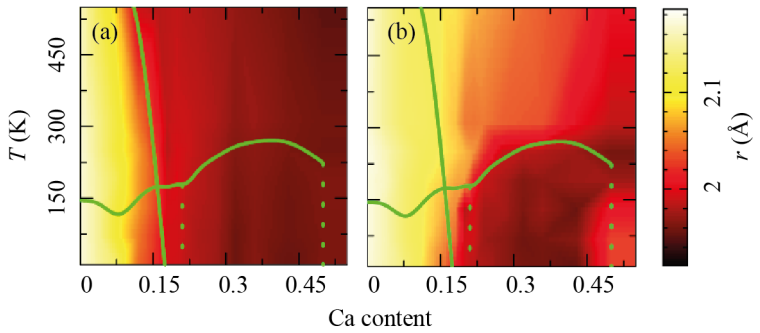


Figure 1.27: Plots of the longest Mn–O distance as function of temperature and composition for the chemical series of doped $La_{1-x}Ca_xMnO_3$. (a) Shows the data obtained from Rietveld refinement and (b) shows the data obtained from PDF analysis. PDF analysis shows sensitivity to the JT distortion and the CMR transition. The solid line curves indicate T_{JT} and T_c phase boundaries. The figures are adapted from Ref. 142.

in the PDF, displayed in Figure 1.27(b). Rietveld refinement of the doped system shows the Mn–O bond as a single distance [Figure 1.27(a)], while the PDF data of the local structure still shows a variation in the local Mn–O bonds. Furthermore, by mapping out the PDF diagram of the end members it was shown that they had very different local and average structure relationships. The local and average structure were almost indistinguishable in $CaMnO_3$ while $LaMnO_3$ formed local ordered clusters of JT distorted domains in the size of 16 Å in the orbital disordered state.[140,141]

In this thesis I examine previously proposed models of the local structure in $LaMnO_3$ and investigate how the local structure changes across composition and temperature in $La_{1-x}Ca_xMnO_3$ using total scattering data, (Chapter 4-5).

PDF analysis also helped to establish a microscopic description of Bi and O′ displacement in the oxide pyrochlore $Bi_2Ti_2O_6O'$ (general formula $A_2B_2O_6O'$). The material has dielectric properties and this is linked to the Bi^{3+} cations which displace in a SOJT distortion.[33,143] The pyrochlore lattice consists of two sublattices; the disordered A_2O' sublattice and the ordered BO_3 sublattice with corner sharing

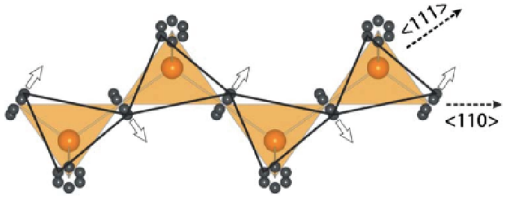


Figure 1.28: Ideal O'Bi_4 sublattice with split-atom Bi positions located on the corners of the orange tetrahedra. The O'Bi_4 sublattice can occur in a zigzag pattern, as shown here for the ideal structure. These distortions are in reality only correlated over short distances.[144]

BO_6 octahedra. Bi occupy the A site where the pyrochlore symmetry imposes O′–Bi–O′ angles of 180°. As a consequence of SOJT distortion of the Bi^{3+} cation this angle will reduce, which in turn can be observed in PDF analysis. A recent study used Reverse Monte Carlo analysis of PDF data to characterise the correlation between local Bi distortions within Bi...Bi pairs [Figure 1.28]. This study indicated that the Bi displacements from its ideal positions correlated over local length scales, which agrees with the idea that pyrochlore compounds are structurally frustrated systems.[144,145]

1.6 Aim and structure of this thesis

The work presented in this thesis concerns the use of neutron + X-ray total scattering to characterise the local structure of canonical transition metal oxides displaying non trivial orbital order or disorder. The thesis aims to address two main topics; first, how the orbitals order in three different transition metal oxides and how the ordering drives the structural changes, and the relation of their orbital arrangements to the physical properties of the material. Second, to study the limitations in state-of-the art PDF analysis in characterising local structure systems with strong static

and dynamic disorder.

The thesis is organised as follows. The majority of the work of this thesis relies on the determination of local crystal structures using diffraction techniques. The types of diffraction experiments, theory, and refinement employed are presented in Chapter 2.

The three results chapters are arranged in terms of the sensitivity of data to orbital ordering. Chapter 3 reports a new model that explains how orbital ordering drives spin-glass formation in $Y_2Mo_2O_7$. The orbitals on the Mo^{4+} site dimerise in pairs and generates a strong enough variation in the superexchange coupling between the two metals to generate enough disorder to cause the spin glass state.

Building on the success of Chapter 3 to characterise complex orbital disordered states, using combined neutron and X-ray total scattering I apply the same techniques in Chapter 4 to investigate the orbital order/disorder transition in $LaMnO_3$. I explore three models, two of which are already presented in the literature and the third proposed by a former student to describe the disordered phase in $LaMnO_3$. The result of fitting the PDF data in the disordered state to the three models surprisingly shows almost no sensitivity to these different models. Nevertheless, I argue that a 3-state Potts description is most strongly supported by my analysis.

In Chapter 5 I make a direct comparison of PDF data at various compositions and temperatures for the CMR family $La_{1-x}Ca_xMnO_3$. I examine three models proposed for the low temperature phase of $La_{0.5}Ca_{0.5}MnO_3$ fitting to new collected PDF data.

The concluding Chapter focusses on the advantages and disadvantages of using PDF analysis to study orbital disorder, informed by the individual studies reported in the earlier chapters. This discussion highlights a number of important challenges and

opportunities for the total scattering community in studying strong-correlated solid materials.

Chapter 2

Methods

2.1 Introduction

This chapter presents the general theoretical background to the key methods I have used to analyse the three materials studied in this thesis. Details regarding the synthesis and specific experimental approaches for each material are given within the relevant chapters.

2.2 Diffraction techniques

The main results in this thesis are derived from diffraction data. Here I will present the principles of the diffraction techniques used. I will begin with introducing the basic principles of scattering theory of the diffraction techniques used to study average structure and local structure. I will also present the more practical aspects of carrying out powder diffraction and total scattering experiments including instrumentation.

2.2.1 Scattering theory

Diffraction has been a fundamental technique for many scientific advances over the last 100 years.[146] Each crystalline solid has its own characteristic diffraction pattern and can be used to identify synthesised samples.[147] The patterns contain information about the crystal structure, geometry, bond lengths, and atom positions, which makes the technique a very strong tool in solid state science.[5,148]

The ability of crystals to diffract X-rays was first observed in 1912 by Max von Laue.[149] The observation of these diffracted beams was recorded on photographic film, resulting in a diffraction pattern related to the atomic structure of the radiated crystal.[150] W. H. Bragg and his son W. L. Bragg were awarded the Nobel prize in 1915 for the first calculation of atom positions within a crystal using X-ray diffraction.[151] W. L. Bragg reasoned that crystals are built up by layers of planes that work as semi transparent mirrors (also known as Miller planes). X-rays are diffracted by these layers in the crystal given by the Miller planes (hkl).[152] Diffraction is possible because the distances between these layers are of the same order as the incident beam wavelength. W. L. Bragg solved the first crytal structure by using the intensities of the Bragg peaks, deriving what we today know as Bragg's law.[153] This basic approach is still used today to calculate patterns of ordered crystal structures in solid state science.[154] Braggs law is described by:

$$n\lambda = 2d_{hkl}\sin(\theta), \tag{2.1}$$

where n is the order of diffraction, λ is the wavelength of the incident beam radiation, d is the separation between the Miller planes of index hkl and θ is the angle between the incoming beam and the diffracted layer.[147] Bragg's law describes the angles at which constructive interference appears. This occurs when the difference in distance travelled by waves diffracted by different planes is equal to an integer number of wavelengths [Figure 2.1].[153] A suitable detector is installed at a known distance from the sample to observe the diffracted X-ray beams. The diffraction from specific Miller plane is observed when Braggs law is fulfilled.[155]

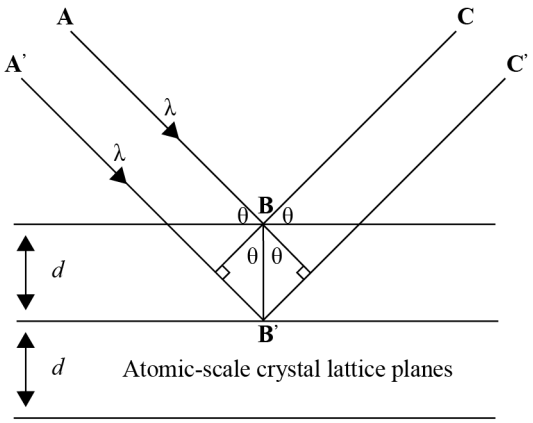


Figure 2.1: An incident parallel beam A scattering from two particles (B and B') separated by the distance d.

The diffraction pattern as a whole represents the Fourier transform of atomic arrangement into reciprocal space. The three dimensional atomic distribution is resolved essentially by transforming the pattern into real space. This is done differently in single crystal diffraction and powder diffraction. In single-crystal diffraction the diffracted peaks contains three-dimensional information of the scattered radiation. In powder diffraction this information is collapsed onto one dimension, which makes it more complicated to analyse.

The peak positions are determined by the unit cell of the crystal. Information about the atom positions within the unit cell are obtained from the amplitudes and the phase of the diffracted beam. For each (hkl) plane the structure factors are described by

$$F_{hkl} = \sum_{j}^{N} f_j \mathrm{exp}[2\pi \mathrm{i}(hx_j + ky_j + lz_j)], \tag{2.2}$$

$$= \sum_{j}^{N} f_j \mathrm{cos}[2\pi(hx_j + ky_j + lz_j)] + \mathrm{i} \sum_{j} f_j \mathrm{sin}[2\pi(hx_j + ky_j + z_j)], \tag{2.3}$$

where f_j is the atomic scattering factor for the j^{th} atom in the unit cell with the coordinates x_j, y_j, z_j. N is the number of atoms in the unit cell. The X-ray scattering factor is linearly proportional to the number of electrons [Figure 2.2].[156] The electron density, ρ, is given by the Fourier transform of the structure factors,

$$\rho(x, y, z) = \frac{1}{V}\sum_{hkl} F_{hkl}\text{exp}[-2\pi\text{i}(hx + ky + lz)], \tag{2.4}$$

where V is the unit cell volume. In diffraction experiments, we do not have access to the complex structure factors (which is also known as the phase problem). Instead, we can use intensities which are related to the structure factor by,

$$I(hkl) \propto |F(hkl)|^2 \tag{2.5}$$

A common approach to overcome the phase problem is to use charge flipping; an iterative structure solution method based on the strongest reflections in the powder pattern. The initial phases are used to drive the structure refinement of the electron density in real space and are used to asses the structure factor in reciprocal space in an experimental diffractogram.[152,157,158]

2.2.2 Powder diffraction

Powder diffraction is a straightforward way to confirm the phase purity of a synthesised sample. A powder sample consists of many small crystals randomly oriented in all directions. Statistically, each set of planes will then be presented from crystals orientated in the Bragg angle, θ, of the incident beam, and thus diffraction will be observed. The random orientation of crystals means that the diffracted beam will

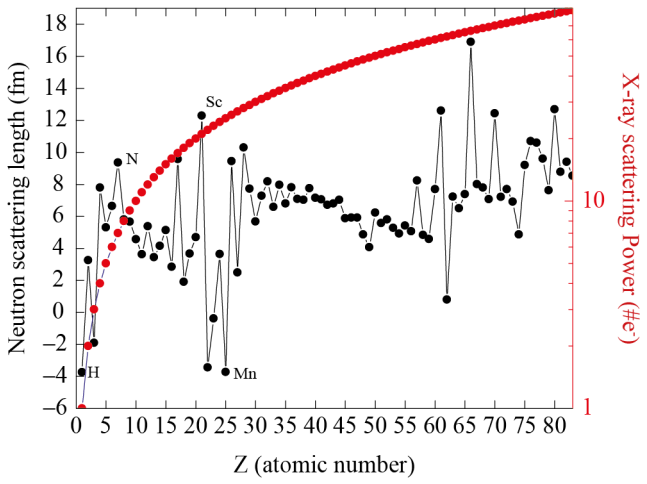


Figure 2.2: Plot of the variation in scattering length between atoms. The scattering lengths of atoms are randomly distributed for neutron scattering while the X-ray scattering factor increases linearly. The X-ray scattering lengths are plotted on a logarithmic Y-axis (right axis).[159]

be displayed as cones of the scattered beam. Intensities of the cones are integrated and transformed into a one-dimensional powder pattern. From the powder pattern three main factors reveal information about the crystal structure: the Bragg peak position, the intensity of the peaks, and the shape of the peaks. The peak positions depend on the size and symmetry of the unit cell. The intensity is affected by the coordinates and electron density (for X-rays) of the atoms and their thermal parameters. Also, if the powder crystals are not randomly orientated in the sample, it is said to display preferred orientation, and this also affects the peak intensity. Finally, grain size, stress, and strain all affect the peak shapes.[160]

Unknown powder patterns are analysed by identifying and indexing the diffracted Bragg peaks and the unit cell symmetry is then proposed. The proposed unit cell symmetry can then be verified by carrying out a Pawley refinement.[161] A Pawley refinement only concerns the unit cell and the symmetry of the cell and refines the

intensities arbitrarily. To refine the exact values for the intensities of the pattern, a full structural model is necessary. When a full structural model is known, a pattern is normally analysed using the Rietveld refinement method. The Rietveld method involves a least-squares approach to refine the structural parameters, including atom positions.[162] The Rietveld method produces a calculated powder pattern, obtained *via* the structure factor expression (equation 2.2), and varies the model to improve the fit to experimental data. The difference between the model and data is calculated using the minimisation function for the refinement and is the function χ^2 obtained from equation,

$$\chi^2 = \sum_{i=1} w_i (Y_\mathrm{o} - Y_\mathrm{c})^2, \tag{2.6}$$

where w_i is a weighting factor, Y_o and Y_c are the observed and calculated powder patterns.

The quality of a refinement is normally evaluated by the R-factor which is calculated as:

$$R = \frac{\sum |F_o - F_c|}{\sum |F_o|}. \tag{2.7}$$

The generalised R factor, called R_w, is the most commonly used value, and is described by,

$$R_w = \sqrt{\frac{\sum w(F_o^2 - F_c^2)^2}{\sum w(F_o^2)}}, \tag{2.8}$$

which gives a better indication of whether to remove or add refined parameters from

a refinement.[163]

Rietveld refinement can be carried out using various software packages. In this thesis Topas academic V 4.1[164] has been used to refine the lattice parameters, thermal parameters, and atom positions across temperature for neutron, X-ray, and combined X-ray and neutron data.

Experimental powder X-ray diffraction

X-ray radiation used for crystallography is normally obtained either from in-house instruments or at synchrotrons. In in-house, X-rays are generated in vacuum tubes in which electrons are fired with high energy into target materials to produce characteristic wavelength. The generated X-ray beam is sent through a filter or a monochromator to isolate the desired wavelengths, so for Cu nothing else except the Cu $K\alpha$ radiation wtih average wavelength 1.5418 Å for Kα1, Kα2 is exposed to the sample. The wavelength is an important consideration in the design of a diffraction experiment, for example, Cu $K\alpha$ causes fluorescence in samples containing iron or cobalt and results in high background scattering in the powder pattern. In these cases either using a different target material or a synchrotron radiation source can be desirable.[147]

Synchrotron radiation sources generate X-rays from a particle accelerator, where an electric field accelerates particles, normally electrons. The electrons are accelerated until they nearly approach the speed of light, released into a storage ring which consists of straight sections joined together by several bending magnets. At the bending magnets and insetion devices, the electrons emit X-rays which are emitted in a small collimated cone, that is passed out to specially designed beamlines for

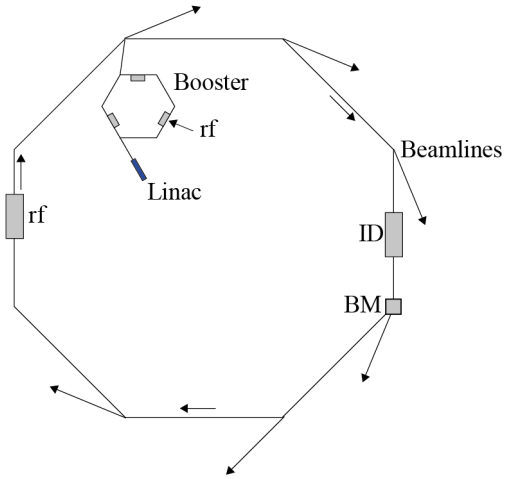


Figure 2.3: The general layout of a synchrotron showing the LINAC where the electrons are produced and accelerated in the booster ring and sent into the storage ring. A bending magnet (BM) and insert device (ID) is where the X-rays are generated and guided to the beamlines for experimental use.

further collimation [Figure 2.3].[165] The collimation depends on what experiments the specific beamline is designed to carry out. For example, short wavelength (high energy) X-rays are more penetrative and can obtain a broader range of reciprocal space vectors (Q). This is of high interest when obtaining *in-situ* or total scattering data, where short collection time or access to large range of reciprocal space is necessary.

The coherent scattering with the electron shells is strongly $\sin(\theta)/\lambda$ dependent which means that scattered intensity decreases significantly at high Q. The rule of thumb is when Q reaches $25\,\text{Å}^{-1}$ the scattering power is very low, and data for values of greater Q are typically hard to analyse.[166]

Neutron powder diffraction

Neutron powder diffraction is another diffraction method, which exploits the interaction between neutrons and the nuclei of atoms in a material. Neutrons are electrically neutral but magnetic polar particles which interact with the nuclei *via* strong nuclear force and with magnetic moments *via* the electromagnetic force.[167] In quantum mechanics, materials have both a particle and wave-like nature, which is also true for neutrons, making it possible to use neutrons as a crystallographic tool. The wavelength of a neutron can be described by the de Broglie equation:

$$\lambda = \frac{h}{m_{\mathrm{n}} v}. \tag{2.9}$$

Here h is Planck's constant, m_{n} is the mass of the neutron and v is the velocity of the neutron ($m_{\mathrm{n}} v$ is the same as the neutron momentum).[167] Similarly to X-rays, neutrons can interact with an atom either by scattering or absorption. During scattering, the neutron can interact with the nucleus in two ways: (i), elastic scattering, where no energy is transferred (diffraction) and this can be coherent or incoherent; (ii) inelastic scattering, where the energy of the scattered radiation is different from the incident radiation. This second type of interaction is used in inelastic neutron spectroscopy (INS) and measures the energy difference of wave vectors of vibrational or magnetic excitations.

In diffraction studies neutron diffraction possesses some advantages compared to X-ray diffraction. Some of the main advantages of using neutrons are as follows:

(i) The scattering cross section does not depend on the number of electrons

[Figure 2.2] which makes it possible to study light atoms (*e.g* hydrogen or lithium);[168]

(ii) Neutrons interact weakly with matter implying that neutrons probe the bulk rather than only the surface. The ability of neutrons to penetrate matter, makes it possible to perform neutron scattering in a broad variety of sample environments;[169]

(iii) The magnetic moment enables to obtain magnetic structures in materials;[170]

(iv) The coherent scattering intensity is independent of Q, so there is no decrease in scattering power at high angles like in the case of X-rays.[167]

Neutron diffraction is a very powerful diffraction tool but the expensive setup and long collection times suggests that neutron experiments should only be performed when other methods are inadequate.

Neutrons can be generated by fission or spallation. In a fission reactor (such as the ILL*) the neutrons are produced as a by-product of nuclear fission. The reactor neutron sources produce a highly continuous flux of neutrons. This method is becoming less common due to the radioactive waste produced and highly-enriched fuel required for a fission reactors to run. The second option are spallation sources, where neutrons are generated by bombarding a heavy metal material with high energy protons. Spallation begins with an ion source that produces negative charged hydrogen ions. The ions are accelerated to very high energies in a linear accelerator and passed through a foil to strip off their electrons. The remaining protons are then sent into a synchrotron and accelerated to high speed and accumulated in clusters.

*https://www.ill.eu/about/what-is-the-ill/

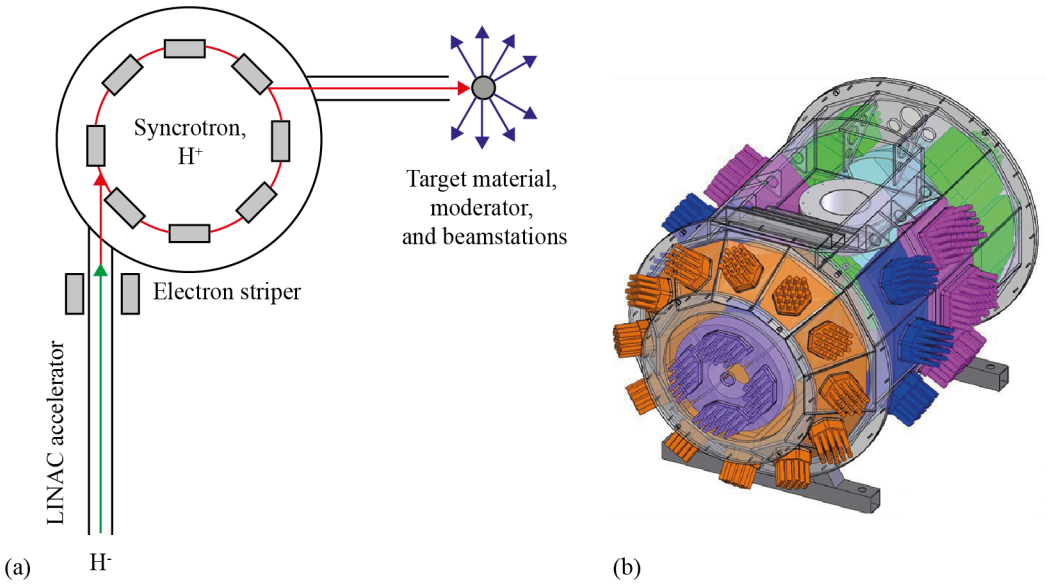


Figure 2.4: (a) Schematic setup of a neutron spallation source. (b) POLARIS diffractometer and arrangement of the detector banks.[171]

The clusters of protons are focused towards a target material. The high–energy pulse of protons releases neutrons from the target material in a sharp pulse with a broad variety of high energies. The sharp pulse of neutrons is then slowed down to use for condensed matter research by guiding it through a moderator. The pulse is then directed to a variety of instruments with special optimised geometry for a variety of specific research purposes. The experimental setup of a spallation source is shown in Figure 2.4. With the spallation approach, neutrons arrive in pulses of different wavelengths — the wavelength is determined from the time it takes for the neutrons to travel from the source to the sample through the detector banks, known as time of flight (ToF). When the ToF is known the velocity can be calculated, the exact wavelength corresponding to a specific d-spacing can be calculated using de Broglie wave equation (2.9). When the wavelength is known, the d-spacing can be determined from Bragg's law (2.1) and the structure can then be analysed. In this

thesis all neutron diffraction experiments presented have been carried out using the ISIS pulsed neutron facility in U.K.*

2.3 Total scattering

In a powder pattern the Bragg peaks reveal the average structure, but all the scattering between the Bragg peaks is normally described as background. In practice this background contains information on the correlations between atoms on a local scale and in particular the deviation from the average structure. This form of scattering is called diffuse scattering. The main reason for ignoring the diffuse scattering is the low intensity which makes it difficult to distinguish from background noise, but this diffuse scattering can have essential information to help understand many materials properties.[145,172,173]

For materials such as liquids and glasses with no long-range order, the characteristic Bragg peaks are absent. To understand short-range order in these materials total scattering has been essential. Therefore, this technique was principally developed to study these types of materials.[174,175] The improvement on instrumentation has made it possible to collect data with much higher resolution and enabled the study of materials that exhibit long-range order but have short-range disorder or *vice versa*. The interest to study the local-range of more crystalline materials is that the local structure is key for physical properties. The local structure can shed light on the correlated ordering between atoms which drives the symmetry in the average structure and is related to the physical properties of a material.[176]

Where Bragg scattering only contains single particle information the diffuse scat-

*http://www.isis.stfc.ac.uk/about/how-isis-works6313.html

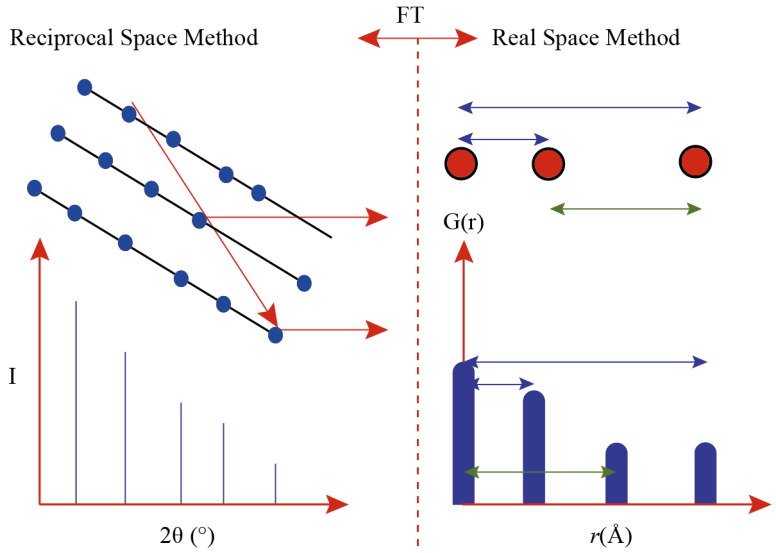


Figure 2.5: (left) Represents a scattered beam in reciprocal space measured as intensities in against scattering angle. (right) Representation of the Fourier transform of the reciprocal space data into real space which gives a histogram of interatomic separations.

tering contains information on two-particle interactions.[177] By Fourier transforming the total scattering data a real space histogram of interatomic distances is obtained, also known as pair distribution function (PDF) [Figure 2.5]. The PDF is effectively a histogram of interatomic separations, making it a very powerful tool for determining the local structure in materials.[145] The peak positions in the histogram corresponds to bond length and the area under a peak gives the coordination number of an atom.[178] The real-space information is similar to that of EXAFS, but the PDF technique is not element specific. Furthermore, PDF can go to longer range order and it is much easier to calculate.[177]

2.3.1 Theory of total scattering

Different formalisms are used in the total scattering community which can lead to confusion with regards to nomenclature. PDFs can be defined by a number of

related equations, which contain the same fundamental information. In this work I have used the definitions by Keen, Ref. 179, in particular I will use $F(Q)$ for total scattering structure factor and $D(r)$ for the PDF (*i.e.* the differential correlation function). A PDF is composed of all the individual partial correlation functions:

$$g_{ij}(r) = \frac{n_{ij}(r)}{4\pi r^2 \mathrm{d}r c_j \rho_o}, \tag{2.10}$$

where $n_{ij}(r)$ is the number of particles of type j between distances r and $r + \mathrm{d}r$ from a particle of type i, c_j is the proportion of species j in the material, and ρ_0 is the average number of density in the material. From this expresion we can determine the total radial distribution function, given here for neutron scattering:

$$G(r) = \sum_{i,j=1}^{n} c_i c_j \bar{b}_i \bar{b}_j [g_{ij}(r) - 1]. \tag{2.11}$$

Here b_i is the coherent bound neutron scattering length of species i. This function is related to the scattering function $F(Q)$ via Fourier transformation:

$$G(r) = \frac{1}{(2\pi)^3 \rho_0} \int_0^\infty 4\pi Q^2 F(Q) \frac{\sin Qr}{Qr} \mathrm{d}Q. \tag{2.12}$$

In this thesis $D(r)$ has been used to present PDF data. This function is related to $G(r)$ by the following:

$$D(r) = 4\pi r \rho_0 G(r). \tag{2.13}$$

The total scattering correlation function obtained from X-ray total scattering is not straightforward because the X-ray scattering factors are Q dependent. This

is not a problem for single element systems, but approximations are necessary to transform multi-element systems. Recently, a way to calculate the exact PDFs from any structure using X-rays has been published.[166] The ability to convert X-ray total scattering data in to real space has made X-ray PDF data much more reliable.

In this thesis I carry out combined neutron and X-ray PDF refinements and in both cases the data are referred to as $D(r)$.

2.3.2 Total scattering measurements

In total scattering experiments the diffuse scattering is of interest and makes the experiments slightly more complicated because of the weak intensity from diffuse scattering compared to Bragg peaks.[176] It is therefore essential to measure the background of the sample environment and subtract this from the measured data to remove as much background as possible.

Equation 2.12 contains an integral over infinite Q, the experimental limitation of finite $Q_{\max}$ introduces artefacts in $D(r)$. Therefore, a large Q-value minimises the truncation effect on the Fourier transformed data (which has a big effect on the resolution in real space). Q is related to θ and λ by:

$$Q = \frac{4\pi}{\lambda}\sin\theta. \tag{2.14}$$

To obtain high resolution real space data it is necessary to collect data at high Q which is derived from the data by:[180]

$$\Delta r = 3.791/Q_{\max}. \tag{2.15}$$

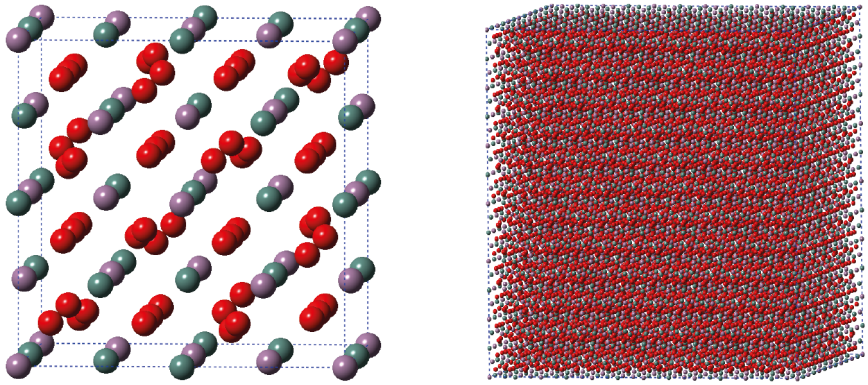
Since $Q_{\max}$ is directly related to the resolution, the choice of instrument is important to obtain a reasonable PDF. From equation 2.14, Q depends on the wavelength: the shorter the wavelength is, the higher the real-space resolution that can be obtained.[173] This limits the resolution of data collected in a laboratory (normally Cu Kα X-rays) with a $Q_{\max} = 8.15\,\text{Å}^{-1}$ which results in a Δr value that is too large for most purposes. New laboratory diffractometers with Ag or Mo as the target material are now available, with a $Q_{\max}$ of 22.48 and $17.72\,\text{Å}^{-1}$, respectively. The highest resolution available is generated at central facilities where high energy beam lines, such as 11-ID-B at the Advanced Photon Source, which can produce $\lambda = 0.143\,\text{Å}$, or XPDF at the Diamond light Source, $\lambda = 0.16\,\text{Å}$. The synchrotron facilities can reach much higher than $25\,\text{Å}^{-1}$ but because of the fall-off in intensity at high Q, data above $25\,\text{Å}^{-1}$ are generally not used.

The highest resolution PDF data are still collected with high energy neutrons because these experiments can reach even further out in reciprocal space (noting neutron scattering is Q independent). Hence, the best total scattering instruments are available at the spallation sources (*e.g.* POLARIS diffractometer at ISIS can reach $Q_{\max} \geq 50\,\text{Å}^{-1}$ or NOMAD diffractometer at SNS with the ability to collect out to $Q_{\max} \geq 90\,\text{Å}^{-1}$).

The lower Q region describes the longest observable structural correlation and does not cause any significant problems in the process of normalising data.

Processing of total scattering data

When total scattering data have been obtained, the data correction is done by subtracting background, beam attenuation, absorption, and multiple scattering. For



(a) (b)

Figure 2.6: (a) A single unit cell of $Y_2Mo_2O_7$ used in small box analysis. (b) A $10\times10\times10$ box of $Y_2Mo_2O_7$. This is a typical starting configuration for big box analysis.

neutron experiments the data are normalised against a vanadium standard collected under the same experimental conditions. Software packages such as GUDRUN program and PDFget(X or N) automate the correction process and Fourier transform the data in to real space.[181,182] In this thesis I only used the GUDRUNN and GUDRUNX programs to normalise obtained data.

Analysis methods of total scattering data

The most common methods to analyse total scattering data are the so-called small-box and "big box" approaches. These approaches are distinguished by the size of the model: small box models consist of a few unit cells, while big box models normally consist of hundred or thousands of unit cells [Figure 2.6].

The big box approach attempts to unify the local and average structure by using a supercell larger than the correlation length of disorder in the material. The most common way to create big box models is by using a Monte Carlo algorithm, generating random atom movement and deciding whether the move should be accepted

or rejected on the basis of minimising configuration energy. In reverse Monte Carlo (RMC) the atoms are moved around and the move is accepted or rejected based on the change made in the fit of calculated to experimental data. A move that reduces the quality of the fit may still be accepted according to a probability (Boltzmann distribution)—this is done to prevent the configuration becoming trapped in a local minimum.[183]

The RMCProfile software package is one of several software packages using a MC algorithm.[183] RMCProfile uses several datasets to drive the structural changes in a refinement. These data include the total scattering function $F(Q)$, Bragg intensities, and the PDF. To achieve the best results, data from X-ray and neutron sources can be used simultaneously: elements that scatter weakly with X-rays may scatter more strongly for neutrons and *vice versa*.

It is important to point out that the final configuration produced is not a unique solution but a possible solution. Hence, it is necessary to build a large collection of equivalent configurations to improve the reliability of any observation and to achieve an idea of their frequency of occurrence. To ensure that the final refinement is reliable it is necessary to check that the structure makes physical sense and that is in good agreement with what is known of the material since the RMC algorithm can make any move to improve the fit which may lead to unphysical structures. To decrease the likelihood of wrong moves occurring different restrains can be included, such as maximum and minimum bond lengths.

The advantage of using the RMC approach that it is not necessary to suggest a starting model for the disordered state. The RMC approach is also very flexible, which means it can be extended to include any experimental data that are compu-

tationally accessible, for example EXAFS.[184] The method does also include some disadvantages, the main drawbacks are the large number of degrees of freedom because of large supercell and the use of $P1$ symmetry.

The small box approach use real-space Rietveld refinement of a structural model for the unit cell with various symmetry restrictions, according to different regions of the PDF. These can then be compared to the average structure to understand how the local and average structure differ over different length scales. The most commonly used program is PDFGui.[185] The PDFGui software refines the local structure using a least-squares method. Periodic boundary conditions allow calculation of the PDF at distances larger than the unit cell used.

The TOPAS software package recently launched a new version (TOPAS 6) including refinement of PDF data using the small box approach. The program can fit the data to local structure and average structure at the same time to keep consistency. Furthermore, the program is significantly faster and more stable than any other program using the small box approach.[186]

The small box approach has been successfully applied to a wide range of problems, especially to correlated disorder in oxides.[142,187] The use of a particular structural model including symmetry approach keeps the number of refined parameters limited to a minimum. The small box approach struggles to deal with situations where interactions between short-range and long-range order are important.[188] Another limitation is the need to choose a particular local structural model before the refinement.

In this thesis I have mainly used the small box approach to analyse PDF data using the software package PDFGui.

2.3.3 Total scattering instruments

Argonne Photon Source, 11-ID-B

The 11-ID-B beamline at APS* is a dedicated X-ray total scattering beamline equipped to operate at very low temperatures. This instrument was preferred for the study of the spin glass state in $Y_2Mo_2O_7$. The instrument has two monochromators installed with energies 58.66 and 86.7 KeV, gives access to $Q_{\max} = 25.0\,\text{Å}^{-1}$. A Perkin Elmer amorphous silicon 2D detector mounted 920 mm away from the sample detects the diffracted beam. The instrument has access to a custom made He cryostat with the ability to collect data down to 5 K. The cryostat is equipped with three slots for sample capillaries and has been used for the work in this thesis.

Diamond Light Source, I15

X-ray total scattering data were also collected on I15† at the Diamond Lightsource. I15 is a high energy beamline (76 keV) with wavelength $\lambda = 0.163\,\text{Å}$. A Perkin Elmer 2D area detector is located close to the sample, giving access to $Q_{\max} = 22.5\,\text{Å}^{-1}$. An Oxford Cryojet 5 was used to collect data in the temperature range of 85-500 K. A gas blower was used to collect scattering data over the temperature range of 20-1000 °C.

ISIS spallation Source POLARIS

The neutron time-of-flight instrument POLARIS‡ diffractometer at ISIS pulsed spallation source was the main neutron instrument used to collect the total scattering

*https://www1.aps.anl.gov/structural-science/Details?beamline_id=16

†http://www.diamond.ac.uk/Beamlines/Engineering-and-Environment/I15-Extreme.html

‡http://www.isis.stfc.ac.uk/instruments/polaris

data. POLARIS is a high intensity, medium resolution instrument and is used to perform rapid characterisation of structures, small amounts of samples and disordered materials.[171] The instrument has an incident wavelength range of 0.1-6.0 Å with a detector span of 2θ = 6-168 ° divided into 6 detector banks. The instrument covers a wide range in reciprocal-space of $0.3 \leq Q \leq 60\,\text{Å}^{-1}$. The instrument was recently upgraded with a radial collimator around the sample position to reduce the background signal from the sample environment. The high intensity and reduced background signal makes up for the lower detector span (compared to other instruments such as GEM), which makes it a good total scattering instrument.[171] Neutron total scattering data presented in the Chapters 3 and 5 were collected at POLARIS.

2.4 SQUID magnetometry

Magnetic properties measurements in each result chapter were carried out on using a Quantum Design MPMS-XL superconducting quantum interference device (SQUID). Approximately 30–50 mg of polycrystalline sample was packed in a gelatine capsule and inserted into a diamagnetic plastic straw. Zero-field Cooling (ZFC) followed by Field Cooling (FC) measurements were made on each sample as a function of temperature. In ZFC the sample was cooled to 5 K before the field of 100 Oe was turned on and the sample response measured over the range 5-300 K. The samples were cooled down again to 5 K but still under the field of 100 Oe and the FC measurements were carried out over the same temperature range.

2.5 Monte Carlo simulations

In this thesis a few Monte Carlo (MC) codes have been developed to generate disordered starting models. MC simulations can be used to model disordered systems and their ground state. By generating a random starting configuration, an energy is determined based on a Hamiltonian. The Hamiltonians used in this thesis will be described in the corresponding results chapters. A change is then made to the system by flipping a spin or a bond orientation and a new energy for the system is calculated. If this energy is lower than the starting energy, the move is accepted. If it has a higher energy a Metropolis algorithm[189] determines whether the change is accepted, this is done to avoid getting trapped in local minima. This process continues to loop until a ground state is reached. In the MC simulation used for the analysis in this thesis, the ground state occurred when the total energy of the system was zero.

Chapter 3

Orbital dimer model for spin-glass formation in $Y_2Mo_2O_7$

3.1 Introduction

The first material investigated for orbital ordering and its effect on the physical properties is the stoichiometric canonical spin-glass (SG) material $Y_2Mo_2O_7$. The search for experimental evidence of atomic disorder to explain the SG state has been the aim of several studies of this system. In this chapter I use neutron and X-ray PDF analysis, first to reproduce previous studies,[190] and then to develop a disordered model that resolves the long standing question as to the origin of static disorder in $Y_2Mo_2O_7$. My model allows the orbitals on the geometric frustrated Mo site to dimerise, displacing in a "2-in/2-out" ice-like fashion.[191] This dimerisation leads to a structural disorder on the Mo site large enough to drive the SG state in $Y_2Mo_2O_7$. This work has been done in collaboration with Dr. J. A. M. Paddison and is published in Phys. Rev. Lett. **118**, 067201 (2017).

3.2 Background

In materials which undergo a SG transition, spins freeze into a metastable arrangement without long-range order.[192–195] It is generally accepted that for a SG state to appear, two conditions must be met: (i) interactions between the spins must be dis-

ordered and (ii) these interactions must also be frustrated or competing.[122,193,194,196] The first experimental evidence for a SG transition was observed in the early 1970s using ac-susceptibility measurements where a magnetic phase transition in a series of randomly diluted magnetic alloys appeared without any sign of long range magnetic ordering in neutron scattering experiments.[197] In the next few years, this type of magnetic phase transition was observed in several materials.[198–200]

The two conditions expected to appear in a SG material can be implemented in various ways. The simplest way to design a material with a SG state is to dope magnetic impurities into a non-magnetic material. This is the case for $Cu_{1-x}Mn_x$ and $Eu_xSr_{1-x}S$.[198,201] At larger concentrations, the spins begin to cluster but still act as a SG. A 2D representation of a magnetic impurity state is shown in Figure 3.1(a).[193]

SG states can also be generated in materials with site disorder where random bond lengths between magnetic atoms causes variation in exchange interactions between magnetic atoms and cause a SG state to occur [Figure 3.1(b)]. This is observed in the site-disordered materials *e.g* $Fe_{1-x}Mn_xTiO_3$, Fe_2TiO_5, and URh_2Ge_2.[198,202,203] The SG state can also appear in well ordered systems. One of the most studied and puzzling prototypical SG materials is the crystallographically well ordered pyrochlore $Y_2Mo_2O_7$. The SG state in $Y_2Mo_2O_7$ was first classified in 1986.[204] Since then, the structure and dynamics of this material have been extensively studied to achieve an understanding of how the SG state can occur in the weakly geometrically frustrated and well ordered $Y_2Mo_2O_7$.

In general, the magnetic pyrochlores have drawn a lot of attention because of their physical properties at low temperature.[205] Examples of the physical properties of

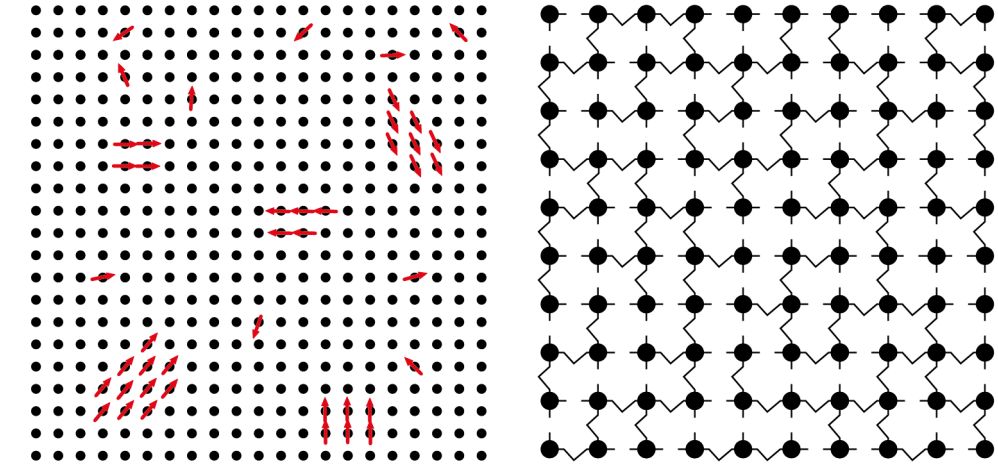


Figure 3.1: (a) 2D random-site model with magnetic impurities doped into a non magnetic material. (b) 2D random-bond spin glass where dashed line denotes ferromagnetic coupling and split bond denotes the antiferromagnetic coupling. The magnetic atoms are fully ordered while the exchange bonds are randomly distributed across the lattice.[193]

pyrochlores that have gained large interest include the spin-ice state in $A_2X_2O_7$ $A = Ho^{3+}$, $X = Dy^{3+}$; Ti^{4+}, Ge^{4+}),[206–208] spin-liquid states in $Tb_2Ti_2O_7$,[209] dynamic spin-ice states in $Pr_2Zr_2O_7$,[210] and the quantum spin-ice state in $Yb_2Ti_2O_7$.[211] Pyrochlores crystallise in a cubic structure with space-group symmetry $Fd\bar{3}m$ and can be thought of as two interpenetrating corner-sharing tetrahedral networks with cationic vertices and vacancy centers.[206] These corner-shared tetrahedral networks are geometrically frustrated and this sublattice topology is well known to be the driving force for all these magnetic properties observed in many of the pyrochlores.[206] The crystallographic positions for the atoms in the pyrochlore structure are displayed in Table 3.1.

In $Y_2Mo_2O_7$ the SG transition occurs at $T_f = 22\,K$[212] as evidenced by a large number of experimental studies: non-linear susceptibility,[212,213] specific heat,[214,215] ac susceptibility,[216] and thermo-remanent magnetisation.[217–219] Inelastic neutron-

Table 3.1: Crystallographic description of the $A_2B_2O_7$ pyrochlore structure in $Fd\bar{3}m$.

Atom	Wyckoff site	Point symmetry	coordinates
A	$16d$	$\bar{3}m$	(1/2, 1/2, 1/2)
B	$16c$	$\bar{3}m$	(0, 0, 0)
O1	$48f$	$2mm$	(x, 1/8, 1/8)
O2	$8b$	$\bar{4}3m$	(3/8, 3/8, 3/8)

scattering,[220] muon-spin rotation (μSR)[221] and neutron spin-echo studies[222,223] all showed a reduction in the spin-relaxation rate as the magnetic transition T_f is crossed, all suggesting a SG transition has occurred in the material. The average crystal structure of $Y_2Mo_2O_7$ has been determined by neutron diffraction measurements and agrees with an ordered pyrochlore structure with space group $Fd\bar{3}m$ [Table 3.1].[190,224] The magnetic Mo^{4+} ions are located in a network of corner-sharing tetrahedra [Figure 3.2(a)]. The O^{2-} ions occupy two inequivalent sites; O1 and O2, with the only free positional parameter x(O1)=0.3382(1) (x in Table 3.1). Each of the Mo^{4+} centres is octahedrally coordinated by six O1 oxygens [Figure 3.2(b)], and the Y^{3+} is coordinated by six O1 and two O2 oxygens [Figure 3.2(c)]. Neighbouring pairs of Mo^{4+} ions are bridged by a single O1, forming the primary magnetic superexchange pathway.

A number of reasons for the SG state to occur have been suggested; the most important of which are summarised here. In other materials, the SG state can be induced by small numbers of vacancies or defects which can be difficult to observe experimentally. For $Y_2Mo_2O_7$, vacancies were calculated for the antisite (Y/Mo exchange): the defect level was calculated to be 1.1% and the oxygen vacancy level was less than 0.4%. These small defect concentrations would be very unlikely to

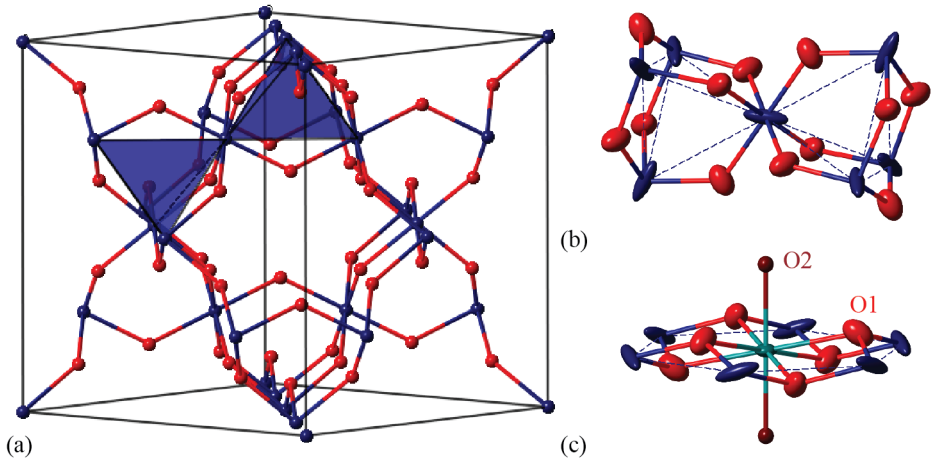


Figure 3.2: (a) Crystal structure of $Y_2Mo_2O_7$ generated from the model of Ref 190: Mo in dark blue, O1 in red, and Y and O2 omitted for clarity. (b) Coordination environment of Mo^{4+} shown with displacement ellipsoids at 50% probability. Prolate Mo^{4+} displacement ellipsoids point along the local-$\langle 111 \rangle$ axes (towards the centres of adjacent tetrahedra). (c) Coordination environment of Y^{3+} (green).

induce the SG behaviour in $Y_2Mo_2O_7$.[225]

Instead it is expected that a mechanism for SG formation involves local Mo^{4+} displacements to generate variation in the magnetic interactions.[226] The clearest experimental signature of anomalies in the Mo site is the large atomic displacement parameter (ADP) obtained from Rietveld refinement to powder neutron diffraction data.[190] This is in good agreement with the observation from an EXAFS study using Mo and Y K-edges, where a large static variation of the Mo–Mo distances $\sigma^2_{\text{stat}} = 0.026(5)\,\text{Å}^2$ was observed.[123] Two ^{89}Y NMR studies showed a broad variety of Y–O environments and were interpreted in terms of a local distortion of the Mo site;[226,227] this explanation was supported by μSR experiments.[228] However, this model was inconsistent with a total scattering study using neutron PDF analysis, where no evidence for local Mo displacement appeared.[190] Instead, it showed variation in Y–O1 distances consistent with a local splitting of the O1 sites. This result

contradicts the EXAFS study of the same material.[123] I will come to show that my own analysis reconcile these two viewpoints.

From a theoretical point of view, several studies on molybdate systems have been carried out and reviewed in Ref. 205. I present the examples that are most relevant to the work presented in this chapter.

Saunders and Chalker explained the SG state in geometrically frustrated magnets with "weak" disorder levels.[229] In this approach, a material is described as weakly disordered when the average exchange constant J is much larger than the fluctuation of the exchange variation.

Shinaoka *et al.* studied a parameterised three-orbital Hubbard model using DFT and concluded that spin and orbital degrees of freedom were strongly coupled for the d^2 configuration.[230] They suggested two models with strong spin-orbit coupling; (i) "4-in/4-out" or (ii) "2-in/2-out" correspond to the combined angular momentum operator both energetically favourable for the local orbital configurations to appear [Figure 3.3]. The "4-in/4-out' model would correspond to a unique ground state in which the symmetry of the average structure is lowered to $F\bar{4}3m$. Extra peaks in the diffraction pattern would be expected; that these are not observed rules out the model. The second model suggested was a "2-in/2-out" configuration which gave rise to many energetically ground states similar to configurational degeneracy of ice-like states on pyrochlore lattice. They did not suggest exactly how this relation could be implemented into the crystal structure but concluded that there is a strong coupling between orbitals and spins in $Y_2Mo_2O_7$ [Figure 3.3].

A second DFT study relaxed the orbital and lattice configuration for different spin structures and obtained various lattice distortions in each case.[206] In both studies a

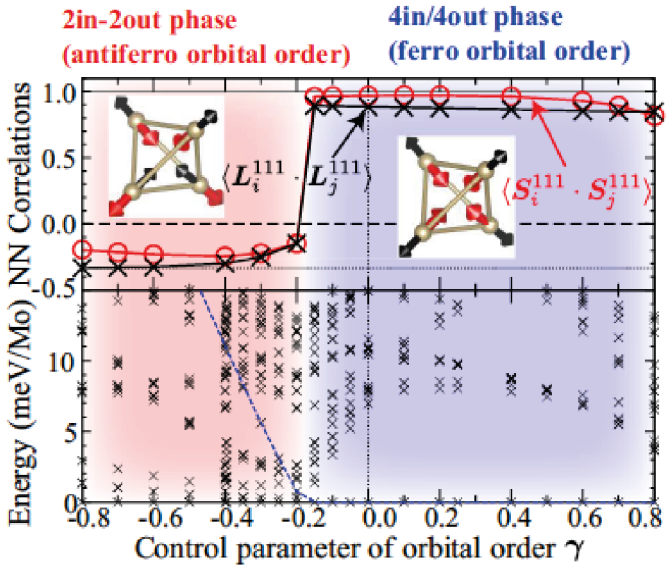


Figure 3.3: Phase diagram of the three-orbital Hubbard model obtained in i Ref 230.The inset shows the '2-in/2-out" (left) and "4-in/4-out" (right). Spin and orbital moments are denoted by the thick red and black arrows, respectively. The figure is adapted from Ref 230.

strong coupling of spin, orbital and lattice degrees of freedom is suggested to be the driving force for the SG state in $Y_2Mo_2O_7$.

In this chapter I present new experimental neutron+X-ray total scattering data on a high-quality $Y_2Mo_2O_7$ sample. These are first modelled using the same approach as in Ref 190. I then present a small-box model that is a good approximant to the manifold of disordered states suggested by the DFT study in Ref 230. In the model development I reassess the assumption from Ref 190 that the absence of obvious Mo–Mo splitting in PDF naturally implies that local Mo displacements do not occur. In fact, I show that the PDF is better represented by a model in which the d^2 orbital on the Mo site dimerise in a "2-in/2-out" configuration, which is distributed through the structure in a disordered fashion. This gives rise to Mo displacements, coupled to O1 displacements, and so leads to a variation in the superexchange cou-

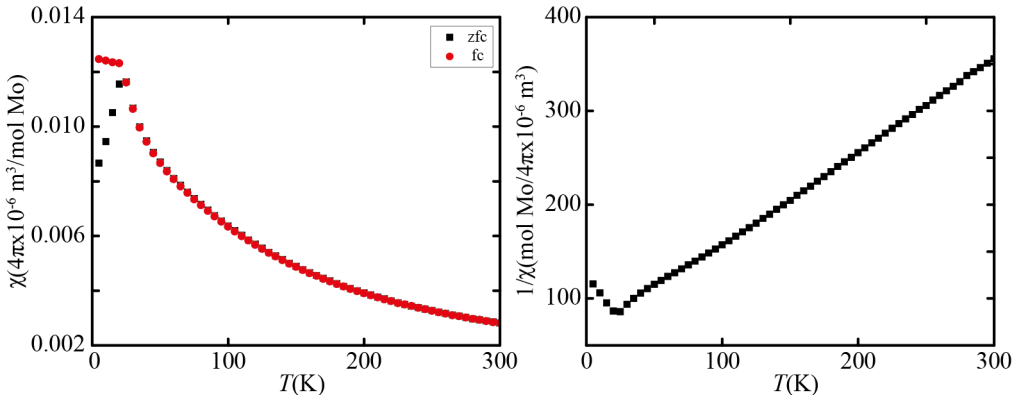


Figure 3.4: (a) Experimental d.c. magnetic susceptibility $\chi(T)$ for $Y_2Mo_2O_7$ for the sample used in this study. (b) The inverse susceptibility ($\chi^{-1}(T)$) of $Y_2Mo_2O_7$. The transition temperature (T_f) in my sample was confirmed at 22 K.

pling that is strong enough to generate the SG state in $Y_2Mo_2O_7$. In this way, I link complex orbital order to SG formation.

3.3 Experimental

3.3.1 Sample Preparation

A 7.5 g sample of $Y_2Mo_2O_7$ was prepared by Dr. Ronghuan Zhang and Prof. Mike Hayward. The sample was synthesised from the starting materials MoO_2 (99.99%) and Y_2O_3 (99.99%) as described in Ref. 204. The two powders were mixed using mortar and pestle in a suitable ratio. The mixture was pelletized and fired at 1300 °C for 48 hours in a CO/CO_2 buffer gas mixture to ensure the correct oxygen stoichiometry. X-ray powder diffraction was used to confirm the phase purity, and the refined lattice parameters were compared with previous published values and were in good agreement with the literature.[204] SQUID magnetometry was used to determine the glass transition temperature, $T_f = 22$ K [Figure 3.4] – this is consistent with previous studies.[212]

3.3.2 Data Collection

Neutron Total Scattering Measurements

Neutron total scattering data were collected on the POLARIS instrument at the ISIS pulsed neutron and muon source.[171] The polycrystalline $Y_2Mo_2O_7$ sample was placed in a thin-walled vanadium can (8 mm diameter and 5.5 cm tall) which was mounted into a custom-designed cryostat. Total scattering data were collected over the reciprocal-space range $0.7 \leq Q \leq 45\,\text{Å}^{-1}$ which gave the most reliable $D(r)$ and excluded most of the diffuse magnetic contribution to the data, which appears at $0.4\,\text{Å}^{-1}$,[220] although it was barely observed above background in the high-Q-optimised measurement. The reciprocal space coverage corresponds to a real-space resolution of the order $\Delta r \simeq 3.791/Q_{\text{max}} = 0.084\,\text{Å}$. Total scattering data were collected for 6 hours at each of the temperatures 5, 15, 30, 50, 100, and 300 K. A 10 minute scan was collected at every 5–10 K during temperature changes. These collections gave data suitable for Rietveld refinement but not PDF determination.

The total scattering data were corrected and placed on an absolute scale using standard methods as implemented in GudrunN software.[181] In this process, I took into account the effects of background scattering, absorption multiple scattering, and beam intensity variations. The Bragg profile function was extracted from the scattering data and used as input for Rietveld analysis. The corrected total scattering data were also transformed into real space data (PDF) using $D(r)$ normalisation, as defined in the Section 2.3.1 and in Ref. 179. The corrected PDF data were used as input files for real-space analysis in PDFGui.[185]

X-ray Total Scattering Measurements

X-ray total scattering data were collected on the 11-ID-B beamline at the Advanced Photon source (APS) at Argonne National Laboratory. A beam with a size of 0.5 mm $\times$ 0.5 mm with an energy of 58 keV and wavelength of 0.2114 Å was used. A Perkin Elmer amorphous silicon 2D detector mounted 92 cm away from the sample setup was used. A small fraction of the sample was loaded in to a 0.5 mm Kapton capillary and mounted together with an empty capillary and a reference sample ($CuFeO_2$) into the custom-designed He cryostat which had space for three capillaries. Each data set was collected at 5 K intervals between 5 and 40 K, then at 10 K intervals between 40 and 180 K, and at 20 K steps between 180 and 300 K. Before each collection, the temperature was stabilised for 5 minutes and a data set of 180 second exposure was collected. Collected data were processed using the program Fit2D[231] where a mask function was used to remove dead pixels in the detector, and each image at each temperature was integrated to convert the data into a one dimensional scattering pattern. The integrated diffraction patterns were refined directly using the TOPAS refinement software.[164] The integrated data were corrected for standard background corrections, data normalisation, and Fourier transformed into real space in the GudrunX software[182] using a value of $Q_{\max} = 25\,\text{Å}^{-1}$. The resulting $D(r)$ function was used as input for PDF refinement in PDFGui.[185]

I use the term $D(r)$ to refer to both neutron and X-ray PDFs in the normalisation outlined above.

3.4 Results

3.4.1 Neutron and X-ray diffraction: Average structure

The average structure of the sample was refined using neutron, X-ray, and a combined refinement between the neutron + X-ray data using the TOPAS software package.[164] The structure was modelled in the conventional cubic space group $Fd\bar{3}m$ for all the collected temperature points, including covering of the SG transition (5 $\leq T \leq$ 300 K). Neutron data collected on POLARIS instrument were fitted together with X-ray data collected at 11-ID-B across the 2θ range of 3.1-33 Å^{-1}. Fits below and above the phase transition of the combined neutron + X-ray refinement are displayed in Figure 3.5. No significant changes in the average structure across the T_f transition appear across the SG regime, in good agreement with previous studies.[190] For the combined refinement, the lattice parameters were coupled to the refined values from X-ray data because of the reciprocal-space resolution of the X-ray measurements. The refined parameters for the combined refinement for the two temperatures are given in Table 3.2; the refined values for each of the individual neutron and X-ray data sets at each temperature are given in Appendix A1. The lattice parameter, x(O1) value, and magnitude of the ADPs are plotted against temperature in Figure 3.6. Considering the relative magnitudes of the ADPs for $Y_2Mo_2O_7$, U_{11}(O1) is significantly larger than rest of the ADPs and remains large upon heating. Furthermore, the ADPs for Mo give rise to the characteristic cigar shape pointing in $\langle 111 \rangle$ direction [Figure 3.2(b)]. The value of U_{11}(Mo) parameter remains almost constant across the temperature range. The rest of the ADP values

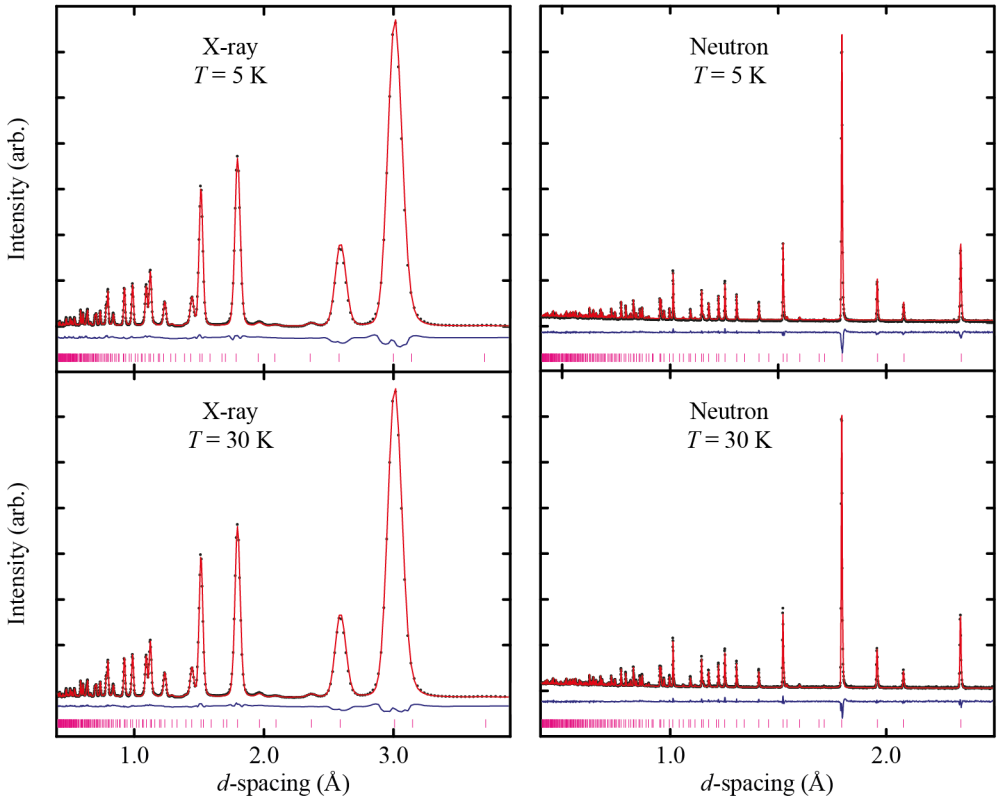


Figure 3.5: Combined neutron and X-ray Rietveld refinement (a) at $T = 5\,\mathrm{K}$ below the freezing temperature T_f and (b) at 30 K above the T_f temperature.

Table 3.2: Parameters obtained from the combined neutron+X-ray Rietveld refinement. The lattice parameters were obtained from the X-ray data only and fixed to this value for the neutron data. The fits are shown in Figure 3.5.

T/K	5 K	30 K
Space-group	$Fd\bar{3}m$	$Fd\bar{3}m$
a	10.2136(3) Å	10.2133(3) Å
x(O1)	0.33816(10)	0.33808(10)
U_{11}(Y)	0.400(13)	0.0415(13)
U_{12}(Y)	−0.080(18)	−0.093(18)
U_{11}(Mo)	0.94(2)	0.94(2)
U_{12}(Mo)	0.70(3)	0.71(3)
U_{11}(O1)	1.20(3)	1.21(3)
U_{22}(O1)	0.62(2)	0.62(2)
U_{23}(O1)	0.05(3)	0.063(3)
U_{11}(O2)	0.37(3)	0.37(3)

show normal thermal behaviour, even that many of them are relatively big. The main conclusion is that my sample is entirely consistent with previously reported observations of stoichiometrically pure $Y_2Mo_2O_7$.[190]

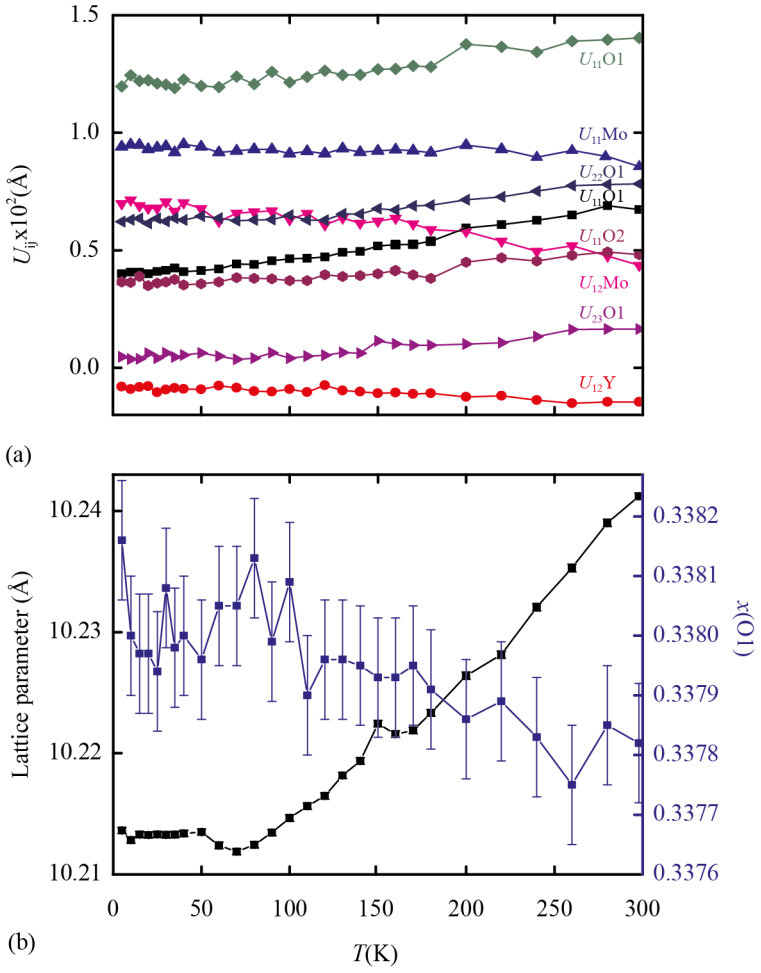


Figure 3.6: (a) Temperature dependence of the anisotropic displacement factors of $Y_2Mo_2O_7$ obtained from combined neutron+X-ray data refinement. (b) The black line is the temperature dependence of the lattice parameter a, and blue is the x(O1) position, against temperature.

3.4.2 Total scattering: local structure

Established small-box model

PDF refinements were carried out using the PDFGui software.[185] In the previous PDF study presented in Ref. 190, the local structure of $Y_2Mo_2O_7$ was analysed using three different models using the conventional $Fd\bar{3}m$ structure. In my study, all of the models were refined using the same procedure as described in Ref. 190. In addition to the structural parameters, four other parameters were refined: fitted scale (for neutron and X-ray data which gives an extra parameter compared to the previous study), as well as the *sratio* and *delta2* parameters which control the PDF widths and their r-dependence. The first model involved isotropic displacement parameters for all atoms and atom positions refined with $Fd\bar{3}m$ symmetry. This model was reported to include 9 fitting parameters. Although these parameters are not listed explicitly, the number would be consistent with the internal degrees of freedom mentioned above. Plot of the fits are compared to previous study and shown in Figure 3.7(a,b,e). The second model refined included anisotropic displacement parameters for all the atoms (listed below), which increased the number of parameters to 13 and these fits are compared with the fits from Ref. 190 [Figure 3.7(c,d,f)].

Isotropic	Anisotropic
U(Mo)	U_{11}(Mo), U_{12}(Mo)
U(Y)	U_{11}(Y), U_{12}(Y)
U(O1)	U_{11}(O1), U_{22}(O1), U_{23}(O1)
U(O2)	U_{11}(O2)

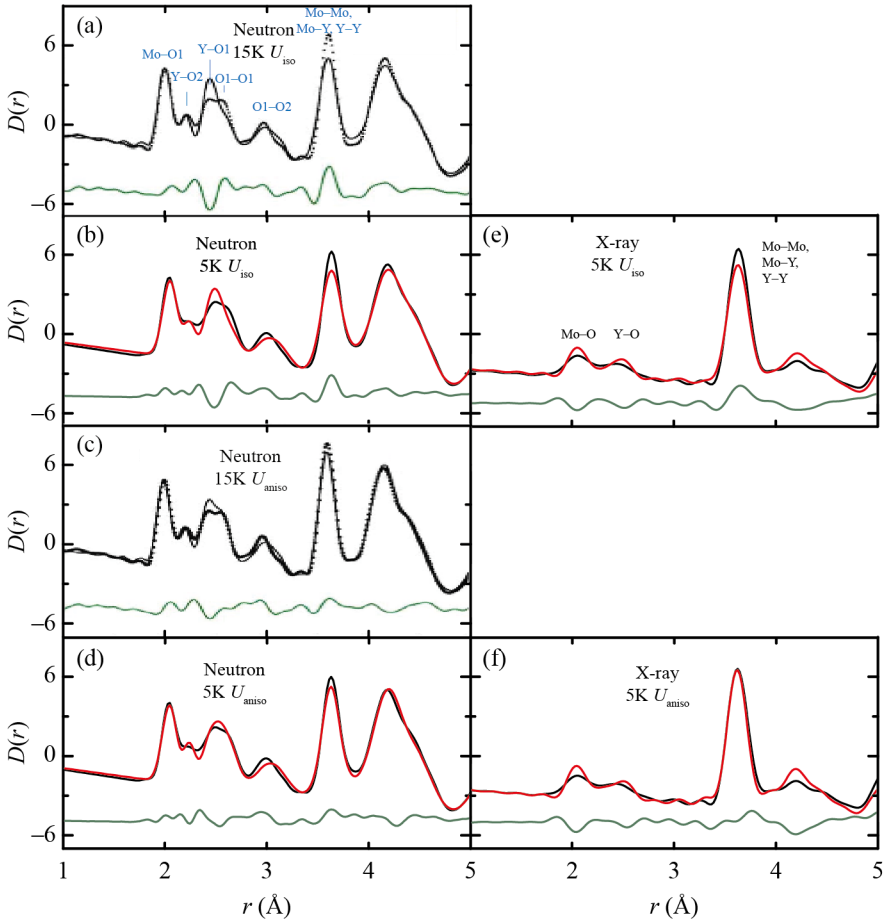


Figure 3.7: Refined fits to the (left) neutron data (a-d) and (right) X-ray data (e,f). (a and c) Reproduction of the fit involving the isotropic displacement (a) and (c) for the anisotropic model both shown in Figure 8 of Ref. 190 described in the text. (b,e) Combined fit to my data using the isotropic displacement model and (d,f) using the anisotropic displacement model. In (a) and (c) data is shown as points and fits as lines; in (b,d,e,f) data are shown as black lines, fits as red lines and data–fit as green lines. My fits are in good agreement with previous study.

The third model involved splitting of the 48 O1 atoms contained in a single $Fd\bar{3}m$ unit cell into two equal sets of 24 (O1a, O1b). These distinct sets were generated from the fractional coordinates $(x, 1/8, 1/8)$ with the starting point of x= 0.389 and 0.3466 including different anisotropic displacement parameters.[190] This should have increased the number of refined parameters by four to give a total of 17. In Ref. 190 the total number of refined parameters was reported to be 16. Since the refined values are not presented, it is not clear whether this is a typographical error or whether an unidentified constraint was used during the refinement.

In using this same split-site model to refine our neutron + X-ray PDF data, I added one additional parameter corresponding to the scale of X-ray data set which was not included in the previous PDF study.[190] I managed to reproduce the first two models without any problems, but with the split-site model (third model) I could not achieve a stable refinement using all 18 parameters. To stabilise the refinement I implemented four constraints that reduced the number of free parameters to 14 and gave a stable refinement:

$$U_{11}(\text{O1a}) = U_{11}(\text{O1b}) \tag{3.1}$$

$$U_{22}(\text{O1a}) = U_{22}(\text{O1b}) \tag{3.2}$$

$$U_{23}(\text{O1a}) = 0 \tag{3.3}$$

$$U_{23}(\text{O1b}) = 0 \tag{3.4}$$

In this way, I constrained the thermal ellipsoids of both types of O1 atoms to be the same, and aligned the principal axes of these ellipsoids with the unit cell axes. Note that the U_{23}(O1) value obtained from Rietveld refinement was close to zero anyway

(*e.g.* = 0.0003(1) Å^2 in Ref. 190).

Nevertheless, my fit to the split-site model is essentially indistinguishable from the fit obtained in the previous study; the two results are compared in Figure 3.8(a,b); the refined values are shown in Table 3.5. These result conclude that my sample and refinement procedures are consistent with the previous study.[190]

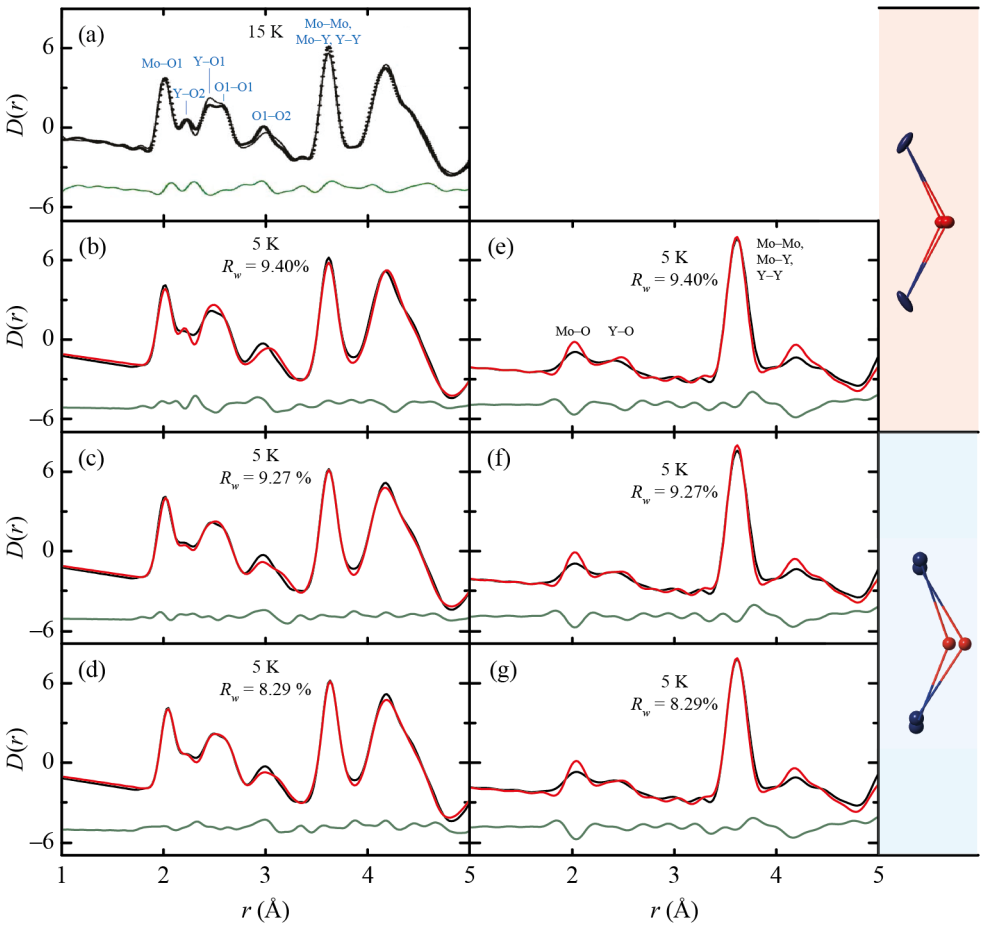


Figure 3.8: Refined PDF fit to (left) neutron data (a-d) and X-ray data (e-g). (a) Reproduction of the fit to neutron PDF data shown in Ref. 190 for the split-site model described in the text. (b,e) Fit of the split-site model to neutron+X-ray PDF data. (c,f) Fit of the orbital-dimer model ($I4_1md$; described in the text) to my neutron+X-ray PDF data. (d) Fit to my neutron+Xray data of the orbital dimer model with maximum number of refined parameters. In (a), data is shown as points and fit as a line; in (b-g) data are shown as black lines, fits as red lines, and data−fit as green lines. The extrema of Mo–O1–Mo conformations accounted for by each model are shown beside the corresponding fit.

3.4.3 Orbital dimer model

In this study of $Y_2Mo_2O_7$ I propose an alternative model of static disorder. My starting point is the observation that Mo ADPs are strongly elongated along the local-$\langle 111 \rangle$ axes in the average structure, presented previously in Figure 3.2(b). This suggests that the Mo^{4+} ions are displaced towards or away from the center of the Mo_4 tetrahedra. A physical reason for Mo displacements, such as polarisation and orbital interactions,[230] requires that the displacements are not random but coupled. From the DFT study using a three-orbital Hubbard model there are two basic possibilities for this coupling. The first requires all Mo ions on a tetrahedron to displace towards its centre or all displace away ("4-in/4-out" state presented in Section 3.2). The second possibility requires two Mo to displace towards its centre and two to displace away ("2-in/2-out" state also presented in Section 3.2). The "4-in/4-out" displacement pattern is ordered and is ruled out in $Y_2Mo_2O_7$ by the absence of changes in the global symmetry which would appear as a consequence of symmetry lowering. In the "2-in/2-out" case the coupling is frustrated and the displacement pattern need not be ordered. In fact, if all "2-in/2-out" states were equally probable, there would be a macroscopic degeneracy of the Mo-displaced configurations analogous to the degeneracy of proton configurations in cubic water ice[191] in which case it is a kind of orbital-ice like state.

I have built a model that can be directly compared with the split site model in terms of its ability to explain the experimental PDF data. I consider an ordered approximant to the ensemble of the disordered "2-in/2-out" states. This is possible because the ordered and disordered "2-in/2-out" states essentially show the same

Table 3.3: Relationship between atom positions in the reference model and the approximate orbital dimer model as described in the text. Each atomic site and the relevant Wyckoff position is given together with the atomic coordinates used in PDFGui refinements.

	Reference structure		Dimer model	
Space group and origin shift	$Fd\bar{3}m$; [0, 0, 0]		$I4_1md$; [0, 0, 0]	
Y	16*d*	$(\frac{1}{2}, \frac{1}{2}, \frac{1}{2})$	8*b*	$(0, y_{\mathrm{Y}}, z_{\mathrm{Y}})$
Mo	16*c*	$(0, 0, 0)$	8*b*	$(0, y_{\mathrm{Mo}}, z_{\mathrm{Mo}})$
O1	48*f*	$(x_{\mathrm{O1}}, \frac{1}{8}, \frac{1}{8})$	4*a*	$(x_{\mathrm{O1a}}, y_{\mathrm{O1a}}, z_{\mathrm{O1a}})$
			4*a*	$(x_{\mathrm{O1b}}, y_{\mathrm{O1b}}, z_{\mathrm{O1b}})$
			4*a*	$(x_{\mathrm{O1c}}, y_{\mathrm{O1c}}, z_{\mathrm{O1c}})$
O2	8*b*	$(\frac{3}{8}, \frac{3}{8}, \frac{3}{8})$	4*a*	$(0, 0, z_{\mathrm{O2}})$

PDF for distances within a single unit cell. The highest symmetry subgroup of $Fd\bar{3}m$ that allows the Mo to displace in a "2-in/2-out" configuration is $I4_1md$.[232] The structure relates to $Fd\bar{3}m$ in the same way as the proton ordered phase in ice XIc relates to the proton-disordered cubic ice Ic.[233] The relation between the $Fd\bar{3}m$ and $I4_1md$ structures is presented in Figure 3.9(a). The tetragonal unit cell has dimensions $a_{\mathrm{t}} = a/\sqrt{2}$ and $c_{\mathrm{t}} = a$. Mo and Y both occupy the 8*b* site at $(0, y, z)$, O2 occupies the 4*a* site at $(0, 0, z)$, and the O1 site is split into three sites: O1a and O1c also occupy the 4*a* site and O1b occupies the 16*c* site at (x, y, z). The relation between the reference symmetry and the orbital dimer symmetry is given in Table 3.3. The Mo point symmetry is lowered from $\bar{3}m$ to m, which is consistent with a first order Jahn-Teller distortion of the d^2 electronic configuration of Mo^{4+}, with a splitting of d^2 states as shown in Figure 3.10. The t_{2g} energy state splits into ${e'}_g$ and a_{1g} with a 16*c* site symmetry, a further splitting with occupation of the a' and a'' will appear to generate the dimerisation along the $\langle 111 \rangle$ axes.

Such a displacement is also consistent with prolate anisotropic atomic displacement

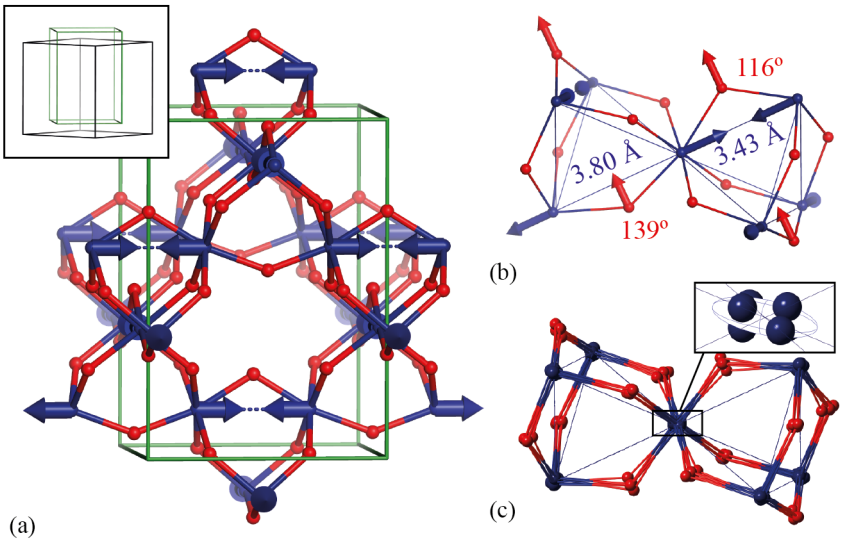


Figure 3.9: (a) Representation of the orbital-dimer model obtained from PDF refinements: Mo displacements are shown as blue arrows, Mo–Mo dimers as blue dashed lines, and O1 atoms in red. The inset shows the relationship between $I4_1md$ and $Fd\bar{3}m$ unit cells. (b) Local Mo environment in the orbital-dimer model, showing Mo displacement directions (blue arrows) and dominant O1 displacement directions (red arrows). (c) Distribution of atomic positions obtained by imposing the full symmetry of the average structure. In the inset, the superposition of displaced Mo sites is compared to the prolate displacement ellipsoid obtained from Rietveld refinement.

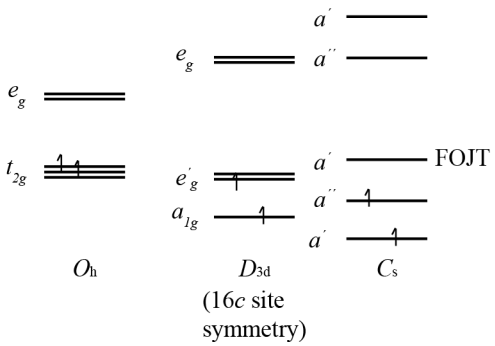


Figure 3.10: The splitting of the crystal field stabilisation energy levels of the d^2 states. This is an illustration of how the orbitals might split on the Mo site to generate a dimerisation of the Mo ions along the $\langle 111 \rangle$ axes.

factors as observed in the in average structure models. At the 16c site, the local $\bar{3}$ axis is aligned with the $\langle 111 \rangle$ axis of the unit cell. This axis splits the 12 $\langle 110 \rangle$-type vectors into two subsets of six, as shown in Figure 3.11: one subset is orthogonal to the $\langle 111 \rangle$ axis and one subset is not. The orbital dimer model involves population of the latter (Wyckoff position 96g; point symmetry m). A displacement tensor assembled from the static displacements in this subset is of the form

$$\begin{bmatrix} 2 & 1 & 1 \\ 1 & 2 & 1 \\ 1 & 1 & 2 \end{bmatrix} \frac{u^2}{2}, \tag{3.5}$$

where u is the magnitude of the displacement along the $\langle 110 \rangle$ directions. This tensor has principal components of magnitude $U_{\max} = 2u^2$ and $U_{\min} = \frac{u^2}{2}$, aligned parallel and perpendicular to [111], respectively; hence it is prolate. Furthermore, the relationships

$$U_{\max} = U_{11} + 2U_{12} \tag{3.6}$$

$$U_{\min} = U_{11} - U_{12} \tag{3.7}$$

for this site then give $u = \sqrt{U_{11}}$ (in the athermal limit). The displacement magnitude u obtained from the Rietveld refined value for U_{11} is 0.118(3) Å, which should represent an overestimate because of the omission of thermal contributions. The displacement magnitude determined in my PDF refinement is $u = 0.093(6)$ Å. The atomic displacement obtained from PDF refinement is in good agreement with the Rietveld result of Ref. 190.

To have the same number of refined parameters in my new model compared to the split-site model, I had to reduce the number of refined parameters to match the split-site model, which was done in the following way: (i) constraining the unit cell parameter $c_t = \sqrt{2a_t}$, so the unit cell remains metrically cubic: (ii) the small displacement parameters of the Y and O2 sites indicate that they are not strongly correlated, displayed in Figure 3.2(c), and I therefore fix them at the average-structure positions of $(0,\frac{3}{4},\frac{1}{8})$ and (0,0,0). (iii) The $I4_1md$ structure allows for Mo displacements within the plane that contains the cubic local-$\langle 111\rangle$ axis (towards or away from the tetrahedron centre) and local-$\langle 110\rangle$ axis (towards or away from neighbouring Mo lying on the same mirror plane). Consequently, two parameters are needed to define the Mo displacement direction, which would increase the number of parameters beyond the split-site model. Such a refinement was stable, however, and showed that the dominant displacement direction is actually the local-$\langle 110\rangle$. Subse-

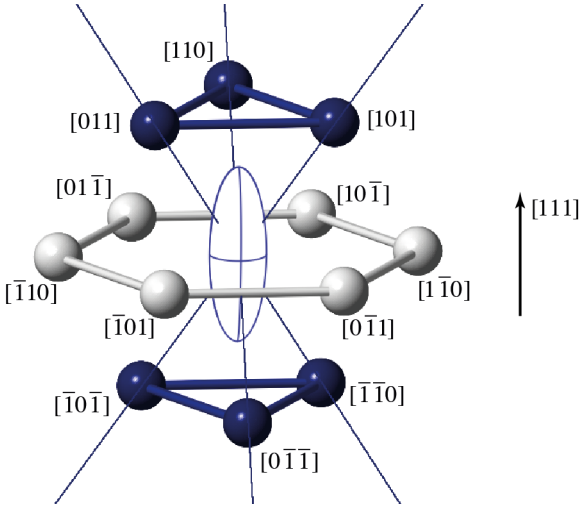


Figure 3.11: Splitting of the 16*c* Mo site in $Fd\bar{3}m$ due to Mo displacements described in the orbital dimer model. The 12 $\langle 110\rangle$-type displacements are split by the local point symmetry into two sets of six: the 96*g* and 96*h* Wyckoff sites (blue and white spheres, respectively). The orbital dimer model involves population of the 96*g* sites; these displacements give rise to a prolate displacement tensor at the 16*c* site.

Table 3.4: Structural parameters for my PDF refinements using the split-site and orbital-dimer models described in the text. Reference values from the split-site refinements of Ref. 190 are shown in italics (* = Rietveld and † = PDF refinements; note that the level of consistency in cell parameters is typical for Rietveld/PDF comparisons). Lattice parameters are given in Å and displacement parameters in 10^{-2} Å^2.

Split-site model[190]			**Orbital dimer model**	
a	10.2255(10)	*10.20753(2)**	$c_\mathrm{t} \equiv \sqrt{2}a_\mathrm{t}$	10.2269(10)
x(O1a)	0.3320(6)	*0.3305(12)†*	y(Mo)	0.7371(8)
x(O1b)	0.3446(6)	*0.3465(13)†*	z(O1a)	0.6938(6)
U_{11}(Y)	0.512(15)	*0.471(7)**	x(O1b)	0.7184(5)
U_{12}(Y)	−0.129(19)	*−0.136(9)**	y(O1b)	0.7910(5)
U_{11}(Mo)	1.39(5)	*1.1(1)**	z(O1b)	0.2467(4)
U_{12}(Mo)	0.93(5)	*0.83(2)**	z(O1c)	0.2709(6)
U_{11}(O1)	1.02(11)	*1.45(2)**	U_iso(Y)	0.355(11)
U_{22}(O1)	0.81(3)	*0.66(1)**	U_iso(Mo)	1.14(5)
U_iso(O2)	0.55(3)	*0.32(2)**	U_iso(O)	0.89(2)

quently, I fixed the local-⟨111⟩ component at zero (z(Mo) ≡ $\frac{5}{8}$), so that the number of parameters was identical to the split-site model. I call this constrained $I4_1md$ model the "orbital dimer" model.

I refined this model against neutron and X-ray PDF data. The fits are compared to the fits I obtained from the split-site model and the published fit in Figure 3.8.[190] With the orbital dimer model I obtained a better fit with an $R_\mathrm{wp} = 9.27\%$, while for the split-site model of Ref 190 I obtained an $R_\mathrm{wp} = 9.40\%$ with the same number of refined structural parameters. The difference of the fit is also observed in the plot where the dimer model accounts better for the low-r peaks. Further evidence for the improved model quality comes from the refinement statistics, where the split site model showed strong covariance between the x(O1a), x(O1b), and U_{11}(O1) parameters. In the refinement of the orbital dimer model no anomalous covariance were observed at any point through the refinement.

Given the robustness of PDF refinement of the orbital dimer model, I investigated

Table 3.5: Structural parameters for a stable refinement of the orbital dimer model including 18 refined parameters. The refinement included the maximum number of refined parameters of the orbital dimer model before it correlated. Lattice parameters are given in Å and displacement parameters in 10^{-2} Å^2.

Orbital dimer model	
$c_\mathrm{t} \equiv \sqrt{2}a_\mathrm{t}$	10.2269(10)
delta2	3.12(10)
sratio	0.839(14)
Neutron scale	5.56(4)
X-ray scale	0.635(12)
U_iso(Mo)	1.28(6)
U_iso(Y)	0.347(12)
y(Mo)	0.7365(9)
z(Mo)	0.6245(8)
z(O2)	0.4935(5)
z(O1a)	0.4400(9)
x(O1b)	0.7157(4)
y(O1b)	0.7886(5)
z(O1b)	0.2433(4)
z(O1c)	0.2681(10)
U_iso(O1a,O1c)	2.00(13)
U_iso(O1b)	0.70(3)
U_iso(O2)	0.62(4)

the possibility of improving the fit to the data by adding more refined structural parameters. I managed to make a robust refinement including 18 parameters and improved the fit with $R_\mathrm{wp} = 8.29\%$ shown in Figure 3.8(d,g); the corresponding refined parameters are given in Table 3.5.

From the refined results of my model I can conclude that absence of visible splitting of the Mo–Mo peak is not inconsistent with the Mo off-centering. In fact, the orbital model includes Mo displacements and robustly improved the fit to experimental data.

3.5 Discussion

3.5.1 Interpretation of Orbital Dimer Model

The physical interpretation of the orbital-dimer model is represented in Figure 3.9. In every Mo_4 tetrahedron, two Mo are displaced towards each other and two away from each other; in each case, the refined displacement magnitude is 0.093(6) Å and the displacement direction is approximately along the line connecting the Mo pair, shown in Figure 3.9(a). The Mo displacements thus describe a covering of the pyrochlore lattice by Mo–Mo dimers (short Mo–Mo distances), with one dimer per tetrahedron. The O1 displacements are correlated with Mo displacements, [Figure 3.9(b)]. When neighbouring Mo atoms displace towards each other, the bridging O1 displaces away from the dimer and the Mo–O1–Mo angle decreases: Conversely, when neighbouring Mo displace away from each other the Mo–O1–Mo angle increases. The effect of O1 displacements is to keep all Mo–O1 distances essentially the same—a result that is perhaps unsurprising on electrostatic grounds but nevertheless explains the lack of visible Mo–O1 peak splitting. In Figure 3.9(c) the distribution of atomic positions obtained by superposing the full $Fd\bar{3}m$ average-structure symmetry on the refined local-structure model is shown. The distribution of local-$\langle 110 \rangle$ Mo displacements has a larger component parallel to the local-$\langle 111 \rangle$ axis than perpendicular to it, consistent with the prolate Mo displacement ellipsoid in the average-structure model (Figure 3.2(b)) and inset on Figure. 3.9(c). Finally, I assume that the ordered $I4_1md$ dimer covering [Figure 3.12(a)] is an *approximant* to the disordered dimer coverings that show the same local displacement patterns.

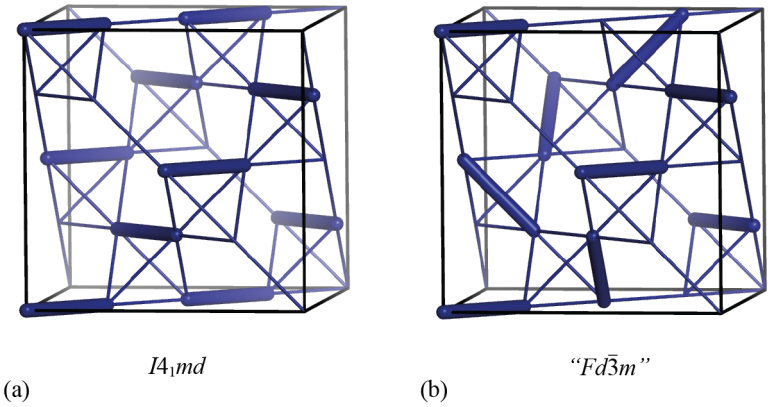


Figure 3.12: (a) Comparison of ordered and disordered coverings of the pyrochlore lattice by Mo–Mo dimers (thick blue lines). The left panel shows the ordered dimer covering for the $I4_1md$ structure, which breaks cubic symmetry. (b) Shows an example of a disordered dimer covering that more closely approximates the true orbital-ice state; spatial averaging over such dimer coverings preserves cubic symmetry.

There is a macroscopic degeneracy of disordered dimer coverings that reproduce the observed $Fd\bar{3}m$ symmetry on spatial averaging; Figure 3.12(b) shows a disordered example that more closely approximates the true structure. This is the same degeneracy responsible for the unusual physics of cubic water ice,[191] spin ices,[207,234] and charge ices.[144,235]

3.5.2 Comparison to previous studies

The orbital-dimer model is consistent with previous experimental studies and theoretical requirements for SG formation. First, ^{89}Y NMR studies[226,227] observed a broad resonance in the Y–O1 environment that is in good agreement to the orbital dimer where displacement from the variation in exchange coupling displaces the O1 and gives rise to 30 distinct Y environments. Second, the Mo displacements split the average Mo–Mo distance into long, short, and intermediate distances in the ratio 1:1:4. This static disorder makes a contribution to the variance in Mo–Mo

distances of 0.012(2) Å^2 which is in qualitative agreement with the EXAFS result (0.026(5) Å^2); moreover, the displacement direction (parallel to Mo–Mo pairs) is consistent with the EXAFS result.[123] This agreement is a positive result because EXAFS should be more sensitive to Mo displacements than the PDF, in which Mo–Mo, Y–Y and Mo–Y peaks overlap and the intermediate Mo–Mo distance is similar to the average Mo–Mo distance.

Thirdly, in previous studies it was shown that variations in exchange interactions around ∼10% may induce SG transitions in geometrically-frustrated magnets.[229,236] In the refinement of the average structure of $Y_2Mo_2O_7$, variations in bond angle of 9° were calculated to yield factor-of-two variations in the magnetic coupling strength.[190] The refined model showed the Mo–O1–Mo angle actually varied with an amount of 23° [Figure 3.9(b)], which is significantly larger than the minimum variation necessary to induce a SG transition. The important thing here is the arrangement of Mo–O1–Mo bond angles is disordered because of the dimer–covering (*i.e.*, the arrangement of short and long Mo–Mo distances are disordered) [Figure. 3.12], and short and long Mo–Mo distances are associated with Mo–O1–Mo bond angles of 116° and 139° degrees, respectively [Figure 3.9(b)]. The dimerisation of the Mo ions presents a clear mechanism for SG formation. Experimentally, the width $\delta \sim 1\,\mathrm{T}$ of the internal-field distribution measured by ^{89}Y NMR at 25 K[227] implies a distribution of exchange energies of approximate width $gS\mu_\mathrm{B}\delta/k_\mathrm{B} \approx 13\,\mathrm{K}$, which is similar to T_f, as expected theoretically.[229,236]

As mentioned in the background section, a theoretical study parameterised a three-orbital Hubbard model using DFT,[230] and concluded that spin and orbital degrees of freedom are strongly coupled for the d^2 configuration and many energetically-

similar spin-orbital ground states exist if the ground state is "2-in/2-out". A second DFT study relaxed the orbital and lattice configuration for different spin structures and obtained different lattice distortions in each case.[206] These studies provide compelling evidence for a strong coupling of spin, orbital, and lattice degrees of freedom. This basically suggests that the Mo dimerisation may be explained by an orbital (JT) mechanism and I therefore interpret the "2-in/2-out" pattern of Mo displacements as the formation of orbital dimers, driven by the Jahn-Teller activity of the d^2 electronic configuration.

3.6 Conclusion

In this chapter I showed that the SG state in $Y_2Mo_2O_7$ is driven by orbital dimerisation of JT active Mo^{4+} ions—a rare example where SG formation is not driven by random compositional or site disorder.[237] While SG formation due to non-random interactions has been studied theoretically,[238] this result represents the first such example for a real SG. This is not the first material where a dimer state plays a key role in determining material properties. A similar conclusion is drawn in the case of Ba_2YMoO_6, where Mo^{5+} spins freeze into a disordered arrangement of spin-singlet dimers;[239] likewise in $CuIr_2O_4$ Ir^{3+}/Ir^{4+} charge ordering occurs simultaneously with spin dimerisation.[240] For future work, I anticipate that a dimer model could be useful in other molybdate pyrochlores such as *e.g.* $Lu_2Mo_2O_7$,[241] $Tb_2Mo_2O_7$,[242,243] and $Dy_2Mo_2O_7$.[244] Interestingly, this model of Mo displacements looks similar to models of Nb displacements in (non-magnetic) niobate pyrochlores,[245,246] suggesting that the proximity of both materials to a metal-insulator transition may be related to orbital dimerisation.[247,248] The result obtained in this chapter suggest some promising

directions for future work on $Y_2Mo_2O_7$. First, a comprehensive single-crystal diffuse scattering study would indicate if a particular subset of dimer coverings is preferred in the system. Second, analysis of the distribution of magnetic couplings may allow a consistent interpretation of fitting to magnetic diffuse-scattering data.[206] Third, the orbital-dimer state proposed should collapse at sufficiently high temperature; *i.e.*, an orbital-ice to orbital-liquid[249,250] transition may be anticipated.

Chapter 4

Local structure study of orbital disorder in $LaMnO_3$

4.1 Introduction

In the previous chapter I successfully applied a combination of neutron+X-ray PDF analysis to investigate orbital disorder in $Y_2Mo_2O_7$. In this chapter I use the same method to study the canonical high-temperature orbital order/disorder transition in $LaMnO_3$. I test three different models of the orbital disordered state: two from previous published work, and a third model proposed by a former student in a RMC investigation of the orbital order/disorder transition in $LaMnO_3$. In contrast to the analysis in Chapter 3, in this case it is far more challenging to distinguish amongst the models in terms of their ability to account for the experimental PDF data that fits the data best. Nevertheless, the analysis of my data show a subtle but consistent preference for the anisotropic Potts model proposed in Ref 114. The result obtained in this chapters raises important questions regarding the use of total scattering in cases where there is strong coupling between static and dynamic disorder.

The sample and data used in this chapter was synthesised and collected by Dr. C. A. Young. I have renormalised and reanalysed all of the data. This work is published in Phys. Rev. B **95**, 174107 (2017).

4.2 Background

4.2.1 Phase behaviour of $LaMnO_3$

As already introduced in Chapter 1 the perovskite manganite family has attracted a lot of attention in the past because of the significant drop in resistivity when a magnetic field is applied (CMR). $LaMnO_3$ is the end member of several doped systems in which CMR appears, $La_{1-x}A_xMnO_3$ in which A = Ba, Ca, Sr.[10,23,95,99] It is well accepted that a transition from an orbital ordered (O') phase to an orbital disordered (O) phase occurs in $LaMnO_3$ at T_{JT}=750 K.[62,135] On doping $LaMnO_3$, the O' transition temperature drops rapidly, such that in the key CMR compositions the disordered O phase is stabilised at temperatures just above the crucial metal-insulator transition [Figure 4.1].[96] Consequently, a microscopic understanding of the orbital order/disorder transition and the disordered phase—even in the parent compound $LaMnO_3$—is of fundamental interest for CMR science.[9,25] In the introduction, it was presented that $LaMnO_3$ has C-type orbital ordering at ambient conditions (page 11). On heating from room temperature, $LaMnO_3$ undergoes two structural phase transitions [Figure 4.1]. The first occurs at 750 K and is isosymmetric—*i.e.*, there is no change in space group symmetry.[62] This is the orbital order/disorder transition and the transition studied in this chapter. The second transition, at 1010 K, is to a rhombohedral phase with a different set of tilts[62] but which also appears to be orbital disordered.[141] Drawing on the approach taken in Ref. 62, I use the labels O', O, and R to represent, respectively, the orthorhombic orbital ordered, orthorhombic orbital disordered, and rhombohedral orbital disordered phases.

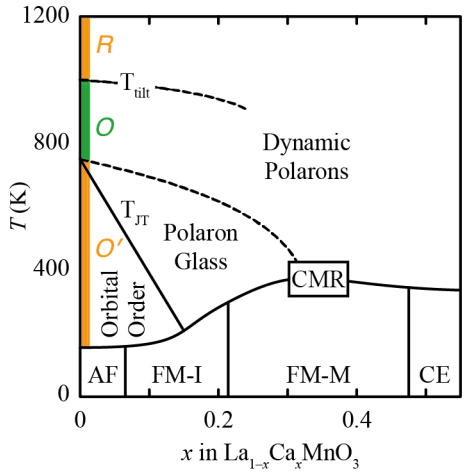


Figure 4.1: Phase diagram for Ca-doped $LaMnO_3$. On heating $LaMnO_3$ to $T_{JT} = 750\,K$ there is an isosymmetric structural transition to the orbital disorder (O) phase, with the same octahedral tilts as in the O' phase but with no obvious JT distortion. On hole doping, the value of T_{JT} decreases such that CMR emerges in $La_{1-x}Ca_xMnO_3$ from the disordered phase. A discontinuous octahedral tilt transition occurs at 1010 K to give a rhombohedral (R) phase that persists until decomposition.

Though isosymmetric, the O'/O transition at $T_{JT} = 750\,K$ has a number of clear experimental signatures. Some of them were presented in section 1.5 but I present an additional overview here. First, there is a convergence of the reduced unit cell parameters, such that the O phase is close to being metrically cubic (hence its "pseudocubic" label).[62,135] The variation in lattice parameters is discontinuous at T_{JT}, identifying the transition as first-order as required for isosymmetric transitions.[251] Second, both neutron and X-ray diffraction show a convergence of the crystallographic Mn–O bond lengths from the three distinct values of the ambient phase to a single effective value [d(Mn–O) $\simeq 2.02$ Å] in the O phase.[62,135] So in this average-structure description the JT distortion appears to vanish on heating through the O'/O transition. Third, there is a volume discontinuity at T_{JT}, with the disordered O phase *ca* 0.4% denser than the ordered O' phase.[135] Fourth, both conductivity and magnetic behaviour change at the transition: resistivity falls by two orders of mag-

nitude, and the Weiss constant increases from $\theta = 52\,\mathrm{K}$ to $\theta = 177\,\mathrm{K}$ in a way that is consistent with isotropic ferromagnetic interactions.[60,129] Fifth, ^{17}O NMR measurements reveal a transition to non-polarised e_g orbital occupation at T_{JT}, indicating long range disorder on the O-sites.[126] Sixth, there is an anomaly in the specific heat capacity, corresponding to a transition entropy $\Delta S = 0.52(2)\,\mathrm{J\,K^{-1}\,mol^{-1}}$.[112] And, seventh, the transition is accompanied by small shifts and increased broadening in the excitation spectrum as measured using either inelastic neutron scattering[252] or Raman spectroscopy.[253]

The primary experimental evidence for the persistence of JT distortions within *O*-phase $LaMnO_3$ comes from techniques able to observe structural correlations over distances of 1–10 Å. The neutron PDF study in Ref. 141 confirmed clearly the absence of any meaningful variation in local Mn–O bond lengths across the O'/O transition. A similar conclusion was drawn from XAS (EXAFS/XANES) studies.[112,254,255] While there seems to be little disagreement as to the persistence of a JT distortion at high temperatures, it was noted first in Ref. 112 and more convincingly in Ref. 255 that the Mn K-edge EXAFS signal varied more strongly across the O'/O transition than for any temperature range within either phase. Nevertheless, taken collectively, these experimental observations clearly identify the O phase of $LaMnO_3$ as an orbital-disorder phase: each MnO_6 octahedron retains a JT distortion but these distortions must propagate without any long-range periodicity.

4.2.2 Orbital correlations in the O phase

Determining the nature of orbital orientation correlations in the absence of long-range orbital order is a problem of significant difficulty.[142,190,226,256,257] As introduced

in Chapter 2, total scattering is one of the few experimental techniques with simultaneous sensitivity to both average and local structure,[145] and so it is no accident that the two studies to attempt data-driven refinement of microscopic models of the orbital-disordered state are based on neutron total scattering measurements.[141,258] The first of these studies employed a "real-space Rietveld" (or "small-box") approach, in which the neutron PDF was fitted using a structural model based on the O' arrangement of orbital orientations.[141] For data collected within the O regime, convincing fits with stable JT distortions could only be obtained for refinements constrained to distances $0 < r < 10\,\text{Å}$. Hence, the model developed in this study effectively describes the O-phase as an incoherent array of nm-sized domains, each with local orbital orientations as in the O' phase.

The second PDF study, presented in Ref. 258, made use of the same data set but employed a custom "big-box" modelling approach based on a combination of geometric modelling and simulated annealing.[258] The key result was an atomistic configuration of $LaMnO_3$ that reproduced the experimental PDF while also preserving—within a predefined tolerance—the local geometry of all JT-distorted MnO_6 coordination polyhedra [Figure 4.2(a,b)]. In this configuration there was some evidence for locally correlated orbital order of the antiferrodistortive C-type ordering; however, the magnitude of the relevant correlation functions was 50 times smaller than in the ordered phase itself. It is possible that the configurations obtained in this PDF study were actually realisations of the correlated disordered state of the anisotropic three-state Potts (3SP) model, as described in Ref. 114 and introduced in Section 1.4.1. In the ordered state only two of the three possible Potts states are occupied to ensure the C-type orbital ordering. For the disordered state three out of three possible Potts

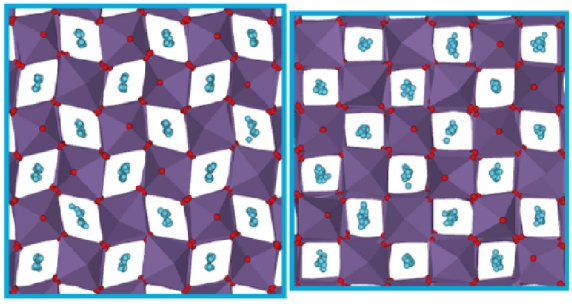


Figure 4.2: Slices of the fitted MnO_6 structures at (a) 300 K and (b) 1050 K showing the arrangement of the MnO_6 octahedra and the La ions (light cyan) are interstitial atoms in the channels. At 300 K the MnO_6 octahedra have a checkerboard arrangement with relatively ordered La ions. At 1050 K the average structure is cubic-like with the MnO_6 octahedra buckled and the La ions are disordered in the channels. The figure is adapted from Ref 258.

states of are occupied, this orientation of the orbitals gives local ordering correlations that do not occur in the ordered state. A visual comparison of the two states is displayed in Figure 4.3(a,b).

The present study builds on that of a previous student Dr. C. A. Young, who carried out a series "big box" models of the PDF data of Ref. 141. His approach was to use the reverse Monte Carlo (RMC) method as implemented in RMCProfile.[183] Whereas the study of Ref. 258 had constrained MnO_6 geometries in terms of the JT distortion found in the low-temperature O' phase, Dr Young's approach employed only data-based closest-approach and "distance-window" constraints that allowed much greater geometric flexibility.[183,259] The unexpected but reproducible result of this analysis was a structural model in which the two long Mn–O bonds in each MnO_6 octahedron formed an angle of $\sim 90°$ rather than $\sim 180°$. This arrangement would correspond to an alternative JT distortion, correlations of which are related to collective "ice-rule-like" states on the cubic lattice;[191] for this reason I will refer

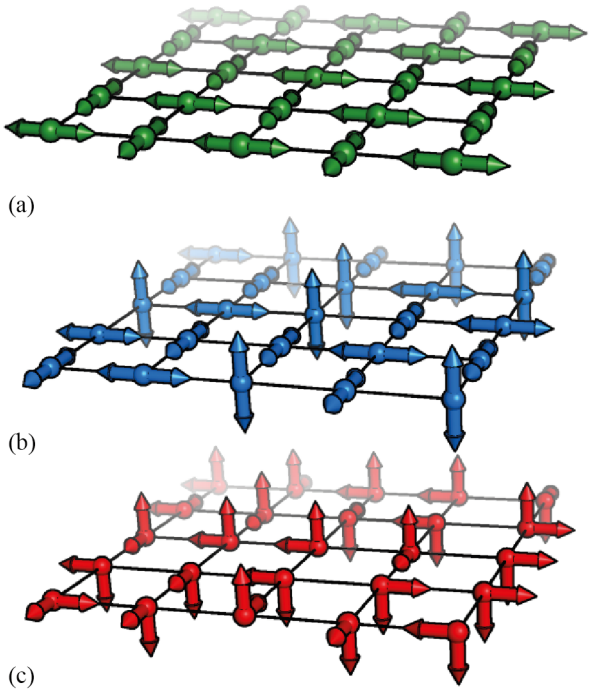


Figure 4.3: Simplified orbital orientations in the (a) C-type, (b) 3SP-type, and (c) L-type orbital models, shown here for a single planar section of the Mn sublattice (spheres). Arrows represent the orientation of long Mn–O bonds.

to the state as the L model [Figure. 4.3(c)]. Though unexpected for $LaMnO_3$, this model relieves the electronic degeneracy of the Mn^{3+} as shown in Figure 4.4 and is known to occur in some Mn^{3+} brownmillerites.[260]

The motivation for revisiting this study is primarily to use a small box approach to investigate the orbital orientation correlations in O-phase $LaMnO_3$ by testing the three models introduced here and also shown in Figure. 4.3. In particular I wish to compare the models for a small and constant number of variances. At face value it would be expected that the models are distinguishable in terms of fitting to experimental neutron and X-ray total scattering data. Surprisingly, my results show that the three models give rise to remarkably similar fits to the data even though they are physically very different. Nevertheless, the data show a subtle but

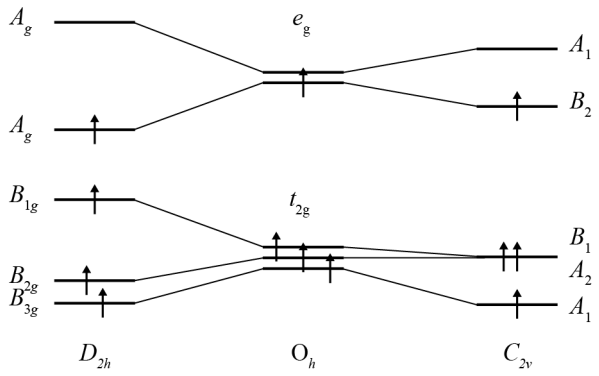


Figure 4.4: The crystal field splittings for the C-type (left) and L-type model (right). The effects of d/p mixing are included where relevant, but $4p$ states have been omitted for clarity.

consistent preference for the anisotropic Potts model.

4.3 Experimental

4.3.1 Sample Preparation

The sample used was prepared by Dr. C. A. Young, Dr F. D. Romero and Prof. M. Hayward using the citrate gel method.[261] I confirmed the phase purity using X-ray diffraction and magnetisation measurements [Figure. 4.5]. The Néel temperature (T_N) was confirmed to be 140 K for the synthesised sample, which is in good agreement with previously-reported values.[262]

4.3.2 Neutron Total Scattering Measurements

Neutron total scattering data were collected by Dr. C. A. Young and Prof. D. A. Keen using the GEM diffractometer at the ISIS pulsed neutron and muon source.[180] The polycrystalline $LaMnO_3$ sample was loaded into a cylindrical vanadium can of 8 mm diameter and 5.8 cm height, and placed in a custom-designed furnace. Total

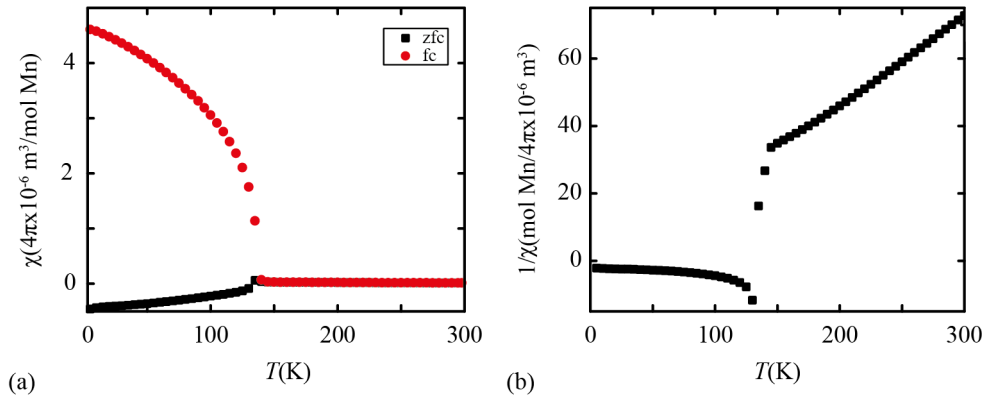


Figure 4.5: Experimental d.c. magnetic susceptibility $\chi(T)$ (a) and inverse susceptibility $\chi^{-1}(T)$ (b) for $LaMnO_3$ for the sample used in this study. The Néel temperature (T_N) is observed as a divergence in the field-cooled (FC) and zero-field-cooled (ZFC) traces at 140 K and as a change in the slope of χ^{-1}.

scattering data were collected over the reciprocal-space range $0.7 \leq Q \leq 40\,\text{Å}^{-1}$, corresponding to a real-space resolution of order $\Delta r \simeq 3.791/Q_{\text{max}} = 0.09\,\text{Å}$. Data collection times were optimised for total scattering measurements; a total of six such measurements at temperatures of 523, 653, 753, 823, 903, and 973 K were performed. These data was collected by Dr. C. A. Young.

For the reexamination of $LaMnO_3$, the total scattering data were renormalised by placing on an absolute scale using standard methods as implemented in the GUDRUN software.[181] In this process I took into account the effects of background scattering, absorption, multiple scattering, and beam intensity variations. As an additional precaution—and motivated by the significant phonon populations at the high temperatures at which the measurements were carried out—I explored the effects of successively including and omitting Placzek inelasticity corrections,[175] and found no meaningful sensitivity to these corrections in the data. The corrected total scattering data were transformed to the pair distribution function using the normalisation defined in Section 2.3.1, and used as input for real-space Rietveld

analysis and direct comparison across temperature. The normalisation process was carried out under the oversight of Prof. D. A. Keen (ISIS). The average structure Rietveld refinements for the neutron data were carried out by former student Dr. C. A. Young; I checked that all the refined parameters at each temperature to ensure they were in good agreement with the literature.

4.3.3 X-ray total scattering Measurements

Variable-temperature X-ray total scattering data were measured by Dr. C. A. Young and Dr. L. D. Connor using the high-energy I12 beamline at the Diamond Light Source (X-ray wavelength $\lambda = 0.14577(1)\,\text{Å}$). I renormalised all these data again in the following way. X-ray total scattering data were collected at 10 K intervals from 523 K to 973 K. For each temperature point, 600 one-second exposures were collected and then averaged. Background measurements were obtained using the scattering from an empty quartz capillary in an otherwise identical setup. Initial data processing was carried out using the Fit2D software.[231] A mask was used to remove dead pixels in the detector, and each image was integrated to give a one dimensional scattering pattern. The integrated diffraction pattern was used directly for Rietveld refinements of the average crystal structure. For PDF refinements, the integrated X-ray scattering data were used as input for the suite of standard background corrections and data normalisation processes as performed using GudrunX.[182] This process yielded the normalised X-ray PDF as defined in Ref. 179. The usable maximum magnitude Q_{max} of the X-ray total scattering function was $22.5\,\text{Å}^{-1}$. For simplicity of representation I use the term $D(r)$ to refer to both neutron and X-ray PDFs in the normalisations outlined above.

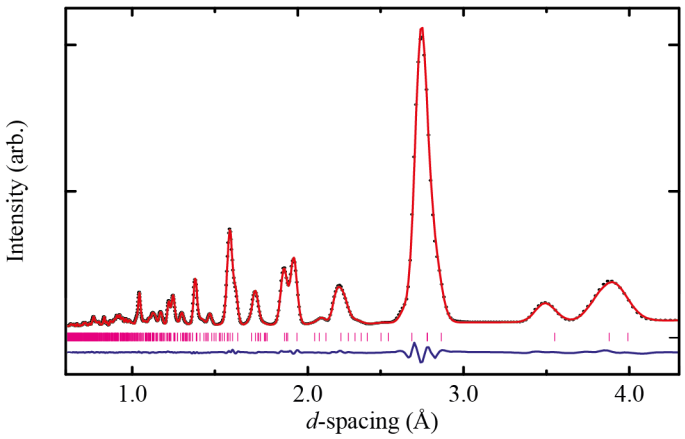


Figure 4.6: A typical Rietveld fit for $LaMnO_3$ to the X-ray data (in this case at 523 K). This quality of fit was consistent across all the temperature points measured. In this case the quality of fit corresponded to a R_{wp}=1.941 %

.

4.3.4 Rietveld refinement

Average structure models of $LaMnO_3$ were refined against both X-ray and neutron total scattering data. The orthorhombic space group *Pnma* was used for the orthorhombic and pseudocubic phases.[62] Atomic displacements were modelled using isotropic atomic displacement parameters. No positional constraints were added beyond those required by the space group. An example of the quality of fit is shown in Figure 4.6.

4.3.5 Comparative PDF refinements

PDF refinements were carried out using the PDFGui software.[185] In this chapter I compare the quality of fits for three orbital correlation models: *C*-type, 3SP-type, and *L*-type, as summarised in Figure 4.3. In order to allow statistically-meaningful direct comparison amongst fits, I identified a suitable small-box approximant for each model such that all three shared a common number of structural degrees of

freedom. This approximant approach was also used in the previous Chapter. The concept is to model the low-r PDF data in terms of a small-box model derived from the known average structure by a specifically chosen symmetry-lowering perturbation. While it is understood that this symmetry-breaking process can in general propagate in so many different ways as to give a large manifold of degenerate disordered states, the approximant represents the highest-symmetry arrangement of the particular perturbation of each model. In this way the number of refineable parameters is kept to a minimum. Hence one expects the quality of PDF fit to decrease as the r-range included in the fit increases.

In my PDF fits, I compare the results for three combinations of PDF data: (i) $1.5 \leq r \leq 6\,\text{Å}$ neutron $D(r)$, (ii) $1.5 \leq r \leq 6\,\text{Å}$ neutron + X-ray $D(r)$, and (iii) $1.5 \leq r \leq 10\,\text{Å}$ neutron + X-ray $D(r)$. The PDFGui parameters $delta_1$, Q_{damp} (X-ray) and Q_{damp} (neutron) were fixed at values of 1.7 Å, 0.0486 Å^{-1}, and 0.0343 Å^{-1} respectively—all the fits are shown in Appendix B2. I now proceed on to describe the three specific approximant models used in the comparative PDF refinements of this study. In each case, I identified the highest-symmetry perturbation of a common parent structure that captures the relevant local orbital correlations for a given model and then parameterised the orbital-driven JT distortion using a single, refineable, distortion parameter (I call this δ). The common parent, or reference–structure was determined as follows. Conventional Rietveld refinement against X-ray and neutron Bragg diffraction data collected at each temperature gave an average structure model in the space group $Pnma$. For each temperature point, the corresponding octahedral tilt magnitude ϕ was then determined from the oxygen atom positions according to the approach outlined in Refs. 62,263. The reference structure for a

given temperature is then also described by the space group *Pnma*–with precisely the same lattice parameters as determined from Rietveld refinement and with La and Mn atoms on their conventional sites (4*c* and 4*b* Wyckoff positions)—but with the oxygen positions now determined purely by the octahedral tilt angle:[263]

$$\begin{aligned} x_{\mathrm{O1}} &= \frac{\cos^2\phi - 1}{2\cos^2\phi + 4}, \\ y_{\mathrm{O1}} &= \frac{1}{4}, \\ z_{\mathrm{O1}} &= \frac{\sqrt{3} + \tan\phi}{\sqrt{12}}, \\ x_{\mathrm{O2}} &= \frac{2 - \sqrt{3}\sin\phi\cos\phi + \cos^2\phi}{8 + 4\cos^2\phi}, \\ y_{\mathrm{O2}} &= -\frac{\tan\phi}{\sqrt{48}}, \\ z_{\mathrm{O2}} &= \frac{3\sqrt{3} + \tan\phi}{\sqrt{48}}. \end{aligned} \tag{4.1}$$

In this way the reference structure effectively represents the Rietveld-refined *Pnma* structure with JT distortions removed.

C-type orbital correlations

For the small-box approximant used to model *C*-type orbital correlations, the relevant distortion parameter must give rise to the correlated JT distortion pattern observed in the (orbital ordered) O' phase as observed experimentally. This type of orbital order has the same space-group symmetry as that of the activated tilts, so this approximant shares the *Pnma* symmetry of the reference structure. The distortion parameter δ is implemented in PDFGui as a variation in the O2 atom position, giving the local orbital correlation pattern shown in Figure 4.7(a). The relationship between atom positions and positional parameters in the reference and

approximant models is given in Table 4.1.

The local structure refinements using this approximant model make use of a total of ten variable parameters using the same definitions as in the previous chapter: (i) Q_{broad}, (ii-iii) relative scale factor for X-ray *vs* neutron data sets, (iv, v) the x_{La} and z_{La} positional parameters of the La atom site, (vi) the JT distortion parameter δ,

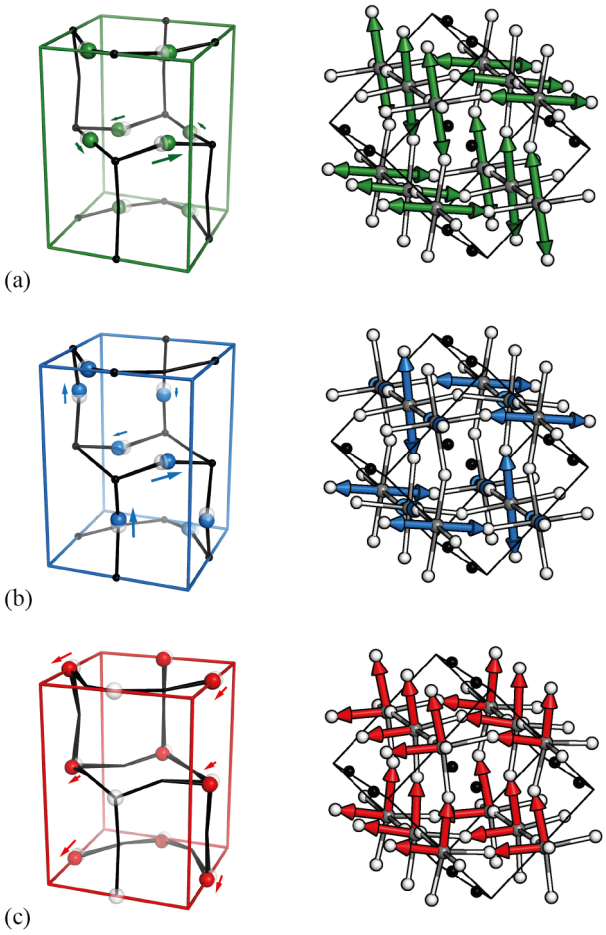


Figure 4.7: Representation of the small-box approximants used in my PDF study of orbital disordered $LaMnO_3$. (a) *C*-type order is generated by collective displacement of O2 atoms (green arrows, left), preserving the *Pnma* symmetry of the undistorted parent structure. (b) 3SP-type order is generated by collective displacements of both O1 and (some) O2 atoms, as indicated by the blue arrows in the left-hand panel. This arrangement has $P2_1/n11$ symmetry (c) *L*-type order results from collective displacement of Mn atoms (red arrows, left) to give an approximant with $Pnm2_1$ symmetry. In each case, the corresponding arrangement of long Mn–O bonds is shown by the arrows in the right-hand panels.

Table 4.1: Relationship between atom positions in reference and approximant small-box models as described in the text. For each model, and for each atomic site, the relevant Wyckoff position is given together with the atom coordinates used as input in my PDFGui refinements. Whereas the values of the parameters x_{La} and z_{La} were taken directly from the results of the Rietveld refinements, the values $x_{\mathrm{O1}}, z_{\mathrm{O1}}, x_{\mathrm{O2}}, y_{\mathrm{O2}}, z_{\mathrm{O2}}$ were determined using Eq. (4.1). Only those parameters marked by an asterisk were allowed to vary during the PDF refinements; variable parameters with the same symbol for a given model were constrained to assume identical values. All models share the same unit cell axes, and hence lattice parameters.

	Reference structure		C-type		3SP-type		L-type	
Space group and origin shift	$Pnma; [0,0,0]$		$Pnma; [0,0,0]$		$P2_1/n11; [0,0,0]$		$Pnm2_1; [\frac{1}{4},\frac{1}{4},0]$	
La	$4c$	$(x_{\mathrm{La}}, \frac{1}{4}, z_{\mathrm{La}})$	$4c$	$(x^*_{\mathrm{La}}, \frac{1}{4}, z^*_{\mathrm{La}})$	$4e$	$(x^*_{\mathrm{La}}, \frac{1}{4}, z^*_{\mathrm{La}})$	$2a$	$(x^*_{\mathrm{La}}, \frac{1}{4}, z^*_{\mathrm{La}})$
							$2a$	$(-x^*_{\mathrm{La}}, \frac{3}{4}, -z^*_{\mathrm{La}})$
Mn	$4b$	$(0,0,\frac{1}{2})$	$4b$	$(0,0,\frac{1}{2})$	$2b$	$(0,0,\frac{1}{2})$	$4b$	$(0,0,\frac{1}{2}+\delta^*)$
					$2d$	$(\frac{1}{2},0,0)$		
O1	$4c$	$(x_{\mathrm{O1}}, \frac{1}{4}, z_{\mathrm{O1}})$	$4c$	$(x_{\mathrm{O1}}, \frac{1}{4}, z_{\mathrm{O1}})$	$4e$	$(x_{\mathrm{O1}}, \frac{1}{4}-\delta^*, z_{\mathrm{O1}})$	$2a$	$(x_{\mathrm{O1}}, \frac{1}{4}, z_{\mathrm{O1}})$
							$2a$	$(-x_{\mathrm{O1}}, \frac{3}{4}, -z_{\mathrm{O1}})$
O2	$8d$	$(x_{\mathrm{O2}}, y_{\mathrm{O2}}, z_{\mathrm{O2}})$	$8d$	$(x_{\mathrm{O2}}+\delta^*, y_{\mathrm{O2}}, z_{\mathrm{O2}}+\delta^*)$	$4e$	$(x_{\mathrm{O2}}+\delta^*, y_{\mathrm{O2}}, z_{\mathrm{O2}}+\delta^*)$	$4b$	$(x_{\mathrm{O2}}, y_{\mathrm{O2}}, z_{\mathrm{O2}})$
					$4e$	$(x_{\mathrm{O2}}+\frac{1}{2}, y_{\mathrm{O2}}, \frac{1}{2}-z_{\mathrm{O2}})$	$4b$	$(-x_{\mathrm{O2}}, -y_{\mathrm{O2}}, -z_{\mathrm{O2}})$

and (vii-x) isotropic displacement parameters for each of the La, Mn, O1, and O2 sites.

3SP-type orbital correlations

For the 3SP-type orbital model I use the highest-symmetry subgroup of *Pnma* which permits JT distortions in the out-of-plane (*b*-axis) direction. Distortion mode analysis using the ISOTROPY software suite[232] identified $P2_1/n11$ as the relevant subgroup, where I have used an unconventional setting of the $P2_1/c$ space group in order to facilitate direct comparison between reference and approximant structures. The monoclinic distortion angle α was fixed at 90° for the same reason. In order to describe a 3SP-type collective JT distortion in terms of the single parameter δ it was necessary for this parameter to vary the positions of both O1-type and O2-type oxygen atoms. The specific implementation is given in Table 4.1, and was chosen so as to ensure similar magnitudes of in-plane and out-of-plane JT distortions. The corresponding orbital correlation pattern is shown in Figure 4.7(b). By design, the total number of variable parameters for this approximant is identical to that for the *C*-type model described above.

L type orbital correlations

The third approximant model corresponds to the alternate JT distortion that had emerged from the preliminary RMC analysis: *i.e.* angles of *ca* 90° between the two long Mn–O bonds at each Mn site. Distortion mode analysis using the ISOTROPY suite identified $Pnm2_1$ as a relevant subgroup of highest symmetry. Again I use an unconventional setting of the space group $Pmn2_1$ to facilitate comparison amongst the various small-box models. In the preliminary RMC configurations, there was

little evidence for distortion of the O_6 coordination octahedra around each Mn; rather the JT distortion was accommodated by displacement of the Mn atom away from the centre of each such octahedron. Consequently, the distortion parameter δ no longer influences the O1 or O2 atom positions in this approximant model, but instead displaces the Mn atoms towards an edge of the corresponding octahedral MnO_6 coordination environments. The RMC refinements indicated a preference for locally-ferroelectric Mn displacement patterns; the $Pnm2_1$ approximant is the simplest model that captures these Mn correlations. This distortion is shown in Figure 4.7(c) and the implementation in PDFGui is given explicitly in Table 4.1. For completeness the number of total free variables is again conserved for this model. More complex approximants in which Mn displacements included out-of-plane components are conceivable but would require a larger number of variables to be refined.

4.3.6 Single-crystal diffuse scattering calculations

Single-crystal diffuse scattering patterns were generated from explicit atomistic realisations of the 3SP- and L-type orbital disorder states. In the 3SP model it is the positions of the O atoms that determines orbital orientations; in the L-type model the key component involves Mn displacements. So that I might calculate diffuse scattering for large $(20 \times 20 \times 20)$ supercells—and hence obtain smoothly continuous diffraction patterns—the ordered component from the atomistic configurations was excluded. The starting atomic configurations of the 3SP and L type models were simulated by developing a custom Monte Carlo code for each composition. Each model has a unique JT distribution which was the constrained in each code. The L model has twelve possible JT environments at each MnO_6 octahe-

dron [Figure 4.3(c)]. 3SP model has three possible JT environments at each MnO_6 [Figure 4.3(b)]. The single-crystal diffuse calculations were carried out using the SingleCrystal software.[264]

4.4 Results and discussion

4.4.1 Neutron and X-ray diffraction: The average structure

For the Rietveld refinement, the starting point was to determine the temperature-dependence of the average structure of $LaMnO_3$ over the temperature range $300 \leq T \leq 1000\,\mathrm{K}$, making use of neutron and X-ray scattering data. The variation in unit cell parameters with temperature was determined; the results are displayed in Figure 4.8(a) and clearly identify the isosymmetric phase transition between O' and O phases on heating above $T_{\mathrm{JT}} \simeq 750\,\mathrm{K}$. This transition was used to cross-calibrate the sample temperatures of X-ray and neutron measurements. The transition is accompanied by a volume collapse of $-0.1499\,\mathrm{cm^3\,mol^{-1}}$ which is similar to the value of $-0.1535\,\mathrm{cm^3\,mol^{-1}}$ noted in Ref. 135 [Figure 4.8(a)]. The reciprocal-space resolution of the measurements is marginally poorer than that used in the study of Ref. 135, which is a consequence of optimising for real-space resolution—this variation is likely responsible for the small unphysical fluctuation in molar volume near T_{JT}. The results of the refinements for the seven temperature points spanning O' and O phases are given in Table 4.2; these values are consistent with those reported in previous study, Ref. 62. As anticipated from the discussion in section 4.2, the key consequences of orbital disorder within the O phase are (i) the emergence of a pseudocubic lattice metric, (ii) the near equivalence of Mn–O bond lengths, and

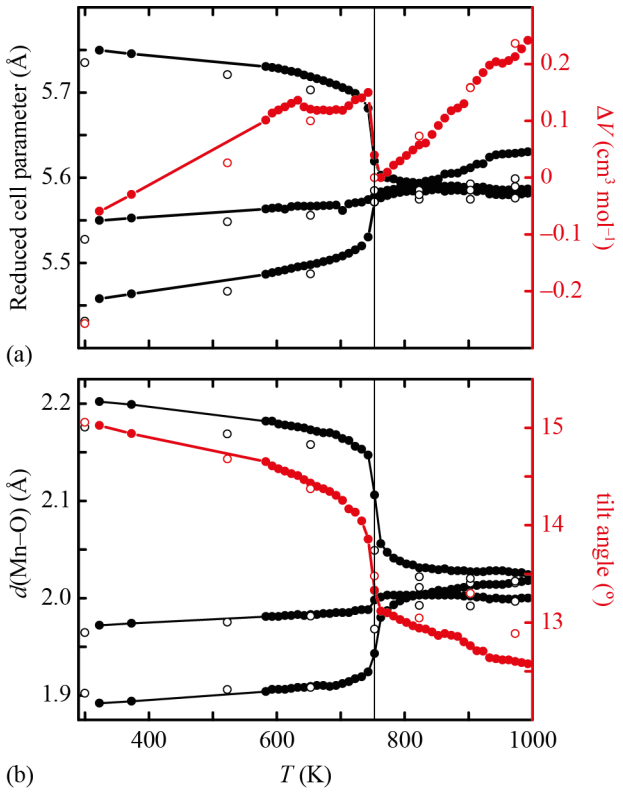


Figure 4.8: Temperature-dependent structural variation in $LaMnO_3$ as determined using Rietveld analysis of X-ray (filled symbols) and neutron (open symbols) to total scattering data. (a) The unit cell metric becomes pseudocubic at T_{JT} with a volume collapse of *ca* $0.15\,cm^3\,mol^{-1}$. (b) The three crystallographically-distinct Mn–O bond lengths also converge at T_{JT}; a modest variation in tilt angle also accompanies the transition.

(iii) the increase in atomic displacement parameters.

The sensitivity of X-ray scattering data to O atom positions is markedly reduced when re-examined in the absence of accompanying neutron scattering data points. Nevertheless, I obtained satisfactory Rietveld refinements at all temperature points collected in my study of the X-ray data (an example of a fit is shown in Figure 4.6). In this way insight into crystallographic variations across the orbital order/disorder transition at a much finer temperature interval than was possible from the neutron scattering measurements are obtained—all the refined parameters at each temperature and a fit at every 50 K are presented in Appendix B2. Figure 4.8(b) shows the

Table 4.2: Structural parameters for $LaMnO_3$ as determined by Rietveld refinement against neutron Bragg diffraction patterns. Included are the two crystallographically-distinct Mn–O–Mn bond angles (θ_1, θ_2), from which the octahedral tilt parameter ϕ was determined according to the method outlined in Ref. 62.

T/K	300	523	653	753	823	903	973
Phase	O'	O'	O'	O	O	O	O
a/Å	5.73484(4)	5.72072(4)	5.70290(5)	5.58482(13)	5.57448(11)	5.57446(7)	5.57592(8)
b /Å	7.68113(5)	7.73080(7)	7.75978(8)	7.8791(3)	7.8910(2)	7.89888(18)	7.90448(18)
c/Å	5.52744(3)	5.54801(4)	5.55559(4)	5.57204(18)	5.58503(16)	5.59239(9)	5.59864(9)
x_{La}	0.04884(7)	0.04397(8)	0.04041(10)	0.02522(17)	0.02136(12)	0.02026(14)	0.01703(14)
z_{La}	0.00802(8)	0.00683(10)	0.00624(12)	0.0041(5)	0.0036(3)	0.0023(5)	0.0014(3)
x_{O1}	0.98790(9)	0.98869(12)	0.98973(14)	0.9905(3)	0.9902(3)	0.9921(3)	0.9911(3)
z_{O1}	0.57395(9)	0.57258(12)	0.57183(13)	0.5691(5)	0.5692(3)	0.5708(4)	0.5675(3)
x_{O2}	0.19346(7)	0.19565(7)	0.19789(8)	0.2156(3)	0.22025(19)	0.2241(2)	0.22411(18)
y_{O2}	0.96418(5)	0.96210(6)	0.96274(6)	0.9619(2)	0.96226(14)	0.96384(19)	0.96247(14)
z_{O2}	0.77436(8)	0.77297(10)	0.77200(12)	0.7741(3)	0.7758(2)	0.7756(2)	0.7730(2)
U_{iso}(La)/Å^2	0.00520(12)	0.00365(12)	0.00420(13)	0.00610(18)	0.01381(19)	0.01595(13)	0.0162(2)
U_{iso}(Mn)/Å^2	0.00227(19)	0.00058(19)	0.0013(2)	0.0038(3)	0.00874(19)	0.01020(17)	0.0111(2)
U_{iso}(O1)/Å^2	0.00679(17)	0.00647(18)	0.0087(2)	0.0152(5)	0.0228(4)	0.0266(5)	0.0274(5)
U_{iso}(O2)/Å^2	0.00603(12)	0.00482(12)	0.00649(14)	0.0130(3)	0.0210(3)	0.0238(3)	0.0253(4)
θ_1/°	155.63	156.17	156.51	157.67	157.62	156.95	158.16
θ_2/°	155.12	155.81	156.47	158.24	158.76	159.52	159.68
ϕ/°	15.06	14.68	14.37	13.48	13.33	13.30	12.89

changes of Mn–O bond lengths and octahedral tilt angles as a function of temperature across this transition. This expected discontinuous convergence of Mn–O bond lengths, together with the small variation in tilt angle at T_{JT} is in good agreement with previous studies.[62,135] The conclusion from the refinement of neutron and X-ray data is that the sample and the temperature dependence of its average structure are consistent with previous observations of stoichiometric $LaMnO_3$.[62,135]

4.4.2 Neutron and X-ray PDF: Direct analysis

The temperature-dependent variation in neutron and X-ray $D(r)$ functions is shown in Figure 4.9. Unlike the previous neutron PDF studies of Refs. 141,258, which did not allow for a direct comparison at distances beyond the nearest Mn–O distance, I present a direct comparison of data out to 10 Å. The new X-ray PDF data show little sensitivity to pairwise correlations involving O atom positions; instead

their temperature-dependent behaviour is indirectly sensitive to cooperative JT phenomena *via* coupling between O displacements and Mn and La atom positions. In the data, a clear consistency in PDFs obtained from independent measurements at different temperatures is observed, with a high ratio of signal-to-noise. The persistence of JT distortions within the orbital-disordered O phase is directly evident in the asymmetry of the nearest-neighbour Mn–O peak of the neutron PDF. The peak at $r \simeq 2\,\text{Å}$ is inverted as a consequence of the negative neutron scattering length of Mn. The reduced real-space resolution of the X-ray PDF data, together with the low X-ray scattering power of Mn and O atoms (relative to La) means that it is not possible to resolve the JT distortion directly from X-ray PDF measurements alone. Nevertheless, in these respects the data are entirely consistent with the results of earlier PDF studies.[141,258]

What is remarkable in the new PDF data is the clear signature of a discontinuous change in the PDFs for both neutron and X-ray measurements across the O'/O orbital order/disorder transition—that involves correlations at interatomic distances less than the dimensions of one unit cell. This discontinuity is evident in the raw PDF data themselves—as displayed Figure 4.9(a,b)—but is even more clearly identified by considering the relative changes in $D(r)$ at specific values of $r < 6\,\text{Å}$. For a given separation of interest r', I used separate linear fits to the $D(r = r', T)$ function for temperatures $T < T_{\text{JT}}$ and $T > T_{\text{JT}}$ to identify expectation values $\tilde{D}_{O'}$ and $\tilde{D}_O$ at 500 and 1000 K *i.e.*, covering the O' and O regimes. Using these expectation values an order parameter was formed:

$$x(r', T) = \frac{D(r', T) - \tilde{D}_O}{\tilde{D}_{O'} - \tilde{D}_O}, \tag{4.2}$$

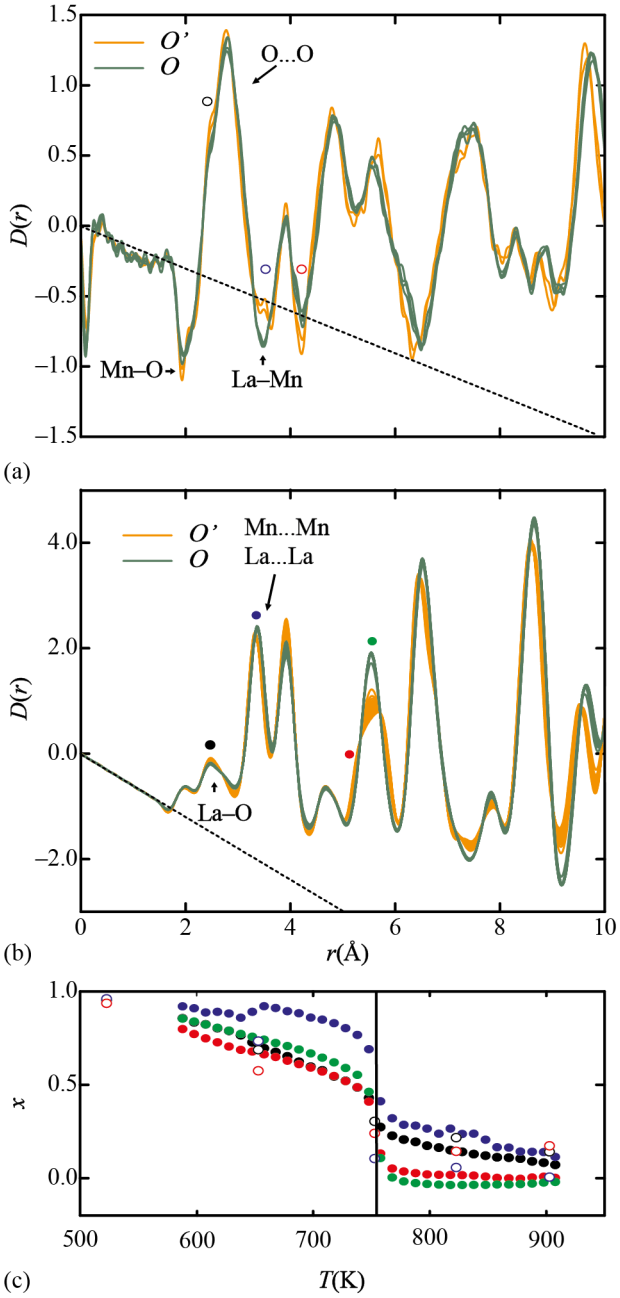


Figure 4.9: Temperature-dependent variation in (a) neutron and (b) X-ray PDFs across the O' (orange lines) / O (green lines) transition. In both panels (a) and (b) the PDF baseline is indicated as a dashed black line. (c) The normalised temperature dependence of PDF intensities x (see main text for derivation) at a variety of key interatomic separations clearly reveals a discontinuous change in local structure accompanying the orbital order–disorder transition. The relevant interatomic separations are indicated in panels (a) and (b) using open and filled circles (neutron and X-ray data, respectively); these symbols correspond to those used in panel (c) to represent the corresponding temperature dependence.

which (by construction) tends to 1 as $T \rightarrow 500\,\mathrm{K}$ and to 0 as $T \rightarrow 1000\,\mathrm{K}$. This process allows me to compare meaningfully the smoothness in variation of $D(r)$ with T for different interatomic separations across both X-ray and neutron PDFs. I calculated $x(r', T)$ functions for seven representative pairwise separations r' in both neutron and X-ray PDFs; the results are shown in Figure 4.9(c) and clearly identify a discontinuous variation in $D(r)$ at T_{JT}. This behaviour is entirely consistent with the previous EXAFS and XANES studies of Refs. 112,255, which also measured a greater difference in signal across T_{JT} than for comparable temperature intervals within either the O' or O phases.

In conventional order/disorder transitions, observed in other studies such as that between the α- and β- phases of SiO_2 cristobalite,[265] the PDF is unchanged at the transition itself for short distances. This is because the local structure in both ordered and disordered states is essentially identical. At high temperatures, the local distortions present within the disordered state are not correlated over macroscopic length-scales, but the correlation length diverges on cooling towards the transition temperature. Hence, such transitions are accompanied by discontinuities in the Bragg diffraction pattern which is sensitive to long-range correlations, without any abrupt change in the accompanying PDF, which is sensitive to short-range correlations. Instead the behaviour observed for $LaMnO_3$ at T_{JT} reflects a local structure transition, as observed in *e.g.* the metal–organic frameworks UiO-66 and NU-1000 during solvent removal,[266] or indeed across the metal–insulator transition in VO_2[267] or the doped manganites $La_xCa_{1-x}MnO_3$.[142] Consequently, from this result it can be assumed that the orbital order/disorder transition in $LaMnO_3$ involves a discontinuous change in local structure, which in turn implies that orbital arrangements

within the high-temperature O phase may be meaningfully different to those in the ordered O' phase. A particular concern in the comparison of the data is the role of inelastic scattering at various temperatures. Irrespective of which normalisation protocol is used for the X-ray or neutron total scattering data, the same trends in the behaviour of $D(r)$ at T_{JT} are observed. Because of this discontinuous change in local structure at T_{JT}, it is anticipated that the C-type orbital correlation model should not provide a meaningful description of local orbital correlations in the O phase.

4.4.3 Neutron and X-ray PDF: PDFGui analysis

In order to achieve a deeper understanding of the local orbital order in O-phase $LaMnO_3$ a series of small-box PDF Rietveld refinements were carried out. The three orbital correlation models used are those described in Section 4.3.5, here I contrast the ability of these models to account for both X-ray and neutron $D(r)$ functions at distances ≤ 6 Å. There are two reasons for using the 6 Å distance: first, it is commensurate with the unit cell dimensions, and so represents a length-scale that is large enough to be sensitive to differences in the various models studied, but also small enough that the use of approximants remains valid; and second, it includes the various interatomic separations highlighted in Figure 4.9(c) for which it is known that $D(r,T)$ is discontinuous at T_{JT}. For completeness I have also compared these results with fits to neutron data alone, and also with fits to combined neutron and X-ray PDFs carried out over the larger range $1.5 \leq r \leq 10$ Å. Such comparisons will allow insight into the robustness of any conclusions drawn with respect to the particular relative weighting of X-ray and neutron data, on the one hand, and the

value of $r_{\max}$ over which fitting is carried out, on the other hand. Within the orbital-ordered O' regime, the PDF data show a clear preference for the C-type orbital correlation model. This is demonstrated in Figure 4.10(a,c), where I compare the quality of fits for all three models to the neutron and X-ray $D(r)$ collected at 653 K. Despite the meaningful differences amongst the three models, and the clear indication from average structure interpretation of the diffraction pattern that $LaMnO_3$ exhibits C-type orbital order at this temperature, the differences in quality of fit for the three models are probably much smaller than what would have been

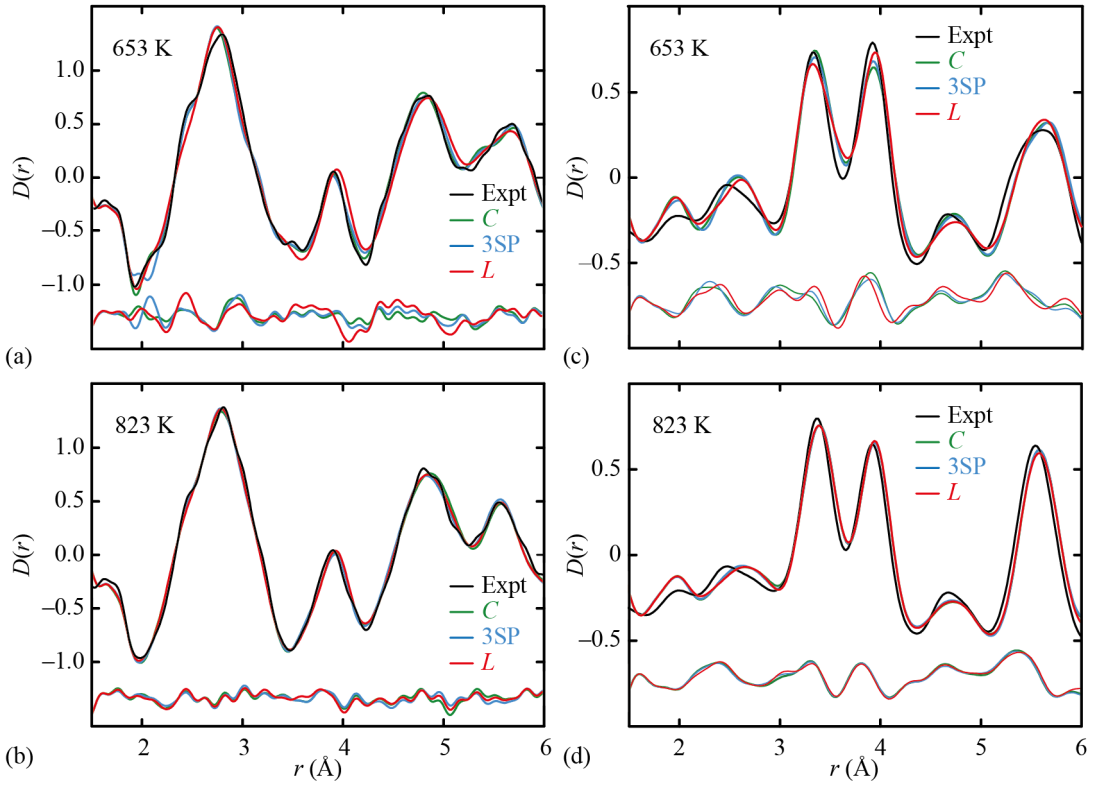


Figure 4.10: Neutron and X-ray PDF fits for data collected within the (a,c) O' and (b,d) O regimes corresponding to neutron (a,b) and X-ray (c,d) data. Experimental data are shown as black lines, and fits shown in green (C-type order), blue (3SP-type order) and red (L-type order). The corresponding difference functions (data−fit) are shown in the relevant colour, shifted vertically. The fits shown here were for PDFGui refinements involving simultaneous neutron and X-ray PDFs.

expected. Nevertheless, the L-type model clearly results in a significantly poorer fit throughout the whole r-region, and the 3SP-type model cannot capture the correct shape of the nearest-neighbour Mn–O peak while also fitting the remainder of the PDF. The refined parameters and qualities of each fit at each temperature are given in Table 4.3.

The magnitude of JT distortion is accounted for by the fitting parameter δ, which is related to the difference between long and short Mn–O bond lengths. Simple geometric considerations give

$$\Delta d(\text{Mn–O}) \simeq k|\delta|\sqrt{a^2 + c^2}, \tag{4.3}$$

where the proportionality factor $k = 2$ (as a consequence that the displacement is linked to two oxygens) for the C- and 3SP-type models, and $k = 1$ for the L-type model (the displacement is refined for one manganese). For the C-type model fitted against neutron and X-ray PDF data collected at 653 K (*i.e.* within the orbital order regime) A JT distortion of 0.25 Å was obtained, which is remarkably similar to the value obtained from Rietveld refinement against Bragg intensities [Δd(Mn–O) $\simeq$ 0.25—0.3 Å; Figure 4.8(c)]. Despite their poorer fits, both 3SP- and L-type models give similar distortions, showing this result is robust to choice of modelling approach. These results are entirely consistent with earlier PDF studies.[141,258] Within the orbital disorder regime, the situation is even less clear-cut. Figure 4.10(b,d), shows the comparison of the fits of the three models against the neutron and X-ray $D(r)$ function collected at 823 K—*i.e.*, within the O phase. These fits are remarkably similar and cannot be discriminated by eye. Numerically, it is found that the 3SP-

Table 4.3: Model parameters for $LaMnO_3$ as determined by PDFGui refinement against both neutron and X-ray PDFs. The highest-quality fit for each temperature point is highlighted in bold: the result shows that the *C*-type approximant best describe the orbital ordered state (as anticipated from the average structure), and the 3SP-type approximant to best describe the orbital disordered state, at all temperature points investigated.

	T/K	Q_{broad}	scale1	scale2	x_{La}	z_{La}	δ	U_{iso}(La)/Å^2	U_{iso}(Mn)/Å^2	U_{iso}(O1)/Å^2	U_{iso}(O2)/Å^2	R_{wp}/%
C	**653**	**0.19(12)**	**0.162(16)**	**0.21(6)**	**0.036(6)**	**0.0120(8)**	**−0.016(5)**	**0.008(7)**	**0.013(15)**	**0.02(2)**	**0.025(12)**	**12.3875**
	753	0.19(13)	0.159(18)	0.20(5)	0.022(9)	0.009(14)	−0.014(7)	0.008(9)	0.02(2)	0.03(5)	0.037(19)	10.7698
	823	0.18(13)	0.160(19)	0.20(5)	0.019(11)	0.010(14)	−0.014(8)	0.009(10)	0.02(2)	0.04(7)	0.04(2)	10.9087
	903	0.17(12)	0.159(19)	0.20(5)	0.017(12)	0.009(16)	−0.013(9)	0.010(10)	0.02(2)	0.05(9)	0.04(3)	10.8627
	973	0.13(11)	0.16(2)	0.18(5)	0.012(17)	0.00(5)	0.013(13)	0.015(12)	0.03(2)	0.04(11)	0.06(5)	10.8156
3SP	653	0.18(12)	0.161(16)	0.21(6)	−0.036(6)	0.012(8)	−0.014(5)	0.008(6)	0.017(18)	0.014(18)	0.028(15)	13.6527
	753	**0.18(13)**	**0.159(18)**	**0.20(5)**	**−0.022(9)**	**0.007(18)**	**−0.014(7)**	**0.009(10)**	**0.02(2)**	**0.03(5)**	**0.04(2)**	**10.4497**
	823	**0.15(12)**	**0.161(19)**	**0.20(5)**	**−0.018(11)**	**0.01(3)**	**0.013(8)**	**0.011(12)**	**0.02(2)**	**0.03(7)**	**0.05(4)**	**10.6293**
	903	**0.15(12)**	**0.161(19)**	**0.20(5)**	**−0.016(13)**	**0.00(4)**	**0.015(10)**	**0.013(12)**	**0.03(2)**	**0.03(8)**	**0.05(5)**	**10.4781**
	973	**0.13(12)**	**0.16(2)**	**0.18(5)**	**−0.014(17)**	**0.00(6)**	**0.012(10)**	**0.015(12)**	**0.03(2)**	**0.04(5)**	**0.08(17)**	**10.6128**
Ice	653	0.16(12)	0.164(17)	0.21(5)	−0.034(8)	0.011(17)	0.033(12)	0.011(8)	0.013(19)	0.02(3)	0.04(2)	16.3559
	753	0.16(10)	0.161(18)	0.20(5)	−0.020(12)	0.01(3)	0.027(17)	0.012(9)	0.02(3)	0.04(8)	0.04(3)	11.0794
	823	0.15(10)	0.162(18)	0.20(5)	−0.017(14)	0.01(4)	0.028(19)	0.013(10)	0.02(4)	0.05(11)	0.05(4)	10.7938
	903	0.15(10)	0.161(19)	0.20(5)	−0.016(15)	0.01(4)	0.03(2)	0.014(12)	0.02(4)	0.05(13)	0.05(5)	10.5081
	973	0.14(10)	0.16(2)	0.18(5)	−0.013(18)	0.00(4)	0.03(2)	0.016(14)	0.02(5)	0.06(18)	0.05(6)	10.6526

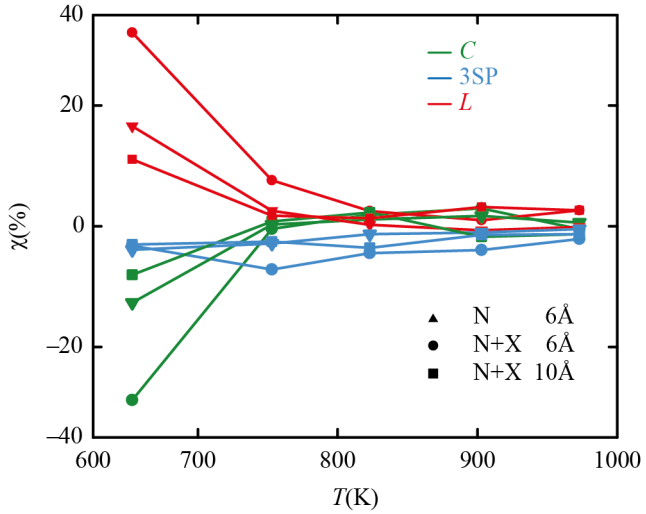


Figure 4.11: Relative goodness-of-fit χ for the various PDF fits described in the text. The three orbital arrangement models are given in the same colours as in Figure 4.10. The different symbols correspond to different fitting protocols: triangles indicate fits to neutron PDF data alone over the real-space range $1.5 \leq r \leq 6\,\text{Å}$, circles to both neutron and X-ray data over the same range, and squares to both data sets but over the increased range $1.5 \leq r \leq 10\,\text{Å}$. I expect the approximant approach to become less reliable at larger r-values, so the most reliable fits correspond to those shown using circles; details of the various refined parameters for these fits are given in Table 4.3.

type orbital correlation model describes the data best, but the corresponding R_{wp} value is only marginally lower than that for either the C- or L-type models, as given Table 4.3. Moreover, different fitting protocols—neutron only *vs* neutron + X-ray, or $r_{\text{max}} = 6\,\text{Å}$ *vs* $10\,\text{Å}$— result in variations in R_{wp} that are of the same order of magnitude as the differences between different models. This point is quantified by comparing the relative quality of fit,

$$\chi = \frac{R_{\text{wp}}}{\langle R_{\text{wp}} \rangle} - 1, \tag{4.4}$$

for the three models and three different fitting regimes as a function of temperature. The value of χ reflects the extent to which a particular model fits more closely ($\chi < 0$) or less closely ($\chi > 0$) than the average fit obtained for a given temperature

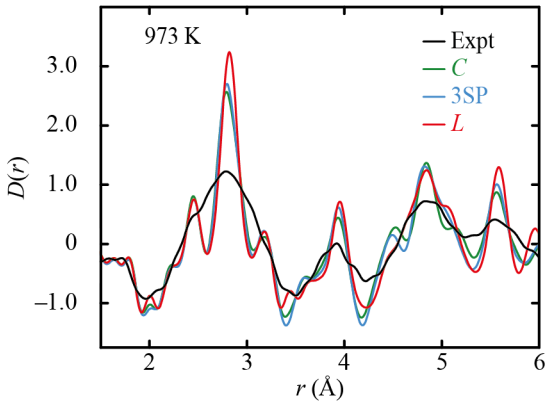


Figure 4.12: Calculated PDF for the three models green (C-type order), blue (3SP-type order) and red (L-type order) using the U_{iso} refined from Rietveld at 300 K and fixed with atomic displacement at 973 K. It clarifies that the thermal displacement may affect the choice of which model best represents the orbital disordered phase.

point. So at 653 K, for example, the C-type orbital model gives the best fit irrespective of the particular fitting protocol adopted. For temperatures above T_{JT}, however, the best-fit model can depend on the fitting protocol, which means that it is not possible to unambiguously identify the orbital arrangement pattern within the O phase from quality of PDF fit alone. The likely origin of the insensitivity in PDF analysis is the large magnitude of thermal motion at temperatures for which the orbital order/disorder state is observed. By recalculating the PDFs for each model using the same instrumental parameters in PDFGui refinements, but reducing the magnitude of thermal parameters to the values obtained from Rietveld refinement at 300 K, there are much clearer differences among the three fits [Figure 4.12]. Nevertheless, some general trends do emerge. Throughout the orbital disorder regime, the 3SP-type arrangement nearly always gives the highest-quality fit-to-data; likewise, the L-type arrangement nearly always gives the worst fit. Moreover, for what I consider to be the most meaningful choice of fitting parameters (neutron and X-ray

data, with $r_{\max} = 6\,\text{Å}$), the 3SP-type model consistently represents the data most closely. Consequently, I cautiously suggest that the local orbital arrangements in orbital-disordered $LaMnO_3$ are more accurately described by the anisotropic 3SP model proposed in Ref. 114 than either the C-type arrangement of the ambient-temperature phase—*i.e.* as proposed in the PDF study of Ref. 141—or the L-type arrangement obtained from RMC analysis.

This conclusion is supported by two other observations. First, the C-type arrangement might have already reasonably been ruled out on the basis that the observation of discontinuous change in the PDF at T_{JT}. If the orbital arrangements within the high-temperature phase would have to share the same experimental pattern as the low-temperature ordered phase, there would not be any reason for such a discontinuity as observed in the direct comparison of the PDF data. And, second, of the two models with different orbital arrangements to that of the ordered phase, it is the 3SP-type arrangement that contains the more conventional local JT distortion of MnO_6 octahedra. While the off-centered distortion of the L-type model is not without precedent in the structural chemistry of manganites,[268] the 180° arrangement of long Mn–O bonds is unquestionably the more frequently observed JT distortion for octahedral Mn^{3+}.

4.4.4 Single-crystal diffuse scattering

To distinguish between the three models it might be expected that single-crystal diffuse scattering measurements are more sensitive than PDF measurements, which are derived from the same scattering function but only after orientational averaging.[269] There are no published single-crystal scattering patterns (either X-ray or neutron)

for $LaMnO_3$ within the orbital disorder regime, and the collection of such data was beyond the scope of this study. Nevertheless, the qualitative form of structured diffuse scattering anticipated for different orbital disorder models is straightforwardly calculated. I proceed to present the results of only two such calculations for the 3SP and L-type disorder models, motions that the C-type orbital disorder model would result in minor diffuse scattering centred on the Bragg peak reflections of the parent orbital-ordered $Pnma$ phase.

Using a Monte Carlo approach I generated atomistic configurations representing a $20 \times 20 \times 20$ supercell of the aristotype perovskite lattice, in which atomic displacements had been introduced to capture the key correlations in the 3SP- and L-type models of orbital disorder in $LaMnO_3$. High-symmetry planes of the corresponding diffraction patterns are shown in Figure 4.13, from which it is evident that both models would result in highly-structured diffuse scattering as anticipated for correlated disordered states.[172] In both cases this scattering takes the form of diffuse rods of intensity oriented parallel to the $\langle 100 \rangle$ axes of the parent reciprocal lattice, with subtly different reflection conditions within the $(hk0)$ plane. The 3SP model also gives rise to a more structured background scattering pattern, which is most clearly seen here in the (hhl) scattering plane, displayed in Figure 4.13(a).

Despite the existence of some differences between these predicted single-crystal diffuse scattering patterns, there are three reasons why experimental diffuse scattering measurements may struggle to conclusively distinguish the two models. First, the Monte Carlo models are defect-free in the sense that the correlated displacements I include exactly satisfy the constraints of the 3SP- and L-type interactions; at the elevated temperatures for which the orbital disorder phase is stable it is rea-

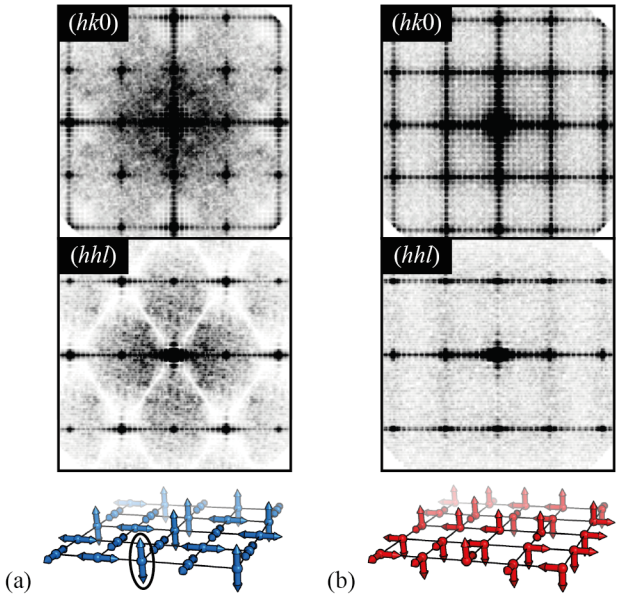


Figure 4.13: Calculated single-crystal diffraction patterns for (a) 3SP-type and (b) *L*-type orbital disorder models as described in the text. The reciprocal space labels are given relative to the reciprocal lattice of the cubic aristotype. The corresponding orbital-driven distortions are represented figuratively in the configurational sections shown at the bottom of each panel. My analysis identifies the 3SP-type model as the most likely description of the orbital disordered state; It is noted that this arrangement destroys the inversion centre at Mn sites (*e.g.* for the circled Mn centre).

sonable that any such constraints are sometimes broken, resulting in broadening of the corresponding diffuse scattering. So, for example, the structured background expected for the (hhl) plane of the 3SP-type orbital disorder model would almost certainly become washed-out in practice; likewise, blurring of the diffuse scattering in the $(hk0)$ plane of the *L*-type orbital disorder model may give the appearance of systematic absences as anticipated for the 3SP-type model. Second, the calculations have been designed to amplify the diffuse scattering (so as to reveal its underlying structure); in reality the intensity would be very low relative to that of the Bragg scattering. In the 3SP-type orbital disorder model, for example, the diffuse scattering arises only from small displacements of O atoms and so in the presence of strong scattering from La it would be almost invisible in X-ray scattering measure-

ments. Third, the significant degree of thermal motion present within the O phase will degrade the diffraction pattern at high-Q where the differences between diffuse scattering are clearest. The calculations shown in Figure 4.13 neglect any dynamic contribution to disorder in $LaMnO_3$.

4.5 Future work and concluding remarks

This study has cautiously identified the three state Potts model of Ref. 114 as providing the best description of orbital disorder in $LaMnO_3$ in terms of its ability to account for the experimental neutron and X-ray PDFs. In this model the Mn JT distortion arrangement is isotropic, which is consistent with the experimental observations of electronic and magnetic isotropy.[60,129] A more subtle consequence of this model is weak inversion-symmetry breaking at the Mn site [Figure 4.13(a)]. In principle this allows for increased d–p mixing, and as such is consistent with the small but reproducible XANES anomalies noted in Refs. 112 to occur at T_{JT}. A variation in the local symmetry of Mn environments is also consistent with renormalisation of the Mn-weighted phonon density of states, which is observed in inelastic neutron scattering measurements.[252] Given the configurational entropy of the 3SP arrangement, it would be expected that the low-frequency orbital rearrangements between equivalent 3SP states would occur over a timescale significantly longer than phonon excitations; this is consistent with the NMR treatment study of Ref. 126. Ahmed and Gearing have already established a link[114] between phase changes in 3SP model and the volume collapse.[135] Moreover, the entropy calculations of Ref. 270—which at face value seemed to establish an inconsistency between the 3SP model and experimental specific heat measurements[112]—later revised in Ref. 113 and so the model

appears to be consistent with a broad range of experimental observations.

The newly collected PDF data made it clear that the O'/O transition in $LaMnO_3$ is fundamentally different to conventional order–disorder transitions in that there is a discontinuity in the PDF data (for X-ray and neutron) at T_{JT}. This same point had also been noted in the EXAFS and NMR studies of Refs. 126,255 but was less clear in earlier PDF studies because of the focus on the variation of the lowest-r Mn–O peak as a function of temperature. From a scientific perspective, the key implication of this discontinuity is that the electronic description of orbital disordered states need not necessarily follow the corresponding ordered states, since orbital arrangements may differ meaningfully between the two. This poses substantial computational challenges because (i) explicit description of disordered orbital arrangements requires large atomistic configurations, and (ii) these states are entropically stabilised and so cannot necessarily be studied meaningfully in the athermal limit. Consequently, it is assumed that further detailed investigation of the orbital disordered states in the $La_{1-x}Ca_xMnO_3$ family may still give useful insight into CMR itself; I study precisely this point in Chapter 5.

Finally, this study has shed light on the methodological limitations of PDF analysis. The original study by former student Dr. C. A. Young using RMC refinements favoured the most disordered representation of orbital disorder this result is a consequence of, on the one hand, the L-type arrangement being more likely to be encountered during refinement than the 3SP- or C-type models, and, on the other hand, the difference in quality of fit for the various models in RMC being insufficiently large to bias against the statistical result. But my own study does also show that the "small-box" modelling is not immune to the uniqueness problem which are

often highlighted for "big-box" modelling using RMC or EPSR.[183,271] In particular, using meaningfully different small-box models in this study gave remarkably similar fits to the disordered state. Surprisingly, the *L*-type model (obtained from RMC) gave a fit-to-data almost indistinguishable from the published PDF fits of earlier studies [Figure. 4.10(b)].[141,258] This suggests that it may not always be sufficient to present a good PDF fit as evidence alone to support a small-box model. This point is relevant to what is observed in the previous chapter where two very different models gave almost equal fits. In the case of $Y_2Mo_2O_7$, it was possible to resolve the orbital ordering state because the temperatures at which the data were collected ($T < 15\,\mathrm{K}$) were much lower than those relevant for the orbital order/disorder transition in $LaMnO_3$. This is a point to which I will return in the concluding discussion of Chapter 6.

Chapter 5

Local structure study of the $La_{1-x}Ca_xMnO_3$ family

5.1 Introduction

In this chapter I present a total scattering study of the local structure in the $La_{1-x}Ca_xMnO_3$ family. The material consists of a strong correlation of the spin, charge, orbital and lattice degrees of freedom which complicate the analysis of this system.[272,273] In the previous chapter, the end member ($LaMnO_3$) was studied to obtain an understanding of its orbital order/disorder transition – this transition is quickly stabilised at lower temperatures on substitution in $La_{1-x}Ca_xMnO_3$ [Figure 5.1]. Here I present new neutron and X-ray PDF data collected as a function of compositions and temperatures. The key results of this study are (i) the observation of a discontinuity in local structure across the orbital order/disorder transition now traversed with composition, and (ii) evaluation of previous proposed models for the charge order/orbital disorder state in $La_{0.5}Ca_{0.5}MnO_3$.

5.2 Background

The $La_{1-x}Ca_xMnO_3$ family has been extensively studied over the last decade because of its ability to show CMR.[274] The strongest CMR state has been observed for the composition $La_{0.67}Ca_{0.33}MnO_3$; this effect has been the subject for several

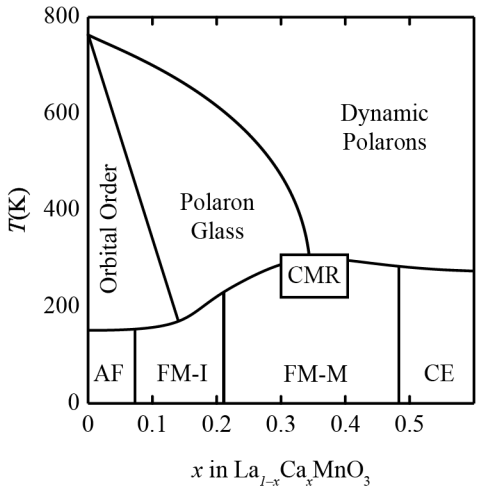


Figure 5.1: Phase diagram for the $La_{1-x}Ca_xMnO_3$ carried out from SQUID data collected on the samples synthesised in this study and Ref 96.

studies.[10,24,61,96,97,275] However, as introduced in Section 1.3.3, development of a microscopic understanding of the CMR state is still a key challenge in the field. Key difficulties in understanding the CMR state includes: the metal-insulator transition, the magnetic ordering, interplay between charge localisation, orbital arrangement, and the spin orientation [Figure 5.1].[142,275]

One common entry point for understanding the CMR state in $La_{1-x}Ca_xMnO_3$ is to focus on the end members $LaMnO_3$ and $La_{0.5}Ca_{0.5}MnO_3$.[272,275–277] As we have seen in Chapter 4, even $LaMnO_3$ presents substantial challenges. The same degree of complication applies to the half-doped $La_{0.5}Ca_{0.5}MnO_3$, where a charge ordered and orbital ordered (CO/OO) state at low temperature has been proposed.[23,24,276,278] While several models have been proposed for the ground state at this composition there is no unique model that is consistent with all experimental studies.[142,275,277,278] I will here give an introduction to the phase diagram of $La_{1-x}Ca_xMnO_3$ and then give a brief introduction to previous studies related to this chapter. I then move on

to introduce previous work carried out on the specific composition, $La_{0.5}Ca_{0.5}MnO_3$, which is the composition I have studied in further details.

5.2.1 $La_{1-x}Ca_xMnO_3$

As already introduced in sections 1.3.3 and 1.4.2, the $La_{1-x}Ca_xMnO_3$ family has attracted a lot of attention due to its ability to show CMR. The phase diagram also shows various physical properties as the concentration of Ca increases [Figure 5.1]. The material is antiferromagnetic at low Ca concentration ($x \simeq 0.08$), with increasing the concentration the material turns into a ferromagnetic insulating state.[279] In further increase of Ca concentration the material becomes ferromagnetic metallic state in which the CMR state occurs ($x \simeq 0.21$). The strongest CMR appears at a concentration of $x = 0.33$, which is expected to be caused by the right ratio of competing polarons and double exchange interactions of the JT active Mn^{3+} ions.[9,61] The understanding on how the Mn^{3+} and Mn^{4+} arranged in structure has therefore been the focus for several studies. Because of the negative scattering length of manganese from neutrons, the main technique has been neutron total scattering to picture the ordering.[110,138,142,277,280,281] The PDF study of Ref. 142 investigated the change in magnitude of the local JT distortion as a function of composition and temperature (also introduced in section 1.5.5) to achieve an understanding on how the Mn–O bonds ordered and changed as a function of concentration and temperature. They observed local JT distortion at each composition, but the magnitude of the distortion decreased when doping Ca [Figure 5.2(a-c)]. Furthermore, they plotted the concentration of Ca as a function of temperature for three different ranges of refining the Mn–O distance which showed the Mn–O JT distortion was conserved

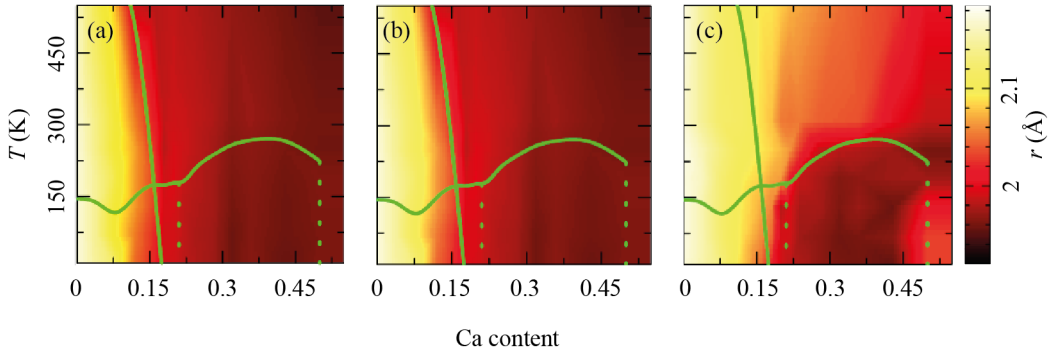


Figure 5.2: Contour plot of the magnitude of Mn–O distances in $La_{1-x}Ca_xMnO_3$ as a function (x, T) obtained from (a) Rietveld refinement and for PDF analysis over the range of (b) 20 Å and (c) 6 Å. The figure is adapted from Ref. 142.

at $r_{max} = 6$ Å, but appeared to vanish when refined to $r_{max} = 20$ Å. For the metallic state, no sign of JT-distortion appeared which was also expected. None of these PDF studies managed to give a clear picture on the structure on microscopic scale.

5.2.2 $La_{0.5}Ca_{0.5}MnO_3$

As introduced in section 5.1 $La_{0.5}Ca_{0.5}MnO_3$ is of particular interest because it is an endmember. This composition is also interesting because it straddles the boundary of antiferromagnetic and ferromagnetic ground states [Figure 5.1].

$La_{0.5}Ca_{0.5}MnO_3$ is isostructural to $LaMnO_3$, consisting of an orthorhombic unit cell with *Pnma* symmetry.[282] It has been reported that the material undergoes magnetic transitions from an antiferromagnet to ferromagnet at $T_N \simeq 155$ K and from a ferromagnet to paramagnet at $T_C \simeq 255$ K. The phase below $T_N \simeq 155$ K has been proposed to be of the CE type implying the presence of CO according to a structure suggested by Goodenough.[272] Specifically, Goodenough proposed that the Mn^{3+} and Mn^{4+} ions ordered in alternating layers along the [100] axes for the orthorhombic

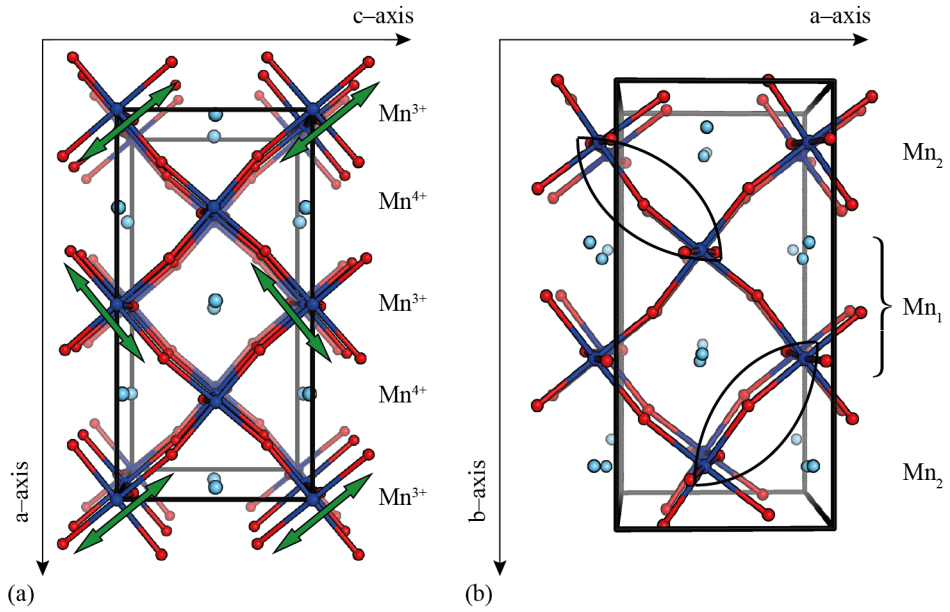


Figure 5.3: (a) The low temperature $La_{0.5}Ca_{0.5}MnO_3$ superstructure proposed by Radaelli *et al*, . (b) Represents the second low temperature $Pr_{0.5}Ca_{0.5}MnO_3$ superstructure proposed by Aladine *et al*, . The black circles shows the Mn—Mn dimerisation.

unit cell with *Pnma* symmetry.[61] The JT active Mn^{3+} ions order in a zigzag pattern and the undistorted Mn^{4+} ions order throughout the structure with a periodicity that is commensurate to the crystal lattice.

In Ref. 275 Radaelli *et al*. interpreted Goodenoughs model experimentally by fitting to neutron and X-ray diffraction data. They realised that the model was overly simplified and this phase was more complex. Instead they developed a more complex model based on the observation of satellite peaks in their data below T_N which they attributed to quasicommensurate modulation of the Mn^{4+} octahedra (I denote it LT-M model), which still agrees with Goodenough's CO/OO model. The model was implemented using a superstructure with $P2_1/m$ symmetry and orthorhombic metric with the a-axis twice as long [Figure 5.3(a)]. Goodenough's CO/OO model was also examined using other experimental methods; an EXAFS study investigated

the local structure around Mn atoms which did not show any linear combination of JT distorted Mn^{3+} and JT-inactive Mn^{4+} octahedra as expected for the CO/OO model. In fact they did not observe any changes in the local structure around the Mn atoms with temperature. They therefore concluded that the free e_g electron was not constrained to a particular atom type as expected for a CO/OO ordering, instead they suggested it was delocalised across Mn–Mn pairs on the atomic scale. For this to be possible the extra e_g electron must be localised in large wavepacks and jump among different clusters which would be the main channel for electrical conduction.[280]

A single-crystal neutron diffraction study of $Pr_{0.5}Ca_{0.5}MnO_3$ showed two inequivalent MnO_6 octahedra both slightly elongated but with very similar Mn–O distances [Figure 5.3(b)].[283] This picture disagrees with separated Mn^{3+} and Mn^{4+} ionic species as proposed in the CO/OO model. Instead they suggested that the Mn–Mn ions dimerised with effective oxidation state $Mn^{3.5+}$: in this model the single e_g electron is shared on the bridging oxygen. This was implemented using an enlarged cell (b'=2b) with an orthorhombic $P2_1nm$ symmetry. This model contained two individual Mn sites with almost equally distorted MnO_6 octahedra. I will be be referring to this as the LT-O model.[278,283]

A XANES study observed two different Mn ions in agreement with the two diffraction studies.[275,283,284] However, the two crystallographic Mn sites could not be considered as purely ionic Mn^{3+} or Mn^{4+} states so are inconsistent with a simple CO/OO model. Instead, they suggested that the CO transition is a structural transition induced by the change in the mean free path of electrons that continue to be thermally active below T_{CO} by forming ferromagnetic Mn–Mn pairs stabilised by the double

exchange process.[284]

The PDF study of Ref. 277 examined the two models (LT-M and LT-O) describing the low temperature state in $La_{0.5}Ca_{0.5}MnO_3$ obtained from average structure refinements. They observed that neither the CO/OO (LT-M) model or the Mn—Mn dimer (LT-O) model fitted the local structure well. Instead they allowed the LT-M model to refine using $P2_1/m$ symmetry without the constraints implemented in the ionic LT-M model. This model (which I denote LT-M′) gave an improved fit and suggested that the orbital ordered state is only partially charge ordered.[277] However, this study did not make a direct analysis of the local structure to examine the distances beyond the nearest Mn–O distance across temperature which indicate whether the Mn^{3+} and Mn^{4+} would order at low temperature in agreement with the CO/OO model.

In this chapter I present newly collected neutron and X-ray PDF data for samples with compositions x=0.09, 0.1, 0.11, 0.2, 0.25, 0.33, 0.4 and 0.5. I will address three key points in this chapter: (i) to investigate the signature of orbital order/disorder transition in the local structure as a function of x in $La_{1-x}Ca_xMnO_3$ at RT. The changes in local structure will be compared to the temperature-driven orbital order/disorder transition in $LaMnO_3$ observed in the previous chapter; (ii) to present a qualitative PDF study of local structure as a function of temperature at the CMR composition ($La_{0.67}Ca_{0.33}MnO_3$) and at the CE ($La_{0.5}Ca_{0.5}MnO_3$) composition; (iii) to re-examine previously proposed models of the low temperature state of $La_{0.5}Ca_{0.5}MnO_3$ composition using PDF and Rietveld analysis.

5.3 Experimental

5.3.1 Sample Preparation

Ca-doped $LaMnO_3$ samples were prepared in collaboration with Dr. Midori Patino and Prof. Mike Hayward *via* a citrate gel method similar to that used in Ref. 261. Stoichiometric quantities of La_2O_3 (99.99%), MnO_2 (99.99%), and $CaCO_3$ (99.99%) powder were dissolved in a minimum quantity of 6 M nitric acid. Two molar equivalents of citric acid and 5 mL of AnalaR ethylene glycol were added, and the solution was heated to 90-100 °C under constant stirring. The mixture turned into a gel before it crystallised into a powder. The powder was ground and heated to 900 °C to burn the small amount of gel left in the sample. The sample was reground and pressed into 10-15 mm pellets and fired at 1350 °C in an oxygen atmosphere for 12 hours. Finally, this process was repeated but with firing under argon flow to ensure no manganese vacancies appeared in the powders due to oxidation.[285] The final product had a mass of 8.5–9.5 g per sample. Samples were synthesised for the compositions x=0.09, 0.1, 0.11, 0.2, 0.25, 0.33, 0.4 and 0.5 in order to explore a large region of the complex LCMO phase diagram [Figure 5.4(b)]. SQUID data and in-house X-ray powder diffraction data (PXRD) at room temperature were collected to ensure each synthesised sample of $La_{1-x}Ca_xMnO_3$ had the desired composition. In Table 5.1 the refined lattice parameters and volume from in-house PXRD are displayed. The La/Ca occupancies were refined to the powder neutron diffraction data since these data are more sensitive to divalent site occupancies compared to medium-resolution synchrotron X-ray data. The magnetic transitions from SQUID

analysis were obtained and compared to the literature.[110,275,286–290]

Iodiometric titration

Iodometric titration experiments were carried out to determine the average oxidation state of the manganese in each sample. Approximately 40 mg of ground sample was placed in a three-necked round bottled flask washed with argon. A constant flow of argon was maintained during the titration. The solution was dissolved in diluted HCL in the concentration of $\sim$ 1:10 HCL: water and excess of KI was added ($\sim$ 0.3 g). A solution of sodium thiosulfate ($Na_2S_2O_3$) was used to titrate the sample against. The concentration of each batch of thiosulfate was accurately determined by carrying out a standardisation titration against acidified potassium iodate with excess of potassium iodide. Few drops of starch were added to help verify the exact end point of the titration. For each sample, three titrations were carried out and the measured values for each composition are shown in Table 5.1. The values are below expected which is assumed to be caused by the lack of fully inert conditions when the experiment was carried out.[291] Although, an over expected value would indicate cation vacancies. As anticipated, the oxidation state increase with Ca. The volume decrease across composition shows that the Ca concentration increases as x increases.

5.3.2 Data Collection

Neutron Total Scattering Measurements

Neutron total scattering data were collected using the POLARIS diffractometer at ISIS.[171] The polycrystalline samples of $La_{1-x}Ca_xMnO_3$ were loaded into cylin-

Table 5.1: The table collected data for $La_{1-x}Ca_xMnO_3$ using different methods and compared with the literature

Sample	**Lattice**			**Volume**	**Frac**	**SQUID**		**Titration**	
-	a/Å	b/Å	c/Å	Å^3	x	T_C obs(K)	T_C lit.(K)	Ox. state(measured)	Ox. state(expected)
$La_{0.09}Ca_{0.91}MnO_3$	5.615(2)	7.723(3)	5.5287(19)	239.74(15)	0.102(7)	-	-	2.97(5)	3.09
$La_{0.1}Ca_{0.9}MnO_3$	5.6010(15)	7.725(2)	5.5265(14)	239.11(11)	0.117(6)	135	135 [286]	2.95(2)	3.1
$La_{0.11}Ca_{0.89}MnO_3$	5.5910(12)	7.7327(16)	5.5270(11)	238.96(8)	0.131(4)	-	-	3.03(4)	3.11
$La_{0.2}Ca_{0.8}MnO_3$	5.4970(9)	7.7724(13)	5.5087(9)	235.36(7)	0.212(5)	185	185 [287]	3.07(4)	3.2
$La_{0.25}Ca_{0.75}MnO_3$	5.481(8)	7.7529(12)	5.4974(8)	233.61(6)	0.260(4)	175	180 [110,288]	3.10(3)	3.25
$La_{0.33}Ca_{0.67}MnO_3$	5.4605(19)	7.734(3)	5.4609(19)	230.63(13)	0.348(4)	250	250 [289]	3.21(8)	3.33
$La_{0.4}Ca_{0.6}MnO_3$	5.4441(12)	7.6903(17)	5.4594(12)	228.57(9)	0.393(4)	250	260 [290]	3.217(7)	3.4
$La_{0.5}Ca_{0.5}MnO_3$	5.419(11)	7.656(15)	5.435(11)	225.5(8)	0.465(4)	- and 230	155 and 230 [275]	3.23(2)	3.5

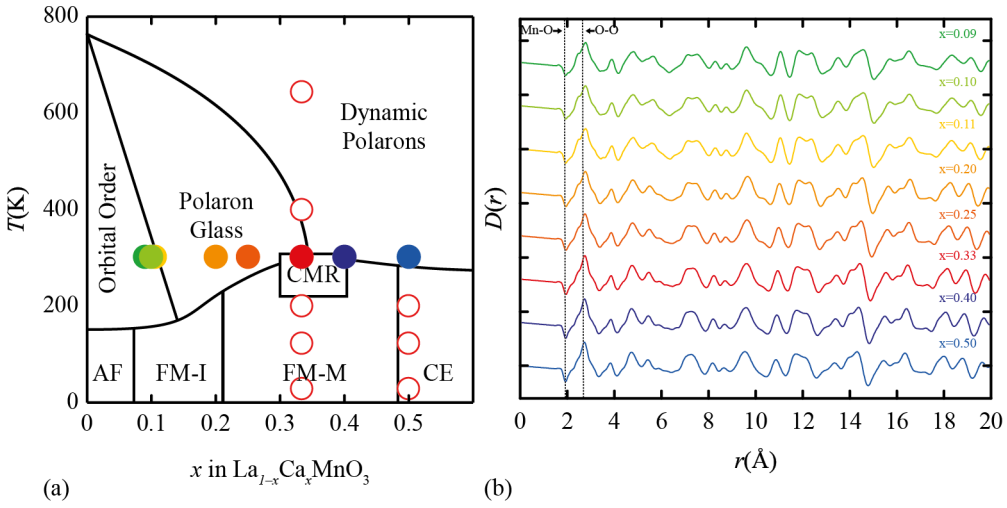


Figure 5.4: (a) Phase diagram of Ca doped $LaMnO_3$ with filled marks indicating the compositions at which data presented (b) were collected. Red circles show the complete temperature range at which neutron PDF data were collected, but not presented here. (b) Shows the neutron PDF for $La_{1-x}Ca_xMnO_3$ at room temperature.

drical vanadium cans of 8 mm diameter, with a height of 5.8 cm, and placed in a custom-designed carousel, itself placed in a custom-designed cryostat. Total scattering data were collected over the reciprocal space range $1.0 \leq Q \leq 45\,\text{Å}^{-1}$, which corresponds to real space resolution of $\Delta r \simeq 3.791/Q_{\text{max}} = 0.084\,\text{Å}$. Data collection times were optimised for total scattering measurements; I performed sixteen total scattering measurements at different temperatures and composition, displayed in Figure 5.4(b).

The total scattering data were corrected and placed on an absolute scale using the standard methods implemented in the GudrunN software.[181] The correction included background subtraction, scattering, absorption, multiple scattering and beam intensity variation. Normalised data across composition are presented in Figure 5.4(b). To stay consistent with the previous PDF study[277] the contribution from magnetic scattering was not subtracted. The magnetic scattering would appear at low Q and

give rise to a small broad wave in real space and would be observed as background noise in real space.[292] This does not have any large effect on my analysis since I have focussed on the sharp peaks in the real space PDFs. The Bragg profile function was extracted from the scattering data and used for Rietveld refinement. The corrected total scattering data were also transformed into PDF using the $D(r)$ normalisation as defined in Chapter 2, which was used for direct comparison and as input for PDF Rietveld refinement.

X-ray Total Scattering Measurements

Variable temperature X-ray total scattering data were obtained on the I15 beamline at the Diamond Light source, with wavelength $\lambda = 0.16421$ Å. Small amounts of the sample from the neutron experiment were finely ground and loaded into a 1 mm Silica capillary. Each capillary was mounted vertically on a rotatable goniometer and the sample temperature was adjusted using a hot air blower and an Oxford cryojet, calibrated with a thermocouple. A beam size of 1.5 mm × 1.5 mm was selected with a Perkin-Elmer flat plate 1621 EN detector mounted 210 mm from the sample. X-ray total scattering data were collected for each sample composition at room temperature. For $x = 0.33$, total scattering scans at the temperatures 100, 200, 400, 500, and 673 K were collected with 5 K intervals from 110 to 400 and 10 K intervals from 400 to 670 K with 5 second scans collected for Rietveld refinement. For each of the total scattering temperature points, 20 scans of 60-second exposure were collected and then averaged. This same setup was used for for $x = 0.5$ but with total scattering scans at 100, and 200 with 5 K intervals from 110 to 300 with 5 second scans collected for Rietveld refinement. Background measurements were collected using an

empty Silica capillary in an identical setup, including the same temperature values. Background measurements for the cryostat and furnace were also collected. Initial data processing was carried out using the *icat* program (program from Diamond). The integrated diffraction pattern was used directly for Rietveld refinements of the average crystal structure. For PDF refinements, the integrated X-ray total scattering data were used as input for the suite of standard background corrections and data normalisation process were performed in GudrunX.[182] The maximum magnitude $Q_{\max}$ of the X-ray total scattering was 21.0 Å^{-1}.

Again in this study I use $D(r)$ to represent combined refinements of neutron and X-ray PDFs.

5.4 Results and discussion

5.4.1 SQUID analysis

Magnetic susceptibility data were collected for the samples $x = 0.1, 0.2, 0.25, 0.33, 0.4,$ and 0.5 using SQUID measurements, a sequence collecting Zero-field Cooling and Field Cooling (ZFC/FC) with field of 100 Oe and hysteresis loops collected at 5 K and 300 K. For the samples with composition $x = 0.09$ and $x = 0.11$ SQUID measurements were not obtained due to limited availability of the SQUID instrument. The phase diagram displayed in Figure 5.4(a) from the magnetic phases for each composition published in the literature were reproduced and used as a guideline for interpretation of the SQUID data presented here.[96]

The behaviour of magnetic susceptibility (ZFC/FC and $\chi^{-1}(T)$) for each sample were used to confirm the magnetic transitions in each sample, shown in Figure 5.5.

The sample $x = 0.1$ undergoes a transition from antiferromagnetic to paramagnetic at T$\simeq$135 K which agrees with the literature.[286] The samples $x = 0.2$ and 0.25, both undergo a transition from paramagnetic to ferromagnetic at the temperatures T$\simeq$185 K and T $\simeq$175 K and are in good agreement with previous published values.[287,293]

The samples with composition $x = 0.33$ and 0.4 are both in the strong CMR region, and undergo a clear transition from paramagnetic to ferromagnetic at T$\simeq$250 K in accordance with previous studies.[289,290,294,295] For the sample with composition $x = 0.4$ a minor broadening of the ZFC slope appears in the ferromagnetic phase. This broadening may be related to minor competing AFM-FM interactions as the sample composition gets closer to the edge of the AFM/FM transition [Figure 5.4(b)] that appears at the composition $x = 0.5$.

The sample with composition $x = 0.5$ is stated in the literature[275] to undergo two magnetic transitions: on cooling it undergoes paramagnetic–ferromagnetic–antiferromagnetic transitions with the CO/OO state to appear in the antiferromagnetic state ($T_{\mathrm{N}}\simeq$ 155 K).[275] The paramagnetic–ferromagnetic transition appears at $T_{\mathrm{C}}\simeq$ 230 K.[296] My collected magnetic susceptibility data (ZFC/FC) for $x = 0.5$ shows a more smooth transition from a paramagnet to a ferromagnet at $T_{\mathrm{C}}\simeq$ 230 K, in comparison to the same transition observed for the compositions $x = 0.33$ and $x = 0.4$. For $x = 0.5$ the ZFC slope in the ferromagnetic state goes into a broad peak without any indication of an antiferromagnetic transition which is not consistent with the literature, where it is stated that a clear transition from antiferromagnetic to ferromagnetic was observed in their ZFC/FC data.[276] However, another study using the same synthesis method as used in this study made nano particles with

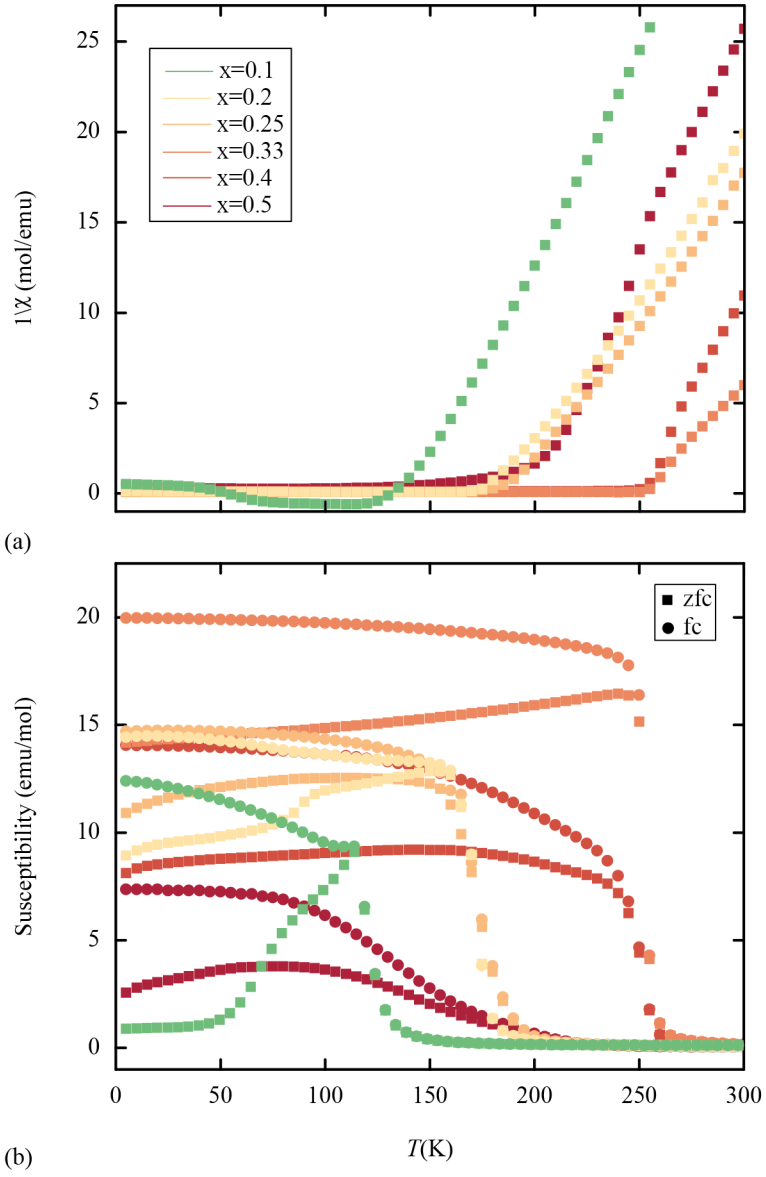


Figure 5.5: SQUID data collected for the six $La_{1-x}Ca_xMnO_3$ compositions. (a) Is the $\chi^{-1}(T)$ plotted against temperature, while (b) Is the magnetic susceptibility $\chi(T)$ data represents the ZFC/FC plotted against temperature.

a size of 25 nm and observed the same broadening of their ZFC/FC slope in the ferromagnetic region as I observe in this study, with no clear antiferromagnet to ferromagnet transition.[296] In a theoretical study it was stated that a smooth transition from the FM state to the AFM state in $La_{0.5}Ca_{0.5}MnO_3$ cannot appear because the two states are so different.[103,273] That explains why the ZFC slope broadens in the FM-AFM state in $La_{0.5}Ca_{0.5}MnO_3$.

Another reason for why no AFM transition appears in my sample might be that the sample is not at the exact $La_{0.5}Ca_{0.5}MnO_3$ composition but slightly shifted into the FM region ($x > 0.5$). The choice of synthesis method seems to have an effect on the final product. I have used the citric gel method since it is stated that it would give rise to less inhomogeneities compared to other methods where starting materials are ground together and heated.[261] I would therefore expect the samples studied here to be more homogeneous than the samples used in previous studies.[275] From SQUID analysis of my samples magnetic transitions for each composition are observed in the preferred regions of the phase diagram and I therefore conclude that my samples are pure.

5.4.2 Average structure refinement

Rietveld refinements

Rietveld refinements of my newly collected in-house XRD, X-ray synchrotron data, and neutron data were all performed as a function of composition and temperature using the Topas software package.[164] The refinements were carried out to confirm that the samples were in the right composition and were consistent with previous average structure studies.[23,275,297] All compositions were refined using an orthorhom-

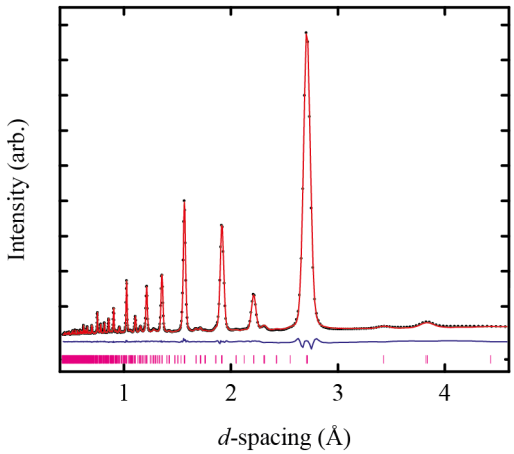


Figure 5.6: X-ray powder diffraction was used to confirm sample purity. This is the $La_{0.5}Ca_{0.5}MnO_3$ sample collected at 105 K from the data collected at I15.

bic unit cell with space group *Pnma*. Atomic displacements were modelled using isotropic atomic displacement for each atom. No positional constrains were added beyond those required by the space group. Not all intensities do fit perfectly, but all peak positions do fit, (Figure 5.6). Refined lattice, volume and fraction parameters as a function of composition at RT are shown in Table 5.1. The X-ray synchrotron data and neutron data for the $La_{0.5}Ca_{0.5}MnO_3$ composition were refined across temperature (110-300 K for the X-ray data and 5 K-300 K for neutron data) and compared to the results of a previous study reported in Ref 275 [Figure 5.8]. Plots at every 50 K for both neutron and X-ray refinements and all refined parameters are attached in Appendix C1. The refined lattice parameters as a function of temperature do not change at the two magnetic transitions which disagrees with previous studies where a clear change at both transitions appear.[272,275,276] The data were collected on instruments (I15 and POLARIS) designed to obtain medium resolution as a consequence of optimising for real-space resolution which gives broader Bragg peaks. The collected data from POLARIS have a resolution of $\Delta d/d$ for bank 5 =

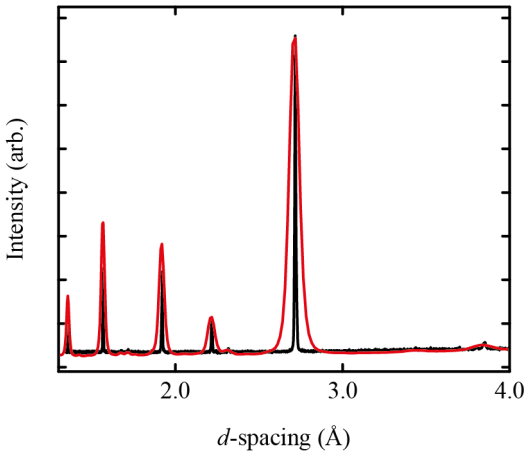


Figure 5.7: Comparison of In-house powder data (black line) and a data set collected at I15 (red line). Both data sets were collected at RT.

0.30% (the highest resolution bank and the one the data were refined to) which is of high enough resolution to observe this change on the lattice. The same appears to be the case for the X-ray data collected at I15, where the resolution is $\Delta Q/Q$ resolution = 0.58%. This clearly shows that the data are of high enough resolution to observe distortions of this size on the lattice as reported in Ref 275. To make sure the sample was polycrystalline the data collected at RT from I15 were compared to in-house XRD data and plotted on top of each other [Figure 5.7]. The result confirms that the sample was pure and crystalline, the peaks on the I15 data is broader as a consequence of the instrumental resolution. I can therefore conclude that my collected data are of high enough resolution and my sample was polycrystalline.

The average structure refinement of the collected data agrees with SQUID data showing no evidence for a transition from a ferromagnetic to an antiferromagnetic phase. From the obtained SQUID results presented in section 5.4.1 it would be unlikely to observe any significant changes to the lattice at $T_N \simeq 155\,\mathrm{K}$ (CO/OO transition) as observed in previous study.[275]

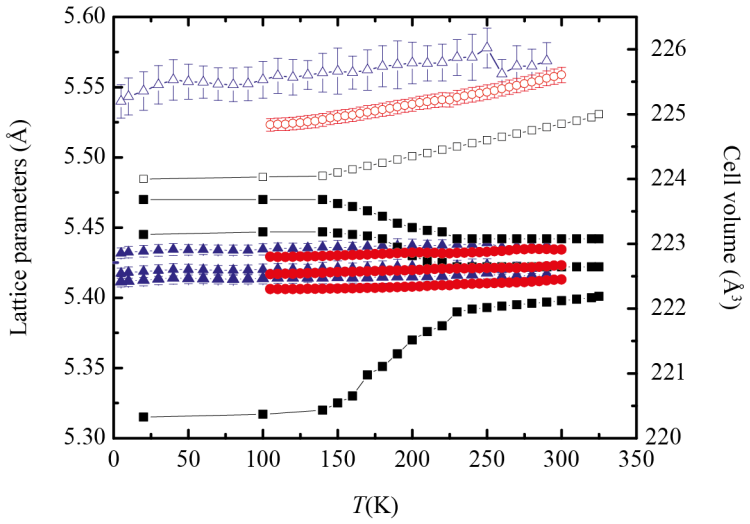


Figure 5.8: Comparison of lattice parameters of $La_{0.5}Ca_{0.5}MnO_3$ as a function of temperature. Black squares are adapted lattice (closed) and volume (open) parameters adapted from Ref. 275. Blue triangles are the lattice and volume parameters obtained Rietveld refinement to neutron data. Red circles are the lattice and volume parameters obtained from Rietveld refinement from X-ray data.

By looking at the change of unit cell volume as a function of temperature, it appears that my sample is $\sim$1 Å^3 bigger than the previous study but it changes around $\sim$1 Å^3 over the measured temperature range, which is in good agreement with the previous study [Figure 5.8]. The results of this study compared to the previous study in Ref. 275 are significantly different across temperature and the only difference between the two studies is the way the samples have been synthesised. In previous study, they used a solid-state reaction to synthesise their sample. This involves mixing of three powders in a stoichiometric ratio related to the desired composition and heating. My sample was synthesised using the gel method which is assumed to allow better mixing of components. As mentioned in section 5.4.1, my sample may not be exactly at the $La_{0.5}Ca_{0.5}MnO_3$ composition, but might consist of a slightly higher concentration of La ions which would explain the minor difference in volume and would then be in the FM regime of the phase diagram [Figure 5.4(b)]. The

variation in volume is not unsurprising as there probably is a minor difference in the sample composition between my study an the previous reported (Ref 275). However the difference in the lattice parameters as a function of temperature would not be expected to disagree with previous study.[275]

From SQUID and average structure analysis we observe structural changes as Ca doping increases and thus there is no clear evidence that the sample synthesised in this study should be wrong. This suggests that the two different synthesis methods may give two different samples. Nevertheless, I went on with the analysis of the data collected for the samples synthesised in this study. I therefore expect that my samples are close to the desired composition. I assume from SQUID analysis and XRD data that my sample is close to the $La_{0.5}Ca_{0.5}MnO_3$ composition and my collected data for further analysis of the local structure and previous proposed models for the CO/OO state is reliable.

5.4.3 Compositional variation in neutron and X-ray PDFs: direct analysis

The study of local structure as a function of composition and temperature in Ref 142 by Billinge *et al*. only focused on the variation in Mn–O bond. They did not focus on whether the local structure changes when crossing the orbital order/disorder transition as function of composition. Here I will show a direct analysis of the PDF data to investigate if the local structure corresponding to one unit cell changes and if there are any similarities to the discontinuity observed in $LaMnO_3$ as a function of temperature.

In the examination of the local structure as a function of composition at room

temperature, direct analysis of the Fourier transformed neutron and X-ray total scattering data have been carried out. The data are plotted on top of each other to observe any significant discontinuity at interatomic distances corresponding to one unit cell [Figure 5.9(a,b)]. In the data a clear consistency in PDFs obtained from independent measurements for different compositions is observed, with a high-signal-to-noise (r<1.0 Å). The persistence of JT-distortions at room temperature as a function of composition is evident by the Mn–O peak of the neutron data [Figure 5.9(a)]. The peak at $r \simeq 2$ Å is inverted as a consequence of the negative neutron scattering length of Mn. For the reduced real-space resolution in the X-ray PDF data [Figure 5.9(b)] the Mn–O peak has larger intensity than in the study of $LaMnO_3$ in previous chapter. However, the resolution of the Mn–O peak is still not good enough to possibly resolve the JT distortion directly from X-ray PDF measurements alone.

The raw PDF for both neutron and X-ray does show a clear signature of discontinuous change across the orbital order/disorder transition at $x \simeq 0.16$. For the neutron data the most significant changes appear at $r \simeq$3.34 Å and $r \simeq$6.36 Å. These points were picked for relative analysis and are shown in Figure 5.9(c). The X-ray PDF data as a function of composition also show significant changes at distances corresponding to one unit cell. The most clear differences appear at $r \simeq$3.62 Å, $r \simeq$5.44 Å, and $r \simeq$6.74 Å and were chosen for relative analysis. The discontinuity in PDF data appears for both neutron and X-ray across the orbital order/disorder transition ($x \simeq 0.16$). Again, this involves correlations at interatomic distances corresponding to one unit cell. The discontinuity in local structure across composition is observed in direct comparison of the PDFs but becomes more evident by considering the

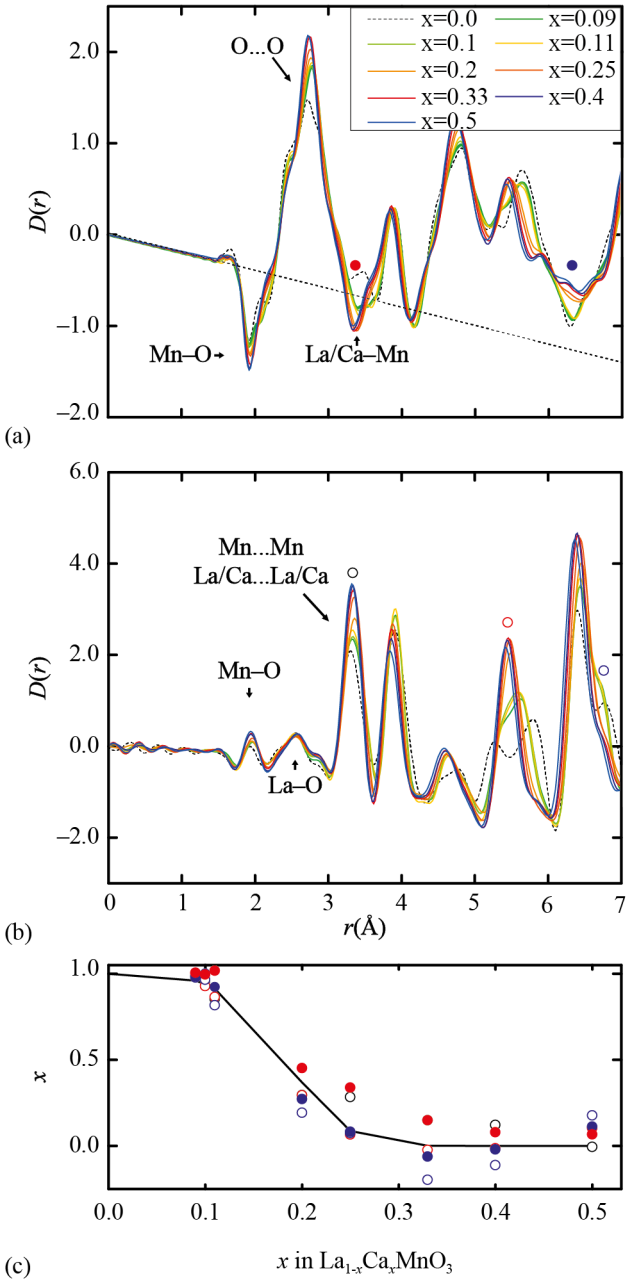


Figure 5.9: Composition-dependent variation in (a) neutron and (b) X-ray PDFs shows the PDF data for $La_{1-x}Ca_xMnO_3$ where x denotes the composition of Ca, all collected at room temperature. The dotted line is $LaMnO_3$ data collected at the same temperature and instrument but for the neutron data the collection times were only 1/6 of time the other data was collected for. This is the of reduced intensities. (c) The normalised composition dependence of PDF intensities derived same way as in Chapter 4 at a variety of interatomic separations where a clear discontinuity in the local structure appear. Using filled and open circles correspond to neutron and X-ray data, respectively and corresponds to those used in panel (c). The black line is a guide for the eye to clarify the transition.

relative changes in $D(r)$ using the same order parameter as in section 4.4.2 [Figure 5.9(c)]. The relative changes for both neutron and X-ray are not as significant as in the previous chapter, but the change in intensity between $x = 0.1$ and $x = 0.2$ are significantly larger than the change between $x = 0.2$ and $x = 0.3$, [Figure 5.9(c)]. As this transition consist of variation in Ca/La and Mn^{3+}/Mn^{4+} concentration the PDF histograms also changes due to composition. The transition is more complicated than the one observed in $LaMnO_3$ as a function of temperature. Nevertheless, the transition in $La_{1-x}Ca_xMnO_3$ as a function of composition is not surprising since the orbital disordered state for $LaMnO_3$ drops rapidly as a function of temperature when doping with Ca and the local structure would be expected change.

To the best of my knowledge, the similarity between the disordered states in $LaMnO_3$ and in the doped $La_{1-x}Ca_xMnO_3$ has not been reported before and justifies new studies of the orbital disordered state. As the states occur around RT for the different compositions the contribution from thermal displacement will be much lower and the PDF data should be more sensitive to different models and it would be expected to be more straight forward to distinguish between (unlike the result obtained in previous chapter). The drawback with this system is the divalent La/Ca site which I expect will complicate the analysis, but a reliable result would still be expected for the doped systems.

5.4.4 Direct comparison of PDFs across temperature for $La_{0.67}Ca_{0.33}MnO_3$

As observed in the previous section of $La_{1-x}Ca_xMnO_3$ the local structure changes as the concentration of Ca increases. In this section I will investigate how the local

structure varies as function of temperature in the CMR state ($x = 0.33$) by using the same analysis technique. As introduced in the background (page 132) the $La_{0.67}Ca_{0.33}MnO_3$ composition has been reported to be the composition where the highest CMR effect has been measured.[93] This is the main reason for why I study this composition here.

Total scattering data were collected in the temperature range of 10–673 K for neutrons, and 105–673 K for X-rays. The total scattering data were Fourier transformed into real space PDFs ($D(r)$) and plotted together to observe any discontinuous changes in the local structure [Figure 5.10(a,b)]. Both data sets show changes in local structure as going from a ferromagnetic (metallic phase) to a paramagnetic (insulating phase) at (T$\simeq$250 K). The differences between the metallic phase and insulating phase become even more evident when considering the relative changes in $D(r)$ using the same order parameter as in section 4.4.2 [Figure 5.10(c)]. The change in intensity clearly changes between the two data sets collected at 200 K and 300 K covering the regime of the transition.

However, the first clear difference is at the characteristic negative Mn–O peak at $r \simeq 2$ Å which goes from a single well defined peak at the metallic phase into a broad peak with a shoulder at the insulating phase. This can be explained by an e_g electron stabilised in the metallic band and when heating the material, the e_g goes into the polaron state.[93,281] The peak at $r \simeq 2.75$ Å includes the O–O distances on the octahedra which broadens across the phase transitions as a consequence of the polarons turning into the glass state. This indicates the formation of local JT distortions in the insulating phase. It also agrees with previous studies where the same trend was observed.[111] In the high temperature state (673 K) the peaks are

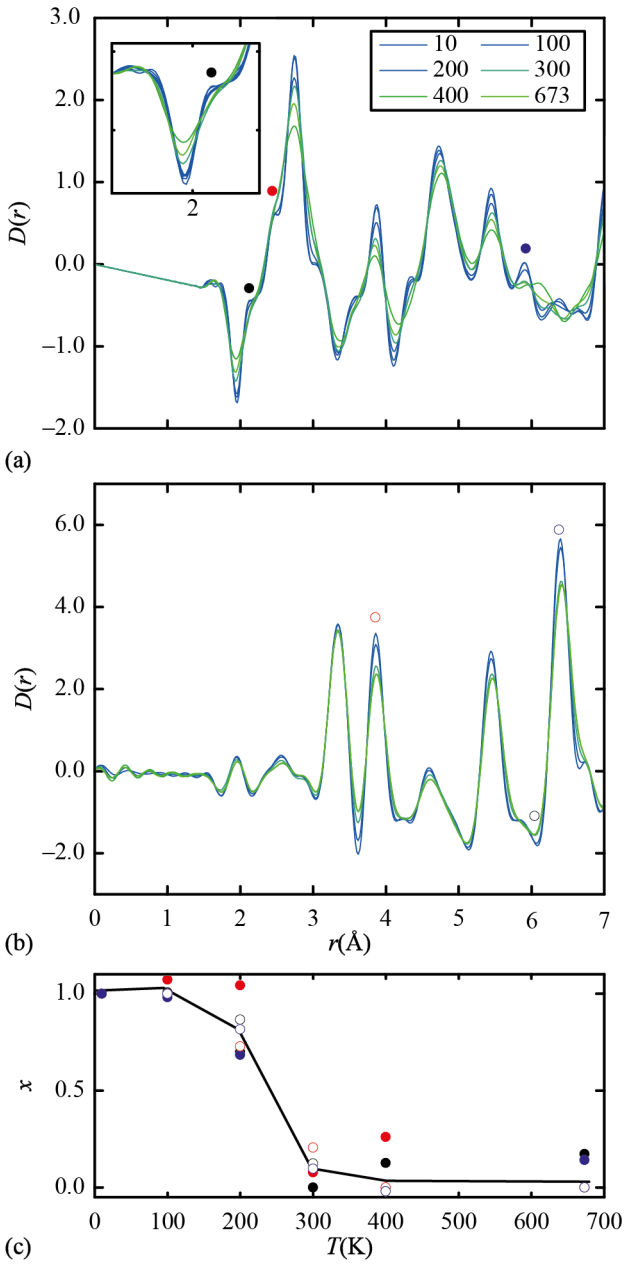


Figure 5.10: Temperature-dependent variation in (a) neutron and (b) X-ray PDFs for $La_{0.67}Ca_{0.33}MnO_3$. (c) Shows the normalised variation of peak intensities across temperature. That makes it more clear that the local structure changes from the metallic state into the polaron state at $T \simeq 250\,\mathrm{K}$.

broad and smooth which may be caused by thermal contributions and the fact that the sample is in the polaron liquid regime, both of which would contribute to the broadening of the peaks.

The X-ray PDF data are again insensitive to O displacements but are indirectly sensitive *via* the coupling to Mn and La/Ca atom positions. The discontinuity across temperature is therefore most obvious at the Mn..Mn, La/Ca..La/Ca peaks.

However, these data are fully consistent with the phase diagram, showing a change in local structure across the metallic-insulating transition.

5.4.5 PDF across temperature for $La_{0.5}Ca_{0.5}MnO_3$

Direct analysis of the local structure for the $La_{0.5}Ca_{0.5}MnO_3$ composition across temperature were also performed. The neutron and X-ray PDF data were again plotted on top of each other to observe any discontinuity in the local structure [Figure 5.11(a,b)]. The neutron PDF data are presented over the temperature range of 5 K to 300 K while the X-ray data are presented in the temperature range of 105–300 K due to the limitation in temperature of the cryostat. Nevertheless, the low temperature state in $La_{0.5}Ca_{0.5}MnO_3$ still appears at 105 K.

For both types of data the local structure only shows a small discontinuity when crossing into the CO/OO regime; the same is true for the ferromagnetic to paramagnetic transition. In the neutron data the Mn–O peak at $r \simeq 2.0$ Å is uniform at 5 K but a small shoulder starts to appear already at 100 K and grows as the temperature increases. The peak at $r \simeq 2.75$ Å including the O–O distances in the octahedra do also broadens as the temperature increases. Compared to the $x = 0.33$ composition study the changes at these two peaks are minor. This is consistent with the presence

of fewer JT active Mn^{3+} ions in this composition but not big enough to conclude much more from direct analysis of the neutron PDF data.

The X-ray PDF shows a more clear discontinuity of the local structure across temperature mainly at the peaks related to the Mn..Mn, La/Ca..La/Ca distances at $r \simeq$ 2.9–4.0 Å across temperature.

However, with only four data points for the neutron data and three for X-ray data the relative changes in $D(r)$ will not give a reasonable picture of the structure across

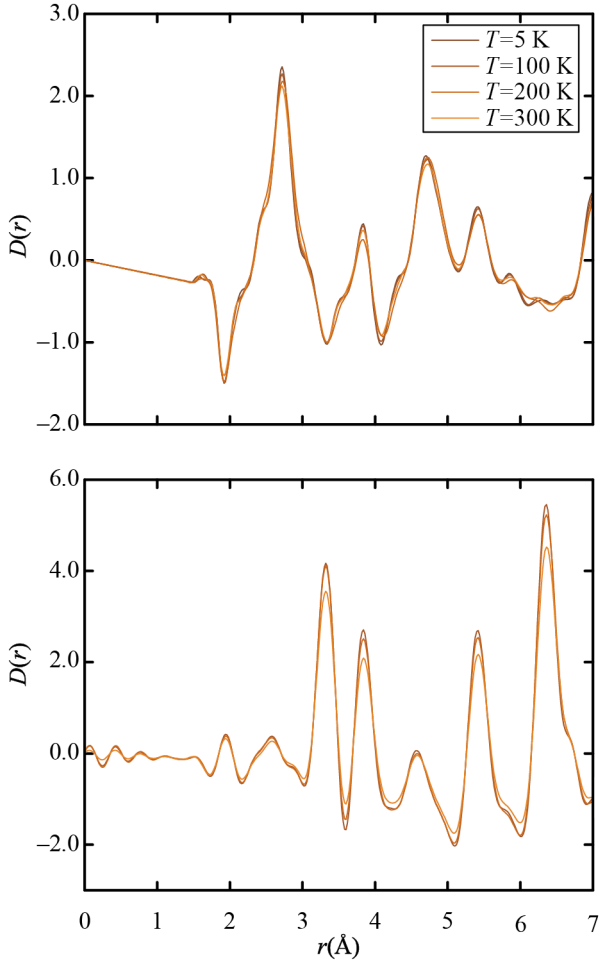


Figure 5.11: Temperature-dependent variation in (a) neutron and (b) X-ray PDFs for $La_{0.5}Ca_{0.5}MnO_3$.

the transitions. Ultimately, for both neutron and X-ray data as a function of temperature no significant changes in local structure are observed. This is in good agreement with the EXAFS study where no change in the local Mn environment as a function of temperature was observed.[280] From the SQUID and average structure analysis on the sample with composition $x = 0.5$ where no evidence for the CO/OO phase was observed, it would therefore be unlikely to observe any large change in local structure across this transition. Also, the inverted Mn–O peak in the neutron data is uniform it would be expected to split if the CO/OO state appeared. This agrees with previous studies suggesting that the Goodenough's CO/OO picture is too simplified.[275,277] The low temperature PDF data for $La_{0.5}Ca_{0.5}MnO_3$ is modelled later to subtract any structural information in this state.

5.4.6 Direct comparison of PDFs as function of composition and temperature in the $La_{1-x}Ca_xMnO_3$ family

In this section, I have plotted all the information together obtained from the direct comparison of PDF data and compared it to the phase diagram of $La_{1-x}Ca_xMnO_3$ [Figure 5.12]. The direct comparison analysis in the three studies have clarified that there is a direct relation between the local structure and the various phases. The orbital order/disorder transition as a function of temperature in $LaMnO_3$ seems to be directly related to the transition that appears at RT when doping in Ca. The local structure of $La_{0.67}Ca_{0.33}MnO_3$ showed variations in the data as the material undergoes a transition from the ferromagnetic metallic state to into the polaron glass state. This clearly shows how much information we actually can obtain simply by comparing raw PDF data.

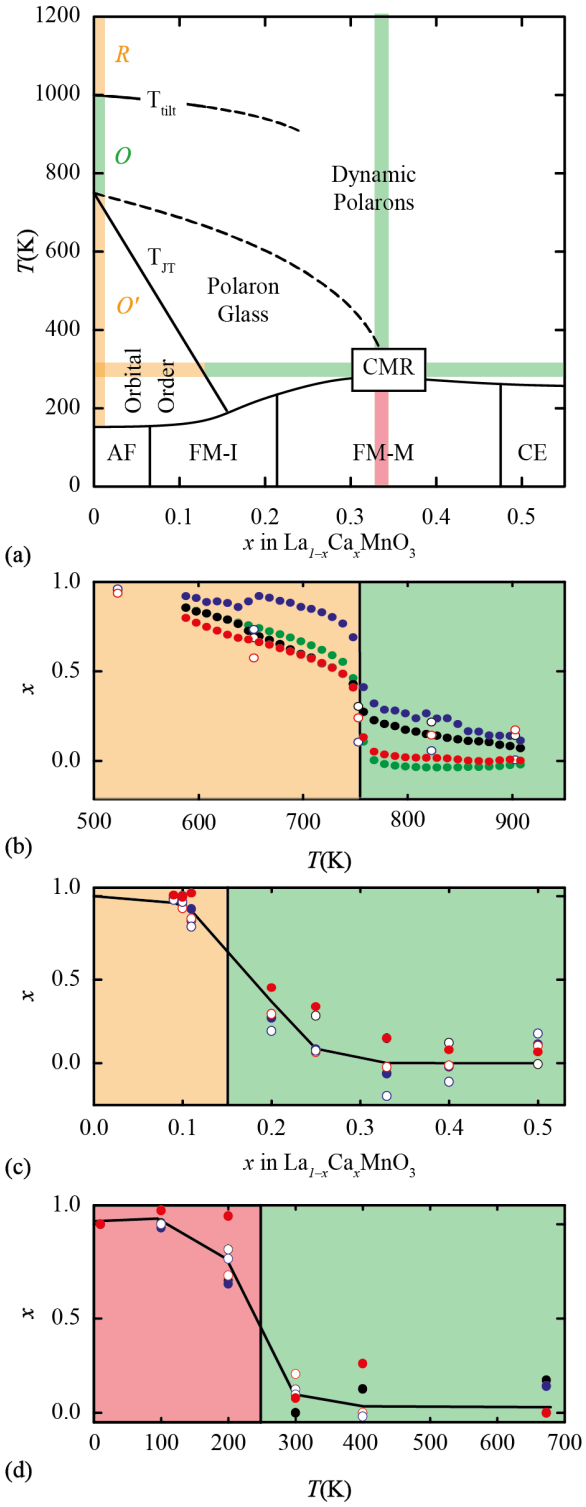


Figure 5.12: Representation of the relation between local structure transition as a function of composition and temperature. (a) Shows the phase diagram of $La_{1-x}Ca_xMnO_3$ showing the compositions studied in this thesis. (b,c,d) The normalised temperature and composition dependence of PDF intensities for (b) temperature dependence of $LaMnO_3$ (c) the dependence of composition of $La_{1-x}Ca_xMnO_3$, and (d) for the temperature dependence in $La_{0.67}Ca_{0.33}MnO_3$. x on the y-axis corresponds to the order parameter, while x on the x-axis in (c) corresponds to the doping concentration. In all three studies the local structure is directly related to the transitions in the phase diagram.

5.4.7 Model comparison from neutron and X-ray scattering

In this section I examine the three models (LT-M, LT-M′, and LT-O) for the CO/OO state introduced in the background by fitting to average structure first and then to my newly collected PDF data. In this section I will re-examine whether the conclusions of Ref 277 on the basis of their neutron PDF data are consistent with my new PDF data. For all three models, refinements were carried out on combined neutron+X-ray data collected at 105 K.

The LT-M and LT-M′ models were refined using a monoclinic unit cell with $P2_1/m$ symmetry with a doubling of the a-axis. In average structure Rietveld refinement the LT-M model consists of two parameters applied to the positions of O, Mn^{4+}, and for the half doped La/Ca atoms denoted Δz and $\Delta z'$. The rest of the atomic position parameters in the unit cell were fixed to the values obtained from refinement using $Pnma$ symmetry reported in Ref. 275, all the parameters are reported in Table 5.2. The refined displacement parameters Δz and $\Delta z'$ were equal to 0.065(10) and 0.011(19) obtained from the refinement, and both fits are shown in Figure 5.13(a,b). The refined values do not deviate significantly from that reported in Ref 275 (Δz=0.018(2) and $\Delta z'$=0.010(1)); and small variation of the refined Δz and $\Delta z'$ compared to previous study may be caused by the lower resolution in my data and the consequence of fitting to neutron+X-ray data.

The second model is an extension of the LT-M model denoted by LT-M′. The atomic positions were refined to freely displace with a $P2_1/m$ symmetry.[277] A fit of the refined model is shown in Figure 5.13(c,d) and fits the data well but the refined crystal structure does not make physical sense, with two manganese ions occupying

Table 5.2: Atomic positions for the LT-M model from combined Rietveld refinement of neutron and X-ray using the $P2_1/m$ symmetry. The refined values $\Delta z = 0.065(10)$ and $\Delta z' = 0.011(19)$. The refined lattice parameters were $a = 10.826(7)$, $b = 7.647(5)$, $c = 5.428(3)$ and R_{wp}=3.92 %. The average positional parameters were fixed to the values obtained in Ref. 275 from refining to $Pnma$ symmetry.

Atom	Wyckoff site	x	y	z
Mn^{3+}	$2a$	0.0	0.0	0.0
Mn^{3+}	$2b$	0.5	0.0	0.0
Mn^{4+}	$4f$	0.25	0.0	0.5–Δz
La(1)	$2e$	0.26	0.25	0.004–$\Delta z'$
La(2)	$2e$	0.76	0.25	0.004+$\Delta z'$
La(3)	$2e$	0.01	0.25	0.496
La(4)	$2e$	0.51	0.25	0.496
O1(1)	$2e$	0995	0.25	0.935
O1(2)	$2e$	0.495	0.25	0.935
O1(3)	$2e$	0.245	0.25	0.565–Δz
O1(4)	$2e$	0.745	0.25	0.565+Δz
O2(1)	$4f$	0.1375	0.034	0.235–Δz
O2(2)	$4f$	0.6375	0.034	0.235+Δz
O2(3)	$4f$	0.1175	0.966	0.725–Δz
O2(4)	$4f$	0.6175	0.966	0.725+Δz

Table 5.3: Atomic positions for the LT-M′ model Rietveld refined of combined neutron and X-ray data (left) compared to the values from Ref. 277. The refined lattice parameters were $a = 10.839(6)$, $b = 7.655(5)$, $c = 5.437(3)$. Atom positions are refined with $P2_1/m$ symmetry constraints with R_{wp}=5.85 %.

Refined values					**Values from Ref 277**		
Atom	Wyckoff site	x	y	z	x	y	z
Mn^{3+}	$2a$	0.0	0.0	0.0	0.0	0.0	0.0
Mn^{3+}	$2b$	0.5	0.0	0.0	0.5	0.0	0.0
Mn^{4+}	$4f$	0.2593(10)	-0.0010(17)	0.509(3)	0.2469(3)	0.0078(3)	0.5157(4)
La(1)	$2e$	0.2599(13)	0.25	-0.006(3)	0.2589(3)	0.25	0.0234(5)
La(2)	$2e$	0.7585(13)	0.25	0.001(3)	0.7644(4)	0.25	–0.0090(5)
La(3)	$2e$	0.0021(14)	0.25	0.498(2)	0.0051(3)	0.25	0.5018(6)
La(4)	$2e$	0.5119(12)	0.25	0.486(2)	0.5121(4)	0.25	0.4924(5)
O1(1)	$2e$	–0.00069(17)	0.25	0.930(3)	0.0003(4)	0.25	–0.0577(6)
O1(2)	$2e$	0.5004(14)	0.25	–0.0459(19)	0.4890(3)	0.25	–0.0662(5)
O1(3)	$2e$	0.2418(17)	0.25	0.568(3)	0.2472(2)	0.25	0.5913(4)
O1(4)	$2e$	0.7494(16)	0.25	0.570(3)	0.7470(4)	0.25	0.5483(5)
O2(1)	$4f$	0.1342(10)	0.0358(16)	0.227(2)	0.1360(3)	0.0345(4)	0.2577(4)
O2(2)	$4f$	0.6375(10)	0.0252(12)	0.2363(19)	0.6355(3)	0.0352(4)	0.2069(4)
O2(3)	$4f$	0.1080(9)	–0.0328(13)	0.716(2)	0.1129(4)	–0.0366(4)	0.7372(3)
O2(4)	$4f$	0.6126(11)	–0.0372(15)	0.727(2)	0.6132(2)	-0.0294(4)	0.7073(4)

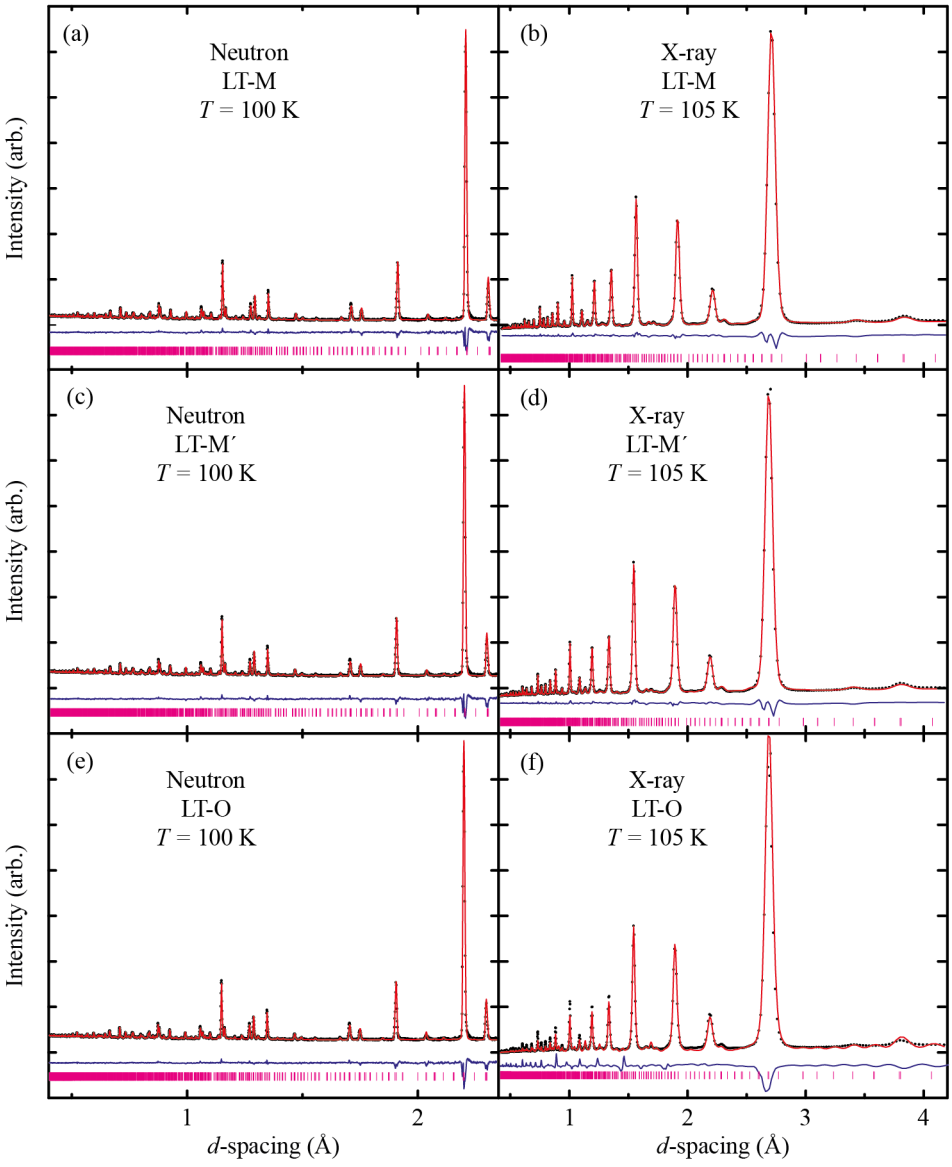


Figure 5.13: Fit of the combined neutron+X-ray Rietveld refinement of the LT-M model(a,b), LT-M′ model(c,d), and LT-O model(e,f). Red lines are the calculated data, black dots are the observed data, blue lines are the difference between observed and calculated data. (a,c,e) Fitting the models to neutron data at 100 K, and (b,d,f) shows the fits to X-ray data at 105 K. The combined refinement obtained a R_{wp}=3.92 % for LT-M, R_{wp}=5.85 % for the LT-M′, and R_{wp}=4.33 % for the LT-O model.

the same site. With the aim of obtaining a stable fit the refinement procedure was carried out by fixing the manganese positions to the values reported in Ref 277 without fitting the data very well. When the manganese position was allowed to refine they moved over to overlay each other. The unphysical result may be caused by the fact that this model includes the refinement of 42 parameters in a combined neutron+X-ray refinement consisting of medium resolution data. The third model, denoted LT-O, allows the Mn—Mn ions to dimerise with an oxidation state of $Mn^{3.5+}$ explained by the unpaired e_g electron to be shared on the linked oxygen, proposed by Daoud-Aladine *et al*. Ref 283 [Figure 5.3(b)]. The model has an orthorhombic lattice with doubled b-axis and atom positions refined with $P2_1nm$ symmetry constraints. The fit to data for LT-O model is shown in Figure 5.13(e,f) where the data fit well but the refined parameters have large uncertainties which makes the fitted model uncertain. This was confirmed from an output of the refined structure which did not make physical sense. The model consist of 41 refined parameters and it is most likely this is the the same case with too many parameters refined to medium resolution data.

From this study I can conclude that the refinement of the LT-O model did not make physical sense. The LT-M′ model fits the data well but the crystal structure obtained from the refinement did not make physical sense. The LT-M did not fit the data as well as LT-M′ but the refined crystal structure agrees with the starting configuration and makes physical sense. This may be caused by the lower number of refined parameters.

However, the result is in good agreement with a previous study (Ref 277) where the average structure refinement did not give a clear answer on which model represents

the data best.

5.4.8 Local structure refinement of the low temperature state in $La_{0.5}Ca_{0.5}MnO_3$

The average structure refinement did not give a clear picture of which model represented the data best. In this section I will carry out a combined neutron+X-ray PDF refinement of the three models. I will again use the advantage of variation in scattering lengths for neutron and X-rays. In the average structure the LT-M′ and LT-O models did not give a stable refinement, here I will show that a stable fit can be obtained for the LT-M′ model and makes physical sense while refinement of the LT-O model again gives an unstable refinement with an unphysical structure. My low temperature PDF data for $La_{0.5}Ca_{0.5}MnO_3$ are used to examine the three models (LT-M, LT-M′, and LT-O) in a series of combined neutron+X-ray PDF refinements. By using the same starting values as ones used for Rietveld refinement and reported in Ref 275,277,278 the models were refined to the PDF data fitting in the range of 1.5–10 Å corresponding to the supercell size of each model. For all models the refined parameters related to the scale of neutron and X-ray data, delta2 (corresponds to the peak broadening), and Q_{broad} were refined and adds four extra parameters to each refinement.

The LT-O model fitted the data with R_{wp}= 10.7% but all the refined atom positions had strong covariance to each other and made the refinement very unstable. The refined structure did not make physical sense and because of the unstable refinement and the unphysical structure the fits are not shown here.

For the LT-M and LT-M′ models stable refinements were obtained and the refined

parameters are listed in Table 5.4 and Table 5.5 for the LT-M model and LT-M′ model respectively. Plots of the fits are displayed in Figure 5.14. For the LT-M model the R_{wp}= 14.9% while the R_{wp} for the LT′ model was 11.5%. The delta2 peak broadening term has a high uncertainty for both refinements which may be caused by the difference in peak broadening between the two datasets.

The output of the refined structures for both models make physical sense and is in good agreement with previous study.[277] The LT-M′ model fits the data best but the number of refined parameters is much higher compared to the LT-M model (46 against 14 parameters) and this result is not surprising. Both models have similar quality of fit in the average structure refinement while the goodness-of-fit for the local structure varies more between the two models. This is also in good agreement with Ref. 277 where they did not observe any significant difference between the models in average structure while the local structure fits were significantly different. The results obtained in my study suggest that even though Radaelli *et al.* made a more complex model of the CO/OO state it still seems to be a simplified picture of the low temperature state of $La_{0.5}Ca_{0.5}MnO_3$.

The refined Mn ion environment for the LT-M′ model are shown in Figure 5.15 and compared to those reported in a previous study (Ref 277). The structure shows two different Mn^{3+} environments and one Mn^{4+} environment. The first Mn^{3+} site shows anisotropic distortion related to the JT effect with a valence state close to 3.5+. The second Mn^{3+} environment has a shorter JT-distortion indicating a valence closer to 4+ than 3+ and a Mn^{4+} that is slightly off-centered. The JT distorted Mn–O bond lengths are shorter than the ones obtained from the end member $LaMnO_3$ suggesting that it does not consist of a system with a perfectly charge ordered state

Table 5.4: Refined parameters for the LT-M and LT-M′ models to combined neutron+X-ray PDF data at 100 K for neutron data and 105 K for X-ray data. The starting parameters were the same as the ones from Rietveld refinements of the average structure shown in Table 5.2 and Table 5.3.

	LT-M model	**LT-M′ model**
Neutron scale	0.137(12)	0.14(13)
X-ray scale	0.18(2)	0.17(2)
delta2	2.5(1.4)	2.6(3.2)
Q_{broad}	0.08(9)	0.08(9)
a	10.85(7)	10.86(10)
b	7.65(5)	7.65(6)
c	5.43(5)	5.43(6)
U_{iso}(La/Ca)	0.003(4)	0.002(4)
$U_{\text{iso}}(\text{Mn}^{3+})$	0.001(5)	0.01(2)
$U_{\text{iso}}(\text{Mn}^{4+})$	0.0055(11)	0.004(11)
U_{iso}(O1)	0.008(10)	0.003(6)
U_{iso}(O2)	0.007(4)	0.006(7)
Δz	0.017(12)	-
$\Delta z'$	-0.01(3)	-

Table 5.5: Refined atomic positions for the LT-M′ model obtained from PDF refinement of combined neutron and X-ray data. Atom positions are refined with $P2_1/m$ symmetry constraints.

Refined values				
Atom	Wyckoff site	x	y	z
Mn^{3+}	$2a$	0.0	0.0	0.0
Mn^{3+}	$2b$	0.5	0.0	0.0
Mn^{4+}	$4f$	0.248(11)	0.00(2)	0.49(3)
La(1)	$2e$	0.253(14)	0.25	–0.02(3)
La(2)	$2e$	0.761(13)	0.25	0.00(3)
La(3)	$2e$	0.0014(15)	0.25	0.49(3)
La(4)	$2e$	501(8)	0.25	0.50(3)
O1(1)	$2e$	0.990(18)	0.25	0.94(4)
O1(2)	$2e$	0.512(18)	0.25	0.96(3)
O1(3)	$2e$	0.245(18)	0.25	0.54(4)
O1(4)	$2e$	0.74(2)	0.25	0.60(3)
O2(1)	$4f$	0.133(15)	0.04(3)	0.21(4)
O2(2)	$4f$	0.646(13)	0.03(2)	0.25(3)
O2(3)	$4f$	0.113(19)	0.97(3)	0.71(4)
O2(4)	$4f$	0.608(19)	0.97(3)	0.72(3)

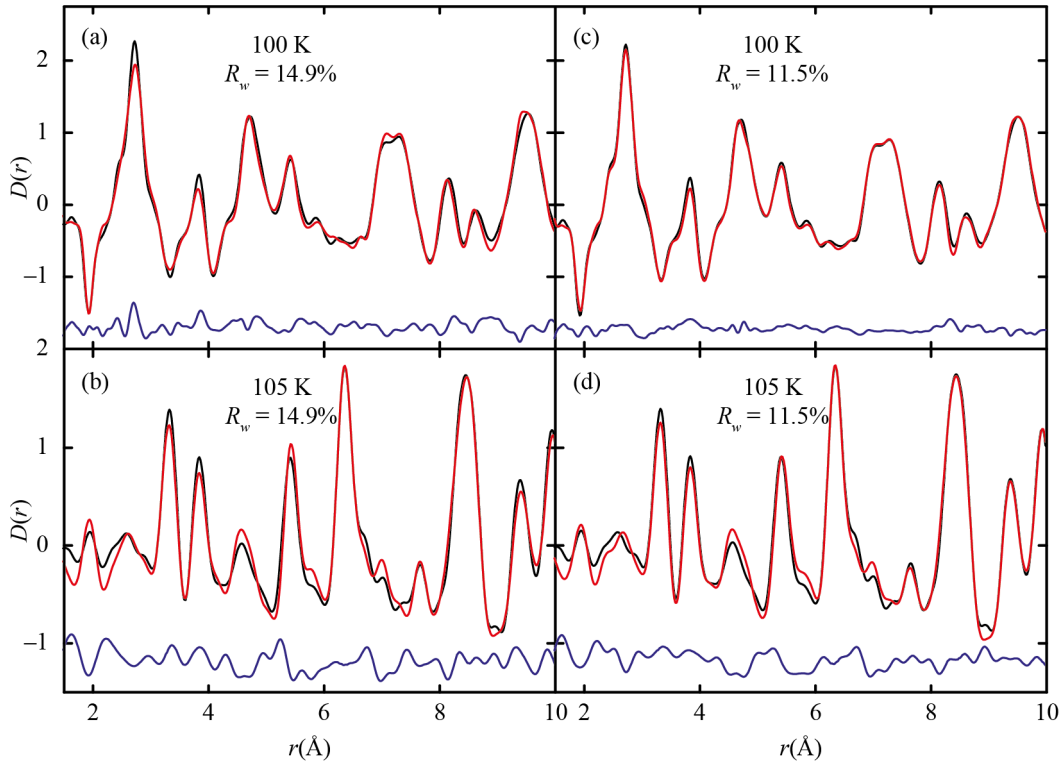


Figure 5.14: Combined neutron+X-ray PDF refinement of the LT-M model (a,b) and LT-M′ model (c,d) for $La_{0.5}Ca_{0.5}MnO_3$ composition. The data are shown as black lines, fits as red lines, and data–fit as blue lines. (a,c) Shows the plots of neutron data collected at 100 K and (b,d) are the plots to the X-ray data collected at 105 K.

with a two phase system of JT-distorted and JT-undistorted MnO_6 octahedra but it is a more complex structure. The refinement of the two models does still not give a clear picture on how the structure on microscopic scale looks like.

In this section I managed to obtain stable fits to PDF data for two of the three models proposed to represent the low temperature state of $La_{0.5}Ca_{0.5}MnO_3$. The model that best fits the data is the LT-M′ model but it has 46 refined parameters and only slightly improves the fit to data. For both models the R_{wp} values are still high and it would not be surprising if a different model would make more physical sense and fit the data even better. I would suggest to examine a charge ordered/orbital

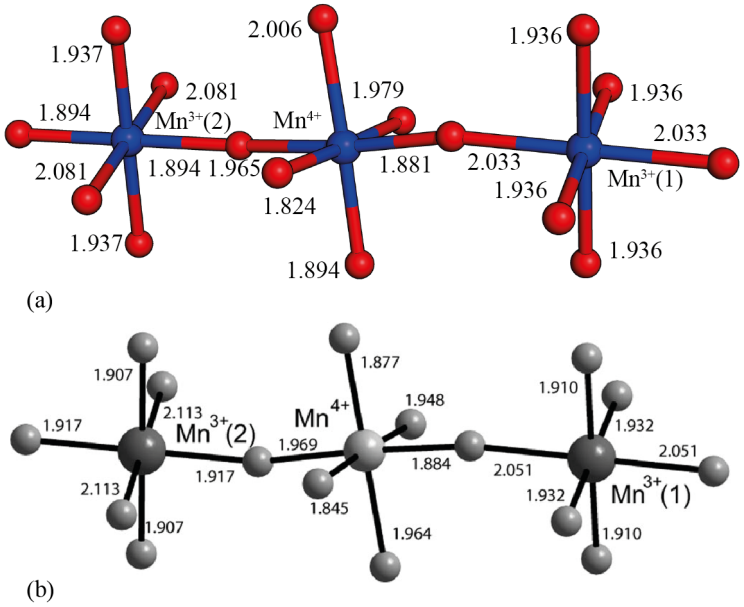


Figure 5.15: Local symmetry around the two Mn sites (blue) (Mn^{4+} and Mn^{3+}) with oxygens (red) bonded to the Mn atoms and refined from the LT-M′ model using PDFGui. The Mn^{3+} octahedron is Jahn-Teller distorted. The Mn^{4+} is not isotropic but slightly off-centered in agreement with the CO/OO model. Figure (b) is adapted from Ref. 277.

disordered (CO/OD) model with the electrons to be ordered in a chequerboard ordering with JT-distortions to arrange in a 3SP configuration allowing the Mn^{3+} to elongate along either x,y, or z without any correlation from next nearest neighbours randomly distributed throughout the structure [Figure 5.16(b)]. From a chemical viewpoint the sample at the half doped composition the CO/OD would make good sense for the half-doped sample.

5.5 Future work and concluding remarks

In this chapter have I managed to synthesise a series of nine different compositions of the $La_{1-x}Ca_xMnO_3$ family using the citric acid gel method.[261] The samples have been characterised using PXRD, PND, titration, and SQUID analysis. Neutron and X-ray total scattering data for each composition were collected at RT and for

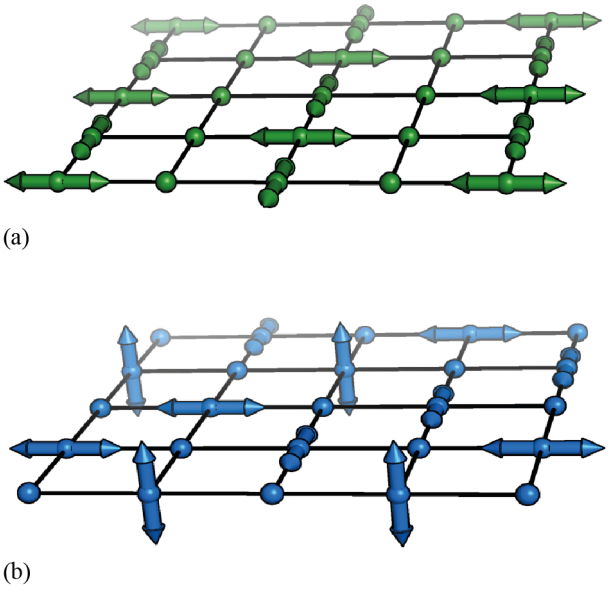


Figure 5.16: A simulated one layer picture of the two states (a) CO/OO and the (b) CO/OD structure which potentially could be the structure representing the low temperature state in $La_{0.5}Ca_{0.5}MnO_3$.

$x = 0.33$ and $x = 0.5$ data were collected as a function of temperature.

In my analysis of $La_{0.5}Ca_{0.5}MnO_3$, SQUID data indicated a strong competition of FM-AFM interactions which disagreed with what previous studies had observed. The average structure refinements for both the neutron and X-ray data did not show any discontinuity of lattice parameters across temperature which also disagreed with a previous study, where a clear change of the lattice was observed. The only difference between this study and the literature study is the synthesis method where I used the citric acid gel method while in the literature three powders in the wanted stoichiometry were mixed and heated. This study has opened the question whether these two synthesis methods obtain the same result. To achieve a conclusion it would be suggested that a new study where both synthesis methods are carried out by the same group and high resolution X-ray or neutron diffraction data

were collected for both synthesised samples. Furthermore, a XANES study of both samples would characterise the oxidation state.

The collected total scattering data across composition were analysed using direct analysis methods. The key result here is that the local structure shows a similar order/disorder transition to that observed at high temperature in the end member $LaMnO_3$. This transition justifies further analysis to hopefully achieve a better picture of the orbital disordered state in the CMR manganite family. In particular to study if a population of 3SP-type states in polaronic regime appears.

I carried out direct analysis of PDF data for the $La_{0.67}Ca_{0.33}MnO_3$ composition as a function of temperature where the local structure was observed to change from a metallic CMR state into a polaron state. This was also expected as the e_g electron goes from being stabilised in the metal state to a polaron state. The orbital ordering of the polaron state would consist of some type of correlations as the sample has excess of Mn^{3+} ions.

The direct analysis of the local structure for the composition $La_{0.5}Ca_{0.5}MnO_3$ across temperature did not show any significant changes and agrees with previous local structure analysis using the EXAFS method.[280] This result agrees with my SQUID analysis and average structure refinement where no obvious changes appeared.

For the $La_{0.5}Ca_{0.5}MnO_3$ composition I carried out a further analysis by examining previous proposed models (LT-M, LT-M′, and LT-O) for the low temperature state. All three models were refined in a combined neutron+X-ray Rietveld refinement. I managed to obtain a stable refinement for the LT-M model while for the other two models unstable refinements with unphysical structures were obtained. This is probably caused by the combination of medium resolution data with the large

number of refined parameters for both models.

However, the models were also refined to the total scattering data, taking the advantage of combined neutron+X-ray refinement. The LT-O model fits the data but had strong covariance between the refined parameters which gave an unphysical crystal structure. The LT-M model fit the data well without any correlations. The LT-M′ model gave a stable fit with a crystal structure that made physical sense and were in good agreement with previous study. The best fit was obtained with the LT-M′ but the number of refined parameters were almost three times bigger than for the LT-M model and therefore not surprising that it fits the data better.

In the analysis of the low temperature state of $La_{0.5}Ca_{0.5}MnO_3$ a 3SP approximant (CO/OD) model covering one unit cell would be worth testing. It would answer two key questions. First, if the model fits the data equally for the LT-M or LT-M′ model it may suggest that the PDF methods is not sensitive enough to solve this state. Second it would show whether the orbitals on the Mn^{3+} ions are randomly distorted in a perfect crystal lattice of alternating Mn^{3+} and Mn^{4+} ions.

This study has shed light on some inconsistencies of the $La_{1-x}Ca_xMnO_3$ family and it is suggested that further analysis to be carried out on some of these problems.

Chapter 6

Conclusion

In this thesis it has been shown that small box approximants modelling to high resolution neutron and X-ray total scattering may be used in combined refinements to obtain structural information on complex systems. This thesis has mainly focussed on using this method to investigate the orbital ordering in three materials where it is known that the ordering plays a key role in physical properties.

The first of the three canonical materials investigated was the spin-glass $Y_2Mo_2O_7$, described in Chapter 3. An alternative model of the orbitals on the Mo site to dimerise driving the disorder to generate the spin-glass state was developed. Using the combined neutron+X-ray PDF analysis I showed that the method was sensitive to these distortions.

The second material studied was the $LaMnO_3$ which is the end member compound of the CMR manganites where a canonical orbital order/disorder transition at high temperature appears, studied in Chapter 4. I used PDF data in this study to show that the transition caused changes in the local structure and these changes were real. When modelling the orbital disordered state I realised it was more challenging to distinguish between the models in terms of their ability to account for the experimental data. The insensitivity in PDF analysis were proved to appear from the large magnitude of thermal motion as a consequence of the transition at high temperature. Nevertheless, the analysis of my data showed a subtle but consistent preference for an anisotropic Potts model.

The third material investigated were the canonical $La_{1-x}Ca_xMnO_3$ family. I studied the change in local structure across various compositions and temperatures presented in Chapter 5. This study showed that the local structure of the orbital order/disorder transition across composition has similar trends as order/disorder transition observed in $LaMnO_3$. The advantage in the doped systems is that the transition is observed at room temperature which lowers the magnitude of thermal motion in the local structure. The disadvantage is the extra degree-of-freedom from the divalent Ca/La site occupancy which may complicate the analysis of the structure.

The study did also shed light on the disagreement between the synthesis methods normally used to prepare this doped family. This will be aim for future studies to make sure on how to synthesise the material in the right way.

The study of the $La_{1-x}Ca_xMnO_3$ family suggested that further analysis of the local structure may help in better understanding this fascinating material.

A second, more general, issue this thesis has managed to shed light on is the limitations of state-of-the art PDF analysis in characterising local structure for systems with strong static or dynamic disorder.

The studies have also shown in particular, the issue on no clear rule for what system can be solved from PDF analysis alone. Common to all three studies is the observation that very different models manage to fit the data almost equally well. This gives the PDF community another challenge in search of models describing the local structure of correlated systems. To obtain reliable results the proposed model should be examined against a unphysical but structurally related model that is fit to the same data. However, a proposed model should also be examined against

other experimental techniques to confirm the reliability of the model. With the recent upgrade of the TOPAS software package it is possible to obtain stable and fast combined refinements to local and average structure data.[186] Also, several studies have successfully shown the advantage of incorporating additional data from various experimental techniques during PDF analysis to help solve problems where PDF analysis alone is insufficient.[281,298–300] This opens up for the analysis of much more complex systems and the examination of proposed models will be more complete. Furthermore, the recent developments such as 3D-ΔPDF approach,[301] and "dynamic" PDF measurements will help the analysis of local structure.[302,303] The 3D-ΔPDF approach is a straightforward method to analyse disorder in materials. This method accesses much higher resolution of PDF peaks in three-dimensional space and allows studies of much more complex disordered systems. The "dynamic" PDF measurements have successfully managed to separate static and vibrational contributions to $D(r)$ peak broadening. This will be helpful in systems where high temperature states are studied. Specifically, this would be very useful in the analysis of the high temperature orbital disordered state in $LaMnO_3$.

Not only have the modelling techniques improved over the last years, also the total scattering instruments have improved. An example of one of the new total scattering instruments is NOMAD at SNS, Oakridge, where the flux is ten times bigger than the flux achieved at ISIS. With this high flux it is possible to reach out to much higher Q and collecting good data on milligram size samples. This will make it possible to collect neutron PDF data on materials where grams of sample synthesis is expensive and complicated.

Within the past years new X-ray total scattering beam lines have been built. One of

them is the beam line, XPDF, at Diamond which makes it possible to quickly collect high resolution X-ray PDF data. The long term plan for XPDF at Diamond is to collaborate with the POLARIS and GEM instruments at ISIS which will make it possible to submit a project proposal including access to beam time at both facilities on the same system. That will promote the use of combined neutron and X-ray PDF analysis which have been proved in this study to give useful information on strongly correlated systems.

With these new developments for both modelling and experimental data collection, the PDF community is heading towards a bright future.

Bibliography

[1] Jonker, G. H.; Van Santen, J. H. *Physica (Amsterdam)* **1950**, *16*, 337–349.

[2] Wu, M. K.; Ashburn, J. R.; Torng, C. J.; Hor, P. H.; Meng, R. L.; Gao, L.; Huang, Z. J.; Wang, Y. Q.; Chu, C. W. *Phys. Rev. Lett.* **1987**, *58*, 908–910.

[3] Mizushima, K.; Jones, P. C.; Wiseman, P. J.; Goodenough, J. B. *Mater. Res. Bull.* **1980**, *15*, 783–789.

[4] Lee, J. H. et al. *Nature* **2010**, *466*, 954–958.

[5] Klug, H. P.; Alexander, L. E. *X-ray diffraction procedures*; Wiley, New York, 1954.

[6] Stenger, C. G. F.; Burggraaf, A. J. *Phys. Status Solidi. A* **1980**, *61*, 653–664.

[7] Edwards, H. L.; Markert, J. T.; de Lozanne, A. L. *Phys. Rev. Lett.* **1992**, *69*, 2967–2970.

[8] Paddison, J. A. M.; Goodwin, A. L. *Phys. Rev. Lett.* **2012**, *108*, 017204.

[9] Millis, A. J. *Nature* **1998**, *392*, 147–150.

[10] Millis, A. J.; Shraiman, B. I.; Mueller, R. *Phys. Rev. Lett.* **1996**, *77*, 175–178.

[11] Bréger, J.; Dupré, N.; Chupas, P. J.; Lee, P. L.; Proffen, T.; Parise, J. B.; Grey, C. P. *J. Am. Chem. Soc.* **2005**, *127*, 7529–7537.

[12] Jahn, H. A.; Teller, E. *Proc. Roy. Soc. A* **1937**, *161*, 220–235.

[13] Halcrow, M. A. *Chem. Soc. Rev.* **2013**, *42*, 1784–1795.

[14] Atkins, P. W.; Overton, T.; Rourke, J.; Weller, M.; Armstrong, F. *Shriver and Atkins' Inorganic Chemistry*, 5th ed.; Oxford University Press, Oxford, 2010.

[15] Hund, F. *Z. Phys.* **1925**, *33*, 855–859.

[16] Bersuker, I. B. *Chem. Rev.* **2001**, *101*, 1067–1114.

[17] Van Vleck, J. H. *J. Chem. Phys.* **1939**, *7*, 72–84.

[18] Popovic, Z.; Satpathy, S. *Phys. Rev. Lett.* **2000**, *84*, 1603–1606.

[19] Kanamori, J. *J. Appl. Phys.* **1960**, *31*, S14–S23.

[20] Sturge, M. D. *Solid State Phys.* **1968**, *20*, 91–211.

[21] Kaplan, S. G.; Quijada, M.; Drew, H. D.; Tanner, D. B.; Xiong, G. C.; Ramesh, R.; Kwon, C.; Venkatesan, T. *Phys. Rev. Lett.* **1996**, *77*, 2081–2084.

[22] O'Brien, M. C. M. *Proc. Roy. Soc. A* **1964**, *281*, 323–339.

[23] Wollan, E. O.; Koehler, W. C. *Phys. Rev.* **1955**, *100*, 545–563.

[24] Goodenough, J. B. *Phys. Rev.* **1955**, *100*, 564–573.

[25] Tokura, Y.; Nagaosa, N. *Science* **2000**, *288*, 462–467.

[26] Hemberger, J.; von Nidda, H. A. K.; Fritsch, V.; Deisenhofer, J.; Lobina, S.; Rudolf, T.; Lunkenheimer, P.; Lichtenberg, F.; Loidl, A.; Bruns, D.; Büchner, B. *Phys. Rev. Lett.* **2003**, *91*, 066403.

[27] Blake, G. R.; Palstra, T. T. M.; Ren, Y.; Nugroho, A. A.; Menovsky, A. A. *Phys. Rev. Lett.* **2001**, *87*, 245501.

[28] Chamberland, B. L. *Crit. Rev. Solid State* **1977**, *7*, 1–31.

[29] Murphy, B.; Aljabri, M.; Ahmed, A. M.; Murphy, G.; Hathaway, B. J.; Light, M. E.; Geilbrich, T.; Hursthouse, M. B. *Dalton Trans.* **2006**, *2*, 357–367.

[30] Lufaso, M. W.; Woodward, P. M. *Acta Crystall. B* **2003**, *60*, 10–20.

[31] Öpik, U.; Pryce, M. H. L. *Proc. Roy. Soc. A* **1957**, *238*, 425–447.

[32] Bersuker, I. B. *Chem. Rev.* **2013**, *113*, 1351–1390.

[33] Pearson, R. G. *Proc. Nat. Acad. Sci.* **1975**, *72*, 2104–2106.

[34] Comès, R.; Lambert, M.; Guinier, A. *Acta Crystall. A* **1970**, *26*, 244–254.

[35] Comès, R.; Lambert, M.; Guinier, A. *Solid State Commun.* **1968**, *6*, 715–719.

[36] Solanki, N. K.; McInnes, E. J. L.; Mabbs, F. E.; Radojevic, S.; McPartlin, M.; Feeder, N.; Davies, J. E.; Halcrow, M. A. *Angew. Chem. Int. Ed.* **1998**, *37*, 2221–2223.

[37] Falvello, L. R. *J. Chem. Soc. Dalton Trans.* **1997**, *23*, 4463–4475.

[38] Louca, D.; Egami, T.; Brosha, E. L.; Röder, H.; Bishop, A. R. *Phys. Rev. B* **1997**, *56*, 8475–8478.

[39] Nakatsuji, S. et al. *Science* **2012**, *336*, 559–563.

[40] Senn, M. S.; Keen, D. A.; Lucas, T. C. A.; Hriljac, J. A.; Goodwin, A. L. *Phys. Rev. Lett.* **2016**, *116*, 207602.

[41] Stroppa, A.; Jain, P.; Barone, P.; Marsman, M.; Perez-Mato, J. M.; Cheetham, A. K.; Kroto, H. W.; Picozzi, S. *Angew. Chem. Int. Ed.* **2011**, *50*, 5847–5850.

[42] Yoshida, H.; Yamaura, J.; Isobe, M.; Okamoto, Y.; Nilsen, G. J.; Hiroi, Z. *Nat. Commun.* **2012**, *3*, 860.

[43] Gehring, G. A.; Gehring, K. A. *Rep. Prog. Phys.* **1975**, *38*, 1.

[44] Ising, E. *Z. Phys.* **1925**, *31*, 253–258.

[45] Buckingham, A. D. *Can. J. Chem.* **1960**, *38*, 300–307.

[46] Walsh, A.; Watson, G. W. *J. Solid State Chem.* **2005**, *178*, 1422–1428.

[47] Walsh, A.; Payne, D. J.; Egdell, R. G.; Watson, G. W. *Chem. Soc. Rev.* **2011**, *40*, 4455–4463.

[48] Maier, J.; Schwitzgebel, G. *Mater. Res. Bull.* **1983**, *18*, 601–608.

[49] Leciejewicz, J. *Acta Crystall.* **1961**, *14*, 1304.

[50] Martinez, G.; Schlüter, M.; Cohen, M. L. *Phys. Rev. B* **1975**, *11*, 651–659.

[51] Lüty, F.; Ortiz-Lopez, J. *Phys. Rev. Lett.* **1983**, *50*, 1289–1292.

[52] Rowe, J. M.; Rush, J. J.; Susman, S. *Phys. Rev. B* **1983**, *28*, 3506–3511.

[53] Rowe, J. M.; Rush, J. J.; Prince, E. *J. Chem. Phys.* **1977**, *66*, 5147–5149.

[54] Rowe, J. M.; Rush, J. J.; Chesser, N. J.; Michel, K. H.; Naudts, J. *Phys. Rev. Lett.* **1978**, *40*, 455–458.

[55] Stokes, H. T.; Hatch, D. M. *Phys. Rev. B* **1984**, *30*, 3845–3858.

[56] Kugel, K. I.; Khomskii, D. I. *Sov. Phys. Usp.* **1982**, *25*, 231–256.

[57] Knox, K. *Acta Crystall.* **1961**, *14*, 583–585.

[58] Beckman, O.; Knox, K. *Phys. Rev.* **1961**, *121*, 376–380.

[59] Okazaki, A.; Suemune, Y. *J. Phys. Soc. Jpn.* **1961**, *16*, 176–183.

[60] Zhou, J.-S.; Goodenough, J. B. *Phys. Rev. B* **1999**, *60*, R15002–R15004.

[61] Goodenough, J. B. *Annu. Rev. Mater. Sci.* **1998**, *28*, 1–24.

[62] Rodriguez-Carvajal, J.; Hennion, M.; Moussa, F.; Moudden, A. H. *Phys. Rev. B* **1998**, *57*, R3189–R3192.

[63] Matsumoto, G. *J. Phys. Soc. Jpn.* **1970**, *29*, 606–615.

[64] Janes, R.; Moore, E. A. *Metal-ligand bonding*, 1st ed.; Royal Society of Chemistry, Milton Keynes, 2004.

[65] Halder, G. J.; Chapman, K. W.; Schlueter, J. A.; Manson, J. L. *Angew. Chem. Int. Ed.* **2011**, *50*, 419–421.

[66] Santini, P.; Carretta, S.; Amoretti, G. *Rev. Mod. Phys.* **2009**, *81*, 807–862.

[67] Kung, H.-H.; Baumbech, R. E.; Bauer, E. D.; Thorsmølle, V. K.; Zhang, W.-L.; Haule, K.; Mydosh, G., J. A. Blumberg *Science* **2015**, *347*, 1339–1342.

[68] Paddison, J. A. M.; Jacobsen, H.; Petrenko, O. A.; Fernandez-Diaz, M. T.; Deen, P. P.; Goodwin, A. L. *Science* **2015**, *350*, 179–181.

[69] Honshima, M.; Ohashi, K. *J. Mater. Eng. Perform.* **1994**, *3*, 218–222.

[70] Sorace, L.; Benelli, C.; Gatteschi, D. *Chem. Soc. Rev.* **2011**, *40*, 3092–3104.

[71] Shull, C. G.; Smart, J. S. *Phys. Rev.* **1949**, *76*, 1256–1257.

[72] Hurd, C. M. *Contemp. Phys.* **1982**, *23*, 469–493.

[73] Goodenough, J. B. *J. Phys. Chem. Solids* **1958**, *6*, 287–297.

[74] Kanamori, J. *J. Phys. Chem. Solids* **1959**, *10*, 87–98.

[75] Moreira dos Santos, A.; Cheetham, A. K.; Atou, T.; Syono, Y.; Yamaguchi, Y.; Ohoyama, K.; Chiba, H.; Rao, C. N. R. *Phys. Rev. B* **2002**, *66*, 064425.

[76] Atou, T.; Chiba, H.; Ohoyama, K.; Yamaguchi, Y.; Syono, Y. *J. Solid State Chem.* **1999**, *145*, 639–642.

[77] Yano, S.; Louca, D.; Neuerfeind, J. C.; Yan, J.-Q.; Zhou, J.-S.; Goodenough, J. B. *Phys. Rev. B* **2014**, *90*, 214111.

[78] De Raychaudhury, M.; Pavarini, E.; Andersen, O. K. *Phys. Rev. Lett.* **2007**, *99*, 126402.

[79] Blake, G. R.; Palstra, T. T. M.; Ren, Y.; Nugroho, A. A.; Menovsky, A. A. *Phys. Rev. B* **2002**, *65*, 174112.

[80] Ren, Y.; Palstra, T. T. M.; Khomskii, D. I.; Pellegrin, E.; Nugroho, A. A.; Menovsky, A. A.; Sawatzky, G. A. *Nature* **1998**, *396*, 441–444.

[81] Wang, Z.; Zhang, B.; Otsuka, T.; Inoue, K.; Kobayashi, H.; Kurmoo, M. *Dalton Trans.* **2004**, *15*, 2209–2216.

[82] Dubbeldam, D.; Walton, K. S.; Ellis, D. E.; Snurr, R. Q. *Angew. Chem. Int. Ed.* **2007**, *46*, 4496–4499.

[83] Deng, H.; Grunder, S.; Cordova, K. E.; Valente, C.; Furukawa, H.; Hmadeh, M.; Gándara, F.; Whalley, A. C.; Liu, Z.; Asahina, S.; Kazumori, H.; O'Keeffe, M.; Terasaki, O.; Stoddart, J. F.; Yaghi, O. M. *Science* **2012**, *336*, 1018–1023.

[84] Li, J.-R.; Kuppler, R. J.; Zhou, H.-C. *Chem. Soc. Rev.* **2009**, *38*, 1477–1504.

[85] Uemura, T.; Yanai, N.; Kitagawa, S. *Chem. Soc. Rev.* **2009**, *38*, 1228–1236.

[86] Myrray, L. J.; Dincă, M.; Long, J. R. *Chem. Soc. Rev.* **2009**, *38*, 1294–1314.

[87] Kurmoo, M. *Chem. Soc. Rev.* **2009**, *38*, 1353–1379.

[88] Goodwin, A. L.; Calleja, M.; Conterio, M. J.; Dove, M. T.; Evans, J. S. O.; Keen, D. A.; Peters, L.; Tucker, M. G. *Science* **2008**, *319*, 794–797.

[89] Hu, K. L.; Kurmoo, M.; Wang, Z.; Gao, S. *Chem. Eur. J.* **2009**, *15*, 12050–12064.

[90] Collings, I. E.; Hill, J. A.; Cairns, A. B.; Cooper, R. I.; Thompson, A. L.; Parker, J. E.; Tang, C. C.; Goodwin, A. L. *Dalton Trans.* **2016**, *45*, 4169–4178.

[91] Röder, H.; Zang, J.; Bishop, A. R. *Phys. Rev. Lett.* **1996**, *76*, 1356–1359.

[92] Uehara, M.; Mori, S.; Chen, C. H.; Cheong, S. W. *Nature* **1999**, *399*, 560–563.

[93] Argyriou, D. N.; Lynn, J. W.; Osborn, R.; Campbell, B.; Mitchell, J. F.; Ruett, U.; Bordallo, H. N.; Wildes, A.; Ling, C. D. *Phys. Rev. Lett.* **2002**, *89*, 036401.

[94] Ramirez, A. P. *J. Phys. Condens. Matt.* **1997**, *9*, 8171–8199.

[95] Rao, C. N. R.; Cheetham, A. K. *Science* **1996**, *272*, 369–370.

[96] Lynn, J. W.; Argyriou, D. N.; Ren, Y.; Chen, Y.; Mukovskii, Y. M.; Shulyatev, D. A. *Phys. Rev. B* **2007**, *76*, 014437.

[97] Tokura, Y. *Rep. Prog. Phys.* **2006**, *69*, 797–851.

[98] Mitchell, J. F.; Argyriou, D. N.; Potter, C. D.; Hinks, D. G.; Jorgensen, J. D.; Bader, S. D. *Phys. Rev. B* **1996**, *54*, 6172–6183.

[99] von Hemlholt, R.; Wecker, J.; Holzapfel, B.; Schultz, L.; Samwer, K. *Phys. Rev. Lett.* **1993**, *71*, 2331–2333.

[100] Chen, Y.; Ueland, B. G.; Lynn, J. W.; Bychkov, G. L.; Barilo, S. N.; Mukovskii, Y. M. *Phys. Rev. B* **2008**, *78*, 212301.

[101] Manh-Huong, P.; Srinivas, V.; Seong-Cho, Y.; Hur, N. H. *J. Appl. Phys.* **2003**, *93*, 8200–8202.

[102] McIlroy, D.; Zhang, J.; Liou, S.-H.; Dowben, P. A. *Phys. Lett. A* **1995**, *207*, 367 – 373.

[103] Dagotto, E.; Hotta, T.; Moreo, A. *Phys. Rep.* **2001**, *344*, 1–153.

[104] Norby, P.; Andersen, I. G. K.; Andersen, E. K.; Andersen, N. H. *J. Solid State Chem.* **1995**, *119*, 191–196.

[105] Solovyev, I.; Hamada, N.; Terakura, K. *Phys. Rev. Lett.* **1996**, *76*, 4825–4828.

[106] Tomioka, Y.; Tokura, Y. *Phys. Rev. B* **2004**, *70*, 014432.

[107] Tokura, Y.; Tomioka, Y. *J. Magn. Magn. Mater.* **1999**, *200*, 1–23.

[108] Larochelle, S.; Mehta, A.; Kaneko, N.; Mang, P. K.; Panchula, A. F.; Zhou, L.; Arthur, J.; Greven, M. *Phys. Rev. Lett.* **2001**, *87*, 095502.

[109] Proffen, T.; Billinge, S. *Appl. Phys. A* **2002**, *74*, 1770–1772.

[110] Billinge, S. J. L.; Proffen, T.; Petkov, V.; Sarrao, J. L.; Kycia, S. *Phys. Rev. B* **2000**, *62*, 1203–1211.

[111] Shatnawi, M.; Božin, E. S.; Mitchell, J. F.; Billinge, S. J. L. *Phys. Rev. B* **2016**, *93*, 165138.

[112] Sánchez, M. C.; Subías, G.; García, J.; Blasco, J. *Phys. Rev. Lett.* **2003**, *90*, 045503.

[113] Ahmed, M. R.; Gehring, G. A. *Phys. Rev. B* **2006**, *74*, 014420.

[114] Ahmed, M. R.; Gehring, G. A. *Phys. Rev. B* **2009**, *79*, 174106.

[115] Dai, P.; Fernandez-Baca, J. A.; Wakabayashi, N.; Plummer, E. W.; Tomioka, Y.; Tokura, Y. *Phys. Rev. Lett.* **2000**, *85*, 2553–2556.

[116] Helton, J. S.; Pajerowski, D. M.; Qiu, Y.; Zhao, Y.; Shulyatev, D. A.; Mukovskii, Y. M.; Bychkov, G. L.; Barilo, S. N.; Lynn, J. W. *Phys. Rev. B* **2014**, *90*, 214411.

[117] Senn, M. S.; Wright, J. P.; Attfield, J. P. *Nature* **2012**, *481*, 173–176.

[118] Yoshida, J.; Lida, S. *J. Phys. Soc. Jpn.* **1977**, *42*, 230–237.

[119] Iizumi, M.; Koetzle, T. F.; Shirane, G.; Chikazumi, S.; Matsui, M.; Todo, S. *Acta Crystall. B* **1982**, *38*, 2121–2133.

[120] Filipponi, A.; Di Cicco, A. *Synchrotron Radiat. News* **1993**, *6*, 13–19.

[121] Rougier, A.; Delmas, C.; Chadwick, A. V. *Solid State Commun.* **1995**, *94*, 123–127.

[122] Binder, K.; Young, A. P. *Rev. Mod. Phys.* **1986**, *58*, 801–976.

[123] Booth, C. H.; Gardner, J. S.; Kwei, G. H.; Heffner, R. H.; Bridges, F.; Subramanian, M. A. *Phys. Rev. B* **2000**, *62*, R755–R758.

[124] Miller, B. L. *NMR Biomed.* **1991**, *4*, 47–52.

[125] Massiot, D.; Fayon, F.; Capron, M.; King, I.; Le Calvé, S.; Alonso, B.; Durand, J. O.; Bujoli, B.; Gan, Z.; Hoatson, G. *Magn. Reson. Chem.* **2002**, *40*, 70–76.

[126] Trokiner, A.; Verkhovskii, S.; Gerashenko, A.; Volkova, Z.; Anikeenok, O.; Mikhalev, K.; Eremin, M.; Pinsard-Gaudart, L. *Phys. Rev. B* **2013**, *87*, 125142.

[127] Kiyama, T.; Itoh, M. *Phys. Rev. Lett.* **2003**, *91*, 167202.

[128] Mochizuki, M.; Imada, M. *Phys. Rev. Lett.* **2003**, *91*, 167203.

[129] Jonker, G. H. *Physica (Amsterdam)* **1956**, *22*, 707–722.

[130] Fink, J.; Schierle, E.; Weschke, E.; Geck, J. *Rep. Prog. Phys.* **2013**, *76*, 056502.

[131] Wilkins, S. B.; Spencer, P. D.; Hatton, P. D.; Collins, S. P.; Roper, M. D.; Prabhakaran, D.; Boothroyd, A. T. *Phys. Rev. Lett.* **2003**, *91*, 167205.

[132] Sternlieb, B. J.; Hill, J. P.; Wildgruber, U. C.; Luke, G. M.; Nachumi, B.; Moritomo, Y.; Tokura, Y. *Phys. Rev. Lett.* **1996**, *76*, 2169–2172.

[133] Murakami, Y.; Kawada, H.; Kawata, H.; Tanaka, M.; Arima, T.; Moritomo, Y.; Tokura, Y. *Phys. Rev. Lett.* **1998**, *80*, 1932–1935.

[134] Murakami, Y.; Hill, J. P.; Gibbs, D.; Blume, M.; Koyama, I.; Tanaka, M.; Kawata, H.; Arima, T.; Tokura, Y.; Hirota, K.; Endoh, Y. *Phys. Rev. Lett.* **1998**, *81*, 582–585.

[135] Chatterji, T.; Fauth, F.; Ouladdiaf, B.; Mandal, P.; Ghosh, B. *Phys. Rev. B* **2003**, *68*, 052406.

[136] Evans, N. L.; Thygesen, P. M. M.; Boström, H. L. B.; Reynolds, E. M.; Collings, I. E.; Phillips, A. E.; Goodwin, A. L. *J. Am. Chem. Soc.* **2016**, *138*, 939–9396.

[137] DiFrancesco, R.; Billinge, S. J. L.; Kwei, G. H.; Neumeier, J. J.; Thompson, J. *Physica B* **1998**, *241*, 421–423.

[138] Billinge, S. J. L.; DiFrancesco, R.; Kwei, G. H.; Neumeier, J. J.; Thompson, J. *Phys. Rev. Lett.* **1996**, *77*, 715–718.

[139] Proffen, T.; DiFrancesco, R.; Billinge, S. J. L.; Brosha, E. L.; Kwei, G. H. *Phys. Rev. B* **1999**, *60*, 9973–9977.

[140] Božin, E. S.; Sartbaeva, A.; Zheng, H.; Wells, S. A.; Mitchell, J. F.; Proffen, T.; Thorpe, M. F.; Billinge, S. J. L. *J. Phys. Chem. Solids* **2008**, *69*, 2146–2150.

[141] Qiu, X. Y.; Proffen, T.; Mitchell, J. F.; Billinge, S. J. L. *Phys. Rev. Lett.* **2005**, *94*, 177203.

[142] Božin, E. S.; Schmidt, M.; DeConinck, A. J.; Paglia, G.; Mitchell, J. F.; Chatterji, T.; Radaelli, P. G.; Proffen, T.; Billinge, S. J. L. *Phys. Rev. B* **2007**, *98*, 137203.

[143] Levin, I.; Amos, T. G.; Nino, J. C.; Vanderah, T. A.; Randall, C. A.; Lanagan, M. T. *J. Solid State Chem.* **2002**, *168*, 69–75.

[144] Shoemaker, D. P.; Seshadri, R.; Hector, A. L.; Llobet, A.; Proffen, T.; Fennie, C. J. *Phys. Rev. B* **2010**, *81*, 144113.

[145] Young, C. A.; Goodwin, A. L. *J. Mater. Chem.* **2011**, *21*, 6464–6476.

[146] Sumner, T. *Science* **2014**, *343*, 1092–1093.

[147] West, A. R. *Basic Solid State Chemistry*, 2nd ed.; Wiley-Blackwell, Chichester, 1999.

[148] Rudolf, P.; Clearfield, A. *Acta Crystall. B* **1985**, *41*, 418–425.

[149] Forman, P. *Arch. Hist. Exact Sci.* **1969**, *6*, 38–71.

[150] Friedrich, W.; Knipping, P.; Laue, M. *Bayer. Akad. Wiss. München* **1912**, 303–322.

[151] Bragg, W. H.; Bragg, W. L. *Proc. R. Soc. Lond. A: Math. Phys. Eng. Sci.* **1913**, *89*, 277–291.

[152] Blake, A. J.; Clegg, W.; Cole, J. M.; Evans, J. S. O.; Main, P.; Parsons, S.; Watkin, D. J. In *Crystal Structure Analysis Principles and Practice*, 2nd ed.; Clegg, W., Ed.; Oxford Science Publications, Oxford, 2009.

[153] Bragg, W. H.; Bragg, W. L. *Roy. Soc. Lond. A: Math. Phys. Eng. Sci.* **1913**, *89*, 248–277.

[154] Brooks-Bartlett, J. C.; Garman, E. F. *Interdiscip. Sci. Rev.* **2015**, *40*, 244–264.

[155] Ziman, J. M. *Principles of the Theory of Solids*; Cambridge University Press, Cambridge, 1972.

[156] Compton, A. H. *Phys. Rev.* **1923**, *21*, 483–502.

[157] Oszlányi, G.; Süto, A. *Acta Crystall. A* **2008**, *64*, 123–134.

[158] Palatinus, L. In *Uniting Electron Crystallography and Powder Diffraction*; Kolb, U., Shankland, K., Meshi, L., Avilov, A., David, W. I., Eds.; Springer Netherlands, 2012; pp 105–116.

[159] Koester, L.; Rauch, H.; Seymann, E. *At. Data Nucl. Data tables* **1991**, *49*, 65–120.

[160] Sivia, D. S. *Elementary Scattering Theory For X-ray and Neutron Users*, 1st ed.; Oxford University Press, Oxford, 2011.

[161] Pawley, G. S. *J. Appl. Crystallogr.* **1981**, *14*, 357–361.

[162] Rietveld, H. M. *J. Appl. Crystallogr.* **1969**, *2*, 65–71.

[163] Powder Diffraction & Rietveld Refinement School. Course notes, 2014.

[164] Coelho, A. TOPAS-Academic version 4.1. 2006.

[165] Wiedemann, H. *Synchrotron Radiation*; Springer-Verlag, Berlin, 2003.

[166] Masson, O.; Thomas, P. *J. Appl. Crystallogr.* **2013**, *46*, 461–465.

[167] Lefmann, K. *Neutron Scattering: Theory, Instrumentation, and Simulation*, 1st ed.; University of Copenhagen, Copenhagen, 2007.

[168] Gibbons, J. H.; Macklin, R. L. *Phys. Rev.* **1959**, *114*, 571–580.

[169] Gabrys, B. J. *Applications of neutron scattering to soft condensed matter*; CRC Press, Amsterdam, 2000.

[170] Rodríguez-Carvajal, J. *Physica B* **1993**, *192*, 55–69.

[171] Hull, S.; Smith, R. I.; David, W. I. F.; Hannon, A. C.; Mayers, J.; Cywinski, R. *Physica B* **1992**, *180*, 1000–1002.

[172] Keen, D. A.; Goodwin, A. L. *Nature* **2015**, *521*, 303–309.

[173] Egami, T.; Billinge, S. J. L. *Underneath the Bragg Peaks: structural analysis of complex materials*, 1st ed.; Pergamon, Oxford, 2003.

[174] Misawa, M.; Price, D.; Suzuki, K. *J. Non-Cryst. Solids* **1980**, *37*, 85 – 97.

[175] Dove, M. T.; Tucker, M. G.; Keen, D. A. *Eur. J. Miner.* **2002**, *14*, 331.

[176] Nield, V. M.; Keen, D. A. *Diffuse Neutron Scattering from Crystalline Materials*, 1st ed.; Oxford University Press, Oxford, 2001.

[177] Billinge, S. J. L.; Kanatzidis, M. G. *Chem. Commun.* **2004**, *7*, 749–760.

[178] Proffen, T.; Billinge, S. J. L.; Egami, T.; Louca, D. *Z. Kristallogr.* **2003**, *204*, 132–143.

[179] Keen, D. A. *J. Appl. Crystallogr.* **2000**, *34*, 172–177.

[180] Hannon, A. C. *Nucl. Instr. Meth. A* **2005**, *551*, 88–107.

[181] Hannon, A. C.; Howells, W. S.; Soper, A. K. *IOP Conference Series* **1990**, *107*, 193.

[182] Soper, A. K.; Barney, E. R. *J. Appl. Crystallogr.* **2011**, *44*, 714–726.

[183] Tucker, M. G.; Keen, D. A.; Dove, M. T.; Goodwin, A. L.; Hui, Q. *J. Phys. Condens. Matt.* **2007**, *19*, 335218.

[184] Krayzman, V.; Levin, I.; Tucker, M. G. *J. Appl. Crystallogr.* **2008**, *41*, 705–714.

[185] Farrow, C. L.; Juhas, P.; Liu, J. W.; Bryndin, D.; Božin, E. S.; Bloch, J.; Proffen, T.; Billinge, S. J. L. *J. Phys. Condens. Matt.* **2007**, *19*, 335219.

[186] Coelho, A. A.; Chater, P. A.; Kern, A. *J. Appl. Crystallogr.* **2015**, *48*, 869–875.

[187] Playford, H. Y.; Hannon, A. C.; Barney, E. R.; Walton, R. I. *Chem. Eur. J.* **2013**, *19*, 2803–2813.

[188] Prill, D.; Juhás, P.; Schmidt, M. U.; Billinge, S. J. L. *J. Appl. Crystallogr.* **2015**, *48*, 171–178.

[189] Metropolis, N.; Rosenbluth, A. W.; Rosenbluth, M. N.; Teller, A. H. *J. Chem. Phys.* **1953**, *21*, 1087.

[190] Greedan, J. E.; Gout, D.; Lozano-Gorrin, A. D.; Derahkshan, S.; Proffen, T.; Kim, H.-J.; Božin, E.; Billinge, S. J. L. *Phys. Rev. B* **2009**, *79*, 014427.

[191] Pauling, L. *J. Am. Chem. Soc.* **1935**, *57*, 2680–2684.

[192] Blundell, S. J. *Magnetism in Condensed Matter*, 1st ed.; Oxford University Press: Oxford, 2001.

[193] Mydosh, J. A. *Rep. Prog. Phys.* **2015**, *78*, 05250501.

[194] Sherrington, D.; Kirkpatrick, S. *Phys. Rev. Lett.* **1975**, *35*, 1792–1796.

[195] Barbara, B.; Malozemoff, A. P.; Imry, Y. *Phys. Rev. Lett.* **1981**, *47*, 1852–1855.

[196] Huang, C. Y. *J. Magn. Magn. Mater.* **1985**, *51*, 1–74.

[197] Cannella, V.; Mydosh, J. A. *Phys. Rev. B* **1972**, *6*, 4220–4237.

[198] Mydosh, J. A. *Spin Glasses: An Experimental Introduction*, 1st ed.; Taylor and Francis, London, 1993.

[199] Aharony, A.; Birgeneau, R. J.; Coniglio, A.; Kastner, M. A.; Stanley, H. E. *Phys. Rev. Lett.* **1988**, *60*, 1330–1333.

[200] Blatter, G.; Feigel'man, M. V.; Geshkenbein, V. B.; Larkin, A. I.; Vinokur, V. M. *Rev. Mod. Phys.* **1994**, *66*, 1125–1388.

[201] Lundgren, L.; Svedlindh, P.; Nordblad, P.; Beckman, O. *Phys. Rev. Lett.* **1983**, *51*, 911–914.

[202] Atzmony, U.; Gurewitz, E.; Melamud, M.; Pinto, H.; Shaked, H.; Gorodetsky, G.; Hermon, E.; Hornreich, R. M.; Shtrikman, S.; Wanklyn, B. *Phys. Rev. Lett.* **1979**, *43*, 782–785.

[203] Süllow, S.; Nieuwenhuys, G. J.; Menovsky, A. A.; Mydosh, J. A.; Mentink, S. A. M.; Mason, T. E.; Buyers, W. J. L. *Phys. Rev. Lett.* **1997**, *78*, 354–357.

[204] Greedan, J. E.; Sato, M.; Yan, X.; Razavi, F. *Solid State Commun.* **1986**, *59*, 895–897.

[205] Gardner, J. S.; Gingras, M. J. P.; Greedan, J. E. *Rev. Mod. Phys.* **2010**, *82*, 53–107.

[206] Silverstein, H. J. et al. *Phys. Rev. B* **2014**, *89*, 054433.

[207] Bramwell, S. T.; Gingras, M. J. P. *Science* **2001**, *294*, 1495–1501.

[208] Zhou, H. D.; Bramwell, S. T.; Cheng, J. G.; Wiebe, C. R.; Li, G.; Balicas, L.; Bloxosom, J. A.; Silverstein, H. J.; Zhou, J. S.; Goodenough, J. B.; Gardner, J. S. *Nat. Commun.* **2011**, *2*, 478.

[209] Del Maestro, A. G.; Gingras, M. J. P. *J. Phys. Condens. Matt.* **2004**, *16*, 3339–3353.

[210] Kimura, K.; Nakatsuji, S.; Wen, J. J.; Broholm, C.; Stone, M. B.; Nishibori, E.; Sawa, H. *Nat. Commun.* **2013**, *4*, 1934.

[211] Chang, L.-J.; Onoda, S.; Su, Y.; Kao, Y.-J.; Tsuei, K.-D.; Yasui, Y.; Kakurai, K.; Lees, M. R. *Nat. Commun.* **2012**, *3*, 992.

[212] Gingras, M. J. P.; Stager, C. V.; Raju, N. P.; Gaulin, B. D.; Greedan, J. E. *Phys. Rev. Lett.* **1997**, *78*, 947–950.

[213] Gingras, M. J. P.; Stager, C. V.; Gaulin, B. D.; Raju, N. P.; Greedan, J. E. *J. Appl. Phys.* **1996**, *79*, 6170–6172.

[214] Blacklock, K.; White, H. W.; Gürmen, E. *J. Chem. Phys.* **1980**, *73*, 1966–1969.

[215] Raju, N. P.; Gmelin, E.; Kremer, R. K. *Phys. Rev. B* **1992**, *46*, 5405–5411.

[216] Miyoshi, K.; Nishimura, Y.; Honda, K.; Fujiwara, K.; Takeuchi, J. *J. Phys. Soc. Jpn.* **2000**, *69*, 3517–3520.

[217] Ali, N.; Hill, P.; Zhang, X.; Willis, F. *J. Alloys Compd.* **1992**, *181*, 281–285.

[218] Dupuis, V.; Vincent, E.; Hammann, J.; Greedan, J. E.; Wills, A. S. *J. Appl. Phys.* **2002**, *91*, 8384–8386.

[219] Ladieu, F.; Bert, F.; Dupuis, V.; Vincent, E.; Hammann, J. *J. Phys. Condens. Matt.* **2004**, *16*, S735.

[220] Gardner, J. S.; Gaulin, B. D.; Lee, S.-H.; Broholm, C.; Raju, N. P.; Greedan, J. E. *Phys. Rev. Lett.* **1999**, *83*, 211–214.

[221] Dunsiger, S. R.; Kiefl, R. F.; Chow, K. H.; Gaulin, B. D.; Gingras, M. J. P.; Greedan, J. E.; Keren, A.; Kojima, K.; Luke, G. M.; MacFarlane, W. A.; Raju, N. P.; Sonier, J. E.; Uemura, Y. J.; Wu, W. D. *J. Appl. Phys.* **1996**, *79*, 6636–6638.

[222] Gardner, J. S.; Ehlers, G.; Heffner, R. H.; Mezei, F. *J. Magn. Magn. Mater.* **2001**, *226*, 460–462.

[223] Gardner, J. S.; Ehlers, G.; Bramwell, S. T.; Gaulin, B. D. *J. Phys. Condens. Matt.* **2004**, *16*, S643.

[224] Reimers, J. N.; Greedan, J. E.; Sato, M. *J. Solid State Chem.* **1988**, *72*, 390–394.

[225] Minervini, L.; Grimes, R. W.; Tabira, Y.; Withers, R. L.; Sickafus, K. E. *Philos. Mag. A* **2002**, *82*, 123–135.

[226] Keren, A.; Gardner, J. S. *Phys. Rev. Lett.* **2001**, *87*, 177201.

[227] Ofer, O.; Keren, A.; Gardner, J. S.; Ren, Y.; MacFarlane, W. A. *Phys. Rev. B* **2010**, *82*, 092403.

[228] Sagi, E.; Ofer, O.; Keren, A.; Gardner, J. S. *Phys. Rev. Lett.* **2005**, *94*, 237202.

[229] Saunders, T. E.; Chalker, J. T. *Phys. Rev. Lett.* **2007**, *98*, 157201.

[230] Shinaoka, H.; Motome, Y.; Miyake, T.; Ishibashi, S. *Phys. Rev. B* **2013**, *88*, 174422.

[231] Hammersley, A. P.; Svensson, S. O.; Hanfland, M.; Fitch, A. N.; Hausermann, D. *High Press. Res.* **1996**, *14*, 235–248.

[232] Stokes, H. T.; Hatch, D. M.; Campbell, B. J. ISOTROPY Software Suite. 2011.

[233] Raza, Z.; Alfe, D.; Salzmann, C. G.; Klimes, J.; Michaelides, A.; Slater, B. *Phys. Chem. Chem. Phys.* **2011**, *13*, 19788–19795.

[234] Zhou, H. D.; Wiebe, C. R.; Janik, J. A.; Balicas, L.; Yo, Y. J.; Qiu, Y.; Copley, J. R. D.; Gardner, J. S. *Phys. Rev. Lett.* **2008**, *101*, 227204.

[235] Fairbank, V. E.; Thompson, A. L.; Cooper, R. I.; Goodwin, A. L. *Phys. Rev. B* **2012**, *86*, 104113.

[236] Andreanov, A.; Chalker, J. T.; Saunders, T. E.; Sherrington, D. *Phys. Rev. B* **2010**, *81*, 014406.

[237] Goremychkin, E. A.; Osborn, R.; Rainford, B. D.; Macaluso, R. T.; Adroja, D. T.; Koza, M. *Nat. Phys.* **2008**, *4*, 766–770.

[238] Villain, J. *J. Phys. C* **1977**, *10*, 1717.

[239] de Vries, M. A.; Mclaughlin, A. C.; Bos, J.-W. G. *Phys. Rev. Lett.* **2010**, *104*, 177202.

[240] Radaelli, P. G.; Horibe, Y.; Gutmann, M. J.; Ishibashi, H.; Chen, C. H.; Ibberson, R. M.; Koyama, Y.; Hor, Y.-S.; Kiryukhin, V.; Cheong, S.-W. *Nature* **2002**, *416*, 155–158.

[241] Clark, L.; Nilsen, G. J.; Kermarrec, E.; Ehlers, G.; Knight, K. S.; Harrison, A.; Attfield, J. P.; Gaulin, B. D. *Phys. Rev. Lett.* **2014**, *113*, 117201.

[242] Gaulin, B. D.; Reimers, J. N.; Mason, T. E.; Greedan, J. E.; Tun, Z. *Phys. Rev. Lett.* **1992**, *69*, 3244–3247.

[243] Singh, D. K.; Helton, J. S.; Chu, S.; Han, T. H.; Bonnoit, C. J.; Chang, S.; Kang, H. J.; Lynn, J. W.; Lee, Y. S. *Phys. Rev. B* **2008**, *78*, 220405.

[244] Katsufuji, T.; Hwang, H. Y.; Cheong, S.-W. *Phys. Rev. Lett.* **2000**, *84*, 1998.

[245] McQueen, T. M.; West, D. V.; Muegge, B.; Huang, Q.; Noble, K.; Zandenberg, H. W.; Cava, R. J. *J. Phys. Condens. Matt.* **2008**, *20*, 235210.

[246] Torigoe, S. et al. *Phys. Rev. B* **2016**, *93*, 085109.

[247] Blaha, P.; Singh, D. J.; Schwarz, K. *Phys. Rev. Lett.* **2004**, *93*, 216403.

[248] Hanasaki, N.; Watanabe, K.; Ohtsuka, T.; Kézsmárki, I.; Iguchi, S.; Miyasaka, S.; Tokura, Y. *Phys. Rev. Lett.* **2007**, *99*, 086401.

[249] Khaliullin, G.; Maekawa, S. *Phys. Rev. Lett.* **2000**, *85*, 3950.

[250] Nakatsuji, S. et al. *Science* **2012**, *336*, 559–563.

[251] Christy, A. G. *Acta Crystall. B* **1995**, *51*, 753–757.

[252] Wdowik, U. D.; Koza, M. M.; Chatterji, T. *Phys. Rev. B* **2012**, *86*, 174305.

[253] Iliev, M. N.; Abrashev, M. V.; Lee, H.-G.; Popov, V. N.; Sun, Y. Y.; Thomsen, C.; Meng, R. L.; Chu, C. W. *Phys. Rev. B* **1998**, *57*, 2872–2877.

[254] Araya-Rodriguez, E.; Ramos, A. Y.; Tolentino, H. C. N.; Granado, E.; Oseroff, S. B. *J. Magn. Magn. Mater.* **2001**, *233*, 88–90.

[255] Souza, R. A.; Souza-Neto, N. M.; Ramos, A. Y.; Tolentino, H. C. N.; Granada, E. *Phys. Rev. B* **2004**, *70*, 214426.

[256] Thygesen, P. M. M.; Paddison, J. A. M.; Zhang, R.; Beyer, K. A.; Chapman, K. W.; Playford, H. Y.; Tucker, M. G.; Keen, D. A.; Hayward, M. A.; Goodwin, A. L. *Phys. Rev. Lett.* **2017**, *118*, 067201.

[257] Keimer, B.; Casa, D.; Ivanov, A.; Lynn, J. W.; Zimmermann, M. V.; Hill, J. P.; Gibbs, D.; Taguchi, Y.; Tokura, Y. *Phys. Rev. Lett.* **2000**, *85*, 3946–3949.

[258] Sartbaeva, A.; Wells, S. A.; Thorpe, M. F.; Božin, E.; Billinge, S. J. L. *Phys. Rev. Lett.* **2007**, *99*, 155503.

[259] Goodwin, A. L.; Tucker, M. G.; Cope, E. R.; Dove, M. T.; Keen, D. A. *Phys. Rev. B* **2005**, *72*, 214304.

[260] Wright, A. P.; Palmer, H. M.; Anderson, P. A.; Greaves, C. *J. Mater. Chem.* **2002**, *12*, 978–982.

[261] Parsons, T. G.; D'Hondt, H.; Hadermann, J.; Hayward, M. A. *Chem. Mater.* **2009**, *21*, 5527–5538.

[262] Ritter, C.; Ibarra, M. R.; De Teresa, J. M.; Algarabel, P. A.; Marquina, C.; Blasco, J.; Garcia, J.; Oseroff, S.; Cheong, S.-W. *Phys. Rev. B* **1997**, *56*, 8902.

[263] O'Keeffe, M.; Hyde, B. G. *Acta Crystall. B* **1977**, *33*, 3802–3813.

[264] Palmer, D. C. SingleCrystal version 2.3. 2015.

[265] Tucker, M. G.; Squires, M. P.; Dove, M. T.; Keen, D. A. *J. Phys. Condens. Matt.* **2000**, *13*, 403.

[266] Platero-Prats, A. E.; Mavradonakis, A.; Gallington, L. C.; Liu, Y.; Hupp, J. T.; Farha, O. K.; Cramer, C. J.; Chapman, K. W. *J. Am. Chem. Soc.* **2016**, *138*, 4178–4185.

[267] Corr, S. A.; Shoemaker, D. P.; Melot, B. C.; Seshadri, R. *Phys. Rev. Lett.* **2010**, *105*, 056404.

[268] Palmer, H. M.; Snedden, A.; Wright, A. J.; Greaves, C. *Chem. Mater.* **2006**, *18*, 1130–1133.

[269] Welberry, T. R.; Weber, T. *Crystallogr. Rev.* **2016**, *22*, 2–78.

[270] Wang, J.-S.; Swendsen, R. H.; Kotecký, *Phys. Rev. B* **1990**, *42*, 2465–2474.

[271] Soper, A. K. *Chem. Phys.* **1996**, *2002*, 295–306.

[272] Huang, Q.; Lynn, J. W.; Erwin, R. W.; Santoro, A.; Dender, D. C.; Smolyaninova, V. N.; Ghosh, K.; Greene, R. L. *Phys. Rev. B* **2000**, *61*, 8895.

[273] Lija, K. J.; Shanmukharao, S. S.; Thomas, S.; Ganesan, V.; Al-Harthi, S.; Liebig, A.; Albrecht, M.; Anantharaman, M. R. *J. Appl. Phys.* **2014**, *116*, 213701.

[274] Jin, S.; Tiefel, T. H.; McCormack, M.; Fastnacht, R. A.; Ramesh, R.; Chen, L. H. *Science* **1994**, *264*, 413–415.

[275] Radaelli, P. G.; Cox, D. E.; Marezio, M.; Cheong, S. W. *Phys. Rev. B* **1997**, *55*, 3015–3023.

[276] Hwang, H. Y.; Cheong, S.-W.; Radaelli, P. G.; Marezio, M.; Batlogg, B. *Phys. Rev. Lett.* **1995**, *75*, 914–917.

[277] Rodriguez, E. E.; Proffen, T.; Rhyne, J. J.; Mitchell, J. F. *Phys. Rev. B* **2005**, *71*, 104430.

[278] Rodríguez-Carvajal, J.; Daoud-Aladine, A.; Pinsard-Gaudart, L.; Fernández-Díaz, M. T.; Revcolevschi, A. *Physica B* **2002**, *320*, 6.

[279] Laiho, R.; Lisunov, K. G.; Lähderanta, E.; Petronko, P.; Salminen, J.; Stamov, V. N.; Zakhalinskii, V. S. *J. Phys. Condens. Matt.* **2000**, *12*, 5751–5764.

[280] Subías, G.; García, J.; Blasco, J.; Sánchez, M. C.; Proietti, M. G. *J. Phys. Condens. Matt.* **2002**, *14*, 5017–5033.

[281] Juhás, P.; Farrow, C. L.; Yang, X.; Knox, K. R.; Billinge, S. J. L. *Acta Crystall. A* **2015**, *71*, 562–568.

[282] Rao, C. N. R.; Cheetham, A. K.; Mahesh, R. *Chem. Mater.* **1996**, *8*, 2421–2432.

[283] Daoud-Aladine, A.; Rodríguez-Carvajal, J.; Pinsard-Gaudart, L.; Fernández-Díaz, M. T.; Revcolevschi, A. *Appl. Phys. A* **2001**, *74*, 1758.

[284] García, J.; Sánchez, M. C.; Blasco, J.; Subías, G.; Proietti, M. G. *J. Phys. Condens. Matt.* **2001**, *13*, 3243–3256.

[285] Dabrowski, B.; Dybzinski, R.; Bukowski, Z.; Chmaissem, O.; Jorgensen, J. D. *J. Solid State Chem.* **1999**, *146*, 448.

[286] Terashita, H.; Neumeier, J. J. *Phys. Rev. B* **2005**, *71*, 134402.

[287] Biotteau, G.; Hennion, M.; Moussa, F.; Rodríguez-Carvajal, J.; Pinsard, L.; Revcolevschi, A.; Mukovskii, Y. M.; Shulyatev, D. *Phys. Rev. B* **2001**, *64*, 104421.

[288] Yi, T.; Gao, S.; Qi, X.; Zhu, Y.; Cheng, F.; Ma, B.; Huang, Y.; Liao, C.; Yan, C. *J. Phys. Chem. Solids.* **2000**, *61*, 1407–1413.

[289] Lynn, J. W.; Erwin, R. W.; Borchers, J. A.; Huang, Q.; Santoro, A. *Phys. Rev. Lett.* **1996**, *76*, 4046.

[290] Kim, D.; Revaz, B.; Zink, B. L.; Hellman, F.; Rhyne, J. J.; Mitchell, J. F. *Phys. Rev. B* **2002**, *89*, 227202.

[291] Kolthoff, I. M.; Belcher, R. *Volumetric Analysis*; Interscience, New York, 1957.

[292] Frandsen, B. A.; Yang, X.; Billinge, S. J. L. *Acta Crystall. A* **2014**, *70*, 3–11.

[293] Khlifi, M.; Bejar, M.; EL Sadek, O.; Dhahri, E.; Ahmed, M. A.; Hlil, E. K. *J. Alloys Compd.* **2011**, *509*, 7410–7415.

[294] Adams, C. P.; Lynn, J. W.; Smolyaninova, V. N.; Biswas, A.; Greene, R. L.; Ratcliff, W.; Cheong, S.-W.; Mukovskii, Y. M.; Shulyatev, D. A. *Phys. Rev. B* **2004**, *70*, 134414.

[295] Huang, Q.; Santoro, A.; Lynn, J. W.; Erwin, R. W.; Borchers, J. A.; Peng, J. L.; Ghosh, K.; Greene, R. L. *Phys. Rev. B* **1998**, *58*, 2684–2691.

[296] Jirák, Z.; Haldová, E.; Kaman, O.; Knížek, K.; Maryško, M.; Pollert, E. *Phys. Rev. B* **2010**, *81*, 024403.

[297] Pissas, M.; Margiolaki, I.; Papavassiliou, G.; Stamopoulos, D.; Argyriou, D. *Phys. Rev. B* **2005**, *72*, 064425.

[298] Cliffe, M. J.; Dove, M. T.; Drabold, D. A.; Goodwin, A. L. *Phys. Rev. Lett.* **2010**, *104*, 125501.

[299] Billinge, S. J. L.; Levin, I. *Science* **2007**, *316*, 561–565.

[300] Božin, E.; Mallikas, C. D.; Souvatzis, P.; Proffen, T.; Spaldin, N. A.; Kanatzidis, M. G.; Billinge, S. J. L. *Science* **2010**, *330*, 1660–1663.

[301] Weber, T.; Simonov, A. *Z. Kristallogr.* **2012**, *227*, 238–247.

[302] Egami, T.; Dmowski, W. *Z. Kristallogr.* **2012**, *227*, 233–237.

[303] Dmowski, W.; Vakhrushev, S. B.; Jeong, I.-K.; Hehlen, M. P.; Trouw, F.; Egami, T. *Phys. Rev. Lett.* **2008**, *100*, 137602.

Appendix A

A1 Obtained values from Rietveld refinement of $Y_2Mo_2O_7$

All the obtained values from the combined neutron+X-ray Rietveld refinement of $Y_2Mo_2O_7$.

Table A1.1: Anisotropic ADPs from combined neutron+X-ray Rietveld refinement at various temperatures.

T/K	R_{wp}/%	a/Å	U_{11}(Y)	U_{12}(Y)	U_{11}(Mo)	U_{12}(Mo)	U_{11}(O1)	U_{22}(O1)	U_{23}(O1)	U_{11}(O2)	x(O1)
5	4.15	10.2136(3)	0.400(13)	-0.080(18)	0.94(2)	0.70(3)	1.20(3)	0.62(2)	0.05(3)	0.37(3)	0.3381(4)
10	4.08	10.2128(3)	0.407(13)	-0.091(18)	0.95(2)	0.71(3)	1.24(3)	0.63(2)	0.04(3)	0.36(3)	0.3380(4)
15	4.15	10.2133(3)	0.407(13)	-0.082(18)	0.95(2)	0.69(3)	1.22(3)	0.64(2)	0.04(3)	0.39(3)	0.3370(4)
20	4.09	10.2133(3)	0.400(13)	-0.078(18)	0.930(19)	0.68(3)	1.22(3)	0.61(2)	0.06(3)	0.35(3)	0.3380(4)
25	4.05	10.2133(3)	0.410(13)	-0.104(17)	0.937(19)	0.68(3)	1.21(3)	0.64(2)	0.04(3)	0.36(3)	0.3379(4)
30	4.08	10.2133(3)	0.415(13)	-0.093(18)	0.94(2)	0.71(3)	1.21(3)	0.62(2)	0.06(3)	0.37(3)	0.3380(4)
35	4.11	10.2133(3)	0.424(13)	-0.086(18)	0.916(19)	0.67(3)	1.19(3)	0.64(2)	0.05(3)	0.38(3)	0.3370(4)
40	4.08	10.2134(3)	0.409(13)	-0.090(18)	0.951(19)	0.70(3)	1.23(3)	0.63(2)	0.06(3)	0.35(3)	0.3380(4)
50	4.21	10.2135(3)	0.414(13)	-0.092(18)	0.94(2)	0.68(3)	1.20(3)	0.65(2)	0.06(3)	0.36(3)	0.3380(4)
60	4.51	10.2124(3)	0.421(14)	-0.076(19)	0.92(2)	0.62(3)	1.19(3)	0.64(2)	0.05(3)	0.37(3)	0.3381(4)
70	4.34	10.2119(3)	0.442(14)	-0.085(19)	0.92(2)	0.66(3)	1.24(3)	0.63(2)	0.04(3)	0.38(3)	0.3381(4)
80	4.44	10.2124(3)	0.440(14)	-0.099(19)	0.93(2)	0.66(3)	1.21(3)	0.63(2)	0.04(3)	0.38(3)	0.3381(4)
90	4.50	10.2135(3)	0.455(14)	-0.101(19)	0.93(2)	0.67(3)	1.26(3)	0.63(2)	0.06(3)	0.38(3)	0.3380(4)
100	4.57	10.2147(3)	0.464(14)	-0.091(19)	0.91(2)	0.63(3)	1.21(3)	0.65(2)	0.04(3)	0.37(3)	0.3381(4)
110	4.46	10.2156(3)	0.466(14)	-0.103(19)	0.92(2)	0.66(3)	1.24(3)	0.63(2)	0.05(3)	0.37(3)	0.3380(4)
120	4.41	10.2165(3)	0.472(14)	-0.074(19)	0.91(2)	0.61(3)	1.26(3)	0.63(2)	0.05(3)	0.40(3)	0.3380(4)
130	4.25	10.2182(3)	0.491(14)	-0.096(19)	0.933(19)	0.64(3)	1.25(3)	0.66(2)	0.07(3)	0.39(3)	0.3380(4)
140	4.33	10.2194(3)	0.495(14)	-0.101(19)	0.92(2)	0.62(3)	1.25(3)	0.65(2)	0.06(3)	0.39(3)	0.3380(4)
150	4.26	10.2225(3)	0.518(14)	-0.108(19)	0.92(2)	0.62(3)	1.27(3)	0.68(2)	0.12(3)	0.40(3)	0.3379(4)
160	4.37	10.2216(3)	0.524(14)	-0.105(19)	0.93(2)	0.64(3)	1.27(3)	0.67(2)	0.10(3)	0.42(3)	0.3379(4)
170	4.42	10.2219(3)	0.525(14)	-0.111(19)	0.92(2)	0.61(3)	1.28(3)	0.69(2)	0.10(3)	0.40(3)	0.3380(4)
180	4.23	10.2233(3)	0.539(14)	-0.108(19)	0.915(19)	0.59(3)	1.28(3)	0.69(2)	0.10(3)	0.38(3)	0.3379(4)
200	4.30	10.2264(3)	0.595(15)	-0.124(19)	0.95(2)	0.58(3)	1.38(3)	0.72(2)	0.10(3)	0.45(3)	0.3379(4)
220	4.32	10.2281(3)	0.609(15)	-0.12(2)	0.93(2)	0.54(3)	1.37(3)	0.73(2)	0.11(3)	0.47(3)	0.3379(4)
240	4.44	10.2320(3)	0.628(15)	-0.14(2)	0.896(19)	0.50(3)	1.34(3)	0.75(2)	0.13(3)	0.45(3)	0.3378(4)
260	4.37	10.2353(3)	0.650(15)	-0.15(2)	0.93(2)	0.52(3)	1.39(4)	0.78(2)	0.16(3)	0.48(3)	0.3378(4)
280	4.13	10.2390(3)	0.690(16)	-0.15(2)	0.899(19)	0.47(3)	1.40(3)	0.78(2)	0.17(3)	0.49(3)	0.3379(4)
298	3.96	10.2412(3)	0.673(16)	-0.15(2)	0.856(18)	0.43(3)	1.40(4)	0.78(2)	0.17(3)	0.48(3)	0.3378(4)

Appendix B

B1 Obtained values for Rietveld refinement of $LaMnO_3$

Table B1.1: Refined parameters from X-ray Rietveld refinements across temperatures for $LaMnO_3$.

T/K	R_{wp}/%	a	b	c	x_{La}	y_{La}	x_{O1}	y_{O1}	x_{O2}	y_{O2}	z_{O2}	U_{iso}(La)/Å^2	U_{iso}(Mn)/Å^2	U_{iso}(O1)/Å^2	U_{iso}(O2)/Å^2
523	1.95	5.7313(4)	7.7602(5)	5.5643(3)	0.75(2)	0.52(3)	0.83(10)	0.04241(14)	0.9935(4)	0.4874(12)		0.0706(19)	0.3031(12)	0.0396(9)	0.7297(16)
533	1.94	5.7300(4)	7.7629(5)	5.5648(4)	0.77(2)	0.47(3)	0.72(10)	0.04232(14)	0.9935(4)	0.4892(12)		0.0705(19)	0.3040(12)	0.0401(9)	0.7287(16)
543	1.94	5.7286(4)	7.7650(5)	5.5654(4)	0.78(2)	0.48(3)	0.73(10)	0.04206(14)	0.9936(4)	0.4893(12)		0.0704(19)	0.3038(12)	0.0401(9)	0.7287(16)
553	1.94	5.7271(4)	7.7675(5)	5.5661(4)	0.79(2)	0.48(3)	0.74(10)	0.04176(14)	0.9936(4)	0.4894(12)		0.070(2)	0.3036(12)	0.0401(9)	0.7289(16)
563	1.94	5.7256(4)	7.7701(5)	5.5668(4)	0.80(2)	0.50(3)	0.75(10)	0.04148(14)	0.9936(4)	0.4895(12)		0.070(2)	0.3034(12)	0.0401(9)	0.7288(16)
573	1.94	5.7240(4)	7.7726(5)	5.5674(4)	0.80(2)	0.51(3)	0.76(10)	0.04117(14)	0.9937(4)	0.4896(13)		0.070(2)	0.3032(13)	0.0401(9)	0.7289(16)
583	1.93	5.7214(4)	7.7739(5)	5.5671(4)	0.82(2)	0.52(3)	0.76(10)	0.04085(14)	0.9938(4)	0.4898(13)		0.070(2)	0.3030(12)	0.0401(9)	0.7291(16)
593	1.93	5.7192(4)	7.7760(5)	5.5673(4)	0.83(2)	0.53(3)	0.77(10)	0.04053(14)	0.9938(4)	0.4897(13)		0.070(2)	0.3028(13)	0.0400(10)	0.7292(16)
603	1.94	5.7169(4)	7.7784(5)	5.5678(4)	0.85(2)	0.54(3)	0.77(10)	0.04020(14)	0.9940(4)	0.4900(13)		0.070(2)	0.3019(13)	0.0401(10)	0.7293(17)
613	1.93	5.7149(4)	7.7812(5)	5.5682(4)	0.85(2)	0.55(3)	0.78(10)	0.03986(14)	0.9940(4)	0.4901(13)		0.070(2)	0.3016(13)	0.0401(10)	0.7293(17)
623	1.93	5.7124(4)	7.7839(5)	5.5686(4)	0.86(2)	0.56(3)	0.79(10)	0.03949(14)	0.9941(4)	0.4902(13)		0.070(2)	0.3013(13)	0.0401(10)	0.7293(17)
633	1.92	5.7097(4)	7.7871(5)	5.5690(4)	0.87(2)	0.57(3)	0.81(10)	0.03910(14)	0.9942(4)	0.4903(13)		0.069(2)	0.3010(13)	0.0404(10)	0.7293(17)
643	1.91	5.7066(5)	7.7906(5)	5.5694(4)	0.88(2)	0.58(3)	0.82(10)	0.03866(14)	0.9943(4)	0.4904(13)		0.069(2)	0.3005(13)	0.0405(10)	0.7294(17)
653	1.9	5.7033(5)	7.7950(6)	5.5702(4)	0.89(2)	0.59(3)	0.85(10)	0.03817(15)	0.9943(4)	0.4907(13)		0.068(2)	0.3001(13)	0.0406(10)	0.7295(17)
663	1.89	5.6992(5)	7.8000(6)	5.5708(4)	0.89(2)	0.60(3)	0.87(10)	0.03759(15)	0.9944(4)	0.4909(13)		0.068(2)	0.2994(13)	0.0408(10)	0.7300(17)
673	1.89	5.6937(5)	7.8068(6)	5.5718(4)	0.93(2)	0.62(3)	0.88(10)	0.03688(15)	0.9946(5)	0.4913(13)		0.067(2)	0.2983(14)	0.0413(10)	0.7297(17)
683	2.08	5.6814(6)	7.8213(7)	5.5743(4)	0.95(2)	0.65(3)	0.89(11)	0.03535(17)	0.9950(5)	0.4936(14)		0.065(3)	0.2964(16)	0.0436(11)	0.7309(19)
693	2.56	5.6194(12)	7.8781(19)	5.5779(12)	1.06(3)	0.70(3)	1.01(14)	0.0286(2)	0.9955(8)	0.4982(19)		0.060(4)	0.288(3)	0.046(2)	0.733(3)
703	2.41	5.6023(14)	7.886(3)	5.5833(18)	1.09(2)	0.72(3)	1.28(14)	0.0255(2)	0.9959(8)	0.493(2)		0.061(5)	0.278(3)	0.046(2)	0.732(3)
713	2.46	5.5991(15)	7.890(3)	5.585(2)	1.10(2)	0.72(3)	1.30(14)	0.0248(2)	0.9960(8)	0.493(2)		0.061(5)	0.276(3)	0.046(2)	0.732(3)
723	2.48	5.5984(15)	7.893(3)	5.586(2)	1.11(2)	0.73(3)	1.31(14)	0.0244(2)	0.9961(9)	0.493(2)		0.061(5)	0.275(3)	0.046(3)	0.732(3)
733	2.5	5.5973(16)	7.895(3)	5.587(3)	1.13(3)	0.74(3)	1.33(14)	0.0240(2)	0.9962(9)	0.494(2)		0.061(5)	0.274(3)	0.046(3)	0.732(3)
743	2.48	5.5950(17)	7.896(4)	5.589(3)	1.13(3)	0.75(3)	1.34(14)	0.0236(2)	0.9962(9)	0.494(2)		0.061(5)	0.273(3)	0.046(3)	0.732(3)
753	2.49	5.5942(17)	7.897(4)	5.591(3)	1.15(2)	0.75(3)	1.35(14)	0.0232(2)	0.9963(9)	0.494(2)		0.060(5)	0.272(3)	0.047(3)	0.732(3)
763	2.49	5.5935(18)	7.899(4)	5.591(3)	1.17(2)	0.76(3)	1.36(14)	0.0229(2)	0.9964(10)	0.494(2)		0.060(5)	0.272(3)	0.047(3)	0.732(3)
773	2.49	5.5913(18)	7.897(4)	5.596(3)	1.18(2)	0.77(3)	1.36(14)	0.0225(2)	0.9965(9)	0.494(2)		0.060(5)	0.271(3)	0.047(3)	0.732(3)
783	2.48	5.5911(18)	7.899(4)	5.597(3)	1.20(2)	0.78(3)	1.37(14)	0.0222(2)	0.9966(10)	0.495(2)		0.060(5)	0.271(3)	0.047(3)	0.733(3)
793	2.48	5.5912(19)	7.900(4)	5.59893)	1.21(2)	0.79(3)	1.38(14)	0.0219(2)	0.9967(10)	0.495(2)		0.059(5)	0.270(3)	0.047(3)	0.733(3)
803	2.47	5.5897(18)	7.897(4)	5.604(3)	1.23(3)	0.80(3)	1.40(14)	0.0216(2)	0.9965(10)	0.494(2)		0.060(5)	0.271(3)	0.047(2)	0.732(3)
813	2.47	5.5901(19)	7.898(4)	5.605(4)	1.24(3)	0.80(3)	1.42(14)	0.0213(2)	0.9966(10)	0.494(2)		0.060(5)	0.270(3)	0.047(2)	0.732(3)
823	2.47	5.5900(19)	7.899(4)	5.605(4)	1.27(3)	0.81(3)	1.42(14)	0.0210(2)	0.9967(10)	0.495(2)		0.059(5)	0.270(3)	0.047(2)	0.733(3)
833	2.46	5.5888(18)	7.898(4)	5.608(4)	1.27(2)	0.82(3)	1.43(14)	0.0208(3)	0.9968(10)	0.495(2)		0.058(5)	0.270(3)	0.047(2)	0.733(3)
843	2.47	5.5889(17)	7.899(4)	5.611(4)	1.28(3)	0.83(3)	1.44(14)	0.0205(3)	0.9968(10)	0.495(2)		0.058(5)	0.270(3)	0.047(2)	0.733(3)
853	2.47	5.5892(17)	7.901(4)	5.612(4)	1.30(3)	0.84(3)	1.47(15)	0.0202(3)	0.9968(10)	0.494(2)		0.057(5)	0.270(3)	0.047(2)	0.733(3)
863	2.46	5.5891(16)	7.899(4)	5.616(3)	1.31(3)	0.85(3)	1.49(15)	0.0199(3)	0.9969(10)	0.495(2)		0.057(5)	0.270(3)	0.047(2)	0.732(3)
873	2.45	5.5894(17)	7.900(4)	5.616(3)	1.32(3)	0.86(3)	1.51(15)	0.0197(3)	0.9968(10)	0.494(2)		0.058(5)	0.270(4)	0.047(2)	0.732(3)
883	2.44	5.5863(12)	7.891(2)	5.627(2)	1.34(3)	0.87(3)	1.56(14)	0.0193(3)	0.9966(9)	0.495(2)		0.057(4)	0.270(4)	0.046(2)	0.732(3)
893	2.44	5.5853(12)	7.891(2)	5.628(2)	1.35(3)	0.88(3)	1.56(14)	0.0191(3)	0.9966(9)	0.495(2)		0.058(4)	0.270(4)	0.0461(19)	0.732(3)
903	2.43	5.5853(11)	7.891(2)	5.6279(19)	1.36(3)	0.88(3)	1.57(14)	0.0188(3)	0.9967(9)	0.495(3)		0.058(4)	0.270(4)	0.0460(19)	0.732(3)
913	2.43	5.5856(11)	7.892(2)	5.6283(19)	1.37(3)	0.89(3)	1.58(14)	0.0186(3)	0.9967(9)	0.495(3)		0.058(4)	0.270(4)	0.0460(19)	0.732(3)
923	2.42	5.5861(11)	7.892(2)	5.6293(19)	1.39(3)	0.90(3)	1.59(14)	0.0183(3)	0.9968(9)	0.495(3)		0.057(4)	0.270(4)	0.0461(19)	0.732(3)
933	2.42	5.5867(11)	7.893(2)	5.6302(19)	1.40(3)	0.90(3)	1.60(14)	0.0181(3)	0.9968(9)	0.495(3)		0.057(4)	0.270(4)	0.0461(19)	0.7319(4)
943	2.41	5.5870(11)	7.895(2)	5.6311(19)	1.42(3)	0.92(3)	1.61(14)	0.0178(3)	0.9969(9)	0.495(3)		0.057(4)	0.270(4)	0.0462(19)	0.732(4)
953	2.41	5.5869(11)	7.895(2)	5.6315(19)	1.43(3)	0.92(3)	1.61(14)	0.0176(3)	0.9970(9)	0.495(3)		0.057(4)	0.270(4)	0.0463(19)	0.732(4)
963	2.41	5.5866(11)	7.896(2)	5.6323(19)	1.44(3)	0.93(3)	1.61(15)	0.0172(3)	0.9970(9)	0.495(3)		0.057(4)	0.268(4)	0.0464(19)	0.732(4)
973	2.39	5.5827(10)	7.8948(18)	5.6376(15)	1.46(2)	0.93(3)	1.61(14)	0.0158(3)	0.9974(9)	0.496(3)		0.056(4)	0.267(4)	0.0471(18)	0.734(4)
983	2.44	5.5740(8)	7.8964(15)	5.6476(10)	1.48(2)	0.93(3)	1.60(15)	0.0116(3)	0.9980(10)	0.501(4)		0.059(4)	0.262(5)	0.0471(17)	0.737(5)
993	2.43	5.5706(9)	7.9035(17)	5.6479(11)	1.50(3)	0.94(3)	1.64(15)	0.0090(6)	0.9982(11)	0.508(5)		0.060(4)	0.257(6)	0.0470(18)	0.741(7)
1003	2.36	5.5683(11)	7.913(2)	5.6447(13)	1.51(2)	0.96(3)	1.57(14)	0.0062(8)	0.9982(11)	0.521(8)		0.061(5)	0.248(8)	0.046(2)	0.749(13)
1013	2.31	5.5673(12)	7.919(2)	5.6422(13)	1.54(2)	0.97(3)	1.26(16)	0.0021(10)	0.9978(12)	0.548(5)		0.072(5)	0.244(8)	0.039(2)	0.754(10)
1023	2.29	5.5661(13)	7.921(3)	5.6407(13)	1.53(2)	0.96(3)	1.19(16)	0.0016(10)	0.9878(13)	0.549(5)		0.076(5)	0.243(8)	0.038(2)	0.755(9)

B1.1 Plot of Rietveld refinements of $LaMnO_3$

Rietveld refinement at every 50 K of X-ray data collected for $LaMnO_3$ sample.

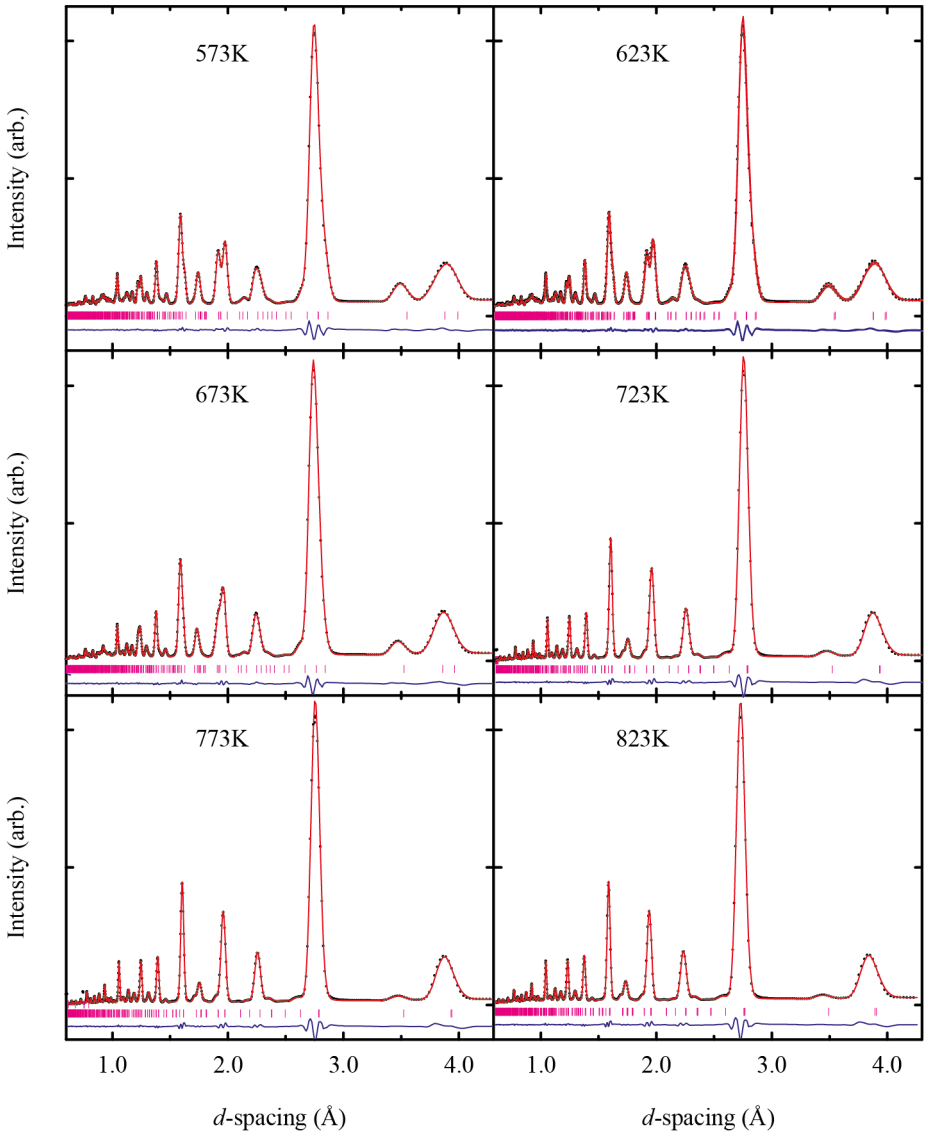


Figure B1.1: Rietveld refinements of $LaMnO_3$ covering the temperature range 573-823 K.

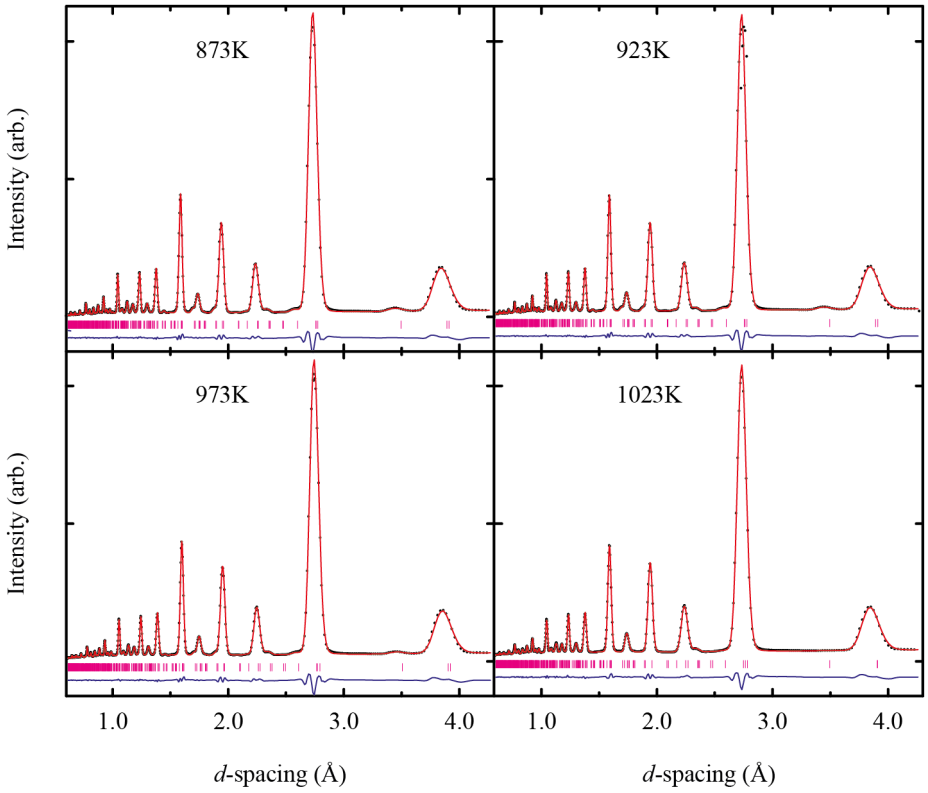


Figure B1.2: Rietveld refinements of $LaMnO_3$ covering the temperature range 823-1023 K.

B2 PDFGui fits of the three models examined across temperature of $LaMnO_3$

The PDF refinement fits to used generate the figure 4.11. Each fit to data for the three $r_{\max}$ values. The $R_{\mathrm{wp}}/\%$ value for each refinement is presented for each plot.

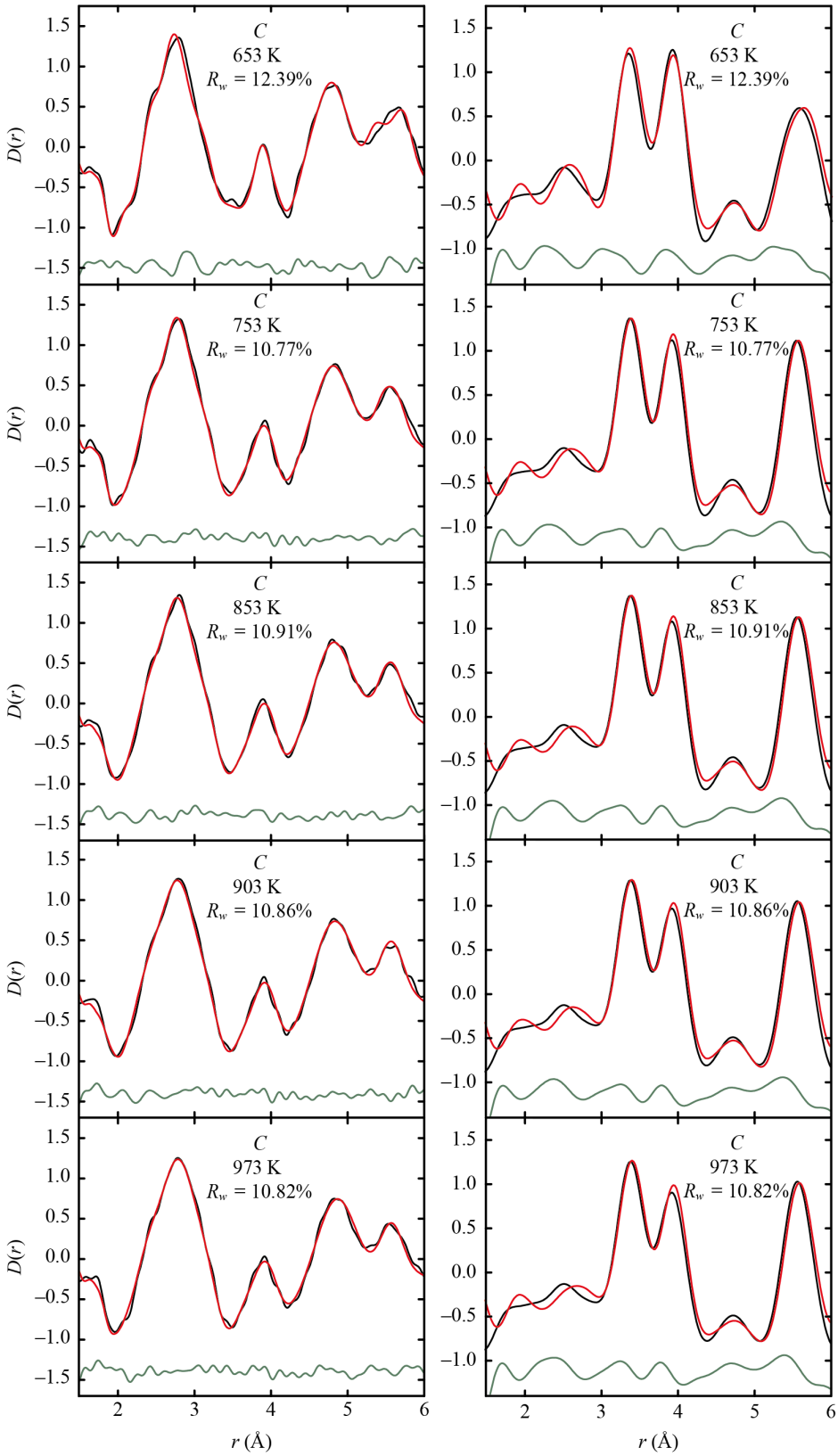


Figure B2.3: Combined PDFgui fits to data using the *C*-type model for neutron (left) and X-ray (right) data. The models were refined using $r_{\max}$=6.0 Å.

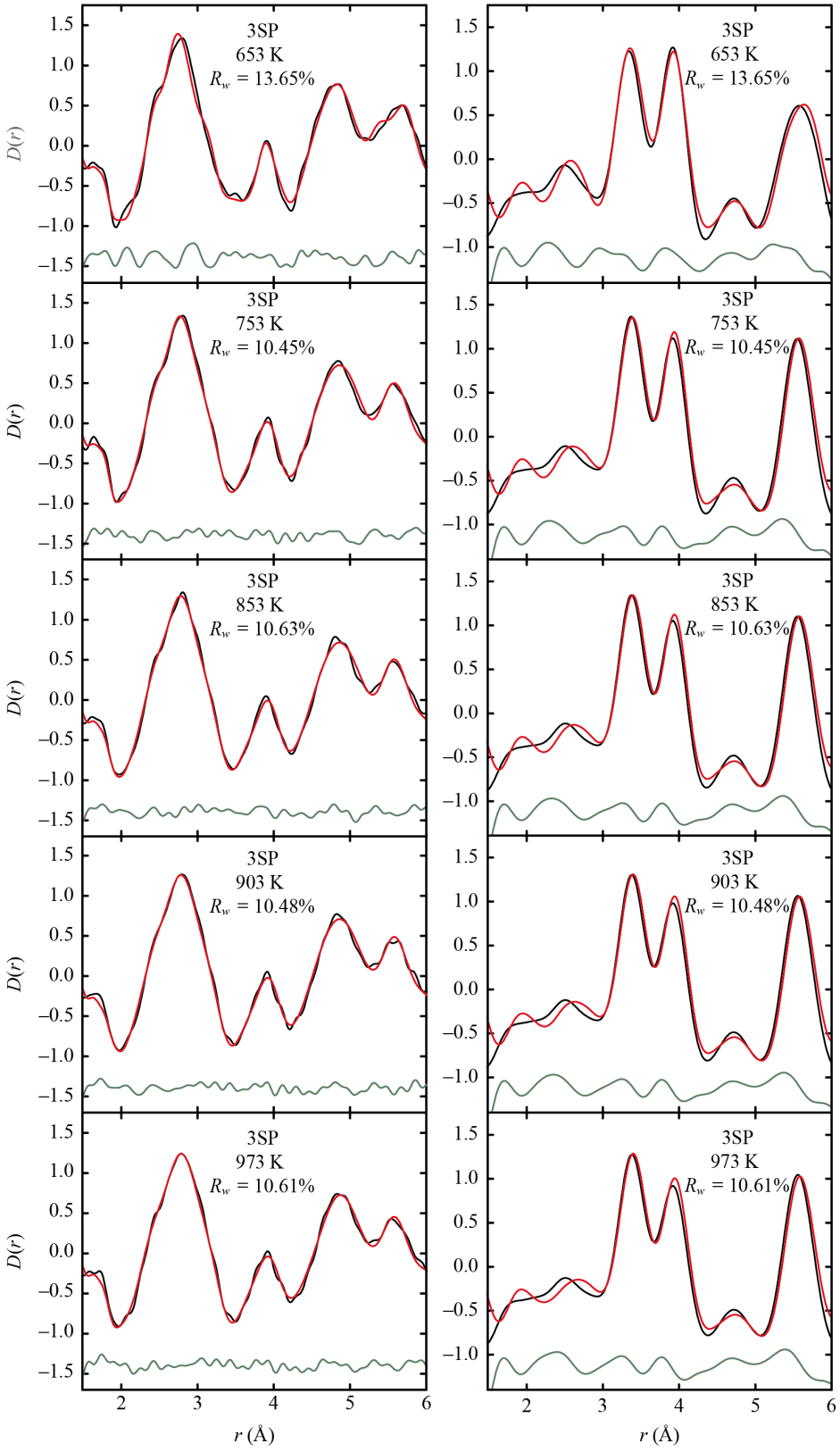


Figure B2.4: Combined PDFgui fits to data using the 3SP model for neutron (left) and X-ray (right) data. The models were refined using r_{max}=6.0 Å.

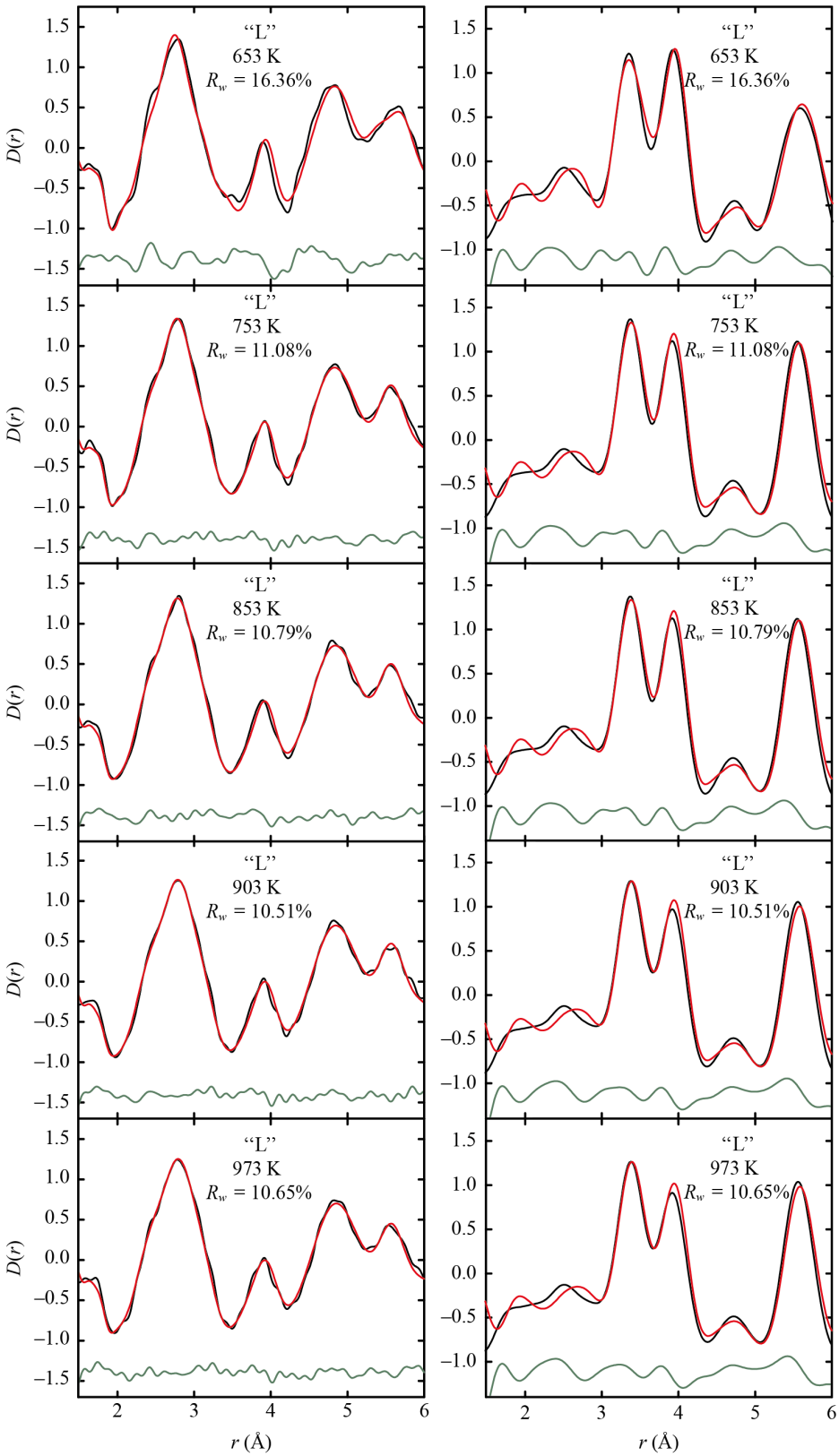


Figure B2.5: Combined PDFgui fits to data using the *L*-type model for neutron (left) and X-ray (right) data. The models were refined using r_{max}=6.0 Å.

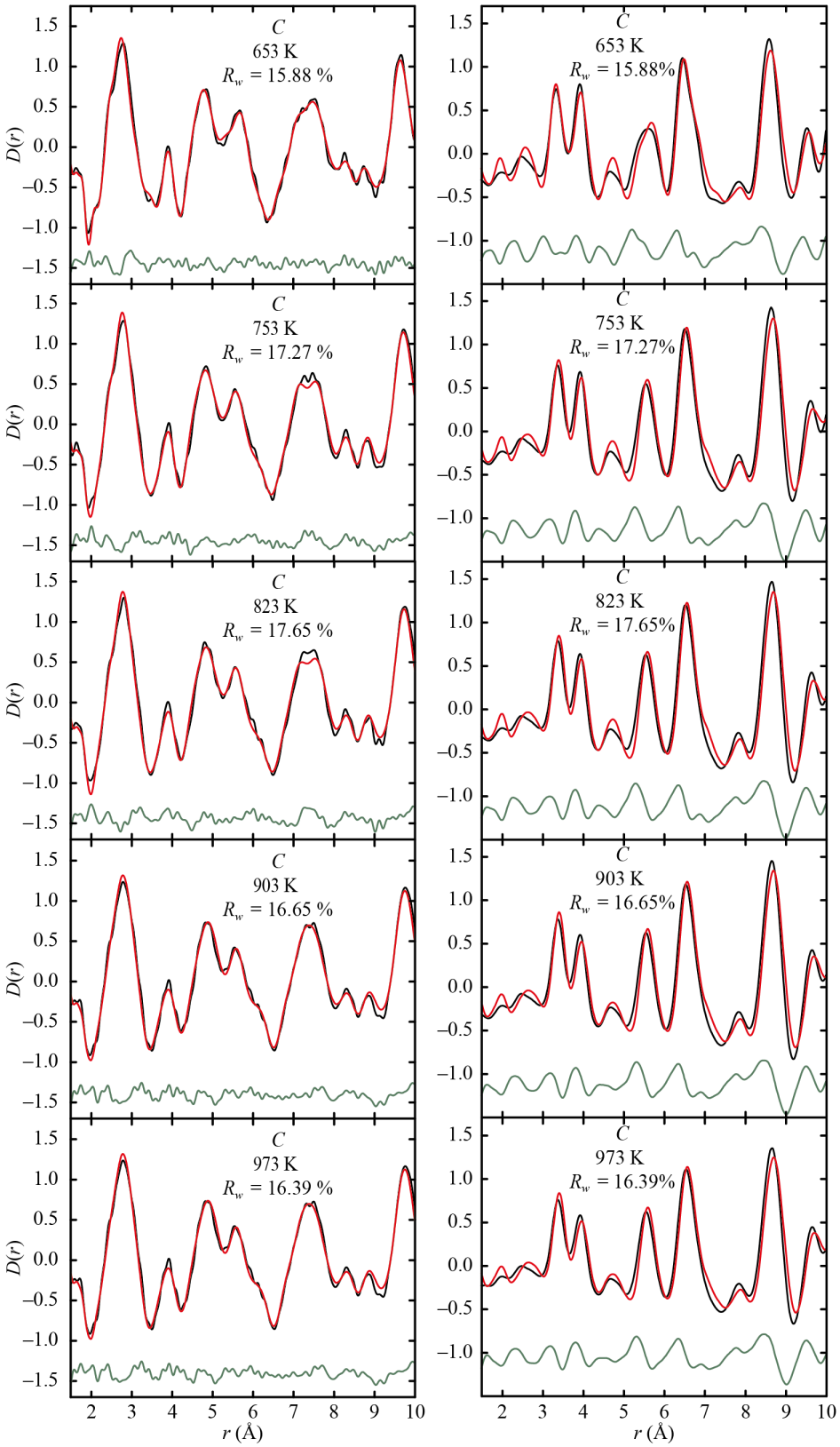


Figure B2.6: Combined PDFgui fits to data using the C-type model for neutron (left) and X-ray (right) data. The models were refined using $r_{\max}$=10.0 Å.

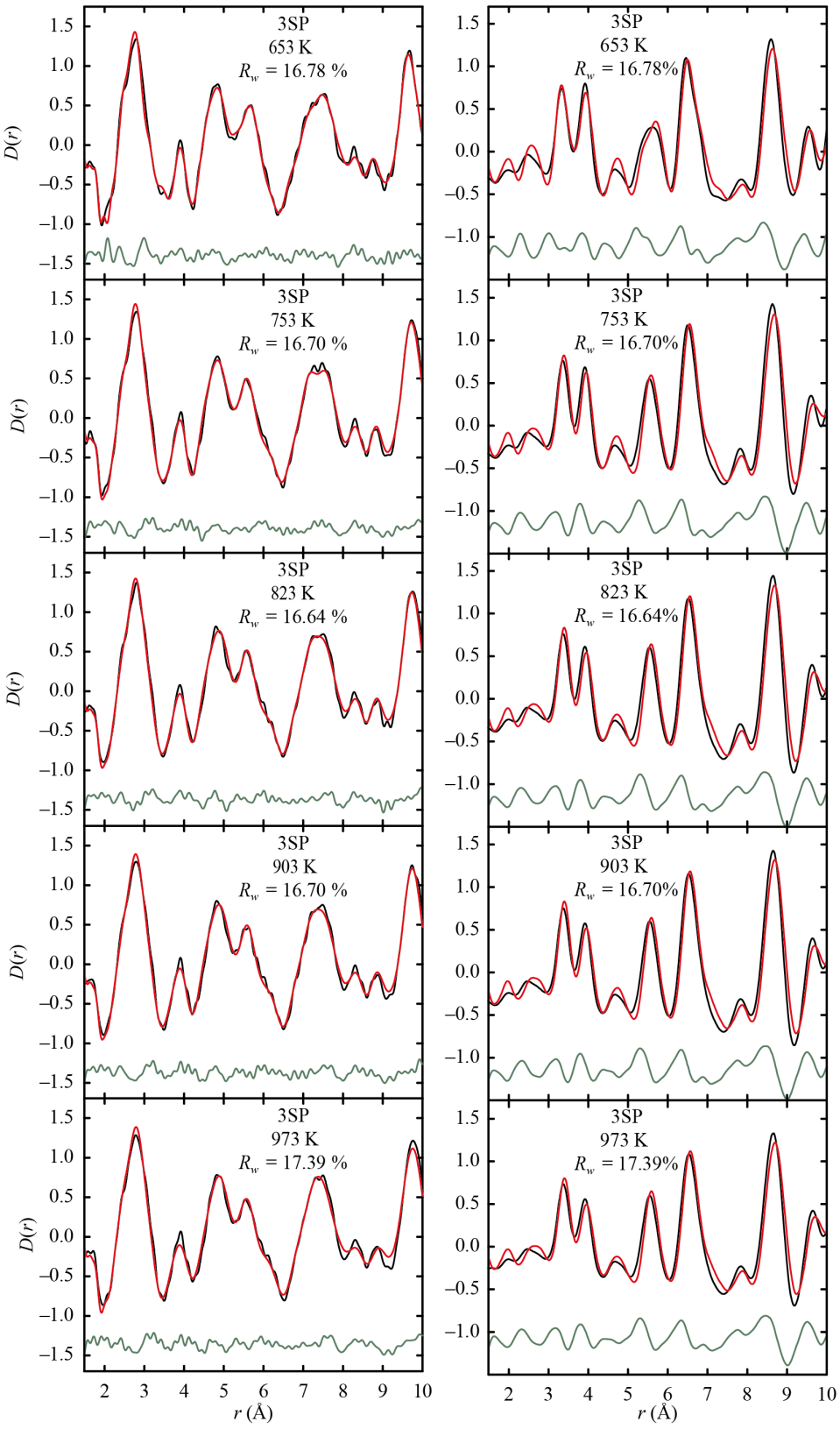


Figure B2.7: Combined PDFgui fits to data using the 3SP model for neutron (left) and X-ray (right) data. The models were refined using r_{max}=10.0 Å.

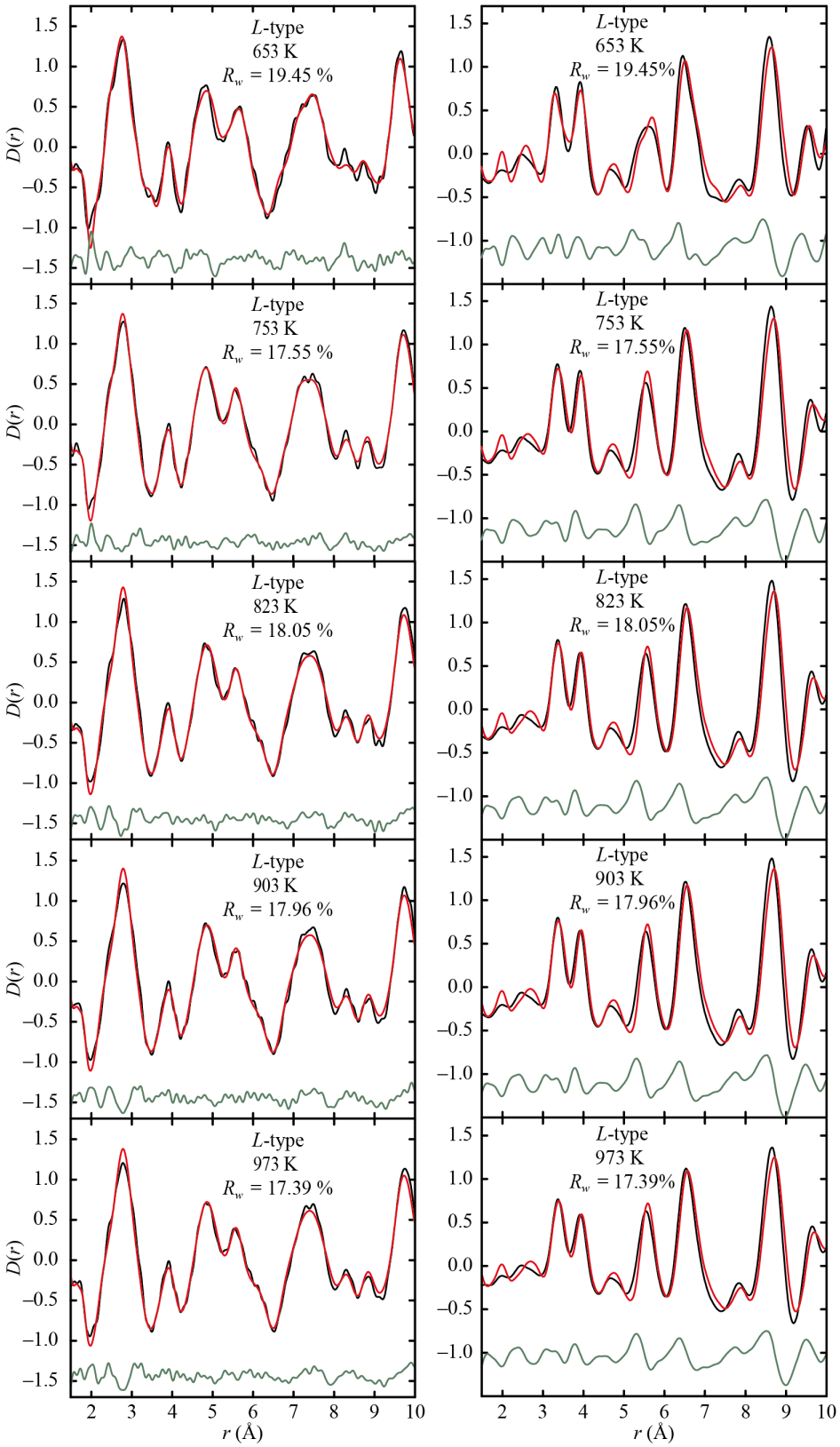


Figure B2.8: Combined PDFgui fits to data using the *L*-type model for neutron (left) and X-ray (right) data. The models were refined using r_{max}=10.0 Å.

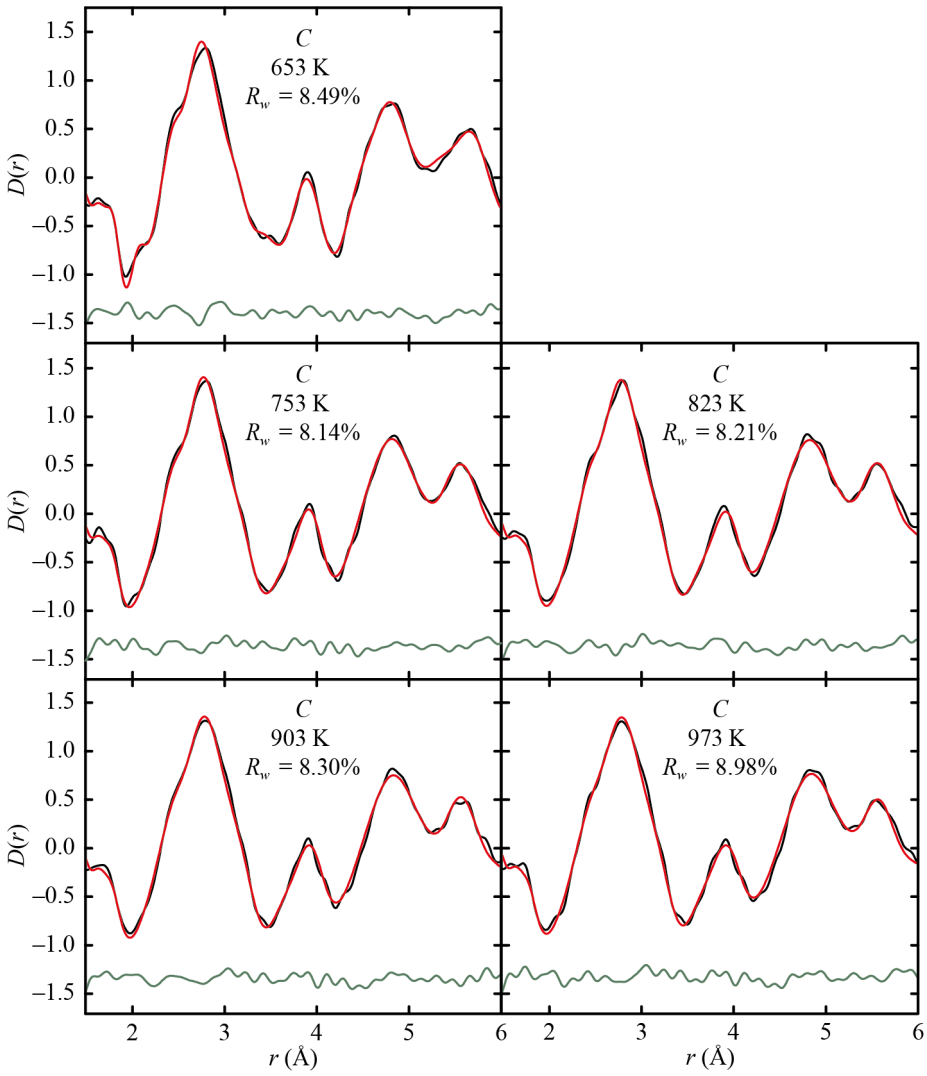


Figure B2.9: PDFgui fits to neutron data using the C-type model across temperature. The models were refined using $r_{\max}$=6.0 Å.

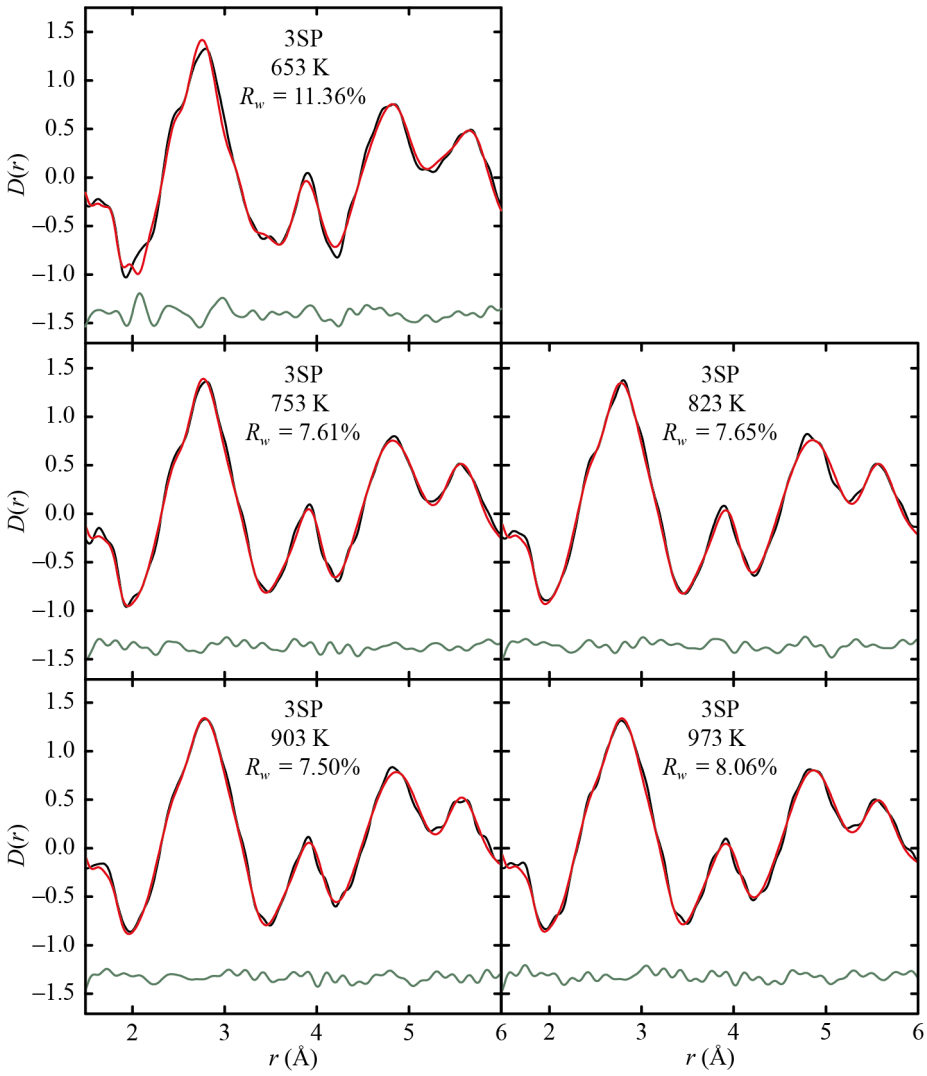


Figure B2.10: PDFgui fits to neutron data using the 3SP model across temperature. The models were refined using $r_{\max}$=6.0 Å.

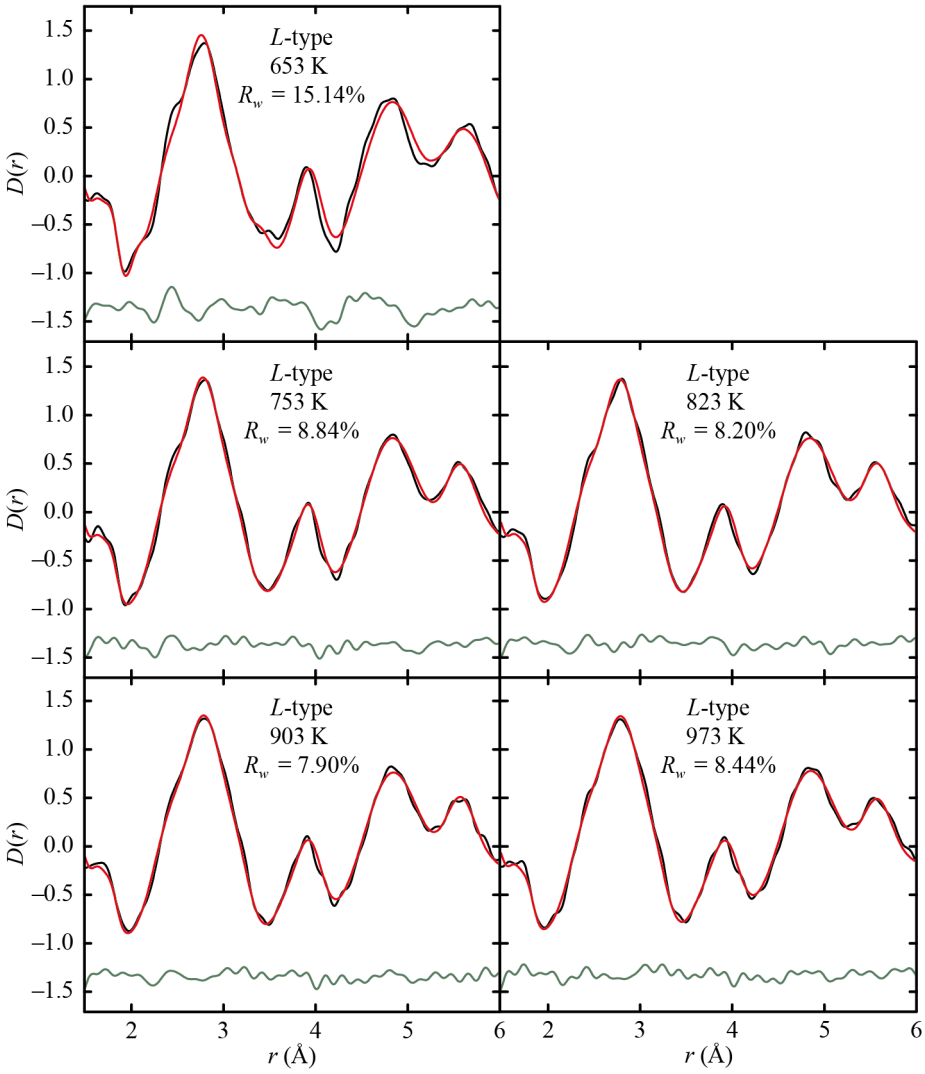


Figure B2.11: PDFgui fits to neutron data using the *L*-type model across temperature. The models were refined using $r_{\max}$=6.0 Å.

Appendix C

C1 Obtained values and plots from Rietveld refinements of $La_{1-x}Ca_xMnO_3$

All the obtained parameters from the Rietveld refinements of $La_{1-x}Ca_xMnO_3$ across temperature from neutron and X-ray data.

Table C1.2: Refined parameters from X-ray Rietveld refinements as a function of temperature for $La_{0.5}Ca_{0.5}MnO_3$.

T/K	R_{wp}/%	a	b	c	U_{iso}(La)/Å^2	U_{iso}(Mn)/Å^2	U_{iso}(O1)/Å^2	U_{iso}(O2)/Å^2	x_{La}	y_{La}	x_{O1}	y_{O1}	x_{O2}	y_{O2}	z_{O2}
105	2.42911	5.4168(12)	7.6453(17)	5.4291(16)	0.372(18)	0.269(18)	0.2(3)	0.62(15)	0.0161(3)	−0.002(1)	0.982(2)	0.586(2)	0.225(3)	0.9768(13)	0.771(3)
110	2.43027	5.4170(12)	7.6455(17)	5.4290(16)	0.379(18)	0.272(18)	0.2(3)	0.63(15)	0.0161(3)	−0.002(1)	0.982(2)	0.586(2)	0.224(3)	0.9769(13)	0.769(3)
115	2.43203	5.4170(12)	7.6455(17)	5.4290(16)	0.384(18)	0.274(18)	0.2(3)	0.62(15)	0.0161(3)	−0.002(1)	0.982(2)	0.586(2)	0.224(3)	0.9770(13)	0.770(3)
120	2.43373	5.4171(12)	7.6455(17)	5.4291(16)	0.387(18)	0.277(18)	0.2(3)	0.64(15)	0.0160(3)	−0.002(1)	0.982(2)	0.586(2)	0.225(3)	0.9770(13)	0.770(3)
125	2.43307	5.4172(12)	7.6455(17)	5.4293(16)	0.391(18)	0.281(19)	0.2(3)	0.64(15)	0.0160(3)	−0.002(1)	0.982(2)	0.586(3)	0.224(3)	0.9769(13)	0.770(3)
130	2.44524	5.4174(12)	7.6456(17)	5.4294(16)	0.394(18)	0.28(2)	0.2(3)	0.63(15)	0.0160(3)	−0.002(1)	0.982(2)	0.587(2)	0.224(3)	0.9771(13)	0.770(3)
135	2.44287	5.4175(12)	7.6457(17)	5.4295(17)	0.395(18)	0.28(2)	0.2(3)	0.63(15)	0.0160(3)	−0.002(1)	0.982(2)	0.587(2)	0.224(3)	0.9771(13)	0.770(3)
140	2.445	5.4178(13)	7.6456(17)	5.4297(17)	0.401(19)	0.286(19)	0.2(3)	0.64(15)	0.0159(3)	−0.002(1)	0.982(2)	0.587(2)	0.225(3)	0.9772(13)	0.770(3)
145	2.43841	5.4180(13)	7.6459(17)	5.4299(17)	0.401(19)	0.289(19)	0.3(3)	0.63(15)	0.0160(3)	−0.003(1)	0.982(2)	0.587(2)	0.224(3)	0.9772(13)	0.770(3)
150	2.44792	5.4182(13)	7.6460(17)	5.4301(17)	0.407(19)	0.289(19)	0.2(3)	0.65(16)	0.0159(3)	−0.002(1)	0.981(2)	0.587(2)	0.225(3)	0.9773(13)	0.769(3)
155	2.4495	5.4184(13)	7.6461(17)	5.4303(17)	0.417(19)	0.288(19)	0.2(3)	0.64(16)	0.0159(3)	−0.002(1)	0.981(2)	0.587(2)	0.224(3)	0.9775(13)	0.770(3)
160	2.46499	5.4185(13)	7.6462(17)	5.4304(17)	0.421(19)	0.288(19)	0.2(3)	0.64(16)	0.0159(3)	−0.002(1)	0.981(2)	0.588(2)	0.224(3)	0.9777(13)	0.770(3)
165	2.46746	5.4187(13)	7.6464(18)	5.4306(17)	0.411(19)	0.294(19)	0.2(3)	0.62(16)	0.0159(3)	−0.003(1)	0.981(2)	0.588(2)	0.224(3)	0.9777(13)	0.769(3)
170	2.46327	5.4188(13)	7.6467(18)	5.4308(17)	0.422(19)	0.292(19)	0.3(3)	0.64(16)	0.0159(3)	−0.003(1)	0.981(2)	0.588(3)	0.224(3)	0.9777(14)	0.770(3)
175	2.47298	5.4190(13)	7.6467(18)	5.4311(18)	0.43(2)	0.29(2)	0.3(3)	0.64(16)	0.0158(3)	−0.003(1)	0.981(3)	0.588(3)	0.224(3)	0.9778(14)	0.769(3)
180	2.48058	5.4192(13)	7.6469(18)	5.4313(17)	0.43(2)	0.29(2)	0.3(3)	0.65(16)	0.0158(3)	−0.003(1)	0.981(3)	0.588(3)	0.224(3)	0.9779(14)	0.769(3)
185	2.48141	5.4193(13)	7.6471(17)	5.4314(17)	0.44(2)	0.30(2)	0.3(3)	0.64(16)	0.0158(3)	−0.003(1)	0.981(3)	0.588(3)	0.224(3)	0.9779(14)	0.770(3)
190	2.489	5.4193(13)	7.6474(17)	5.4317(17)	0.43(2)	0.30(2)	0.3(3)	0.64(16)	0.0158(3)	−0.003(1)	0.981(3)	0.589(3)	0.225(4)	0.9781(14)	0.771(3)
195	2.49589	5.4195(13)	7.6476(17)	5.4319(17)	0.43(2)	0.30(2)	0.3(3)	0.64(16)	0.0158(3)	−0.003(1)	0.981(3)	0.589(3)	0.224(3)	0.9781(14)	0.770(3)
200	2.51239	5.4196(13)	7.6478(16)	5.4320(17)	0.44(2)	0.30(2)	0.3(3)	0.62(16)	0.0157(3)	−0.003(1)	0.981(3)	0.589(3)	0.224(3)	0.9781(14)	0.769(3)
205	2.52998	5.4199(13)	7.6481(16)	5.4323(17)	0.44(2)	0.31(2)	0.3(3)	0.61(16)	0.0156(3)	−0.003(1)	0.981(3)	0.589(3)	0.224(3)	0.9783(14)	0.770(3)
210	2.5184	5.4202(14)	7.6486(16)	5.4319(18)	0.45(2)	0.31(2)	0.3(3)	0.64(16)	0.0156(3)	−0.003(1)	0.981(3)	0.589(3)	0.224(4)	0.9783(14)	0.770(3)
215	2.51538	5.4204(14)	7.6490(17)	5.4318(18)	0.45(2)	0.31(2)	0.3(3)	0.64(16)	0.0156(3)	−0.003(1)	0.981(3)	0.589(3)	0.224(4)	0.9784(14)	0.769(3)
220	2.51138	5.4207(14)	7.6494(18)	5.4317(18)	0.46(2)	0.31(2)	0.3(3)	0.63(16)	0.0155(3)	−0.003(1)	0.981(3)	0.589(3)	0.224(3)	0.9785(14)	0.769(3)
225	2.51075	5.4207(14)	7.6494(18)	5.4316(18)	0.46(2)	0.31(2)	0.3(3)	0.64(16)	0.0155(3)	−0.003(1)	0.981(3)	0.589(3)	0.224(4)	0.9785(14)	0.769(4)
230	2.49849	5.4208(14)	7.6502(19)	5.4319(18)	0.47(2)	0.32(2)	0.2(3)	0.67(16)	0.0154(3)	−0.003(1)	0.981(3)	0.588(3)	0.225(4)	0.9785(14)	0.770(4)
235	2.49195	5.4209(14)	7.6505(19)	5.4321(18)	0.47(2)	0.32(2)	0.3(3)	0.70(16)	0.0154(3)	−0.003(1)	0.981(3)	0.588(3)	0.225(4)	0.9785(14)	0.769(4)
240	2.48524	5.4210(14)	7.6507(19)	5.4322(18)	0.49(2)	0.32(2)	0.3(3)	0.72(17)	0.0153(3)	−0.003(1)	0.981(3)	0.588(3)	0.225(4)	0.9785(14)	0.769(4)
245	2.48799	5.4210(14)	7.651(2)	5.4324(19)	0.48(2)	0.33(2)	0.3(3)	0.72(17)	0.0153(3)	−0.003(1)	0.981(3)	0.588(3)	0.224(3)	0.9786(14)	0.768(4)
250	2.47962	5.4212(14)	7.651(2)	5.4326(19)	0.47(2)	0.33(2)	0.3(3)	0.74(17)	0.0153(3)	−0.003(1)	0.981(3)	0.588(3)	0.225(4)	0.9785(14)	0.769(4)
255	2.47795	5.4212(14)	7.6514(19)	5.4330(19)	0.48(2)	0.33(2)	0.4(3)	0.77(17)	0.0152(3)	−0.003(1)	0.981(3)	0.588(3)	0.226(4)	0.9785(14)	0.770(4)
260	2.47545	5.4213(14)	7.6518(19)	5.4333(19)	0.48(2)	0.34(2)	0.4(3)	0.75(17)	0.0152(3)	−0.003(1)	0.981(3)	0.588(3)	0.225(4)	0.9784(14)	0.769(4)
265	2.46599	5.4214(14)	7.6520(19)	5.4337(19)	0.49(2)	0.34(2)	0.4(3)	0.75(17)	0.0151(3)	−0.003(1)	0.981(3)	0.588(3)	0.225(4)	0.9784(14)	0.769(4)
270	2.46079	5.4212(14)	7.6522(19)	5.4345(19)	0.49(2)	0.34(2)	0.5(3)	0.76(17)	0.0151(3)	−0.0030(9)	0.981(3)	0.588(3)	0.225(4)	0.9783(14)	0.769(4)
275	2.46925	5.4215(14)	7.6525(19)	5.4345(19)	0.49(2)	0.34(2)	0.5(3)	0.76(17)	0.0151(4)	−0.0030(9)	0.981(3)	0.588(3)	0.225(4)	0.9783(14)	0.769(4)
280	2.45941	5.4217(14)	7.6528(19)	5.4348(19)	0.49(2)	0.34(2)	0.5(3)	0.75(16)	0.0150(4)	−0.0030(9)	0.980(3)	0.588(3)	0.224(4)	0.9784(14)	0.769(4)
285	2.46266	5.4220(14)	7.6534(19)	5.4347(19)	0.50(2)	0.34(2)	0.5(3)	0.74(17)	0.0150(4)	−0.0030(9)	0.980(3)	0.588(3)	0.224(4)	0.9785(14)	0.768(4)
290	2.4701	5.4224(14)	7.6540(19)	5.4346(19)	0.50(2)	0.33(2)	0.5(3)	0.75(17)	0.0150(4)	−0.0030(9)	0.980(3)	0.589(3)	0.225(4)	0.9787(14)	0.769(4)
295	2.47809	5.4228(15)	7.655(2)	5.434(2)	0.50(2)	0.33(2)	0.6(3)	0.74(17)	0.0150(4)	−0.003(1)	0.980(3)	0.589(3)	0.225(4)	0.9787(14)	0.769(4)
300	2.47432	5.4231(15)	7.655(2)	5.434(2)	0.51(2)	0.33(2)	0.693)	0.74(17)	0.0150(4)	−0.003(1)	0.980(3)	0.589(3)	0.225(4)	0.9788(14)	0.768(4)

Table C1.3: Refined parameters from neutron Rietveld refinements as a function of temperatures for $La_{0.5}Ca_{0.5}MnO_3$.

T/K	R_{wp}/%	a	b	c	U_{iso}(La)/Å^2	U_{iso}(Mn)/Å^2	U_{iso}(O1)/Å^2	U_{iso}(O2)/Å^2	x_{La}	y_{La}	x_{O1}	y_{O1}	x_{O2}	y_{O2}	z_{O2}
5	3.25	5.418(4)	5.418(4)	7.653(5)	5.432(4)	0.512(16)	0.385(19)	0.69(2)	0.740(18)	0.0166(3)	0.0027(6)	0.9925(6)	0.5648(4)	0.2251(3)	0.96763(18) 0.00018 0.7728(3)
10	3.62	5.418(4)	5.418(4)	7.654(6)	5.433(4)	0.532(18)	0.38(2)	0.73(3)	0.714(19)	0.0159(4)	0.0028(7)	0.9919(7)	0.5647(5)	0.2248(3)	0.9676(2) 0.0002 0.7733(3)
20	3.74	5.419(4)	5.419(4)	7.655(6)	5.433(4)	0.527(19)	0.35(2)	0.72(3)	0.72(2)	0.0163(4)	0.0026(7)	0.9924(7)	0.5647(5)	0.2250(3)	0.9674(2) 0.00021 0.7725(4)
30	3.7	5.420(4)	5.420(4)	7.656(6)	5.434(4)	0.521(19)	0.38(2)	0.68(3)	0.74(2)	0.0163(4)	0.0025(7)	0.9924(7)	0.5642(5)	0.2248(3)	0.9676(2) 0.00021 0.7730(4)
40	3.73	5.420(4)	5.420(4)	7.657(6)	5.435(4)	0.525(19)	0.36(2)	0.71(3)	0.73(2)	0.0166(4)	0.0020(7)	0.9921(7)	0.5645(5)	0.2250(3)	0.9675(2) 0.00021 0.7729(4)
50	3.73	5.420(4)	5.420(4)	7.657(5)	5.434(4)	0.532(19)	0.38(2)	0.69(3)	0.75(2)	0.0165(4)	0.0026(7)	0.9923(7)	0.5647(5)	0.2248(4)	0.9676(2) 0.00021 0.7730(4)
60	3.64	5.420(4)	5.420(4)	7.657(5)	5.435(3)	0.522(18)	0.40(2)	0.69(3)	0.74(2)	0.0162(4)	0.0030(7)	0.9916(6)	0.5646(5)	0.2250(3)	0.9675(2) 0.00021 0.7726(3)
70	3.66	5.420(4)	5.420(4)	7.656(5)	5.434(4)	0.526(18)	0.40(2)	0.71(3)	0.74(2)	0.0162(4)	0.0026(7)	0.9927(7)	0.5648(5)	0.2249(3)	0.9676(2) 0.00021 0.7730(4)
80	3.67	5.420(4)	5.420(4)	7.656(5)	5.434(4)	0.551(19)	0.37(2)	0.71(3)	0.76(2)	0.0164(4)	0.0027(7)	0.9925(7)	0.5652(5)	0.2250(3)	0.9678(2) 0.00021 0.7730(4)
90	3.56	5.421(4)	5.421(4)	7.657(5)	5.435(4)	0.549(19)	0.39(2)	0.71(3)	0.76(2)	0.0159(4)	0.0031(7)	0.9915(7)	0.5648(5)	0.2250(3)	0.9678(2) 0.00021 0.7727(3)
100	3.61	5.421(4)	5.421(4)	7.658(6)	5.435(4)	0.570(19)	0.39(2)	0.72(3)	0.81(2)	0.0166(4)	0.0025(7)	0.9918(7)	0.5647(5)	0.2250(4)	0.9679(2) 0.00021 0.7731(4)
110	3.62	5.421(4)	5.421(4)	7.658(5)	5.436(4)	0.569(19)	0.39(2)	0.72(3)	0.81(2)	0.0167(4)	0.0032(7)	0.9923(7)	0.5647(5)	0.2248(4)	0.9676(2) 0.00021 0.7729(4)
120	3.58	5.421(4)	5.421(4)	7.658(5)	5.436(4)	0.573(19)	0.44(2)	0.79(3)	0.79(2)	0.0159(4)	0.0029(7)	0.9924(7)	0.5646(5)	0.2252(3)	0.9674(2) 0.00021 0.7726(4)
130	3.53	5.422(4)	5.422(4)	7.658(4)	5.436(3)	0.574(19)	0.44(2)	0.77(3)	0.84(2)	0.0162(4)	0.0023(7)	0.9926(7)	0.5644(5)	0.2249(4)	0.9676(2) 0.00021 0.7729(4)
140	3.55	5.422(4)	5.422(4)	7.658(6)	5.437(4)	0.59(2)	0.43(2)	0.76(3)	0.84(2)	0.0162(4)	0.0030(7)	0.9921(7)	0.5643(5)	0.2248(4)	0.9677(2) 0.00021 0.7729(4)
150	3.6	5.422(5)	5.422(5)	7.658(7)	5.437(5)	0.60(2)	0.43(2)	0.78(3)	0.86(2)	0.0164(4)	0.0027(7)	0.9928(7)	0.5641(5)	0.2248(4)	0.9677(2) 0.00022 0.7731(4)
160	3.53	5.422(4)	5.422(4)	7.658(5)	5.437(4)	0.64(2)	0.42(2)	0.82(3)	0.86(2)	0.0158(4)	0.0029(7)	0.9914(7)	0.5647(5)	0.2254(4)	0.9675(2) 0.00021 0.7728(4)
170	3.49	5.422(4)	5.422(4)	7.658(6)	5.437(4)	0.65(2)	0.45(2)	0.83(3)	0.91(2)	0.0156(4)	0.0018(7)	0.9922(7)	0.5644(5)	0.2251(4)	0.9679(2) 0.00021 0.7729(4)
180	3.55	5.423(4)	5.423(4)	7.659(6)	5.438(4)	0.63(2)	0.46(2)	0.85(3)	0.88(2)	0.0155(4)	0.0030(7)	0.9927(8)	0.5642(5)	0.2252(4)	0.9678(2) 0.00022 0.7731(4)
190	3.47	5.423(5)	5.423(5)	7.659(7)	5.438(5)	0.65(2)	0.46(2)	0.86(3)	0.91(2)	0.0155(4)	0.0020(7)	0.9931(8)	0.5651(5)	0.2251(4)	0.9680(2) 0.00022 0.7728(4)
200	3.53	5.423(4)	5.423(4)	7.659(6)	5.438(5)	0.66(2)	0.47(2)	0.86(3)	0.91(2)	0.0151(5)	0.0020(7)	0.9930(8)	0.5642(5)	0.2249(4)	0.9678(2) 0.00022 0.7730(4)
210	3.44	5.423(4)	5.423(4)	7.659(5)	5.438(4)	0.66(2)	0.49(2)	0.86(3)	0.94(2)	0.0148(4)	0.0019(2)	0.9923(7)	0.5642(5)	0.2250(4)	0.9679(2) 0.00022 0.7726(4)
220	3.47	5.423(4)	5.423(4)	7.660(6)	5.438(4)	0.66(2)	0.47(2)	0.88(3)	0.94(2)	0.0153(4)	0.0024(2)	0.9921(7)	0.5641(5)	0.2253(4)	0.9678(2) 0.00022 0.7724(4)
230	3.44	5.424(4)	5.424(4)	7.661(6)	5.439(4)	0.66(2)	0.47(2)	0.87(3)	0.93(2)	0.0150(4)	0.0027(7)	0.9927(8)	0.5642(5)	0.2253(4)	0.9681(2) 0.00022 0.7730(4)
240	3.37	5.424(5)	5.424(5)	7.661(7)	5.439(5)	0.69(2)	0.45(2)	0.90(3)	0.93(2)	0.0147(5)	0.0022(7)	0.9929(8)	0.5637(5)	0.2254(4)	0.9679(2) 0.00021 0.7726(4)
250	3.42	5.424(4)	5.424(4)	7.663(6)	5.440(4)	0.69(2)	0.47(2)	0.90(3)	0.93(2)	0.0147(5)	0.0028(7)	0.9921(8)	0.5638(5)	0.2255(4)	0.9680(2) 0.00022 0.7727(4)
260	3.34	5.423(3)	5.423(3)	7.662(4)	5.439(3)	0.70(2)	0.46(2)	0.92(3)	0.92(2)	0.0148(4)	0.0022(7)	0.9923(7)	0.5639(5)	0.2255(4)	0.9681(2) 0.00021 0.7726(4)
270	3.36	5.424(4)	5.424(4)	7.663(6)	5.440(4)	0.71(2)	0.50(2)	0.91(3)	0.94(2)	0.0142(5)	0.0020(7)	0.9933(8)	0.5633(5)	0.2255(4)	0.9678(2) 0.00022 0.7724(4)
280	3.29	5.424(4)	5.424(4)	7.664(5)	5.440(4)	0.71(2)	0.47(2)	0.90(3)	0.95(2)	0.0140(5)	0.0020(7)	0.9920(7)	0.5627(5)	0.2254(4)	0.9680(2) 0.00021 0.7724(4)
290	3.34	5.424(4)	5.424(4)	7.665(6)	5.441(4)	0.70(2)	0.49(2)	0.94(3)	0.96(2)	0.0140(5)	0.0013(7)	0.9926(8)	0.5627(5)	0.2256(4)	0.9681(2) 0.00022 0.7725(4)

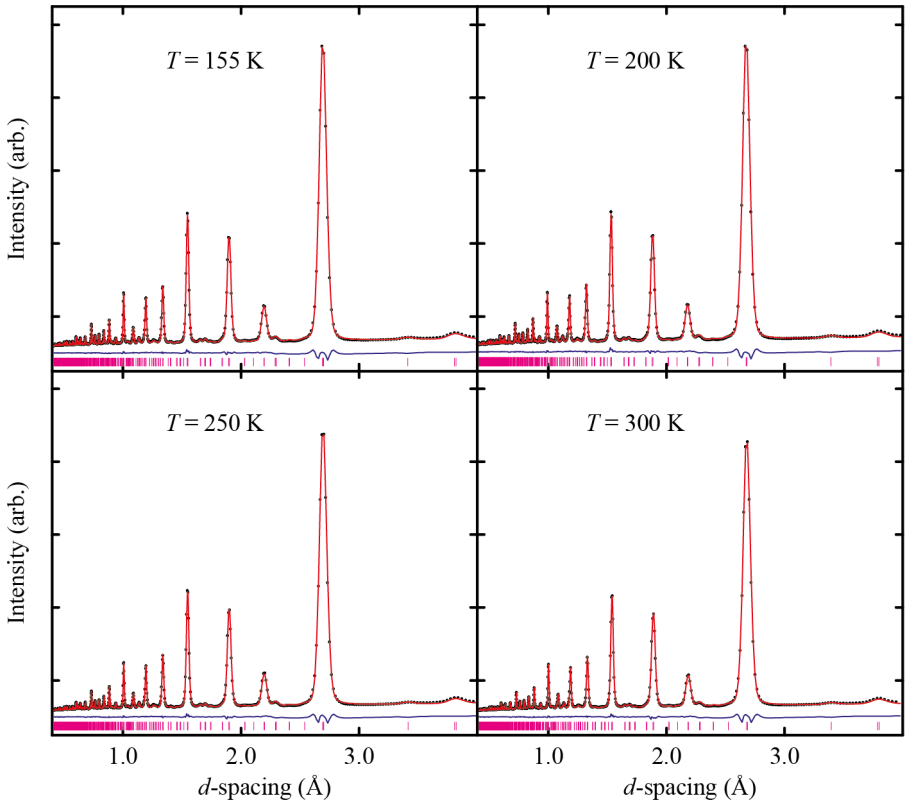


Figure C1.12: Rietveld refinements of $La_{1-x}Ca_xMnO_3$ covering the temperature range 150-300 K.

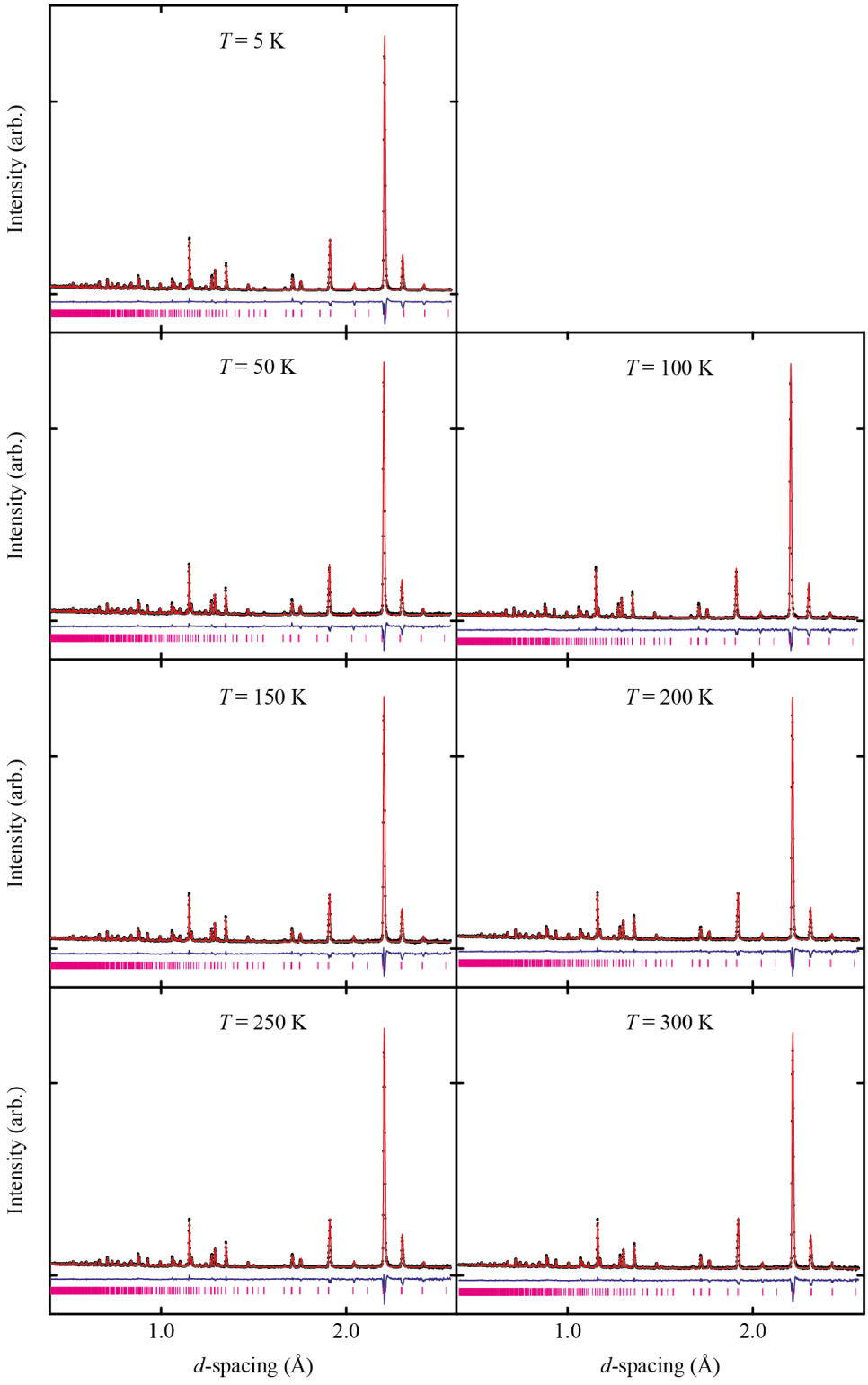


Figure C1.13: Rietveld refinements of $La_{1-x}Ca_xMnO_3$ covering the temperature range 5-300 K.

Publications

Articles written from this thesis are listed below along with the location of the work on which they are based. In addition, articles relating to work carried out during this same time period, but not included in this thesis, are listed.

- *Orbital Dimer Model for Spin-Glass State in $Y_2Mo_2O_7$*
  P. M. M. Thygesen, J. A. M. Paddison, R. Zhang, K. A. Beyer, K. W. Chapman, H. Y. Playford, M. G. Tucker, D. A. Keen, M. A. Hayward, and A. L. Goodwin *Phys. Rev. Lett.* **118** 067201 (2017)
  Chapter 3

- *Local structure study of the orbital order/disorder transition in $LaMnO_3$*

  P. M. M. Thygesen, C. A. Young, E. O. R. Beake, F. D. Romero, L. D. Connor, T. E. Proffen, A. E. Phillips, M. G. Tucker, M. A. Hayward, D. A. Keen, and A. L. Goodwin *Phys. Rev. B* **213** 174107 (2017)
  Chapter 4

- *Exploration of Antiferromagnetic CoO and NiO using Reverse Monte Carlo Total Neutron Scattering Refinement*
  P. J. Saines, L. Timm, M. G. Tucker, D. A. Keen, **P. M. M. Thygesen**, and A. L. Goodwin *Phys. Scr.* **91** 114004 (2016)

- *Control of Multipolar and Orbital order in Perovskite-like $[C(NH_2)_3]Cu_xCd_{1-x}(HCOO)_3$ Metal-Organic Frameworks*
  N. E. Evans, **P. M. M. Thygesen**, H. L. Bostrom, E. M. Reynolds, I. E. Collings, A. E. Phillips, and A. L. Goodwin *J. Am. Chem. Soc.* **138** 9393–9396 (2016)

- *Searching beyond Gd for Magnetocaloric frameworks: Magnetic properties and interactions of the $Ln(HCO_2)_3$ series*
  P. J. Saines, J. A. M. Paddison **P. M. M. Thygesen**, and M. G. Tucker *Mater. Horiz.* **2** 528–535 (2015)

Orbital Dimer Model for the Spin-Glass State in $Y_2Mo_2O_7$

Peter M. M. Thygesen,[1] Joseph A. M. Paddison,[1,2,3,*] Ronghuan Zhang,[1] Kevin A. Beyer,[4] Karena W. Chapman,[4] Helen Y. Playford,[2] Matthew G. Tucker,[2,5,6] David A. Keen,[2] Michael A. Hayward,[1] and Andrew L. Goodwin[1]
[1]*Department of Chemistry, University of Oxford, South Parks Road, Oxford OX1 3QR, United Kingdom*
[2]*ISIS Facility, Rutherford Appleton Laboratory, Harwell Campus, Didcot, Oxfordshire OX11 0QX, United Kingdom*
[3]*School of Physics, Georgia Institute of Technology, 837 State Street, Atlanta, Georgia 30332-0430, USA*
[4]*Advanced Photon Source, Argonne National Laboratory, Argonne, Illinois 60439, USA*
[5]*Diamond Light Source, Chilton, Oxfordshire OX11 0DE, United Kingdom*
[6]*Spallation Neutron Source, Oak Ridge National Laboratory, Oak Ridge, Tennessee 37831, USA*
(Received 9 March 2016; published 8 February 2017)

The formation of a spin glass generally requires that magnetic exchange interactions are both frustrated and disordered. Consequently, the origin of spin-glass behavior in $Y_2Mo_2O_7$—in which magnetic Mo^{4+} ions occupy a frustrated pyrochlore lattice with minimal compositional disorder—has been a longstanding question. Here, we use neutron and x-ray pair-distribution function (PDF) analysis to develop a disorder model that resolves apparent incompatibilities between previously reported PDF, extended x-ray-absorption fine structure spectroscopy, and NMR studies, and provides a new and physical explanation of the exchange disorder responsible for spin-glass formation. We show that Mo^{4+} ions displace according to a local "two-in–two-out" rule on each Mo_4 tetrahedron, driven by orbital dimerization of Jahn-Teller active Mo^{4+} ions. Long-range orbital order is prevented by the macroscopic degeneracy of dimer coverings permitted by the pyrochlore lattice. Cooperative O^{2-} displacements yield a distribution of Mo–O–Mo angles, which in turn introduces disorder into magnetic interactions. Our study demonstrates experimentally how frustration of atomic displacements can assume the role of compositional disorder in driving a spin-glass transition.

DOI: 10.1103/PhysRevLett.118.067201

In a spin-glass transition, spins freeze into a metastable arrangement without long-range order [1–4]. It is generally accepted that two conditions must be satisfied for a spin-glass transition to occur: interactions between spins must be disordered and these interactions must also be frustrated or competing [2,3,5,6]. In canonical spin glasses—e.g., dilute magnetic alloys such as $Cu_{1-x}Mn_x$ [7] and site-disordered crystals such as Fe_2TiO_5 [8]—the nature of the structural disorder that causes disorder in magnetic interactions is well understood. However, spin-glass behavior is also observed in apparently well-ordered crystals where the geometry of the magnetic lattice alone can generate frustration [9–11]. Here, the mechanism of spin-glass formation poses an important challenge for theory [12–14]. The prototypical material that shows this anomalous behavior is $Y_2Mo_2O_7$—a system with apparently unremarkable levels of structural disorder, but with thermodynamic properties indistinguishable from canonical spin glasses [15].

The structure and dynamics of $Y_2Mo_2O_7$ have been extensively studied. The conventional nature of the spin-glass transition (freezing temperature $T_f = 22$ K [16]) has been shown by measurements including nonlinear susceptibility [16,17], specific heat [18,19], ac susceptibility [20], thermoremanent magnetization [21–23], inelastic neutron scattering [24], muon-spin rotation [25], and neutron spin echo [26,27]. Neutron-diffraction measurements show that the average structure is well described by the ordered pyrochlore model (space group $Fd\bar{3}m$) both below and above T_f [28,29]. In this structure, the average positions of magnetic Mo^{4+} ions describe a network of corner-sharing tetrahedra [Fig. 1(a)]. There are two inequivalent O sites, O1 and O2; each Mo^{4+} is octahedrally coordinated by O1 [Fig. 1(b)], and each Y^{3+} is coordinated by six O1 and two O2 [Fig. 1(c)]. Each pair of Mo neighbors is bridged by a

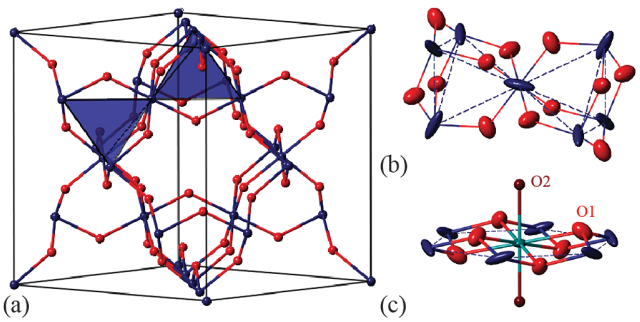


FIG. 1. (a) Crystal structure of $Y_2Mo_2O_7$ generated from the model of Ref. [29]: Mo in dark blue, O1 in red, and Y and O2 omitted for clarity. (b) Coordination environment of Mo^{4+} shown with displacement ellipsoids at 50% probability. Prolate Mo^{4+} displacement ellipsoids point along the local-$\langle 111 \rangle$ axes (towards the centers of adjacent tetrahedra). (c) Coordination environment of Y^{3+} (green).

 © 2017 American Physical Society

single O1, forming the main magnetic superexchange pathway. The degree of site mixing and O nonstoichiometry is too small to measure [28,29] and is calculated to be minimal (∼1%) [30].

A plausible explanation for spin-glass formation invokes local Mo^{4+} displacements to generate variation in exchange interactions [31]. Arguably the clearest experimental signature of anomalies on the Mo site is its large and anisotropic atomic displacement parameter obtained from Rietveld refinement to powder neutron-diffraction data [29] [Fig. 1(b)]. Consistent with this, an extended x-ray-absorption fine structure spectroscopy (EXAFS) study (Mo and Y K edges) showed a large static variance in Mo–Mo distances, $\sigma^2_{\rm stat} = 0.026(5)$ Å^2 [32]. Two ^{89}Y NMR studies revealed a distribution of Y environments that was interpreted in terms of a local distortion of the Mo site [31,33], an explanation supported by muon-spin rotation experiments [34]. There is a problem with this proposal, however: a state-of-the-art study using neutron pair-distribution function (PDF) analysis found no evidence for local Mo displacements [29]. Instead, it showed variation in Y–O1 distances consistent with a local splitting of the O1 site—a result interpreted as contradicting the EXAFS study [29,32].

In this Letter, we argue that a disorder model that reconciles these apparently contradictory results can explain the exchange disorder responsible for spin-glass formation in $Y_2Mo_2O_7$. We critically reassess the key assumption [29] that the absence of obvious Mo–Mo splitting in the PDF implies that local Mo displacements do not occur. We show that the PDF is actually better represented by a model in which Mo ions are displaced, consistent with EXAFS [32], and these Mo displacements are coupled to O1 displacements. In our model, Mo displacements obey a "two-in–two-out" rule on each Mo_4 tetrahedron. This can be interpreted as the formation of Mo–Mo dimers, driven by orbital interactions between Jahn-Teller active Mo^{4+} ions. These orbital dimers do not show long-range order because the pyrochlore lattice supports a macroscopic degeneracy of dimer coverings; this same type of degeneracy is responsible for, e.g., magnetic disorder in spin-ice materials [35]. Because Mo–Mo dimer coverings are disordered and coupled with O1 displacements, there is a disordered arrangement of Mo–O1–Mo bond angles, which introduces sufficient variation in magnetic exchange interactions [12,13] to explain spin-glass formation.

Our Letter is structured as follows. After describing our experiments, we first reproduce the best fit to PDF data obtained previously [29]. We then describe the simplest orbital-dimer model, which is a crystalline approximant to a more complex disordered state. We demonstrate that this model yields a better fit to PDF data than the previous model [29], for the same number of structural parameters. Finally, we show that our model is consistent with previous experimental studies [31–33] and with theoretical requirements for spin-glass formation.

A polycrystalline sample of $Y_2Mo_2O_7$ (8 g) was prepared by firing stoichiometric amounts of Y_2O_3 and MoO_2 for 12 h at 1400 °C using CO/CO_2 as buffer gas [36]. The value of T_f determined from measurements of the field-cooled and zero-field-cooled magnetization was consistent with the previously reported value (22 K) [37]. Neutron and x-ray total-scattering data were collected on the POLARIS instrument at ISIS [38] and the 11-ID-B beam line at the APS, respectively. All data were corrected for background scattering and absorption using the GUDRUN program [39] (based on the ATLAS routines [40]). The reciprocal-space range used was $1.0 \le Q \le 25$ Å^{-1} for the x-ray data and $0.7 \le Q \le 45$ Å^{-1} for the neutron data. This excludes most of the diffuse magnetic contribution to the neutron data, which peaks at 0.4 Å^{-1} [24] and was barely observed above background in our high-Q-optimized measurement. All PDF analysis was performed using the PDFGUI program [41] by refinement to both x-ray and neutron PDFs over the range $0 < r < 10$ Å, with a weighting factor chosen so that both data sets contributed approximately equally.

In the previous PDF study [29], the local structure of $Y_2Mo_2O_7$ was modeled using the conventional $Fd\bar{3}m$ structure with O1 sites partitioned equally between two sites (O1a, O1b) generated from the fractional coordinates $(x, 1/8, 1/8)$ with different x; we call this the "split-site model." We first checked that we could reproduce the fit obtained in Ref. [29] using this model and our new data. We found that stable refinement required the use of constraints on the anisotropic displacement parameters for the O1a/O1b sites—hence, we have marginally fewer parameters than Ref. [29] (see Ref. [42]). Nevertheless, our fit for the split-site model is essentially indistinguishable from that in Ref. [29] [Figs. 2(a) and 2(b)]; values of refined parameters are compared in Table I. We conclude that our sample, data, and refinement procedures are consistent with Ref. [29].

We now propose an alternative model of static disorder in $Y_2Mo_2O_7$. Our starting point is the observation that Mo atomic displacement parameters are strongly elongated along the local-$\langle 111 \rangle$ axes in the average-structure model [Fig. 1(b)]. This suggests that Mo^{4+} ions are locally displaced towards or away from the centers of Mo_4 tetrahedra. Physically reasonable mechanisms for Mo displacements, such as charge polarization and orbital interactions [44], require that displacements are not random but coupled. There are two basic possibilities for this coupling. It may require that all Mo on a tetrahedron displace towards its center or all displace away ("four-in–four-out" state); alternatively, it may require that two Mo displace towards the center and two displace away (two-in–two-out state). The former displacement pattern is necessarily ordered and is ruled out in $Y_2Mo_2O_7$ by the absence of global symmetry lowering. In the latter case, by contrast, the coupling is frustrated and the displacement pattern need

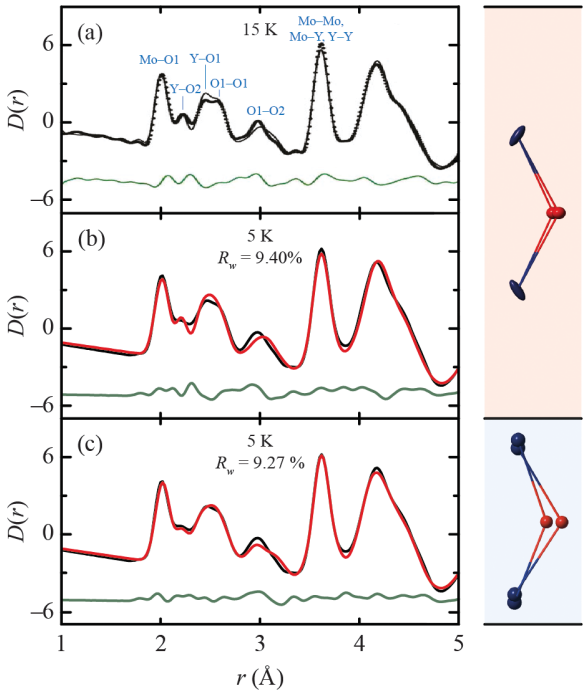


FIG. 2. (a) Reproduction of the fit to neutron PDF data shown in Fig. 8 of Ref. [29] for the split-site model described in the text. (b) Fit of the split-site model to our neutron PDF data. (c) Fit of the orbital-dimer model ($I4_1md$, described in the text) to our neutron PDF data. In (a), data are shown as points and fit as a line; in (b) and (c), data are shown as black lines, fits as red lines, and difference (data − fit) functions as green lines. The extrema of Mo–O1–Mo conformations accounted for by each model are shown beside the corresponding fit.

not be ordered at all. In fact, if all two-in–two-out states were equally probable, there would be a macroscopic degeneracy of Mo-displaced configurations analogous to the degeneracy of proton configurations in cubic water ice [45]—i.e., an orbital-ice state.

To build a model that can be directly compared with the split-site model in terms of its ability to explain the experimental PDF, we consider an ordered approximant to the ensemble of disordered two-in–two-out states. This is possible because ordered and disordered two-in–two-out states show essentially the same PDF for distances within a single unit cell. The highest-symmetry subgroup of $Fd\bar{3}m$ that permits two-in–two-out Mo displacements is $I4_1md$. This structure is shown in Fig. 3(a), and relates to $Fd\bar{3}m$ in the same way as the proton-ordered ice phase XIc relates to proton-disordered cubic ice Ic [46]. The tetragonal unit cell has dimensions $a_t = a/\sqrt{2}$ and $c_t = a$. Both Mo and Y occupy the $8b$ site at $(0, y, z)$, O2 occupies the $4a$ site at $(0, 0, z)$, and the O1 site is split into three sites: O1a and O1c also occupy the $4a$ site and O1b occupies the $16c$ site at (x, y, z). The Mo point symmetry is lowered from $\bar{3}m$ to m, which is consistent with a Jahn-Teller-type distortion of the d^2 electronic configuration of Mo^{4+}.

TABLE I. Structural parameters for our PDF refinements using the split-site and orbital-dimer models. Reference values from the split-site refinements of Ref. [29] are shown in italics (* denotes Rietveld and † denotes PDF refinements; note that the consistency in cell parameters is typical for Rietveld and PDF comparisons). Lattice parameters are given in Angstroms (Å) and displacement parameters in 10^{-2} Å^2.

Split-site model [29]			*Orbital dimer model*	
a	10.2255(10)	*10.20753(2)**	$c_t \equiv \sqrt{2}a_t$	10.2269(10)
x(O1a)	0.3320(6)	*0.3305(12)†*	y(Mo)	0.7371(8)
x(O1b)	0.3446(6)	*0.3465(13)†*	z(O1a)	0.6938(6)
U_{11}(Y)	0.512(15)	*0.471(7)**	x(O1b)	0.7184(5)
U_{12}(Y)	−0.129(19)	*−0.136(9)**	y(O1b)	0.7910(5)
U_{11}(Mo)	1.39(5)	*1.1(1)**	z(O1b)	0.2467(4)
U_{12}(Mo)	0.93(5)	*0.83(2)**	z(O1c)	0.2709(6)
U_{11}(O1)	1.02(11)	*1.45(2)**	U_{iso}(Y)	0.355(11)
U_{22}(O1)	0.81(3)	*0.66(1)**	U_{iso}(Mo)	1.14(5)
U_{iso}(O2)	0.55(3)	*0.32(2)**	U_{iso}(O)	0.89(2)

We reduce the number of refined parameters in our $I4_1md$ model to match the split-site model in the following way. First, we constrain the ratio of unit-cell dimensions $c_t = \sqrt{2}a_t$, so that the parent cell remains metrically cubic. Second, the small displacement parameters of the Y and O2 sites indicate that they are not strongly disordered [Fig. 1(c)]; we therefore fix them at their average-structure positions of $(0, \frac{3}{4}, \frac{1}{8})$ and (0,0,0), respectively. Finally, the $I4_1md$ structure allows for Mo displacements within the plane that contains the cubic local-$\langle 111\rangle$ axis (towards or away from the tetrahedron center) and local-$\langle 110\rangle$ axis (towards or away from neighboring Mo lying on the same mirror plane). Consequently, two parameters are needed to define the Mo displacement direction, which would increase the number of parameters beyond the split-site model. Such a refinement was stable, however, and showed that the dominant displacement direction is actually the local $\langle 110\rangle$. Subsequently, we fixed the local-$\langle 111\rangle$ component at zero [$z(\mathrm{Mo}) \equiv \frac{5}{8}$], so that the number of parameters was identical to the split-site model. We call this constrained $I4_1md$ model the "orbital dimer" model.

The fit to neutron data for this model is presented in Fig. 2(c); values of refined parameters are given in Table I, and the fit to x-ray data is given in Ref. [42]. The quality of fit for the orbital-dimer model is higher than for the split-site model ($R_{wp} = 9.27\%$ versus 9.40%) despite employing the same number of structural parameters. Moreover, the orbital-dimer model accounts more convincingly for the low-r peaks. Further evidence for improved model quality comes from the refinement statistics: whereas the split-site model showed strong covariance (> 80%) between the x(O1a), x(O1b), and U_{11}(O1) parameters, the orbital-dimer refinement yielded no anomalous covariance terms; in fact, a robust refinement with $R_{wp} = 8.29\%$ could also be achieved with more structural parameters [42].

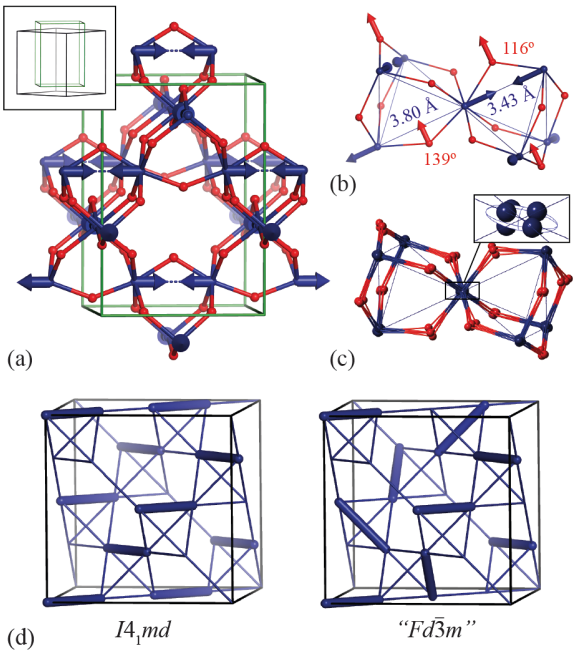


FIG. 3. (a) Representation of the orbital-dimer model obtained from PDF refinements: Mo displacements are shown as blue arrows, Mo–Mo dimers as blue dashed lines, and O1 atoms in red. The inset shows the relationship between $I4_1md$ and $Fd\bar{3}m$ unit cells. (b) Local Mo environment in the orbital-dimer model, showing Mo displacement directions (blue arrows) and dominant O1 displacement directions (red arrows). (c) Distribution of atomic positions obtained by imposing the full symmetry of the average structure. In the inset, the superposition of displaced Mo sites is compared to the prolate displacement ellipsoid obtained from Rietveld refinement. (d) Comparison of ordered and disordered coverings of the pyrochlore lattice by Mo–Mo dimers (thick blue lines). The left panel shows the ordered dimer covering for the $I4_1md$ structure, which breaks cubic symmetry. The right panel shows an example of a disordered dimer covering that more closely approximates the true orbital-ice state; spatial averaging over such dimer coverings preserves cubic symmetry.

We therefore conclude that the absence of visible splitting of the Mo–Mo peak is not inconsistent with Mo off centering. On the contrary, our model includes Mo displacements and robustly yields an improved fit to experimental data [Fig. 2].

The orbital-dimer model is represented in Fig. 3. In every Mo_4 tetrahedron, two Mo atoms are displaced towards each other and two away from each other; in each case, the refined displacement magnitude is 0.093(6) Å and the displacement direction is along the line connecting the Mo pair [Fig. 3(a)]. The Mo displacements thus describe a covering of the pyrochlore lattice by Mo–Mo dimers (short Mo–Mo distances), with one dimer per tetrahedron. The O1 displacements are correlated with Mo displacements as shown in Fig. 3(b). When neighboring Mo displace towards each other, the bridging O1 displaces away from the dimer and the Mo–O1–Mo angle decreases; conversely, when neighboring Mo displace away from each other the Mo–O1–Mo angle increases. The effect of O1 displacements is to keep all Mo–O1 distances essentially the same—a result that is perhaps unsurprising on electrostatic grounds but nevertheless explains the lack of visible Mo–O1 peak splitting. Figure 3(c) shows the distribution of atomic positions obtained by superposing the full $Fd\bar{3}m$ average-structure symmetry on the refined local-structure model. The distribution of local-$\langle 110\rangle$ Mo displacements has a larger component parallel to the local-$\langle 111\rangle$ axis than perpendicular to it, consistent with the prolate Mo displacement ellipsoid in the average-structure model [Fig. 1(b) and inset to Fig. 3(c)] [42]. Finally, we stress that the ordered $I4_1md$ dimer covering [left panel of Fig. 3(d)] is an approximant to disordered dimer coverings that show the same local displacement patterns. There is a macroscopic degeneracy of disordered dimer coverings that reproduce the observed $Fd\bar{3}m$ symmetry on spatial averaging; the right panel of Fig. [3] shows a disordered example that more closely approximates the true structure. This is the same degeneracy responsible for the unusual physics of cubic water ice [45], spin ices [35,47], and charge ices [48,49].

Crucially, the orbital-dimer model is consistent with previous experimental studies and theoretical requirements for spin-glass formation. The O1 displacement gives rise to 30 distinct Y environments, consistent with the broad resonance observed in ^{89}Y NMR studies [31,33]. The Mo displacements split the average Mo–Mo distance into long, short, and intermediate distances in the ratio 1:1:4. This static disorder makes a contribution to the variance in Mo–Mo distances of 0.012(2) Å^2, in qualitative agreement with the EXAFS result [0.026(5) Å^2]; moreover, the displacement direction (parallel to Mo–Mo pairs) is consistent with EXAFS [32]. This agreement is encouraging because EXAFS should be more sensitive to Mo displacements than the PDF, in which Mo–Mo, Y–Y and Mo–Y peaks overlap and our intermediate Mo–Mo distance is similar to the average Mo–Mo distance. It has been shown that small (∼10%) variations in exchange interactions may induce spin-glass transitions in geometrically frustrated magnets [12,13]. In $Y_2Mo_2O_7$, variations in bond angle of 9° are calculated to yield factor-of-2 variations in the magnetic coupling strength [29]. Our results show that the Mo–O1–Mo angle actually varies by a significantly larger amount, 23° [Fig. 3(b)]. Importantly, the arrangement of Mo–O1–Mo bond angles is disordered; this is because the dimer covering (i.e., the arrangement of short and long Mo–Mo distances) is disordered [Fig. 3(d)], and short and long Mo–Mo distances are associated with Mo–O1–Mo bond angles of 116° and 139°, respectively [Fig. 3(b)]. Hence, Mo dimerization presents a clear mechanism to generate exchange disorder responsible for spin-glass freezing. Experimentally, the width $\delta \sim 1$ T of the internal-field distribution measured by ^{89}Y NMR at 25 K [33] implies a distribution of exchange energies of approximate

width $gS\mu_B\delta/k_B \approx 13$ K, which is similar to T_f, as expected theoretically [12,13]. Theoretical studies suggest that Mo dimerization may be explained by an orbital (Jahn-Teller) mechanism. A recent study parametrized a three-orbital Hubbard model using density functional theory [44], and concluded that spin and orbital degrees of freedom are strongly coupled for the d^2 configuration and many energetically similar spin-orbital excited states exist if the ground state is two-in–two-out. A second DFT study relaxed the orbital and lattice configuration for different spin structures and obtained different lattice distortions in each case [50]. These studies provide compelling evidence for a strong coupling of spin, orbital, and lattice degrees of freedom. We therefore interpret the two-in–two-out pattern of Mo displacements as the formation of orbital dimers, driven by the Jahn-Teller activity of the d^2 electronic configuration.

Our results show that the spin-glass state in $Y_2Mo_2O_7$ is driven by orbital dimerization of Jahn-Teller active Mo^{4+} ions—a rare example where spin-glass formation is not driven by random compositional or site disorder [51]. While spin-glass formation due to nonrandom interactions has been studied theoretically [52], to the best of our knowledge this represents the first such example for a real spin glass. Yet, dimer states play a key role in determining other properties of materials. In LiV_2O_4, charge dimerization on V_4 tetrahedra may explain the observed heavy-fermion behavior [53]. In Ba_2YMoO_6, Mo^{5+} spins freeze into a disordered arrangement of spin-singlet dimers [54], while in $CuIr_2O_4$ Ir^{3+}/Ir^{4+} charge ordering accompanies spin dimerization [55]. Dimer models may be relevant to other molybdate pyrochlores: e.g., $Lu_2Mo_2O_7$ [56], $Tb_2Mo_2O_7$ [57,58], and $Dy_2Mo_2O_7$ [59]. Interestingly, our model of Mo displacements resembles models of Nb displacements in (nonmagnetic) niobate pyrochlores [60,61], suggesting that the proximity of both materials to a metal-insulator transition may be related to orbital dimerization [62,63]. Our results suggest three promising directions for future work on $Y_2Mo_2O_7$. First, a comprehensive single-crystal diffuse scattering study would indicate the extent to which a particular subset of dimer coverings is preferentially selected. Second, analysis of the distribution of magnetic couplings may allow a consistent interpretation of puzzling magnetic diffuse-scattering data [50]. Third, the orbital-dimer state we propose should collapse at sufficiently high temperature; i.e., an orbital-ice to orbital-liquid [64,65] transition may be anticipated.

We thank A. Simonov, J. R. Stewart, M. Mourigal, C. R. Wiebe, H. J. Silverstein, M. J .P. Gingras, F. Flicker, and J. S. Gardner for useful discussions. We acknowledge the Rutherford Appleton Laboratory for access to the ISIS Neutron Source. This research used resources of the Advanced Photon Source, a U.S. Department of Energy (DOE) Office of Science User Facility operated for the DOE Office of Science by Argonne National Laboratory under Contract No. DE-AC02-06CH11357. P. M. M. T., J.A.M.P., and A. L. G. acknowledge financial support from the Science and Technology Facilities Council (UK), Engineering and Physical Sciences Research Council (UK) (EP/G004528/2), and the European Research Council (Grant Ref: 279705). J.A.M.P. acknowledges funding from Georgia Tech's College of Sciences, and Churchill College, Cambridge.

*paddison@gatech.edu

[1] S. J. Blundell, *Magnetism in Condensed Matter* (Oxford University Press, Oxford, 2001).
[2] J. A. Mydosh, Rep. Prog. Phys. **78**, 052501 (2015).
[3] D. Sherrington and S. Kirkpatrick, Phys. Rev. Lett. **35**, 1792 (1975).
[4] B. Barbara, A. P. Malozemoff, and Y. Imry, Phys. Rev. Lett. **47**, 1852 (1981).
[5] K. Binder and A. P. Young, Rev. Mod. Phys. **58**, 801 (1986).
[6] C. Y. Huang, J. Magn. Magn. Mater. **51**, 1 (1985).
[7] L. Lundgren, P. Svedlindh, P. Nordblad, and O. Beckman, Phys. Rev. Lett. **51**, 911 (1983).
[8] U. Atzmony, E. Gurewitz, M. Melamud, H. Pinto, H. Shaked, G. Gorodetsky, E. Hermon, R. M. Hornreich, S. Shtrikman, and B. Wanklyn, Phys. Rev. Lett. **43**, 782 (1979).
[9] P. Schiffer, A. P. Ramirez, D. A. Huse, P. L. Gammel, U. Yaron, D. J. Bishop, and A. J. Valentino, Phys. Rev. Lett. **74**, 2379 (1995).
[10] C. R. Wiebe, J. E. Greedan, P. P. Kyriakou, G. M. Luke, J. S. Gardner, A. Fukaya, I. M. Gat-Malureanu, P. L. Russo, A. T. Savici, and Y. J. Uemura, Phys. Rev. B **68**, 134410 (2003).
[11] E. M. Benbow, N. S. Dalal, and S. E. Latturner, J. Am. Chem. Soc. **131**, 3349 (2009).
[12] T. E. Saunders and J. T. Chalker, Phys. Rev. Lett. **98**, 157201 (2007).
[13] A. Andreanov, J. T. Chalker, T. E. Saunders, and D. Sherrington, Phys. Rev. B **81**, 014406 (2010).
[14] A. D. LaForge, S. H. Pulido, R. J. Cava, B. C. Chan, and A. P. Ramirez, Phys. Rev. Lett. **110**, 017203 (2013).
[15] J. S. Gardner, M. J. P. Gingras, and J. E. Greedan, Rev. Mod. Phys. **82**, 53 (2010).
[16] M. J. P. Gingras, C. V. Stager, N. P. Raju, B. D. Gaulin, and J. E. Greedan, Phys. Rev. Lett. **78**, 947 (1997).
[17] M. J. P. Gingras, C. V. Stager, B. D. Gaulin, N. P. Raju, and J. E. Greedan, J. Appl. Phys. **79**, 6170 (1996).
[18] K. Blacklock, H. W. White, and E. Gürmen, J. Chem. Phys. **73**, 1966 (1980).
[19] N. P. Raju, E. Gmelin, and R. K. Kremer, Phys. Rev. B **46**, 5405 (1992).
[20] K. Miyoshi, Y. Nishimura, K. Honda, K. Fujiwara, and J. Takeuchi, J. Phys. Soc. Jpn. **69**, 3517 (2000).
[21] N. Ali, P. Hill, X. Zhang, and F. Willis, J. Alloys Compd. **181**, 281 (1992).
[22] V. Dupuis, E. Vincent, J. Hammann, J. E. Greedan, and A. S. Wills, J. Appl. Phys. **91**, 8384 (2002).
[23] F. Ladieu, F. Bert, V. Dupuis, E. Vincent, and J. Hammann, J. Phys. Condens. Matter **16**, S735 (2004).
[24] J. S. Gardner, B. D. Gaulin, S.-H. Lee, C. Broholm, N. P. Raju, and J. E. Greedan, Phys. Rev. Lett. **83**, 211 (1999).

[25] S. R. Dunsiger, R. F. Kiefl, K. H. Chow, B. D. Gaulin, M. J. P. Gingras, J. E. Greedan, A. Keren, K. Kojima, G. M. Luke, W. A. MacFarlane, N. P. Raju, J. E. Sonier, Y. J. Uemura, and W. D. Wu, J. Appl. Phys. **79**, 6636 (1996).
[26] J. Gardner, G. Ehlers, R. Heffner, and F. Mezei, J. Magn. Magn. Mater. **226–230**, 460 (2001).
[27] J. S. Gardner, G. Ehlers, S. T. Bramwell, and B. D. Gaulin, J. Phys. Condens. Matter **16**, S643 (2004).
[28] J. N. Reimers, J. E. Greedan, and M. Sato, J. Solid State Chem. **72**, 390 (1988).
[29] J. E. Greedan, D. Gout, A. D. Lozano-Gorrin, S. Derahkshan, T. Proffen, H.-J. Kim, E. Božin, and S. J. L. Billinge, Phys. Rev. B **79**, 014427 (2009).
[30] L. Minervini, R. W. Grimes, Y. Tabira, R. L. Withers, and K. E. Sickafus, Philos. Mag. A **82**, 123 (2002).
[31] A. Keren and J. S. Gardner, Phys. Rev. Lett. **87**, 177201 (2001).
[32] C. H. Booth, J. S. Gardner, G. H. Kwei, R. H. Heffner, F. Bridges, and M. A. Subramanian, Phys. Rev. B **62**, R755 (2000).
[33] O. Ofer, A. Keren, J. S. Gardner, Y. Ren, and W. A. MacFarlane, Phys. Rev. B **82**, 092403 (2010).
[34] E. Sagi, O. Ofer, A. Keren, and J. S. Gardner, Phys. Rev. Lett. **94**, 237202 (2005).
[35] S. T. Bramwell and M. J. P. Gingras, Science **294**, 1495 (2001).
[36] M. Sato, X. Yan, and J. E. Greedan, Z. Anorg. Allg. Chem. **540**, 177 (1986).
[37] J. E. Greedan, M. Sato, X. Yan, and F. S. Razavi, Solid State Commun. **59**, 895 (1986).
[38] S. Hull, R. I. Smith, W. I. F. David, A. C. Hannon, J. Mayers, and R. Cywinski, Physica (Amsterdam) **180B–181B**, 1000 (1992).
[39] A. K. Soper and E. R. Barney, J. Appl. Crystallogr. **44**, 714 (2011).
[40] A. C. Hannon, W . S. Howells, and A. K. Soper, in *ATLAS: A Suite of Programs for the Analysis of Time-of-flight Neutron Diffraction Data from Liquid and Amorphous Samples–1990*, Neutron Scattering Data Analysis 1990, edited by M. W. Johnson, Inst. Phys. Conf. Ser. No. 107 (Institute of Physics and Physical Society, London, 1990).
[41] C. L. Farrow, P. Juhas, J. W. Liu, D. Bryndin, E. S. Božin, J. Bloch, T. Proffen, and S. J. L. Billinge, J. Phys. Condens. Matter **19**, 335219 (2007).
[42] See Supplemental Material at http://link.aps.org/supplemental/10.1103/PhysRevLett.118.067201, which includes Ref. [43], discussion of model parameters, results of a further PDF refinement, x-ray PDF fits, and discussion of Mo displacement anisotropy.
[43] D. A. Keen, J. Appl. Crystallogr. **34**, 172 (2001).
[44] H. Shinaoka, Y. Motome, T. Miyake, and S. Ishibashi, Phys. Rev. B **88**, 174422 (2013).
[45] L. Pauling, J. Am. Chem. Soc. **57**, 2680 (1935).
[46] Z. Raza, D. Alfe, C. G. Salzmann, J. Klimes, A. Michaelides, and B. Slater, Phys. Chem. Chem. Phys. **13**, 19788 (2011).
[47] H. D. Zhou, C. R. Wiebe, J. A. Janik, L. Balicas, Y. J. Yo, Y. Qiu, J. R. D. Copley, and J. S. Gardner, Phys. Rev. Lett. **101**, 227204 (2008).
[48] D. P. Shoemaker, R. Seshadri, A. L. Hector, A. Llobet, T. Proffen, and C. J. Fennie, Phys. Rev. B **81**, 144113 (2010).
[49] V. E. Fairbank, A. L. Thompson, R. I. Cooper, and A. L. Goodwin, Phys. Rev. B **86**, 104113 (2012).
[50] H. J. Silverstein, K. Fritsch, F. Flicker, A. M. Hallas, J. S. Gardner, Y. Qiu, G. Ehlers, A. T. Savici, Z. Yamani, K. A. Ross, B. D. Gaulin, M. J. P. Gingras, J. A. M. Paddison, K. Foyevtsova, R. Valenti, F. Hawthorne, C. R. Wiebe, and H. D. Zhou, Phys. Rev. B **89**, 054433 (2014).
[51] E. A. Goremychkin, R. Osborn, B. D. Rainford, R. T. Macaluso, D. T. Adroja, and M. Koza, Nat. Phys. **4**, 766 (2008).
[52] J. Villain, J. Phys. C **10**, 1717 (1977).
[53] P. Fulde, A. N. Yaresko, A. A. Zvyagin, and Y. Grin, Europhys. Lett. **54**, 779 (2001).
[54] M. A. de Vries, A. C. Mclaughlin, and J.-W. G. Bos, Phys. Rev. Lett. **104**, 177202 (2010).
[55] P. G. Radaelli, Y. Horibe, M. J. Gutmann, H. Ishibashi, C. H. Chen, R. M. Ibberson, Y. Koyama, Y.-S. Hor, V. Kiryukhin, and S.-W. Cheong, Nature (London) **416**, 155 (2002).
[56] L. Clark, G. J. Nilsen, E. Kermarrec, G. Ehlers, K. S. Knight, A. Harrison, J. P. Attfield, and B. D. Gaulin, Phys. Rev. Lett. **113**, 117201 (2014).
[57] B. D. Gaulin, J. N. Reimers, T. E. Mason, J. E. Greedan, and Z. Tun, Phys. Rev. Lett. **69**, 3244 (1992).
[58] D. K. Singh, J. S. Helton, S. Chu, T. H. Han, C. J. Bonnoit, S. Chang, H. J. Kang, J. W. Lynn, and Y. S. Lee, Phys. Rev. B **78**, 220405 (2008).
[59] T. Katsufuji, H. Y. Hwang, and S-W. Cheong, Phys. Rev. Lett. **84**, 1998 (2000).
[60] T. M. McQueen, D. V. West, B. Muegge, Q. Huang, K. Noble, H. W. Zandbergen, and R. J. Cava, J. Phys. Condens. Matter **20**, 235210 (2008).
[61] S. Torigoe, Y. Ishimoto, Y. Aoishi, H. Murakawa, D. Matsumura, K. Yoshii, Y. Yoneda, Y. Nishihata, K. Kodama, K. Tomiyasu, K. Ikeda, H. Nakao, Y. Nogami, N. Ikeda, T. Otomo, and N. Hanasaki, Phys. Rev. B **93**, 085109 (2016).
[62] P. Blaha, D. J. Singh, and K. Schwarz, Phys. Rev. Lett. **93**, 216403 (2004).
[63] N. Hanasaki, K. Watanabe, T. Ohtsuka, I. Kézsmárki, S. Iguchi, S. Miyasaka, and Y. Tokura, Phys. Rev. Lett. **99**, 086401 (2007).
[64] G. Khaliullin and S. Maekawa, Phys. Rev. Lett. **85**, 3950 (2000).
[65] S. Nakatsuji, K. Kuga, K. Kimura, R. Satake, N. Katayama, E. Nishibori, H. Sawa, R. Ishii, M. Hagiwara, F. Bridges, T. U. Ito, W. Higemoto, Y. Karaki, M. Halim, A. A. Nugroho, J. A. Rodriguez-Rivera, M. A. Green, and C. Broholm, Science **336**, 559 (2012).

PHYSICAL REVIEW B **95**, 174107 (2017)

Local structure study of the orbital order/disorder transition in $LaMnO_3$

Peter M. M. Thygesen,[1] Callum A. Young,[1] Edward O. R. Beake,[1,2] Fabio Denis Romero,[1] Leigh D. Connor,[3] Thomas E. Proffen,[4] Anthony E. Phillips,[2] Matthew G. Tucker,[3,4,5] Michael A. Hayward,[1] David A. Keen,[5] and Andrew L. Goodwin[1,*]

[1]*Department of Chemistry, University of Oxford, South Parks Road, Oxford OX1 3QR, United Kingdom*
[2]*School of Physics and Astronomy, Queen Mary University of London, Mile End Road, London E1 4NS, United Kingdom*
[3]*Diamond Light Source, Chilton, Oxfordshire, OX11 0DE, United Kingdom*
[4]*Spallation Neutron Source, Oak Ridge National Laboratory, Oak Ridge, Tennessee 37831, USA*
[5]*ISIS Facility, Rutherford Appleton Laboratory, Harwell Campus, Didcot, Oxfordshire OX11 0QX, United Kingdom*

(Received 22 February 2017; published 30 May 2017)

We use a combination of neutron and x-ray total scattering measurements together with pair distribution function (PDF) analysis to characterize the variation in local structure across the orbital order/disorder transition in $LaMnO_3$. Our experimental data are inconsistent with a conventional order/disorder description of the transition, and reflect instead the existence of a discontinuous change in local structure between ordered and disordered states. Within the orbital ordered regime, the neutron and x-ray PDFs are best described by a local structure model with the same local orbital arrangements as those observed in the average (long-range) crystal structure. We show that a variety of meaningfully different local orbital arrangement models can give fits of comparable quality to the experimental PDFs collected within the disordered regime; nevertheless, our data show a subtle but consistent preference for the anisotropic Potts model proposed previously [M. R. Ahmed and G. A. Gehring, Phys. Rev. B **79**, 174106 (2009)]. The key implications of this model are electronic and magnetic isotropy together with the loss of local inversion symmetry at the Mn site. We conclude with a critical assessment of the interpretation of PDF measurements when characterizing local symmetry breaking in functional materials.

DOI: 10.1103/PhysRevB.95.174107

I. INTRODUCTION

Orbital degrees of freedom play a key role in the physics of colossal magnetoresistance (CMR) [1–4], frustrated magnetism [5,6], ferroelectricity [7,8], spin-glass formation [9], and magnetoelectric coupling [10]. In all cases, it is the existence and nature of correlations between local orbital states that gives rise to the relevant phenomena of interest. Long-range orbital order can assume many forms, but its nature is usually evident crystallographically *via* coupling between orbital occupancy/orientation and bond strain. This coupling results in long-range symmetry breaking, such as occurs in the cooperative Jahn-Teller (JT) state of $KCuF_3$ [11]. In favorable cases, resonant x-ray scattering and charge density measurements also provide direct experimental evidence of long-range orbital order [12–15]. By contrast, the microscopic nature of orbital disordered states, as implicated in the phenomenology of CMR [16], is notoriously difficult to determine experimentally. Certain probes (e.g., EXAFS, PDF, NMR) remain sensitive to the presence of local orbital–strain coupling in the absence of long-range orbital order but their sensitivity to *correlations* between orbital orientations in such states is either negligible or poorly understood.

Of the many systems known to exhibit orbital disorder, few can be more important than $LaMnO_3$. The parent of the $La_{1-x}A_xMnO_3 (A = Ca, Sr, Ba)$ families of CMR manganites [1,3,17,18], $LaMnO_3$ has long assumed a special position among functional oxides [19–21]. Its orthorhombic-pseudocubic transition at $T_{JT} = 750$ K is widely viewed as the canonical orbital order/disorder transition [22–24]. The same transition precedes CMR itself within the doped manganites [25–28] and is implicated more generally in charge and orbital ordering in a variety of other functional condensed phases [29–31].

Despite this importance, there remains no clear consensus regarding the microscopic nature of orbital disorder in $LaMnO_3$ itself. Zhou and Goodenough initially interpreted high-temperature resistivity and thermoelectric measurements in terms of dynamic cooperative JT distortions [22]. In this picture, orbital-driven distortions are similar in ordered and disordered states: the key difference is a transition from fixed to fluctuating collective orbital orientations. A conceptually similar model was proposed in the neutron PDF study of Qiu *et al.*, where the orbital disordered phase was interpreted in terms of nm-sized domains with local (now static) orbital arrangements identical to those in the ordered state [24]. These two models are consistent with conventional order/disorder descriptions: i.e., ordered and disordered states share a common local structure but temporal and/or configurational averaging leads to a finite correlation length in the disordered regime [32]. By contrast, Ahmed and Gehring reproduced the order parameter behavior measured in resonant x-ray scattering experiments [33] using the so-called anisotropic Potts model, which describes a transition to a meaningfully different local arrangement of JT distortions at high temperatures [34].

Motivated by the success of combined x-ray/neutron PDF measurements in characterizing local orbital order in systems such as $Y_2Mo_2O_7$ [9], we sought to establish whether a similar approach might shed new light on the nature of orbital disorder in high-temperature $LaMnO_3$. The scattering contrast between x-ray and neutron measurements in principle heightens experimental sensitivity to different pairwise contributions to the PDF, and so is particularly useful in high-symmetry structures

*andrew.goodwin@chem.ox.ac.uk

 ©2017 American Physical Society

such as pyrochlores and perovskites [35]. In this paper, we report a series of high-real-space-resolution x-ray and neutron PDF data collected across the $LaMnO_3$ orbital order/disorder transition. We show first the unsurprising result that these data unambiguously identify the nature of orbital order at temperatures below T_{JT}. We then report the discovery of a discontinuous change in the PDF at T_{JT}, overlooked in earlier PDF studies and ostensibly inconsistent with a conventional order/disorder transition. Within the high-temperature orbital disordered regime, we find that the PDF data are in fact remarkably poor at discriminating models representing a variety of different locally correlated orbital arrangements. We argue this insensitivity arises because the variation in pairwise correlations for different models becomes commensurate with the magnitude of thermal motion at these elevated temperatures. We cautiously identify a subtle but persistent preference for the anisotropic Potts model proposed in Ref. [34]. This assignment is consistent with the discontinuous change in local structure at T_{JT} evident in our newly obtained data. Our results suggest that short-range orbital correlations in the disordered phases of doped (CMR) manganites may be subtly but meaningfully different to those observed in the ordered regime.

Our paper is arranged as follows. We begin with a review of the current experiment-driven understanding of the orbital order/disorder transition in $LaMnO_3$, together with a structural description of the different correlated orbital arrangement models considered in our subsequent analysis. In Sec. III we summarize the experimental and analytical methods we have used, including a description of the key local structure models investigated in our study. We proceed to present our x-ray and neutron total scattering measurements, together with the results of conventional Rietveld analysis (average structure) and direct interrogation of the experimental PDFs (local structure). We then explore the ability of various orbital arrangement models to account for the PDF data we have measured within both orbital ordered and disordered regimes. Having established the difficulty of unambiguous interpretation of the disordered state, we consider the potential role of single-crystal diffuse scattering measurements in future studies. Our paper concludes with a short discussion of the implications of our study for CMR science, on the one hand, and for PDF studies of functional materials in general, on the other hand.

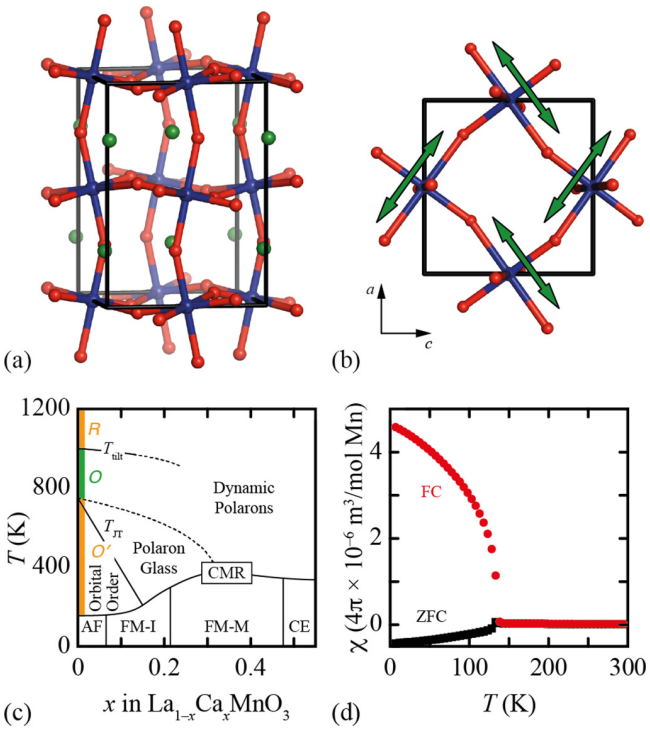


FIG. 1. Structure and phase behavior of $LaMnO_3$. (a) The ambient (O') structure consists of a framework of corner-sharing MnO_6 octahedra (Mn atoms blue; O atoms red), with La atoms (green) occupying 12-coordinate extra framework sites. The presence of octahedral tilts confers orthorhombic *Pnma* symmetry; in this representation, the *b* axis is vertical and the *c* axis approximately horizontal. (b) Axial JT distortions are arranged with the same periodicity as the octahedral tilts. Long Mn–O bonds (indicated by arrows) are approximately confined within the (a,c) planes; this particular arrangement results in a small difference between the *a* and *c* lattice parameters. (c) On heating $LaMnO_3$ to $T_{JT} = 750$ K, there is an isosymmetric structural transition to the orbital disorder (O) phase, with the same octahedral tilts as in the O' phase but with no discernible JT distortion. On hole doping, the value of T_{JT} decreases such that CMR emerges in $La_{1-x}Ca_xMnO_3$ from the disordered phase. A discontinuous octahedral tilt transition occurs at 1010 K to give a rhombohedral (R) phase that persists until decomposition. (d) Experimental dc magnetic susceptibility χ for $LaMnO_3$ for the sample used in our study. The Néel temperature (T_N) is observed as a divergence in the field-cooled (FC) and zero-field-cooled (ZFC) traces at 140 K.

II. ORBITAL ORDER IN LANTHANUM MANGANITE

The issue of orbital order in $LaMnO_3$ arises fundamentally from the degeneracy of the $Mn^{3+}t^3e^1d$-electron configuration [22]. This degeneracy is lifted by a JT distortion of the [MnO_6] coordination environment, which acts to couple Mn–O bond displacements with orbital occupancies, and hence structural and electronic degrees of freedom [36]. Crystallographic measurements of $LaMnO_3$ performed under ambient conditions indicate that these distortions (and hence orbital occupancies) are ordered throughout the crystal lattice, with a periodicity that coincides with that imposed by the octahedral tilt system also present [23]. This periodicity accounts for the orthorhombic *Pnma* symmetry of the orbital-ordered phase [Fig. 1(a)]. There is a single Mn environment (Wyckoff site 4*b*; site symmetry $\bar{1}$) and three symmetry-inequivalent pairs of Mn–O bonds: "long" (2.1 Å), "medium" (2.0 Å), and "short" (1.9 Å). The long and short bonds alternate within the (a,c) plane [Fig. 1(b)] to give an arrangement sometimes referred to as *C*-type orbital order [37]. In this case, the specific octahedral tilts present mean that the projection of the long bonds is slightly greater along *a* than *c* and so the difference in these two lattice parameters is actually related to the presence of orbital order.

This particular type of orbital order is known to have a direct effect on the transport and magnetic properties of ambient $LaMnO_3$ [22,38]: the material is an insulator with strongly anisotropic magnetic interactions, as evidenced by a

Curie-Weiss constant $\theta = 52$ K that represents a compromise between ferromagnetism within the (a,c) plane and antiferromagnetic interactions between adjacent (a,c) planes (i.e., along b).

A. Orbital order/disorder transition

On heating from room temperature, $LaMnO_3$ undergoes two structural phase transitions [Fig. 1(c)]. The first occurs at 750 K and is isosymmetric, i.e., there is no change in space group symmetry [23]. This is the orbital order/disorder transition at the heart of this study. The second transition, at 1010 K, is to a rhombohedral phase with a different set of tilts [23] but which also supports orbital disorder [24]. Drawing on the approach taken in Ref. [20] we use the labels O', O, and R to represent, respectively, the orthorhombic orbital ordered, orthorhombic orbital disordered, and rhombohedral orbital disordered phases.

Although isosymmetric, the O'/O transition at $T_{JT} = 750$ K has a number of clear experimental signatures. First, there is a convergence of the reduced unit-cell parameters, such that the O phase is close to being metrically cubic (hence its "pseudocubic" label) [23,39]. The variation in lattice parameters is discontinuous at T_{JT}, identifying the transition as first order as required for isosymmetric transitions [40]. Second, both neutron and x-ray diffraction show a convergence of the crystallographic Mn–O bond lengths from the three distinct values of the ambient phase to a single effective value [d(Mn–O) $\simeq 2.02$ Å] in the O phase [23,39]. So, in this average-structure sense the JT distortion appears to vanish on heating through the O'/O transition. Third, there is a volume discontinuity at T_{JT}, with the disordered O phase about 0.4% denser than the ordered O' phase [39]. Fourth, both conductivity and magnetic behavior change at the transition: resistivity falls by two orders of magnitude, and the Weiss constant switches to a value $\theta = 177$ K that is consistent with isotropic ferromagnetic interactions within the O phase [22,38]. Fifth, ^{17}O NMR measurements reveal a transition to nonpolarized e_g orbital occupation at T_{JT}, indicating the population of MHz-frequency electronic fluctuations [41]. Sixth, there is an anomaly in the specific-heat capacity, corresponding to a transition entropy $\Delta S = 0.52(2)\,\mathrm{J\,K^{-1}\,mol^{-1}}$ [42]. And, seventh, the transition is accompanied by small shifts and increased broadening in the excitation spectrum as measured using either inelastic neutron scattering [43] or Raman spectroscopy [44].

The primary experimental evidence for the persistence of JT distortions within O-phase $LaMnO_3$ comes from techniques capable of probing structural correlations over distances of 1–10 Å. The neutron PDF study of Ref. [24] confirmed clearly the absence of any meaningful variation in local Mn–O bond lengths across the O'/O transition. A similar conclusion was drawn from x-ray absorption (EXAFS/XANES) studies [42,45,46]. While there seems to be little disagreement as to the persistence of a JT distortion at high temperatures, it was noted first in Ref. [42] and more convincingly in Ref. [46] that the Mn K-edge EXAFS signal varied more strongly across the O'/O transition than for any temperature range within either phase. This is a point to which we will return later in our own study. Nevertheless, taken collectively, these experimental observations clearly identify the O phase of $LaMnO_3$ as an orbital disorder phase: each MnO_6 octahedron retains a JT distortion, but these distortions must propagate without any long-range periodicity.

B. Orbital correlations in the O phase

Determining the nature of orbital orientation correlations in the absence of long-range orbital order is a problem of significant difficulty [9,27,47–49]. Total scattering is one of the few experimental techniques with simultaneous sensitivity to both average and local structure [50,51], and so it is no accident that the two studies (of which we are aware) to attempt data-driven refinement of microscopic models of the orbital disordered state are based on neutron total scattering measurements [24,52]. The first of these studies employed a "real-space Rietveld" (or "small-box" [53]) approach, in which the neutron PDF was fitted using a structural model based on the O' arrangement of orbital orientations [24]. For data collected within the O regime, convincing fits with stable JT distortions could only be obtained for refinements constrained to distances $0 < r < 10$ Å. Hence, the model developed in this study effectively describes the O phase as an incoherent array of nm-sized domains, each with local orbital orientations as in the O' phase.

The second PDF study [52] made use of the same data set, but employed a custom "big-box" modeling approach [53,54] based on a combination of geometric modeling and simulated annealing [52]. The key result was an atomistic configuration of $LaMnO_3$ that reproduced the experimental PDF while also preserving, within a predefined tolerance, the local geometry of all JT-distorted MnO_6 coordination polyhedra. In this configuration, there was some evidence for locally correlated orbital order of the antiferrodistortive C type; however, the magnitudes of the relevant correlation functions were 50 times smaller than in the ordered phase itself.

In hindsight, it is possible that the configurations obtained in this PDF study were actually realizations of the correlated disordered state of the anisotropic three-state Potts (3SP) model, as described in Ref. [34] and summarized here for completeness. The 3SP model is a statistical model in which each MnO_6 octahedron is free to adopt one of three possible states, corresponding to the three possible axes along which opposing pairs of long Mn–O bonds might orient. Neighboring octahedra interact via two terms governing coupling of JT orientations, chosen so as to ensure C-type orbital order as the system ground state. On heating, the model undergoes a first-order phase transition to a disordered state in which antiferrodistortive coupling is (initially) strictly preserved but long-range orbital order is lost. Whereas the ground state samples only two of the three possible Potts states, the disordered state samples all three; this distinction means that the disordered phase supports local orbital orientation correlations that do not occur in the ordered regime. A visual comparison of the two states is given in Figs. 2(a) and 2(b).

In anticipation of this study, we had carried out our own "big-box" modeling of the PDF data of Ref. [24] (see Supplemental Material [55] for summary). Our approach

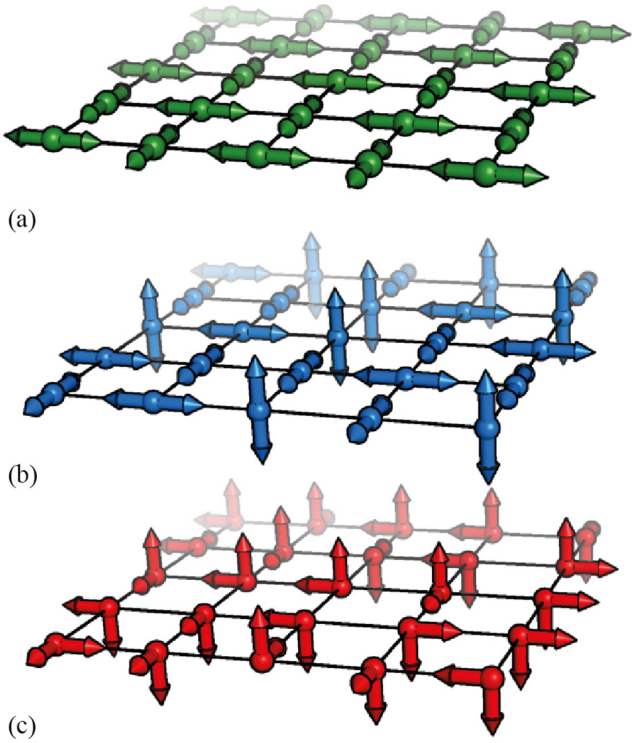


FIG. 2. Simplified orbital orientations in the (a) C-type, (b) 3SP-type, and (c) L-type orbital models, shown here for a single planar section of the Mn sublattice (spheres). Arrows represent the orientation of long Mn–O bonds.

had been to use the reverse Monte Carlo (RMC) method as implemented in RMCProfile [56]. Whereas the study of Ref. [52] had constrained MnO_6 geometries in terms of the JT distortion found in the low-temperature O' phase, our own modeling employed only data-based closest-approach and "distance-window" constraints that allow much greater geometric flexibility [56,57]. The unexpected but reproducible result of this analysis was a structural model in which the two long Mn–O bonds in each MnO_6 octahedron formed an angle of $\sim 90^\circ$ rather than $\sim 180^\circ$. Now adjacent to one another, the long Mn–O bonds form an "L" shape, and so we refer to this state as L-type orbital order [Fig. 2(c)]. One effect of this bond arrangement is an off-centering of the Mn^{3+} cation towards a single edge of its [MnO_6] coordination environment. Because there are 12 such edges, this arrangement would carry with it a much greater configurational degeneracy than either C- or 3SP-type orbital states. Our RMC configurations suggest not all such states are equally likely: instead, a definitive "ice-rules-like" constraint [58] emerged such that no two long Mn–O bonds were ever found to coincide at a single O atom. Even this local constraint leaves accessible a large configurational landscape associated with the L-type orbital order, as evidenced by the geometrically related "C2C" procrystalline arrangement described in Ref. [59]. Although unexpected for $LaMnO_3$, this type of distortion nevertheless relieves the electronic degeneracy of the Mn^{3+} ion (see Supplemental Material [55]) and is known to occur in some Mn^{3+} brownmillerites [60–62]. Consequently, the model could not be dismissed out of hand.

One might expect the three candidate models for orbital orientation correlations in O-phase $LaMnO_3$ shown in Fig. 2 to be distinguishable in terms of their ability to account for experimental neutron and x-ray total scattering data. We proceed to assess precisely this point. Anticipating our results, we will come to show that the three models, as physically different as they are, give rise to remarkably similar fits to data as a result of the large magnitude of thermal motion for $T > T_{JT}$.

III. METHODS

A. Sample preparation and characterization

A polycrystalline sample of stoichiometric $LaMnO_3$ (6.5 g) was prepared using the citrate gel method. Stoichiometric quantities of polycrystalline La_2O_3 and MnO_2 were dissolved in a minimum of 6 M nitric acid. Two molar equivalents of citric acid and 5 mL of ethylene glycol were added and the solutions heated with constant stirring [63]. The resulting gel was dried and ground to fine powder, placed in a crucible and heated in air to 1000 °C for 10 h. The powder was reground, pressed into pellets, and fired at 1350 °C under flowing oxygen for 40 h. Finally, the pellets were reground once more, pressed, and fired at 1350 °C under flowing argon. Phase purity was confirmed by x-ray diffraction and magnetization measurements [Fig. 1(d)]. The Néel temperature (T_N) was confirmed to be 140 K for our sample, which is in good agreement with previously reported values [64].

B. Neutron total scattering

Neutron total scattering data were collected using the GEM diffractometer at the ISIS pulsed neutron and muon source [65]. The polycrystalline $LaMnO_3$ sample was loaded into a cylindrical vanadium can of 8 mm diameter and 5.8 cm height, and placed in a custom-designed furnace. Total scattering data were collected over the reciprocal-space range $0.7 \leqslant Q \leqslant 40\,\text{Å}^{-1}$, corresponding to a real-space resolution of order $\Delta r \simeq 3.791/Q_{max} = 0.09\,\text{Å}$. Data collection times were optimized for total scattering measurements; we performed a total of six such measurements at temperatures of 523, 653, 753, 823, 903, and 973 K. In a separate experiment, we collected an additional neutron total scattering data set at 300 K. Both sample size and counting time were reduced for this measurement, yielding poorer counting statistics relative to our higher-temperature measurements.

Following collection, the total scattering data were corrected and placed on an absolute scale using standard methods as implemented in the GUDRUN software [66]. In this process, we took into account the effects of background scattering, absorption, multiple scattering, and beam intensity variations. As an additional precaution, and motivated by the significant phonon populations at the high temperatures at which our measurements were carried out, we explored the effects of successively including and omitting Placzek inelasticity corrections [67], and found no meaningful sensitivity to these corrections in our data. The Bragg profile function was extracted from the scattering data collected by the detector banks centered on $2\theta = 34^\circ$, 62°, 92°, and 146° and used as input for Rietveld analysis in the GSAS software [68]. The corrected total scattering data were also transformed to the pair

distribution function [we used the "$G^{\mathrm{PDF}}(r)$" normalization as defined in Ref. [69]], which was then used as input for real-space Rietveld analysis in the PDFGUI software [70].

C. X-ray total scattering

Variable-temperature x-ray total scattering data were measured using the high-energy I12 beamline at the Diamond Light Source [71] [x-ray wavelength $\lambda = 0.14577(1)$ Å]. A small fraction of the same polycrystalline sample of $LaMnO_3$ used for neutron scattering measurements was finely ground and loaded into a 1-mm quartz capillary. The capillary was mounted vertically on a rotatable goniometer, and the sample temperature adjusted using a hot air blower calibrated *in situ* with a thermocouple. A beam size of 1.5 mm × 1.5 mm was selected, and a Thales Pixium RF4343 2D detector (CsI scintillator, 430 mm × 430 mm) mounted 474 mm from the sample collected the data. Only the top half of the detector was used to avoid problems caused by pixel mismatch at the connection between the two halves. The beam was centered in the corner of this half to allow scattering to be detected to as high an angle as possible. X-ray total scattering data were collected at 10-K intervals from 523 to 973 K. For each temperature point, 600 one-second exposures were collected and then averaged. Background measurements were obtained using the scattering from an empty quartz capillary in an otherwise identical setup. Initial data processing was carried out using the FIT2D software [72]. A mask was used to remove dead pixels in the detector, and each image was integrated to give a one-dimensional scattering pattern. The integrated diffraction pattern was used directly for Rietveld refinements of the average crystal structure, making use of the TOPAS refinement software [73]. For PDF refinements, the integrated x-ray scattering data were used as input for the suite of standard background corrections and data normalization processes as performed using GUDRUNX [74]. This process yielded the normalized x-ray PDF as defined in Ref. [69]. The usable maximum magnitude Q_{max} of the x-ray total scattering function was 22.5 $\mathrm{Å}^{-1}$.

For ease of representation, we use the term $G(r)$ to refer to both neutron and x-ray PDFs in the particular normalizations outlined above.

D. Comparative PDF refinements

PDF refinements were carried out using the PDFGUI software as described in Ref. [70]. In our study, we compare the quality of fits for three orbital-correlation models: *C*-type, 3SP-type, and *L*-type, as summarized in Fig. 2. In order to allow statistically meaningful direct comparison amongst fits, we identified a suitable small-box approximant for each model such that all three models shared a common number of structural degrees of freedom. This approximant approach is described fully in Ref. [9], but we proceed to summarize the key points here. The concept is to fit the low-*r* PDF data in terms of a small-box model derived from the known average structure by a specifically chosen symmetry-lowering perturbation. While it is understood that this symmetry-breaking process can in general propagate in so many different ways as to give a large manifold of degenerate disordered states, the approximant represents the highest-symmetry arrangement of the particular perturbation of interest. In this way, the number of refinable parameters is kept to a minimum. Hence, one expects the quality of PDF fit to decrease as the *r* range included in the fit increases. In our PDF fits, we compare the results for three combinations of PDF data: (i) $1.5 \leqslant r \leqslant 6$ Å neutron $G(r)$, (ii) $1.5 \leqslant r \leqslant 6$ Å neutron + x-ray $G(r)$, and (iii) $1.5 \leqslant r \leqslant 10$ Å neutron + x-ray $G(r)$. The PDFGUI parameters δ_1, Q_{damp} (x-ray), and Q_{damp} (neutron) were fixed at values of 1.7, 0.0486, and 0.0343 $\mathrm{Å}^{-1}$, respectively.

We proceed to describe the three specific approximant models used in our comparative PDF refinements. In each case, we identify the highest-symmetry perturbation of a common parent structure that captures the relevant local orbital correlations for a given model and then parametrize the orbital-driven JT distortion using a single, refinable, distortion parameter (we call this δ). The common parent, or reference, structure was determined as follows. Conventional Rietveld refinement against x-ray and neutron Bragg diffraction data collected at each temperature gave an average structure model in the space group *Pnma*. For each temperature point, the corresponding octahedral tilt magnitude ϕ was then determined from the oxygen atom positions according to the approach outlined in Refs. [23,75]. The reference structure for a given temperature is then also described by the space group *Pnma*, with precisely the same lattice parameters as determined by Rietveld refinement and with La and Mn atoms on their conventional sites (4*c* and 4*b* Wyckoff positions, respectively), but with the oxygen positions now determined solely by the octahedral tilt angle [75]:

$$
\begin{aligned}
x_{\mathrm{O1}} &= \frac{\cos^2\phi - 1}{2\cos^2\phi + 4}, \\
y_{\mathrm{O1}} &= \frac{1}{4}, \\
z_{\mathrm{O1}} &= \frac{\sqrt{3} + \tan\phi}{\sqrt{12}}, \\
x_{\mathrm{O2}} &= \frac{2 - \sqrt{3}\sin\phi\cos\phi + \cos^2\phi}{8 + 4\cos^2\phi}, \\
y_{\mathrm{O2}} &= -\frac{\tan\phi}{\sqrt{48}}, \\
z_{\mathrm{O2}} &= \frac{3\sqrt{3} + \tan\phi}{\sqrt{48}}.
\end{aligned}
\tag{1}
$$

In this way, the reference structure effectively represents the Rietveld-refined *Pnma* structure with JT distortions removed.

1. *C*-type orbital correlations

For the small-box approximant used to model *C*-type orbital correlations, the relevant distortion parameter must give rise to the correlated JT distortion pattern observed in the (orbital ordered) *O*′ phase as observed experimentally. This type of orbital order has the same space-group symmetry as that of the activated tilts, so this approximant shares the *Pnma* symmetry of the reference structure. The distortion parameter δ is implemented in PDFGUI as a variation in the O2 atom

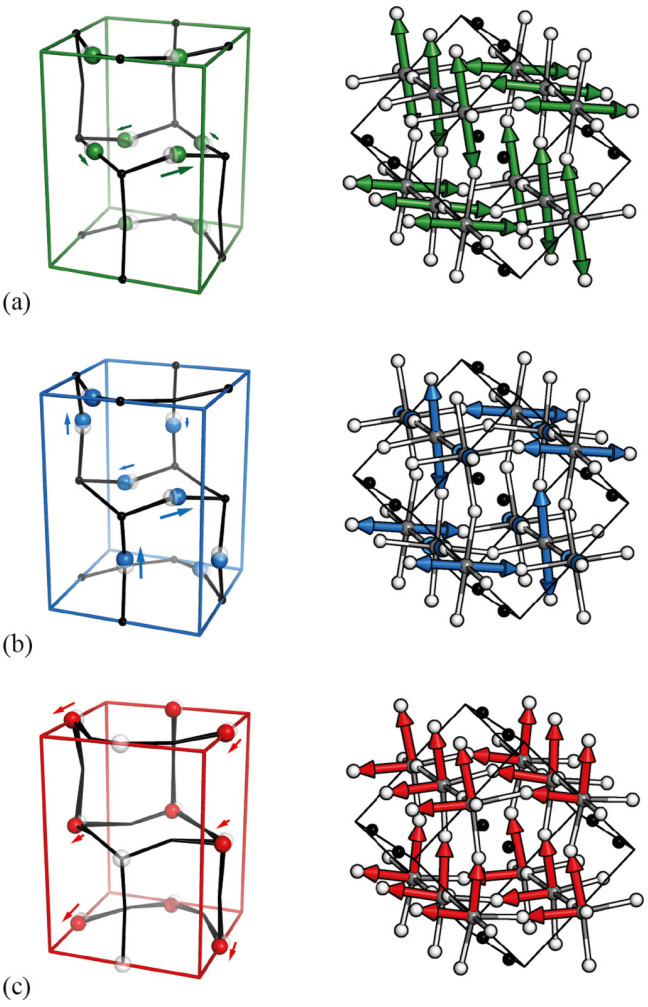


FIG. 3. Representation of the small-box approximants used in our PDF study of orbital disordered $LaMnO_3$. (a) *C*-type order is generated by collective displacement of O2 atoms (green arrows, left), preserving the *Pnma* symmetry of the undistorted parent structure. (b) 3SP-type order is generated by collective displacements of both O1 and (some) O2 atoms, as indicated by the blue arrows in the left-hand panel. This arrangement has $P2_1/n11$ symmetry (c) *L*-type order results from collective displacement of Mn atoms (red arrows, left) to give an approximant with $Pnm2_1$ symmetry. In each case, the corresponding arrangement of long Mn–O bonds is shown by the arrows in the right-hand panels.

position, giving the local orbital correlation pattern shown in Fig. 3(a). The relationship between atom positions and positional parameters in the reference and approximant models is given explicitly in Table I.

PDFGUI refinements using this approximant model make use of total of 10 variable parameters (see Ref. [70] for definitions): (i) Q_{broad}, (ii) an overall scale factor, (iii) a relative scale factor for x-ray versus neutron data sets, (iv), (v) the x_{La} and z_{La} positional parameters of the La atom site, (vi) the JT distortion parameter δ, and (vii)–(x) isotropic displacement parameters for each of the La, Mn, O1, and O2 sites.

2. 3SP-type orbital correlations

For the 3SP-type orbital model we use the highest-symmetry subgroup of *Pnma* which permits JT distortions in the out-of-plane (*b*-axis) direction. Distortion mode analysis using the ISOTROPY software suite [76] identified $P2_1/n11$ as the relevant subgroup, where we have used an unconventional setting of the $P2_1/c$ space group in order to facilitate direct comparison between reference and approximant structures. The monoclinic distortion angle α was fixed at 90° for the same reason. So as to describe a 3SP-type collective JT distortion in terms of the single parameter δ it was necessary for this parameter to vary the positions of both O1-type and O2-type oxygen atoms. Our specific implementation is given in Table I, and was chosen so as to ensure similar magnitudes of in-plane and out-of-plane JT distortions. The corresponding orbital correlation pattern is shown in Fig. 3(b). By design, the total number of variable parameters for this approximant is identical to that for the *C*-type model described above.

3. L-type orbital correlations

Our third and final approximant model corresponds to the alternate JT distortion that had emerged from our preliminary RMC analysis, i.e., angles of about 90° between the two long Mn–O bonds at each Mn site. Distortion mode analysis using the ISOTROPY suite identified $Pnm2_1$ as a relevant subgroup of highest symmetry. (Again we use an unconventional setting of the space group $Pmn2_1$ to facilitate comparison among our various small-box models.) In our preliminary RMC configurations, there was little evidence for distortion of the O_6 coordination octahedra around each Mn; rather, the JT distortion was accommodated by displacement of the Mn atom away from the center of each such octahedron. Consequently, the distortion parameter δ no longer influences the O1 or O2 atom positions in this approximant model, but instead displaces the Mn atoms towards an edge of the corresponding octahedral MnO_6 coordination environments. Our RMC refinements indicated a preference for locally ferroelectric Mn displacement patterns; the $Pnm2_1$ approximant is the simplest model that captures these Mn correlations. This distortion is shown in Fig. 3(c) and the implementation in PDFGUI is given explicitly in Table I. We note for completeness that the total number of free variables is again conserved for this model. More complex approximants in which Mn displacements included out-of-plane components are conceivable but would require a larger number of variables to be refined.

E. Single-crystal diffuse scattering calculations

Single-crystal diffuse scattering patterns were generated from explicit atomistic realizations of the 3SP- and *L*-type orbital disorder states. In the former case, it is the positions of apical O atoms that determines orbital orientations; in the latter case, the key component involves Mn displacements. So that we might calculate diffuse scattering for large ($20 \times 20 \times 20$) supercells, and hence obtain smoothly continuous diffraction patterns, we excluded the ordered component from our atomistic configurations. The role of dynamic disorder was not taken into account. The calculations themselves were carried out using the SINGLECRYSTAL software [77].

TABLE I. Relationship between atom positions in reference and approximant small-box models as described in the text. For each model, and for each atomic site, the relevant Wyckoff position is given together with the atom coordinates used as input in PDFGUI refinements. Whereas the values of the parameters x_{La} and z_{La} were taken directly from the results of our Rietveld refinements, the values $x_{O1}, z_{O1}, x_{O2}, y_{O2}, z_{O2}$ were determined using Eq. (1). Only those parameters marked by an asterisk were allowed to vary during PDFGUI refinements; variable parameters with the same symbol for a given model were constrained to assume identical values. All models share the same unit-cell axes, and hence lattice parameters.

Space group and origin shift	Reference structure *Pnma*; [0,0,0]		*C*-type *Pnma*; [0,0,0]		3SP-type $P2_1/n11$; [0,0,0]		*L*-type $Pnm2_1$; $[\frac{1}{4},\frac{1}{4},0]$	
La	4*c*	$(x_{La}, \frac{1}{4}, z_{La})$	4*c*	$(x^*_{La}, \frac{1}{4}, z^*_{La})$	4*e*	$(x^*_{La}, \frac{1}{4}, z^*_{La})$	2*a*	$(x^*_{La}, \frac{1}{4}, z^*_{La})$
							2*a*	$(-x^*_{La}, \frac{3}{4}, -z^*_{La})$
Mn	4*b*	$(0,0,\frac{1}{2})$	4*b*	$(0,0,\frac{1}{2})$	2*b*	$(0,0,\frac{1}{2})$	4*b*	$(0,0,\frac{1}{2}+\delta^*)$
					2*d*	$(\frac{1}{2},0,0)$		
O1	4*c*	$(x_{O1}, \frac{1}{4}, z_{O1})$	4*c*	$(x_{O1}, \frac{1}{4}, z_{O1})$	4*e*	$(x_{O1}, \frac{1}{4}-\delta^*, z_{O1})$	2*a*	$(x_{O1}, \frac{1}{4}, z_{O1})$
							2*a*	$(-x_{O1}, \frac{3}{4}, -z_{O1})$
O2	8*d*	(x_{O2}, y_{O2}, z_{O2})	8*d*	$(x_{O2}+\delta^*, y_{O2}, z_{O2}+\delta^*)$	4*e*	$(x_{O2}+\delta^*, y_{O2}, z_{O2}+\delta^*)$	4*b*	(x_{O2}, y_{O2}, z_{O2})
					4*e*	$(x_{O2}+\frac{1}{2}, y_{O2}, \frac{1}{2}-z_{O2})$	4*b*	$(-x_{O2}, -y_{O2}, -z_{O2})$

IV. RESULTS AND DISCUSSION

A. Neutron and x-ray diffraction: The average structure

Our starting point was to determine the temperature-dependent behavior of the average structure of $LaMnO_3$ over the temperature range $300 \leqslant T \leqslant 1000$ K, as reflected by the Bragg component of the neutron and x-ray total scattering functions. Using Rietveld refinement, we determined the variation in unit-cell parameters with temperature; our results [Fig. 4(a)] clearly identify the isosymmetric phase transition between O' and O phases on heating above $T_{JT} \simeq 750$ K. We used this transition to cross calibrate the sample temperatures of x-ray and neutron measurements. We find the transition to be accompanied by a volume collapse of $-0.1499\,\mathrm{cm^3\,mol^{-1}}$ [Fig. 4(a)], which is similar to the value of $-0.1535\,\mathrm{cm^3\,mol^{-1}}$ noted in Ref. [39]. The reciprocal-space resolution of our measurements is marginally poorer than that used in the study of Ref. [39] (a consequence of optimizing for real-space resolution); this discrepancy is likely responsible for the small unphysical fluctuation in molar volume near T_{JT}. The most reliable structural models were obtained using Rietveld refinement of our neutron scattering measurements. The results of our refinements for the seven such temperature points spanning O' and O phases are given in Table II; these values are consistent with those reported in Ref. [23]. In some parameters there is a small discontinuity between our refined values at 300 and 523 K which we attribute to the poorer counting statistics for the former data set (see Supplemental Material [55] for further discussion). As anticipated from our discussion in Sec. II A, we find the key consequences of orbital disorder within the O phase to be (i) the emergence of a pseudocubic lattice metric, (ii) the near equivalence of Mn–O bond lengths, and (iii) the increase in atomic displacement parameters.

Although the sensitivity of x-ray scattering data to O atom positions is markedly reduced when interrogated in the absence of accompanying neutron scattering data, we nevertheless obtained satisfactory Rietveld refinements at all temperature points probed in our x-ray study. In this way we obtained insight into crystallographic variations across the orbital order/disorder transition at a much finer temperature interval than was feasible from our neutron scattering measurements.

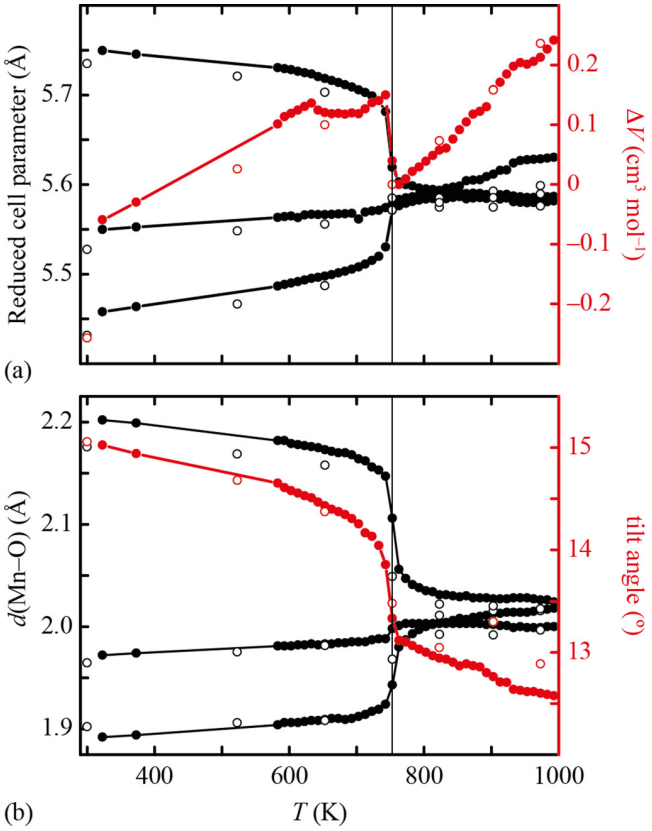


FIG. 4. Temperature-dependent structural variation in $LaMnO_3$ as determined using Rietveld analysis of x-ray (filled symbols) and neutron (open symbols) total scattering data. (a) The unit-cell metric becomes pseudocubic at T_{JT} with a volume collapse of about $0.15\,\mathrm{cm^3\,mol^{-1}}$. (b) The three crystallographically distinct Mn–O bond lengths also converge at T_{JT}; a modest variation in tilt angle also accompanies the transition.

TABLE II. Structural parameters for $LaMnO_3$ as determined by Rietveld refinement against neutron Bragg diffraction patterns. Included are the two crystallographically distinct Mn–O–Mn bond angles (θ_1,θ_2), from which the octahedral tilt parameter ϕ was determined according to the method outlined in Ref. [23].

T (K)	300	523	653	753	823	903	973
Phase	O'	O'	O'	O	O	O	O
a (Å)	5.73484(4)	5.72072(4)	5.70290(5)	5.58482(13)	5.57448(11)	5.57446(7)	5.57592(8)
b (Å)	7.68113(5)	7.73080(7)	7.75978(8)	7.8791(3)	7.8910(2)	7.89888(18)	7.90448(18)
c (Å)	5.52744(3)	5.54801(4)	5.55559(4)	5.57204(18)	5.58503(16)	5.59239(9)	5.59864(9)
x_{La}	0.04884(7)	0.04397(8)	0.04041(10)	0.02522(17)	0.02136(12)	0.02026(14)	0.01703(14)
z_{La}	0.00802(8)	0.00683(10)	0.00624(12)	0.0041(5)	0.0036(3)	0.0023(5)	0.0014(3)
x_{O1}	0.98790(9)	0.98869(12)	0.98973(14)	0.9905(3)	0.9902(3)	0.9921(3)	0.9911(3)
z_{O1}	0.57395(9)	0.57258(12)	0.57183(13)	0.5691(5)	0.5692(3)	0.5708(4)	0.5675(3)
x_{O2}	0.19346(7)	0.19565(7)	0.19789(8)	0.2156(3)	0.22025(19)	0.2241(2)	0.22411(18)
y_{O2}	0.96418(5)	0.96210(6)	0.96274(6)	0.9619(2)	0.96226(14)	0.96384(19)	0.96247(14)
z_{O2}	0.77436(8)	0.77297(10)	0.77200(12)	0.7741(3)	0.7758(2)	0.7756(2)	0.7730(2)
U_{iso}(La) (Å^2)	0.00520(12)	0.00365(12)	0.00420(13)	0.00610(18)	0.01381(19)	0.01595(13)	0.0162(2)
U_{iso}(Mn) (Å^2)	0.00227(19)	0.00058(19)	0.0013(2)	0.0038(3)	0.00874(19)	0.01020(17)	0.0111(2)
U_{iso}(O1) (Å^2)	0.00679(17)	0.00647(18)	0.0087(2)	0.0152(5)	0.0228(4)	0.0266(5)	0.0274(5)
U_{iso}(O2) (Å^2)	0.00603(12)	0.00482(12)	0.00649(14)	0.0130(3)	0.0210(3)	0.0238(3)	0.0253(4)
θ_1 (deg)	155.63	156.17	156.51	157.67	157.62	156.95	158.16
θ_2 (deg)	155.12	155.81	156.47	158.24	158.76	159.52	159.68
ϕ (deg)	15.06	14.68	14.37	13.48	13.33	13.30	12.89

In Fig. 4(b) we show the evolution of Mn–O bond lengths and octahedral tilt angles as a function of temperature across this transition. We find the expected discontinuous convergence of Mn–O bond lengths, together with a small variation in tilt angle at T_{JT} that (to the best of our knowledge) has not been reported in previous studies [23,39]. Our conclusion in these various respects is simply that our sample and the temperature dependence of its average structure are entirely consistent with previous observations of stoichiometric $LaMnO_3$.

B. Neutron and x-ray PDF: Direct analysis

The temperature-dependent variation in neutron and x-ray $G(r)$ functions is shown in Fig. 5. These data represent the key experimental results of our study. We note in particular that the previous PDF studies of Ref. [52] do not include x-ray PDF measurements; moreover, the neutron PDFs as reported do not allow for direct comparison at distances beyond the nearest Mn–O separation. While our x-ray PDF data show little sensitivity to pairwise correlations involving O atom positions, their temperature-dependent behavior is nevertheless indirectly sensitive to cooperative JT phenomena *via* coupling between O displacements and Mn and La atom positions. In our data, we find excellent consistency in PDFs obtained from independent measurements at different temperatures, with a high ratio of signal to noise. The persistence of JT distortions within the orbital disordered O phase is directly evident in the asymmetry of the nearest-neighbor Mn–O peak of the neutron PDF ($r \simeq 2$ Å; note the peak is inverted as a consequence of the negative neutron scattering length of Mn). The reduced real-space resolution of our x-ray PDF data, together with the low x-ray scattering power of Mn and O atoms (relative to La) means that we cannot resolve the JT distortion directly from our x-ray PDF measurements. Nevertheless, in these respects our data are entirely consistent with the results of earlier PDF studies [24,52].

What is particularly notable in our PDF data is the clear signature of a discontinuous change in PDFs, both neutron and x ray, across the O'/O orbital order/disorder transition that involves correlations at interatomic distances commensurate with the unit-cell dimensions. This discontinuity is evident in the raw PDF data themselves [Figs. 5(a) and 5(b)] but is even more clearly identified by considering the relative changes in $G(r)$ at specific values of $r < 6$ Å. For a given separation of interest r', we used separate linear fits to the $G(r = r',T)$ function for temperatures $T < T_{JT}$ and $T > T_{JT}$ to identify expectation values $\tilde{G}_{O'}$ and $\tilde{G}_O$ at 500 and 1000 K (i.e., deep within the O' and O regimes, respectively). Using these expectation values we form the local order parameter [78]

$$x(r',T) = \frac{G(r',T) - \tilde{G}_O}{\tilde{G}_{O'} - \tilde{G}_O}, \tag{2}$$

which (by construction) tends to unity as $T \to 500$ K and to zero as $T \to 1000$ K. This process allows us to compare meaningfully the smoothness in variation of $G(r)$ with T for different interatomic separations across both x-ray and neutron PDFs. We calculated $x(r',T)$ functions for seven representative pairwise separations r' in both neutron and x-ray PDFs; the results are shown in Fig. 5(c) and clearly identify a discontinuous variation in $G(r)$ at T_{JT}. This behavior is entirely consistent with the EXAFS and XANES studies of Refs. [42,46], which also measured a greater difference in signal across T_{JT} than for comparable temperature intervals within either the O' or O phases.

In conventional order/disorder transitions, such as that between the α and β phases of SiO_2 cristobalite [79] or the primitive and body-centered phases of Cu_3Au [80,81], the PDF is unchanged at the transition itself for short distances.

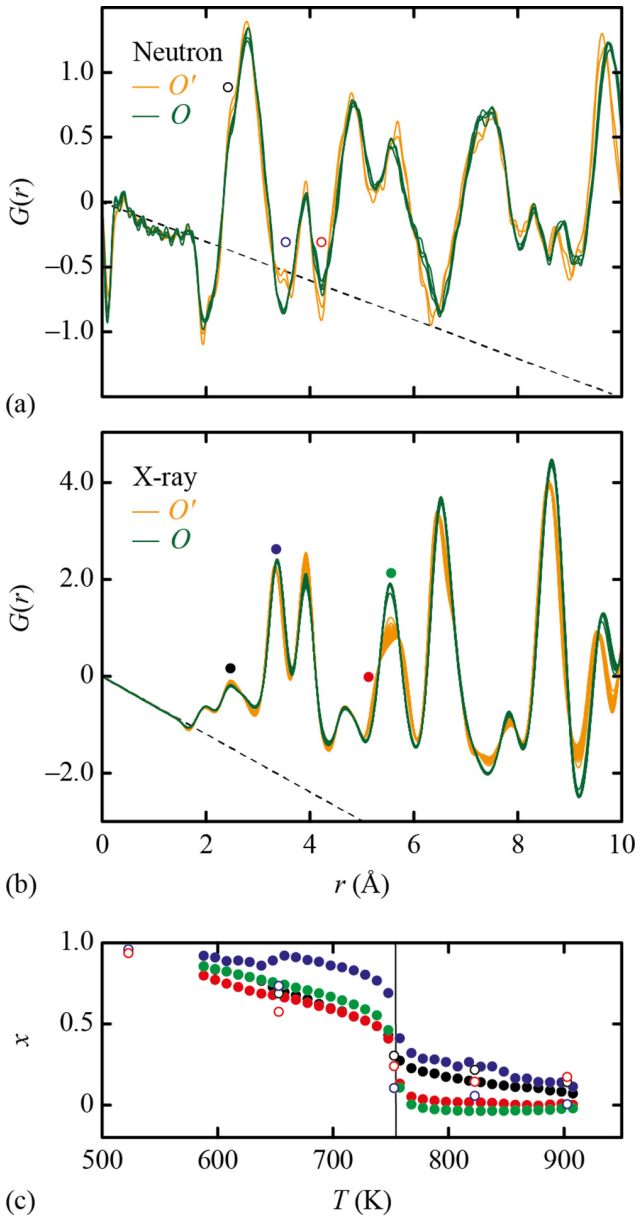


FIG. 5. Temperature-dependent variation in (a) neutron and (b) x-ray PDFs across the O' (orange lines) / O (green lines) transition. In both (a) and (b) the PDF baseline is indicated as a dashed black line. (c) The normalized temperature dependence of PDF intensities x (see main text for derivation) at a variety of key interatomic separations clearly reveals a discontinuous change in local structure accompanying the orbital order/disorder transition. The relevant interatomic separations are indicated in (a) and (b) using open and filled circles (neutron and x-ray data, respectively); these symbols correspond to those used in (c) to represent the corresponding temperature dependence.

This is because the local structure in both ordered and disordered states is essentially identical. At high temperatures, the local distortions present within the disordered state are not correlated over macroscopic length scales, but the correlation length diverges on cooling towards the transition temperature. Hence, such transitions are accompanied by discontinuities in the Bragg diffraction pattern (which is sensitive to long-range correlations), without any abrupt change in the accompanying PDF (sensitive to short-range correlations). It is only at larger separations (e.g., the Si . . . Si separation in cristobalite [79]) that significant changes in the PDF are evident. Instead, the behavior we observe for $LaMnO_3$ at T_{JT} reflects a local structure transition, as observed in, e.g., the metal-organic frameworks UiO-66 and NU-1000 during solvent removal [82] or indeed across the metal-insulator transition in VO_2 (Ref. [83]) or the doped manganites $La_xCa_{1-x}MnO_3$ [27]. Consequently, we can be confident that the orbital order/disorder transition in $LaMnO_3$ involves a discontinuous change in local structure, which in turn implies that orbital arrangements within the high-temperature O phase may be meaningfully different to those in the ordered O' phase [84]. In this respect, we anticipate that the C-type orbital correlation model should not provide a meaningful description of local orbital correlations in the O phase. We comment that, given that isosymmetric transitions are intrinsically first-order [40], it would be difficult to rationalize the bulk thermodynamic anomalies of $LaMnO_3$ at T_{JT} in the absence of any discontinuity in local structure.

C. Neutron and x-ray PDF: PDFGUI analysis

In order to achieve a deeper understanding of the local orbital order in O-phase $LaMnO_3$, we proceeded to carry out a series of small-box PDF refinements using the PDFGUI suite of programs [70]. We consider the three orbital correlation models described in Sec. III D, and interpret the contrasting ability of these models to account for both x-ray and neutron $G(r)$ functions at distances $\leqslant 6$ Å. The importance of this particular 6-Å distance is twofold: first, it is commensurate with the unit-cell dimensions, and so represents a lengthscale that is large enough to be sensitive to differences in the various models we study, but also small enough that the use of approximants remains valid; and, second, it includes the various interatomic separations highlighted in Fig. 5(c) for which we know $G(r,T)$ to be discontinuous at T_{JT}. For completeness, we will also compare these results with fits to neutron data alone, and also with fits to combined neutron and x-ray PDFs carried out over the larger range of separations $1.5 \leqslant r \leqslant 10$ Å. Such comparisons will allow us insight into the robustness of any conclusions drawn with respect to the particular relative weighting of x-ray and neutron data, on the one hand, and value of r_{max} over which fitting is carried out, on the other hand.

Within the orbital-ordered O' regime, the PDF data show a clear preference for the C-type orbital correlation model. We demonstrate this point in Fig. 6(a), where we compare the quality of fits for all three models to the neutron $G(r)$ collected at 653 K. Despite the meaningful differences among the three models, and the clear indication from conventional (average structure) interpretation of the diffraction pattern that $LaMnO_3$ exhibits C-type orbital order at this temperature, the differences in quality of fit for the three models are probably much smaller than intuition might have suggested. Nevertheless, the L-type model clearly results in a significantly poorer fit throughout the whole r region, and the 3SP-type model cannot capture the correct shape of the nearest-neighbor Mn–O peak while also fitting the remainder of the PDF. The

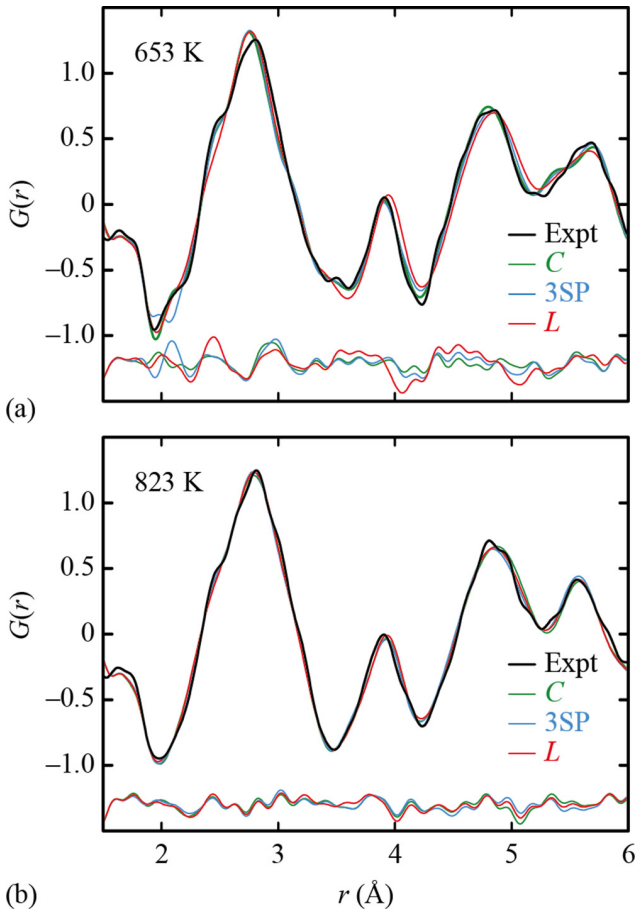


FIG. 6. Neutron PDF fits for data collected within the (a) O' and (b) O regimes. Experimental data are shown as black lines, and fits shown in green (C-type order), blue (3SP-type order), and red (L-type order). The corresponding difference functions (data − fit) are shown in the relevant color, shifted vertically by 1.25 units. The fits shown here were for PDFGUI refinements involving simultaneous fits to x-ray PDFs (see Supplemental Material [55]).

refined parameters and qualities of fit are given explicitly in Table III.

The magnitude of JT distortion is accounted for by the fitting parameter δ, which is related to the difference between long and short Mn–O bond lengths. Simple geometric considerations give

$$\Delta d(\text{Mn–O}) \simeq k|\delta|\sqrt{a^2 + c^2}, \tag{3}$$

where the proportionality factor $k = 2$ for the C- and 3SP-type models, and $k = 1$ for the L-type model. For the C-type model fitted against neutron and x-ray PDF data collected at 653 K (i.e., within the orbital order regime) we obtain a JT distortion of 0.25 Å, which is remarkably similar to the value obtained from Rietveld refinement against Bragg intensities [Δd(Mn–O) $\simeq$ 0.25–0.3 Å; Fig. 4(c)]. Despite their poorer fits, both 3SP- and L-type models give similar distortions, showing this result is robust to choice of modeling approach. These results are entirely consistent with earlier PDF studies [24,52].

Within the orbital disorder regime, the situation is substantially less clear cut. In Fig. 6(b), we compare the fits for our three models against the neutron $G(r)$ function collected at 823 K, i.e., within the O phase. These fits are remarkably similar and cannot be discriminated by eye. Numerically, we find the 3SP-type orbital correlation model describes the data best, but the corresponding R_{wp} value is only marginally lower than that for either the C- or L-type models (Table III). Moreover, different fitting protocols (neutron only versus neutron + x ray, or $r_{\text{max}} = 6$ Å versus 10 Å, result in variations in R_{wp} that are of the same order of magnitude as the differences between candidate models. We quantify this point by comparing in Fig. 7 the relative quality of fit

$$\chi = \frac{R_{\text{wp}}}{\langle R_{\text{wp}} \rangle} - 1 \tag{4}$$

for our three models and three different fitting regimes as a function of temperature. The value of χ reflects the extent to which a particular model fits more closely ($\chi < 0$) or less closely ($\chi > 0$) than the average fit obtained for a given temperature point. So, at 653 K, for example, the C-type orbital model gives the best fit irrespective of the particular fitting protocol adopted. For temperatures above T_{JT}, however, the best-fit model can depend on the fitting protocol, which means that it is not possible to identify unambiguously the orbital arrangement pattern within the O phase from quality of PDF fit alone. We attribute this insensitivity to the large magnitude of thermal motion at temperatures for which the orbital disordered state is observed. Indeed, the relatively large uncertainties we observe for the set of PDF parameters Q_{broad}, δ, U_{iso} are a clear indication of the difficulty of separating the individual effects of instrumental resolution, thermal motion, and static orbital disorder at these elevated temperatures (Table III). If we recalculate the PDFs for each model using the same parameters obtained in our PDFGUI refinements but reduce the magnitude of thermal parameters to ambient-temperature values, then much clearer differences among the various fits emerge (see Supplemental Material [55]).

Nevertheless, we can draw some general conclusions from the results shown in Fig. 7. Throughout the orbital disorder regime, the 3SP-type arrangement nearly always gives the highest-quality fit to data, even if the relative χ values for the C- and L-type models depend on the particular fitting protocol used. Moreover, for what we consider to be the most meaningful choice of fitting parameters (neutron and x-ray data, with $r_{\text{max}} = 6$ Å), the 3SP-type model consistently represents the data most closely. Consequently, we cautiously suggest that the local orbital arrangements in orbital disordered $LaMnO_3$ are more accurately described by the 3SP model of Ref. [34] than either the C-type arrangement of the ambient-temperature phase, i.e., as proposed in the PDF study of Ref. [24] or the L-type arrangement that emerges from RMC analysis.

This conclusion is supported by two other observations. First, we might have already reasonably ruled out the C-type arrangement on the basis that we observe a discontinuous change in PDF at T_{JT}. Were the orbital arrangements within the high-temperature phase to share the same pattern as the low-temperature ordered phase, then there would be no reason

TABLE III. Model parameters for $LaMnO_3$ as determined by PDFGUI refinement against both neutron and x-ray PDFs. The highest-quality fit for each temperature point is highlighted in bold: we find the *C*-type approximant to best describe the orbital-ordered state (as anticipated from the average structure), and the 3SP-type approximant to best describe the orbital disordered state, at all temperature points investigated.

	T(K)	Q_{broad} (Å^{-1})	Scale1	Scale2	x_{La}	z_{La}	δ	U_{iso}(La) (Å^2)	U_{iso}(Mn) (Å^2)	U_{iso}(O1) (Å^2)	U_{iso}(O2) (Å^2)	R_{wp}(%)
C	**653**	**0.19(12)**	**0.162(16)**	**0.21(6)**	**0.036(6)**	**0.0120(8)**	**−0.016(5)**	**0.008(7)**	**0.013(15)**	**0.02(2)**	**0.025(12)**	**12.3875**
	753	0.19(13)	0.159(18)	0.20(5)	0.022(9)	0.009(14)	−0.014(7)	0.008(9)	0.02(2)	0.03(5)	0.037(19)	10.7698
	823	0.18(13)	0.160(19)	0.20(5)	0.019(11)	0.010(14)	−0.014(8)	0.009(10)	0.02(2)	0.04(7)	0.04(2)	10.9087
	903	0.17(12)	0.159(19)	0.20(5)	0.017(12)	0.009(16)	−0.013(9)	0.010(10)	0.02(2)	0.05(9)	0.04(3)	10.8627
	973	0.13(11)	0.16(2)	0.18(5)	0.012(17)	0.00(5)	0.013(13)	0.015(12)	0.03(2)	0.04(11)	0.06(5)	10.8156
3SP	653	0.18(12)	0.161(16)	0.21(6)	−0.036(6)	0.012(8)	−0.014(5)	0.008(6)	0.017(18)	0.014(18)	0.028(15)	13.6527
	753	**0.18(13)**	**0.159(18)**	**0.20(5)**	**−0.022(9)**	**0.007(18)**	**−0.014(7)**	**0.009(10)**	**0.02(2)**	**0.03(5)**	**0.04(2)**	**10.4497**
	823	**0.15(12)**	**0.161(19)**	**0.20(5)**	**−0.018(11)**	**0.01(3)**	**0.013(8)**	**0.011(12)**	**0.02(2)**	**0.03(7)**	**0.05(4)**	**10.6293**
	903	**0.15(12)**	**0.161(19)**	**0.20(5)**	**−0.016(13)**	**0.00(4)**	**0.015(10)**	**0.013(12)**	**0.03(2)**	**0.03(8)**	**0.05(5)**	**10.4781**
	973	**0.13(12)**	**0.16(2)**	**0.18(5)**	**−0.014(17)**	**0.00(6)**	**0.012(10)**	**0.015(12)**	**0.03(2)**	**0.04(5)**	**0.08(17)**	**10.6128**
L	653	0.16(12)	0.164(17)	0.21(5)	−0.034(8)	0.011(17)	0.033(12)	0.011(8)	0.013(19)	0.02(3)	0.04(2)	16.3559
	753	0.16(10)	0.161(18)	0.20(5)	−0.020(12)	0.01(3)	0.027(17)	0.012(9)	0.02(3)	0.04(8)	0.04(3)	11.0794
	823	0.15(10)	0.162(18)	0.20(5)	−0.017(14)	0.01(4)	0.028(19)	0.013(10)	0.02(4)	0.05(11)	0.05(4)	10.7938
	903	0.15(10)	0.161(19)	0.20(5)	−0.016(15)	0.01(4)	0.03(2)	0.014(12)	0.02(4)	0.05(13)	0.05(5)	10.5081
	973	0.14(10)	0.16(2)	0.18(5)	−0.013(18)	0.00(4)	0.03(2)	0.016(14)	0.02(5)	0.06(18)	0.05(6)	10.6526

for such a discontinuity. And, second, of the two models with different orbital arrangements to that of the ordered phase, it is the 3SP-type arrangement that contains the more conventional local JT distortion of MnO_6 octahedra. While the off-centered distortion of the *L*-type model is not without precedent in the structural chemistry of manganites [60–62], the 180° arrangement of long Mn–O bonds is unquestionably the more frequently observed JT distortion for octahedral Mn^{3+} [36]. One might also have expected a clearer discontinuity in the manganese atomic displacement parameter at T_{JT} were the *O* phase to involve Mn off centering.

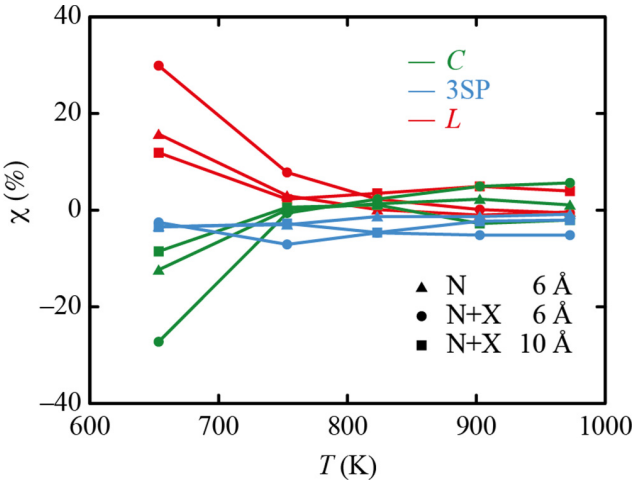


FIG. 7. Relative goodness of fit χ for the various PDF fits described in the text. The three orbital arrangement models are given in the same colors as in Fig. 6. The different symbols correspond to different fitting protocols: triangles indicate fits to neutron PDF data alone over the real-space range $1.5 \leqslant r \leqslant 6$ Å, circles to both neutron and x-ray data over the same range, and squares to both data sets but over the increased range $1.5 \leqslant r \leqslant 10$ Å. We expect the approximant approach to become less reliable at larger r values, so the most reliable fits correspond to those shown using circles; details of the various refined parameters for these fits are given in Table III.

D. Single-crystal diffuse scattering

In principle, one might expect greater sensitivity in distinguishing these three models using single-crystal diffuse scattering measurements than PDFs, which are derived from the same scattering function but only after orientational averaging [85]. We are not aware of any published single-crystal scattering patterns (either x-ray or neutron) for $LaMnO_3$ within the orbital disorder regime, and the collection of such data was beyond the scope of our own study. Nevertheless, the qualitative form of structured diffuse scattering anticipated for different orbital disorder models is straightforwardly calculated and may be of use in future investigations. We proceed to present the results of two such calculations for the 3SP- and *L*-type disorder models, noting that the *C*-type orbital disorder model would result only in a diffuse component centered on Bragg reflections of the parent orbital-ordered *Pnma* phase.

Using a Monte Carlo approach, we generated atomistic configurations representing a $20 \times 20 \times 20$ supercell of the aristotypic perovskite lattice, in which atomic displacements had been introduced to capture the key correlations in the 3SP- and *L*-type models of orbital disorder in $LaMnO_3$. High-symmetry planes of the corresponding diffraction patterns are shown in Fig. 8, from which it is evident that, in the absence of thermal disorder, both models would result in highly structured diffuse scattering as anticipated for correlated disordered states [86]. In both cases, this scattering takes the form of diffuse rods of intensity oriented parallel to the $\langle 100 \rangle^*$ axes of the parent reciprocal lattice, with subtly different reflection conditions within the $(hk0)$ plane. The 3SP model also gives rise to a more structured background scattering pattern, which is most clearly seen here in the (hhl) scattering plane [Fig. 8(a)].

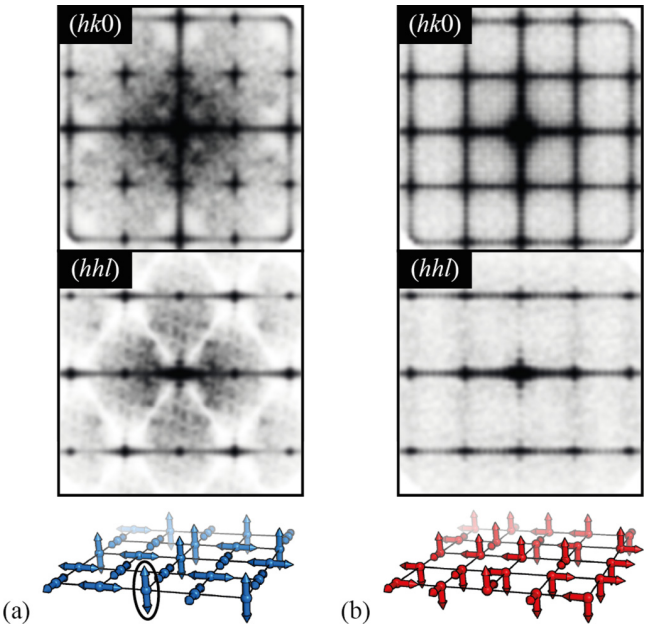


FIG. 8. Calculated single-crystal diffraction patterns for (a) 3SP-type and (b) L-type orbital disorder models as described in the text. The reciprocal space labels are given relative to the reciprocal lattice of the cubic aristotype. The corresponding orbital-driven distortions are represented figuratively in the configurational sections shown at the bottom of each panel. Our analysis identifies the 3SP-type model as the most likely description of the orbital disordered state; we note that this arrangement destroys the inversion center at Mn sites (e.g., for the circled Mn center).

Despite the existence of some differences between these predicted single-crystal diffuse scattering patterns, there are three reasons why experimental diffuse scattering measurements may nevertheless struggle to conclusively discriminate between the two models. First, our Monte Carlo models are defect free in the sense that the correlated displacements we include exactly satisfy the constraints of the 3SP- and L-type interactions; at the elevated temperatures for which the orbital disorder phase is stable, it is reasonable that any such constraints are sometimes broken, resulting in broadening of the corresponding diffuse scattering. So, for example, the structured background expected for the (hhl) plane of the 3SP-type orbital disorder model would almost certainly become washed out in practice; likewise blurring of the diffuse scattering in the ($hk0$) plane of the L-type orbital disorder model may give the appearance of systematic absences as anticipated for the 3SP-type model. Second, our calculations have been designed to amplify the diffuse scattering (so as to reveal its underlying structure); in reality, the intensity would be very low relative to that of the Bragg scattering. In the 3SP-type orbital disorder model, for example, the diffuse scattering arises only from small displacements of O atoms and so in the presence of strong scattering from La would be essentially invisible in x-ray scattering measurements. And, third, the significant degree of thermal motion present within the O phase will degrade the diffraction pattern at high Q where the differences between in diffuse scattering are clearest. The calculations in Fig. 8 neglect any dynamic contribution to disorder in $LaMnO_3$.

V. CONCLUDING REMARKS

Our study has cautiously identified that the three-state Potts model of Ref. [34] provides the best description of orbital disorder in $LaMnO_3$ in terms of its ability to account for the experimental neutron and x-ray PDFs. Implicit in this model is an isotropic Mn orbital arrangement, which is consistent with the experimental observations of electronic and magnetic isotropy [22,38]. A more subtle corollary of this model is weak inversion-symmetry breaking at the Mn site [Fig. 8(a)]. In principle, this allows for increased d–p mixing, and as such is consistent with the small but reproducible XANES anomalies noted in Refs. [42] to occur at T_{JT}. A variation in the local symmetry of Mn environments is also consistent with renormalization of the Mn-weighted phonon density of states, as suggested by inelastic neutron scattering measurements [43]. Given the configurational entropy of the 3SP arrangement, one expects low-frequency orbital rearrangements between equivalent 3SP states occurring over a time scale significantly longer than phonon excitations; this is consistent with the NMR treatment of Ref. [41]. Ahmed and Gehring have already established a link [34] between phase changes in the 3SP model and volume collapse [39]. Moreover, the entropy calculations of Ref. [87], which at face value seemed to establish an inconsistency between the 3SP model and experimental specific-heat measurements [42], were later revised in Ref. [88] and so the model appears to be consistent with a broad range of experimental observations.

Our experimental PDF data also make clear that the O'/O transition in $LaMnO_3$ is fundamentally different to conventional order-disorder transitions in that there is a discontinuity in the evolution of the PDF at T_{JT}. This same point had effectively been noted in the EXAFS and NMR studies of Refs. [41,46] but was less clear in earlier PDF studies because of the (understandable) focus on the evolution of the lowest-r Mn-O peak as a function of temperature. From a scientific perspective, the key implication of this discontinuity is that the electronic description of orbital disordered states need not necessarily follow from our understanding of the corresponding ordered states since orbital arrangements may differ meaningfully between the two. This poses substantial computational challenges because (i) explicit description of disordered-orbital arrangements requires large atomistic configurations, and (ii) these states are entropically stabilized and so cannot necessarily be studied meaningfully in the athermal limit. Consequently, we anticipate that further detailed investigation of the orbital disordered states in the broader $La_{1-x}Ca_xMnO_3$ family, and in particular in the vicinity of the CMR transition, may provide useful insight into CMR itself.

We conclude with a brief discussion of the important methodological limitations of PDF analysis that our study has brought to light. That our preliminary RMC refinements favored the most disordered description of orbital disorder is hardly surprising: on the one hand, the L-type arrangement is simply more likely to be encountered during refinement than either the 3SP- or C-type models; and, on the other hand, the difference in quality of fit for the various models is insufficiently large to bias against the statistical result. But, what our study emphasizes is that "small-box" modeling is not itself immune to the uniqueness problem often highlighted

only for "big-box" approaches (e.g., RMC and Empirical Potential Structure Refinement (EPSR)) [56,89]. In particular, meaningfully different small-box models give remarkably similar fits to PDF data collected within the orbital disorder regime; even the RMC-derived L-type model gives a fit to data that is essentially indistinguishable from the published PDF fits of earlier studies [Fig. 6(b)] [24,52], and we certainly cannot rule out the possibility that alternative models also yield fits of the same quality. Hence, it may not always be sufficient to present a satisfactory, or even excellent, PDF fit as evidence in support of a particular small-box model. This specific point is of relevance to the problem of disorder in the spin glass $Y_2Mo_2O_7$, where very different real-space models again give almost-equivalent PDF fits [9,47]. Here, the issue of orbital disorder is resolvable only because the temperatures involved ($T < 50$ K) are so much lower than those of relevance to $LaMnO_3$. Looking forward, one particular challenge for the PDF community is the development of a more complete understanding of which problems are definitively solvable using PDF analysis and which are not. Recent developments such as (i) the 3D-ΔPDF approach [90], (ii) "dynamic" PDF measurements which can in principle separate static and vibrational contributions to $G(r)$ peak broadening [91,92], and/or (iii) the ability to incorporate additional data from a variety of experimental techniques during PDF analysis [93–96] offer a particular sense of optimism in this regard.

ACKNOWLEDGMENTS

We acknowledge support in the form of beamtime provision from the ISIS (GEM beamline) and Diamond (I12 beamline; Experiment No. EE7904) facilities. P.M.M.T., C.A.Y., and A.L.G. acknowledge financial support from the EPSRC (Grant No. EP/G004528/2) and the ERC (Grant No. 279705).

[1] A. J. Millis, B. I. Shraiman, and R. Mueller, Phys. Rev. Lett. **77**, 175 (1996).
[2] A. J. Millis, Nature (London) **392**, 147 (1998).
[3] C. N. R. Rao and A. K. Cheetham, Science **272**, 369 (1996).
[4] Y. Tokura and N. Nagaosa, Science **288**, 462 (2000).
[5] S. Nakatsuji, K. Kuga, K. Kimura, R. Satake, N. Katayama, E. Nishibori, H. Sawa, R. Ishii, M. Hagiwara, F. Bridges *et al.*, Science **336**, 559 (2012).
[6] H. Yoshida, J.-I. Yamaura, M. Isobe, Y. Okamoto, G. J. Nilsen, and Z. Hiroi, Nat. Commun. **3**, 860 (2012).
[7] M. S. Senn, D. A. Keen, T. C. A. Lucas, J. A. Hriljac, and A. L. Goodwin, Phys. Rev. Lett. **116**, 207602 (2016).
[8] A. Stroppa, P. Jain, P. Barone, M. Marsman, J. M. Perez-Mato, A. K. Cheetham, H. W. Kroto, and S. Picozzi, Angew. Chem. Int. Ed. **50**, 5847 (2011).
[9] P. M. M. Thygesen, J. A. M. Paddison, R. Zhang, K. A. Beyer, K. W. Chapman, H. Y. Playford, M. G. Tucker, D. A. Keen, M. A. Hayward, and A. L. Goodwin, Phys. Rev. Lett. **118**, 067201 (2017).
[10] P. G. Radaelli, D. E. Cox, M. Marezio, and S.-W. Cheong, Phys. Rev. B **55**, 3015 (1997).
[11] A. Okazaki and Y. Suemune, J. Phys. Soc. Jpn. **16**, 176 (1961).
[12] M. Kubota, H. Nakao, Y. Murakami, Y. Taguchi, M. Iwama, and Y. Tokura, Phys. Rev. B **70**, 245125 (2004).
[13] K. Kato, Y. Moritomo, M. Takata, H. Tanaka, and N. Hamada, Phys. Rev. B **77**, 081101 (2008).
[14] M. Takata, E. Nishibori, K. Kato, M. Sakata, and Y. Moritomo, J. Phys. Soc. Jpn. **68**, 2190 (1999).
[15] T. S. Koritsanszky and P. Coppens, Chem. Rev. **101**, 1583 (2001).
[16] A. P. Ramirez, J. Phys.: Condens. Matter **9**, 8171 (1997).
[17] R. von Helmolt, J. Wecker, B. Holzapfel, L. Schultz, and K. Samwer, Phys. Rev. Lett. **71**, 2331 (1993).
[18] E. O. Wollan and W. C. Koehler, Phys. Rev. **100**, 545 (1955).
[19] G. H. Jonker and J. H. Van Santen, Physica (Amsterdam) **16**, 337 (1950).
[20] J. B. Goodenough, Phys. Rev. **100**, 564 (1955).
[21] N. Mathur, Nature (London) **390**, 229 (1997).
[22] J.-S. Zhou and J. B. Goodenough, Phys. Rev. B **60**, R15002 (1999).
[23] J. Rodriguez-Carvajal, M. Hennion, F. Moussa, A. H. Moudden, L. Pinsard, and A. Revcolevschi, Phys. Rev. B **57**, R3189 (1998).
[24] X. Qiu, T. Proffen, J. F. Mitchell, and S. J. L. Billinge, Phys. Rev. Lett. **94**, 177203 (2005).
[25] Y. Tokura, A. Urushibara, Y. Moritomo, T. Arima, G. Asamitsu, A. Kido, and N. Furukawa, J. Phys. Soc. Jpn. **63**, 3931 (1994).
[26] B. B. Van Aken, O. D. Jurchescu, A. Meetsma, Y. Tomioka, Y. Tokura, and T. T. M. Palstra, Phys. Rev. Lett. **90**, 066403 (2003).
[27] E. S. Božin, M. Schmidt, A. J. DeConinck, G. Paglia, J. F. Mitchell, T. Chatterji, P. G. Radaelli, T. Proffen, and S. J. L. Billinge, Phys. Rev. Lett. **98**, 137203 (2007).
[28] J. W. Lynn, D. N. Argyriou, Y. Ren, Y. Chen, Y. M. Mukovskii, and D. A. Shulyatev, Phys. Rev. B **76**, 014437 (2007).
[29] J. M. De Teresa, M. R. Ibarra, P. A. Algarabel, C. Ritter, C. Marquina, J. Blasco, J. García, A. del Moral, and Z. Arnold, Nature (London) **386**, 256 (1997).
[30] C. P. Adams, J. W. Lynn, Y. M. Mukovskii, A. A. Arsenov, and D. A. Shulyatev, Phys. Rev. Lett. **85**, 3954 (2000).
[31] H. Y. Hwang, S.-W. Cheong, P. G. Radaelli, M. Marezio, and B. Batlogg, Phys. Rev. Lett. **75**, 914 (1995).
[32] M. A. Halcrow, Chem. Soc. Rev. **42**, 1784 (2013).
[33] Y. Murakami, J. P. Hill, D. Gibbs, M. Blume, I. Koyama, M. Tanaka, H. Kawata, T. Arima, Y. Tokura, K. Hirota *et al.*, Phys. Rev. Lett. **81**, 582 (1998).
[34] M. R. Ahmed and G. A. Gehring, Phys. Rev. B **79**, 174106 (2009).
[35] J. N. Reimers, J. E. Greedan, and M. Sato, J. Solid State Chem. **72**, 390 (1988).
[36] J. B. Goodenough, Annu. Rev. Mater. Sci. **28**, 1 (1998).
[37] G. Matsumoto, J. Phys. Soc. Jpn. **29**, 606 (1970).
[38] G. H. Jonker, Physica (Amsterdam) **22**, 707 (1956).
[39] T. Chatterji, F. Fauth, B. Ouladdiaf, P. Mandal, and B. Ghosh, Phys. Rev. B **68**, 052406 (2003).
[40] A. G. Christy, Acta Crystallogr. Sect. B **51**, 753 (1995).
[41] A. Trokiner, S. Verkhovskii, A. Gerashenko, Z. Volkova, O. Anikeenok, K. Mikhalev, M. Eremin, and L. Pinsard-Gaudart, Phys. Rev. B **87**, 125142 (2013).

[42] M. C. Sánchez, G. Subías, J. García, and J. Blasco, Phys. Rev. Lett. **90**, 045503 (2003).

[43] U. D. Wdowik, M. M. Koza, and T. Chatterji, Phys. Rev. B **86**, 174305 (2012).

[44] M. N. Iliev, M. V. Abrashev, H.-G. Lee, V. N. Popov, Y. Y. Sun, C. Thomsen, R. L. Meng, and C. W. Chu, Phys. Rev. B **57**, 2872 (1998).

[45] E. Araya-Rodriguez, A. Y. Ramos, H. C. N. Tolentino, E. Granado, and S. B. Oseroff, J. Magn. Magn. Mater. **233**, 88 (2001).

[46] R. A. Souza, N. M. Souza-Neto, A. Y. Ramos, H. C. N. Tolentino, and E. Granado, Phys. Rev. B **70**, 214426 (2004).

[47] J. E. Greedan, D. Gout, A. D. Lozano-Gorrin, S. Derahkshan, T. Proffen, H.-J. Kim, E. S. Božin, and S. J. L. Billinge, Phys. Rev. B **79**, 014427 (2009).

[48] B. Keimer, D. Casa, A. Ivanov, J. W. Lynn, M. V. Zimmermann, J. P. Hill, D. Gibbs, Y. Taguchi, and Y. Tokura, Phys. Rev. Lett. **85**, 3946 (2000).

[49] A. Keren and J. S. Gardner, Phys. Rev. Lett. **87**, 177201 (2001).

[50] S. J. L. Billinge and M. G. Kanatzidis, Chem. Commun.749 (2004).

[51] C. A. Young and A. L. Goodwin, J. Mater. Chem. **21**, 6464 (2011).

[52] A. Sartbaeva, S. A. Wells, M. F. Thorpe, E. S. Božin, and S. J. L. Billinge, Phys. Rev. Lett. **99**, 155503 (2007).

[53] T. Egami and S. J. L. Billinge, *Underneath the Bragg Peaks: Structural Analysis of Complex Materials* (Pergamon, Oxford, 2003).

[54] R. L. McGreevy and L. Pusztai, Mol. Simul. **1**, 359 (1988).

[55] See Supplemental Material at http://link.aps.org/supplemental/10.1103/PhysRevB.95.174107 for a brief description of x-ray PDF fits, the interplay of static and dynamic disorder in PDF refinements, RMC refinement and analysis, atomic displacement parameters from Rietveld refinements, and crystal field splitting of the *L*-type Jahn-Teller distortion.

[56] M. G. Tucker, D. A. Keen, M. T. Dove, A. L. Goodwin, and Q. Hui, J. Phys.: Condens. Matter **19**, 335218 (2007).

[57] A. L. Goodwin, M. G. Tucker, E. R. Cope, M. T. Dove, and D. A. Keen, Phys. Rev. B **72**, 214304 (2005).

[58] L. Pauling, J. Am. Chem. Soc. **57**, 2680 (1935).

[59] A. R. Overy, A. B. Cairns, M. J. Cliffe, A. Simonov, M. G. Tucker, and A. L. Goodwin, Nat. Commun. **7**, 10445 (2016).

[60] G. E. Assey, A. M. Butcher, R. J. Butcher, and Y. Gultneh, Acta Crystallogr. Sect. E **66**, m1384 (2010).

[61] A. J. Wright, H. M. Palmer, P. A. Anderson, and C. Greaves, J. Mater. Chem. **12**, 978 (2002).

[62] H. M. Palmer, A. Snedden, A. J. Wright, and C. Greaves, Chem. Mater. **18**, 1130 (2006).

[63] T. G. Parsons, H. D'Hondt, J. Hadermann, and M. A. Hayward, Chem. Mater. **21**, 5527 (2009).

[64] C. Ritter, M. R. Ibarra, J. M. De Teresa, P. A. Algarabel, C. Marquina, J. Blasco, J. García, S. Oseroff, and S.-W. Cheong, Phys. Rev. B **56**, 8902 (1997).

[65] A. C. Hannon, Nucl. Instrum. Methods Phys. Res. Sect. A **551**, 88 (2005).

[66] A. C. Hannon, W. S. Howells, and A. K. Soper, Inst. Phys. Conf. Ser. **107**, 193 (1990).

[67] M. T. Dove, M. G. Tucker, and D. A. Keen, Eur. J. Miner. **14**, 331 (2002).

[68] T. H. Toby, J. Appl. Crystallogr. **34**, 210 (2001).

[69] D. A. Keen, J. Appl. Crystallogr. **34**, 172 (2001).

[70] C. L. Farrow, P. Juhas, J. W. Liu, D. Bryndin, E. S. Božin, J. Bloch, T. Proffen, and S. J. L. Billinge, J. Phys.: Condens. Matter **19**, 335219 (2007).

[71] M. Drakopoulos, T. Connolley, C. Reinhard, R. Atwood, O. Magdysyuk, N. Vo, M. Hart, L. Connor, B. Humphreys, G. Howell *et al.*, J. Synchrotron Radiat. **22**, 828 (2015).

[72] A. P. Hammersley, S. O. Svensson, M. Hanfland, A. N. Fitch, and D. Häusermann, High Press. Res. **14**, 235 (1996).

[73] A. Coelho, TOPAS-Academic version 4.1 (2006).

[74] A. K. Soper and E. R. Barney, J. Appl. Crystallogr. **44**, 714 (2011).

[75] M. O'Keeffe and B. G. Hyde, Acta Crystallogr. Sect. B **33**, 3813 (1977).

[76] H. T. Stokes, D. M. Hatch, and B. J. Campbell, ISOTROPY Software Suite (2011).

[77] D. C. Palmer, SingleCrystal version 2.3 (2015).

[78] K. R. Knox, E. S. Božin, C. D. Malliakas, M. G. Kanatzidis, and S. J. L. Billinge, Phys. Rev. B **89**, 014102 (2014).

[79] M. G. Tucker, M. P. Squires, M. T. Dove, and D. A. Keen, J. Phys.: Condens. Matter **13**, 403 (2001).

[80] T. Proffen, Z. Kristallogr. **215**, 661 (2000).

[81] T. Proffen, V. Petkov, S. J. L. Billinge, and T. Vogt, Z. Kristallogr. **217**, 47 (2002).

[82] A. E. Platero-Prats, A. Mavrandonakis, L. C. Gallington, Y. Liu, J. T. Hupp, O. K. Farha, C. J. Cramer, and K. W. Chapman, J. Am. Chem. Soc. **138**, 4178 (2016).

[83] S. A. Corr, D. P. Shoemaker, B. C. Melot, and R. Seshadri, Phys. Rev. Lett. **105**, 056404 (2010).

[84] We note that we have tested the robustness of the behavior shown in Fig. 5(c) to variations in data processing. A particular concern is the role of inelastic scattering at elevated temperatures. Irrespective of the particular normalization protocol we use for treating our x-ray or neutron total scattering data, we obtain essentially identical trends in the behavior of $G(r)$ at T_{JT}.

[85] T. R. Welberry and T. Weber, Crystallogr. Rev. **22**, 2 (2016).

[86] D. A. Keen and A. L. Goodwin, Nature (London) **521**, 303 (2015).

[87] J.-S. Wang, R. H. Swendsen, and R. Kotecký, Phys. Rev. B **42**, 2465 (1990).

[88] M. R. Ahmed and G. A. Gehring, Phys. Rev. B **74**, 014420 (2006).

[89] A. K. Soper, Chem. Phys. **202**, 295 (1996).

[90] T. Weber and A. Simonov, Z. Kristallogr. **227**, 238 (2012).

[91] T. Egami and W. Dmowski, Z. Kristallogr. **227**, 233 (2012).

[92] W. Dmowski, S. B. Vakhrushev, I.-K. Jeong, M. P. Hehlen, F. Trouw, and T. Egami, Phys. Rev. Lett. **100**, 137602 (2008).

[93] S. J. L. Billinge and I. Levin, Science **316**, 561 (2007).

[94] M. J. Cliffe, M. T. Dove, D. A. Drabold, and A. L. Goodwin, Phys. Rev. Lett. **104**, 125501 (2010).

[95] E. S. Božin, C. D. Malliakas, P. Souvatzis, T. Proffen, N. A. Spaldin, M. G. Kanatzidis, and S. J. L. Billinge, Science **330**, 1660 (2010).

[96] P. Juhás, C. L. Farrow, X. Yang, K. R. Knox, and S. J. L. Billinge, Acta Crystallogr. Sect. A **71**, 562 (2015).

IOPscience iopscience.iop.org

Home Search Collections Journals About Contact us My IOPscience

Exploration of antiferromagnetic CoO and NiO using reverse Monte Carlo total neutron scattering refinements

This content has been downloaded from IOPscience. Please scroll down to see the full text.

2016 Phys. Scr. 91 114004

(http://iopscience.iop.org/1402-4896/91/11/114004)

View the table of contents for this issue, or go to the journal homepage for more

Download details:

IP Address: 129.67.19.88
This content was downloaded on 23/05/2017 at 16:25

Please note that terms and conditions apply.

You may also be interested in:

RMCProfile: reverse Monte Carlo for polycrystalline materials
Matthew G Tucker, David A Keen, Martin T Dove et al.

Modelling of lattice and magnetic thermal disorder in manganese oxide
A Mellergård, R L McGreevy, A Wannberg et al.

Structural and magnetic disorder inLa1-xSrxMnO3
A Mellergård, R L McGreevy and S G Eriksson

Flexibility of zeolitic imidazolate framework structures studied by neutron total scattering and the reverse Monte Carlo method
E O R Beake, M T Dove, A E Phillips et al.

Reverse Monte Carlo modelling of crystalline disorder
D A Keen, M G Tucker and M T Dove

Local structure correlations in plastic cyclohexane—a reverse Monte Carlo study
Nicholas P Funnell, Martin T Dove, Andrew L Goodwin et al.

New insights into the phase diagram of a magnetic perovskite, LaCo1/3Mn2/3O3
C L Bull, H Y Playford, K S Knight et al.

Magnetic diffuse scattering and the triple-Q structure in FCC -MnNi
M W Long and O Moze

OPEN ACCESS

Made open access 14 December 2016

IOP Publishing | Royal Swedish Academy of Sciences

Physica Scripta

Phys. Scr. **91** (2016) 114004 (8pp)

doi:10.1088/0031-8949/91/11/114004

Exploration of antiferromagnetic CoO and NiO using reverse Monte Carlo total neutron scattering refinements

Lisa Timm[1], Matthew G Tucker[2], David A Keen[2], Peter M M Thygesen[1], Paul J Saines[1,3] and Andrew L Goodwin[1]

[1] Inorganic Chemistry Laboratory, Department of Chemistry, University of Oxford, South Parks Road, Oxford OX1 3QR, UK
[2] ISIS Facility, Rutherford Appleton Laboratory, Harwell Campus, Didcot OX11 0QX, UK
[3] School of Physical Sciences, University of Kent, Canterbury CT2 7NH, UK

E-mail: P.Saines@kent.ac.uk

Received 6 July 2016, revised 23 August 2016
Accepted for publication 5 September 2016
Published 18 October 2016



Abstract

The atomic and magnetic structures of CoO and NiO have been probed using reverse Monte Carlo (RMC) refinements of neutron total scattering data. The results obtained show that the known magnetic structure for NiO can be recovered by the RMC process starting from random spin configurations, but it is insensitive to the spin direction in the {111} ferromagnetic planes. Refinements of the magnetic structure of CoO starting from random spin configurations result in collinear or non-collinear magnetic structures, consistent with those reported by other techniques. Starting from an ordered collinear spin structure for CoO and NiO leads to different results than when starting from a random arrangement of spins, which is evidence for configurational bias that highlights the need to take care when selecting a starting model for RMC refinements of magnetic structures.

S Online supplementary data available from stacks.iop.org/PS/91/114004/mmedia

Keywords: total neutron scattering, antiferromagnet, rock salt oxides, reverse Monte Carlo

(Some figures may appear in colour only in the online journal)

1. Introduction

Reverse Monte Carlo (RMC) refinements of neutron diffraction data have shown tremendous promise in recent years as a way of uncovering new information about low dimensional and frustrated magnets [1]. The RMC process involves fitting a large supercell of a structure to the data with the addition of magnetic spins to at least some of the atoms in this supercell required to fit magnetic scattering [2–4]. In general two common approaches can be taken to this, depending on whether the compound of interest features significant magnetoelastic coupling, where the emergence of magnetic order causes substantial distortions to the crystallographic structure of a material. In cases where magnetoelastic coupling is minimal, and the local positions of the magnetic cations are well characterised by the average structure, it is possible to approach refinements by fixing the atomic positions and only allowing magnetic spin orientations to refine [4, 5]. In this case fits can be made simply to the magnetic scattering alone, ideally measured using polarised neutrons. This approach has been found to be useful for a large number of exotic low dimensional and frustrated materials, especially because it does not require the use of a preconceived magnetic structure [1].

Many important materials, however, feature very strong magnetoelastic coupling including magnetostriction alloys [6], multiferroic oxides [7], and even metal-organic frameworks, where it has been shown to cause negative thermal expansion [8]. In RMC refinements of such materials, it is necessary to refine both atomic positions and spin orientation while fitting to the total scattering from the sample [9]. Such studies reported thus far have been largely restricted to binary

 © 2016 The Royal Swedish Academy of Sciences Printed in the UK

Original content from this work may be used under the terms of the Creative Commons Attribution 3.0 licence.
Any further distribution of this work must maintain attribution to the author(s) and the title of the work, journal citation and DOI.

systems, due to their challenging nature, including selected members of the antiferromagnetic transition metal rock salts MO (M = Mn, Fe, Co and Ni) [2, 10–12]. The magnetic structures of these materials are well known, from the pioneering work of Shull [13] more than fifty years ago, to have $\mathbf{k} = [½,½,½]_c$ propagation vectors (note that subscript c will be used throughout when taking reference with regards to the parent cubic structure). This is consistent with a rhombohedral structure in which the dominant coupling is superexchange interactions between next-nearest neighbour cations. In line with this MnO, $Fe_{1-x}O$ and NiO have large rhombohedral structural distortions, which enable the next-nearest neighbour cations to get closer together, strengthening the interactions between them [13, 14]. The magnetic structures of these compounds contain $\{111\}_c$ sheets in which nearest neighbour cations are, unfavourably, ferromagnetically coupled. In $Fe_{1-x}O$ the spins are perpendicular to the $\{111\}_c$ plane while in MnO and NiO they lie in the plane of the sheets [13, 14]. The Bragg intensities of the essentially rhombohedral diffraction patterns of MnO and NiO are insensitive to the spin orientation in these planes, although at least for NiO other techniques suggest the spins are oriented along the $\langle 11\bar{2}\rangle_c$ axis [15].

The magnetic structure of CoO is somewhat more controversial, with both a collinear, essentially rhombohedral, structure and non-collinear magnetic structures fitting the magnetic Bragg reflections [16]. The collinear structure of CoO, which is generally favoured, is similar to that of the other rock salts, with spins close to the $\langle 113\rangle_c$ axis [16, 17]. It is, however, inconsistent with the large tetragonal structural distortion that accompanies its magnetic ordering at T_N, 289 K. While evidence that the crystallographic structure of CoO is monoclinic has emerged from high-resolution studies in recent years [18, 19], resolving this discrepancy, additional weak magnetic reflections have been observed from single crystal neutron diffraction that are not consistent with a collinear structure [20].

Recent RMC refinements of MnO and $Fe_{0.90}O$ have provided new insights into these oxides. MnO has been confirmed to adopt a monoclinic magnetic structure, as long known to be required from theory, with evidence being found for the magnetic spins in MnO on average pointing along the $\langle 11\bar{2}\rangle_c$ axis and featuring significant modulated out-of-plane component [11]. For $Fe_{0.90}O$, where the moment has long been known to be, on average, perpendicular to the $\{111\}_c$ planes RMC refinements have revealed that the reduced magnetic moment arises, at least in part, from a deviation of spins from the $\langle 111\rangle_c$ towards $\langle 110\rangle_c$ directions in three of the four distinct groups of ions related by the face-centring operation [12]. This, at least partially, lifts the magnetic frustration caused by unfavourable ferromagnetic nearest-neighbour coupling within the $\{111\}_c$ planes. In the light of these results we have, therefore, expanded our work on this series to CoO and NiO, to explore whether RMC refinements can provide new insights into these archetypical antiferromagnets. We have carried out fits starting from both the known collinear magnetic structures and random arrangements of spins to test what effect the starting model has on the magnetic structure refined using the RMC technique. For NiO our results confirm that, below its Néel temperature at 528 K, all spin orientations lie within the {111} planes but we find no evidence to support a particular orientation of the spins within these planes. We also recover both collinear and non-collinear magnetic structures from our refinements of CoO. We find strong evidence that the results obtained from the magnetic refinement depends on whether ordered or random spin configurations are used as a starting point, a warning of the need to take care when selecting starting models for RMC magnetic refinements.

2. Experimental

Data were collected on 7 and 8 g samples of NiO and CoO, respectively, which were used as purchased from Sigma-Aldrich. Their purity was checked by x-ray diffraction and thermogravimetric analysis was used to confirm the samples were single phase and stoichiometric with regards to oxygen content. High quality data suitable for neutron total scattering analysis were collected using the GEM diffractometer [21] at the ISIS neutron source, Rutherford Appleton Laboratories over the range of $0.3 < Q < 50$ A^{-1} with counting times of 900 μA hr. The samples were held in 8 mm diameter vanadium cans in a GEM low-temperature furnace at or above room temperature or in a closed-cycle refrigerator when cooled below room temperature. Measurements of the empty instrument, empty sample environments and empty vanadium can were also carried out to correct for the instrumental background and scattering from a vanadium rod was used to produce a normalised total scattering structure factor $F(Q)$ (herein we use the terminology of Keen [22]). To obtain $F(Q)$ for total scattering analysis for NiO the data from different detector banks were merged and normalised using the programme Gudrun [23]. The stronger magnetic scattering from CoO required that self-normalisation and a 'Top Hat' correction were performed manually after background subtraction and merging were carried out.

RMC fits to these total scattering data were carried out using the RMCProfile [9] suite of programmes by similar methodology to that employed for MnO and $Fe_{0.90}O$ to fit $F(Q)$ and Bragg data sets. The Bragg data were initially fitted in GSAS [24] via the EXPGUI interface [25] to obtain lattice parameters, and background and instrumental constants, using Chebyschev polynomials and an Ikeda-Carpenter function, respectively, which were kept fixed during the RMC refinements. The Rietveld fits were carried out using cubic and tetragonal models for NiO and CoO, respectively, as the additional splitting indicative of symmetry lowering to rhombohedral and monoclinic phases, respectively, could not be observed due to the moderate resolution data obtained. The models used for RMC refinements contained about 10 000 atoms in a 12 × 12 × 12 supercell of the nuclear cubic unit cell of NiO or 14**a** × 14**a** × 10**c** supercells of the nuclear tetragonal supercell of CoO. It should be noted that RMCProfile [9] does not apply any symmetry elements so refined models are allowed to have P1 symmetry. 16 distinct

starting models were used for each material, 8 from an ordered arrangement of spins and pairs of refinements from four different random spin configurations. The ordered magnetic starting models for NiO had ferromagnetically coupled {111} planes with spins pointing in the $[11\bar{2}]_c$ direction, as well established by magnetisation measurements. For CoO the ordered magnetic starting models had magnetic spins oriented along the $[1,1,\overline{3.4}]_c$ axis, which was found to give an improved fit to the data in Rietveld refinements compared to the $[11\bar{3}]_c$ direction in previous models [17]. In the RMC refinements the magnitude of the magnetic moments were fixed at 2.8 μ_B for Ni^{2+}, as calculated from the quantised spin-only formula, and 4 μ_B for Co^{2+}. Ni–O and Co–O bonds were constrained to lie between 1.60–2.60 Å and 1.50–2.50 Å, respectively using so-called 'distance window' constraints. Similar constraints were placed on nearest neighbour metal–metal bonds and oxygen–oxygen bonds at 2.50–3.34 and 2.50–3.50 Å for NiO and CoO, respectively. Refinements allowed either atomic positions or the cation spin orientations to change, by moving atom positions or spin orientations by random fractions of a maximum move size, for four alternating periods in order to minimise the cost function:

$$\chi^2_{\mathrm{RMC}} = \sum_m \chi^2_m,$$

where the χ^2_m corresponds to the goodness of fit to the $F(Q)$, $\chi^2_{F(Q)}$, and Bragg, $\chi^2_{\mathrm{Profile}}$ datasets. The individual χ^2 functions being minimised were, where t is the neutron time-of-flight:

$$\chi^2_{F(Q)} = \sum_j [F_{\mathrm{calc}}(Q_j) - F_{\mathrm{exp}}(Q_j)]^2 \, \sigma^{-2}_{F(Q)},$$

$$\chi^2_{\mathrm{Profile}} = \sum_j [I^{\mathrm{calc}}_{\mathrm{profile}}(t_j) - I^{\mathrm{exp}}_{\mathrm{profile}}(t_j)]^2 \, \sigma^{-2}_{\mathrm{profile}}.$$

The Monte Carlo algorithm avoids local minima by accepting individual moves that degrade the fit to the data with a probability that is close to inversely proportional to the magnitude of how worse they make the fit. Refinements were carried out with the Bragg and $F(Q)$ datasets weighted approximately equally and with σ values that ensured a reasonable proportion of moves, between 20% and 80%, are accepted. For the σ values used in this study it was found to be necessary to allow atomic structure and magnetic structure refine for two and one days per period for NiO and CoO, respectively, in which time about 2.5 and 10 million moves were accepted, respectively. This led to RMC refinements for NiO and CoO taking a total of 8 and 4 days respectively at which point the change in χ^2_{RMC} over several hours for each refinement was approximately an order of magnitude less that the variations between different refinements. These were carried out using a computer with 12 3.06 GHz Intel Xeon processors and 64 GB RAM, with refinements running on one processor each in parallel. Maximum move sizes for atomic positions were set at 0.054 Å and 0.100 Å for the cations and anions, respectively, with the maximum change in spin orientation vector set at 0.05; spin orientation changes are implemented by changing a unitary spin vector by a faction of this maximum move and renormalizing to ensure the overall magnitude of the spin is retained. For refinements of the crystallographic and magnetic structure the Bragg dataset from banks at 50°–75° (bank 4) and 24°–45° (bank 3) were used respectively; the former contains data at higher Q, allowing atomic positions to be refined more precisely while the latter enabled all magnetic reflections to be observed at lower Q. For CoO due to the method used to normalise the $F(Q)$ data the scale for the Bragg and $F(Q)$ datasets had to be refined separately.

3. Results and discussion

3.1. NiO

Rietveld fits to diffraction data obtained from NiO in the paramagnetic phase at 548 and 673 K using all five detector banks did not significantly improve when the oxygen occupancies were allowed to refine, confirming the sample is stoichiometric. Lattice parameters of 4.194 050(5) Å and 4.210 1680(5) Å, were obtained at 548 K and 673 K, respectively. Fits to data collected at 300 K confirmed this result and a fit using a cubic model gave a lattice parameter of $a = 4.178\ 349(6)$ Å, with the magnetic intensities being well fitted by the established model with spins oriented along the $\langle 11\bar{2}\rangle_c$ direction with a magnitude of 1.698(4) μ_B (see figure S1) [14].

RMC fits to total scattering patterns collected at 300 K, starting from both ordered and disordered magnetic structures, gave equally good fits to the data with the average and standard deviation of the eight fits of the χ^2 of each type of 11.7(1.1)% and 11.9(8)% (see figure 1). Examination of the RMC-refined crystallographic structure did not reveal any large structural distortions or clustering, with the distribution of atoms around any one position in the collapsed supercell being uniformly spherical (see figure S2). The average nearest neighbour distances obtained from the RMC refinements were equivalent for both refinements starting from ordered and random spin configurations with Ni–O, Ni–Ni and O–O distances of 2.075(14) Å, 2.942(14) Å and 2.941(16) Å for those starting from ordered structures compared to 2.075(13) Å, 2.942(12) Å and 2.941(15) Å for those starting from initially random magnetic structures; by comparison the distances obtained from the average structure were 2.089 Å, 2.954 Å and 2.954 Å (uncertainties for the bond distances obtained by the Rietveld method are not given as these are in the 7th significant figure).

The magnetic structures refined using RMC appear very disordered (see figure 2 for a typical example) but as the scale of the nuclear and magnetic phases in the refinement were fixed to be the same the well-ordered nuclear structure suggest this is a reasonable representation of the spin orientation at ambient temperature. Analysis of the magnetic structures obtained from RMC refinements indicated that in all cases the antiferromagnetic coupling of $\{111\}_c$ ferromagnetic planes is recovered from the data (see figure S3).

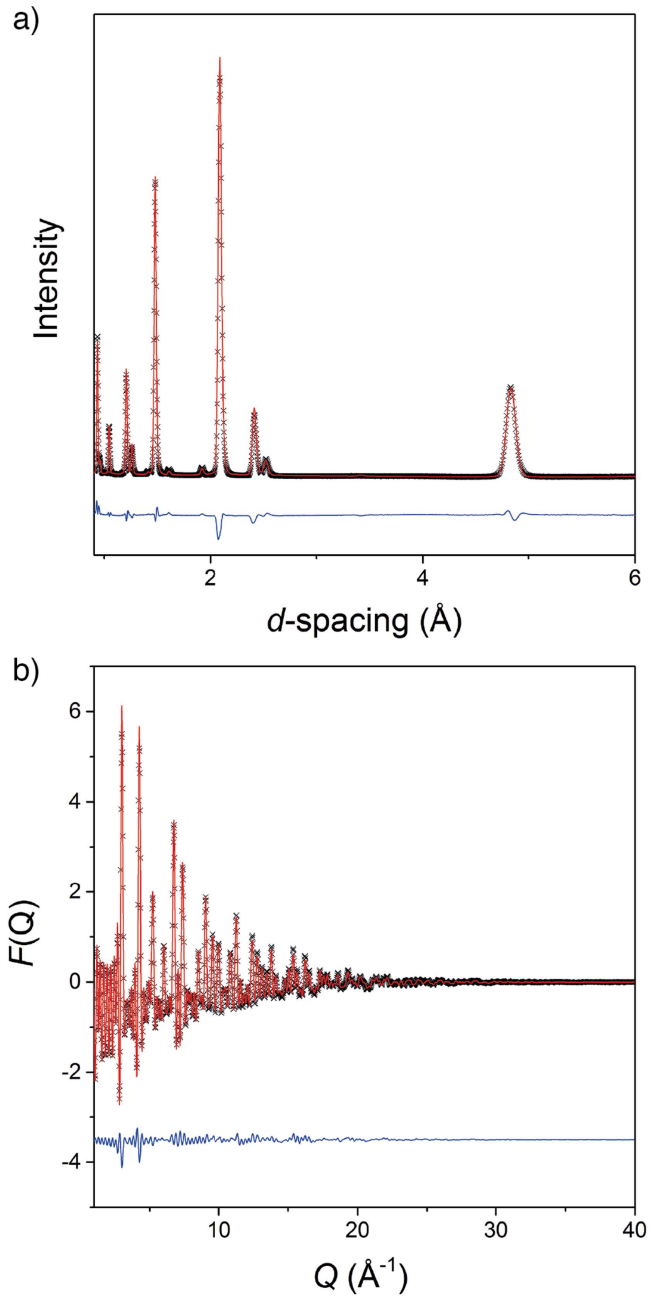


Figure 1. Representative RMC fits to (a) Bragg data from detector bank 3 of the GEM diffractometer and (b) total scattering data, respectively, for NiO. The crosses and upper and lower lines represent the experimental data, calculated fits and the difference between them.

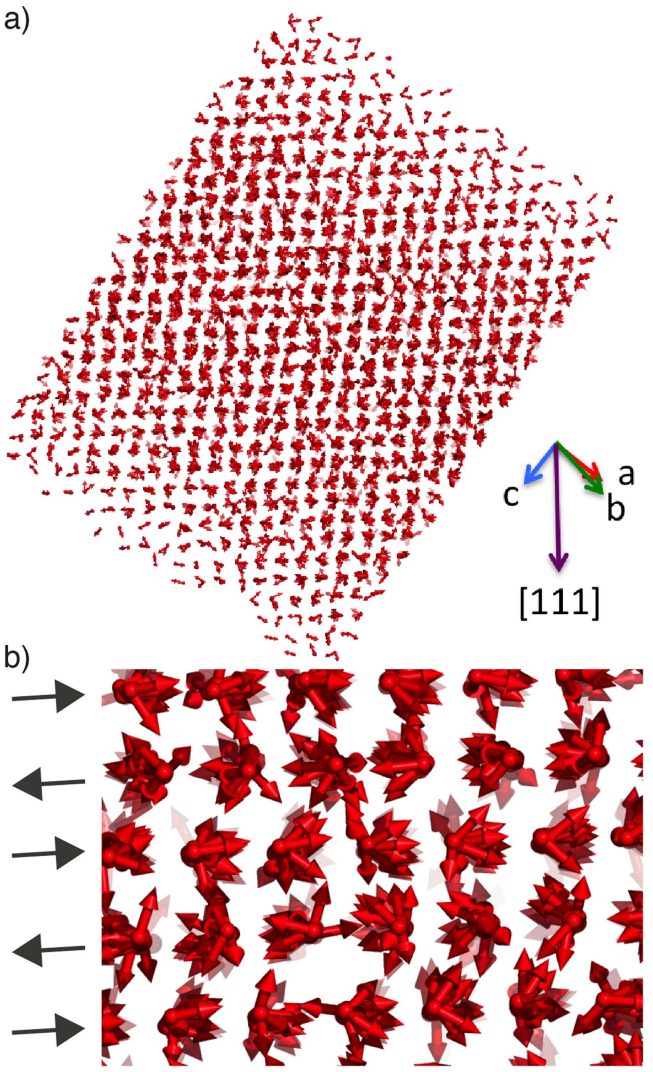


Figure 2. Spin orientations of Ni in RMC refined structures of NiO are shown as arrows. This refinement started from an ordered spin configuration and the oxygen atoms are omitted for clarity. (a) Shows the entire magnetic configuration while (b) magnifies a small section highlighting the {111} ferromagnetic planes.

In the case of those refinements starting from ordered magnetic structures the spins remained oriented along the $\langle 11\bar{2}\rangle_c$ directions, mostly along the $[11\bar{2}]_c$ axis although some refined to the symmetry equivalent $[11\bar{2}]_c$ axis (see figure 3). The moments in those refinements starting from boxes of random spins were significantly more disordered with it not always being possible to determine a clear spin direction. The moments in these models were found to remain confined along the $\{111\}_c$ planes, without a clear preference for the $\langle 11\bar{2}\rangle_c$ directions. Configurations starting from random orientation are not biased towards any kind of order but will select a random direction within the $\{111\}_c$ planes, providing the most disordered results that fit the data. This suggests the data are quite insensitive to any particular spin direction within the $\{111\}_c$ planes. Refinements starting with spins oriented along various directions in the 60° crystallographically distinct range of orientations in the $\{111\}_c$ planes of a monoclinic magnetic structure for NiO may indicate some subtle improvement for particular directions indicative of a preferred orientation, as found in the previous study of Goodwin *et al* [11] for MnO, but such refinements are beyond the scope of this study. Those starting from ordered magnetic structures exhibit initial configurational bias due to the difficulty in reorienting spins away from their ordered direction since these are close to values required for a good fit to be obtained. Attempts were made to probe whether the spin orientations of different atoms in the $2\mathbf{a}_c \times 2\mathbf{a}_c \times 2\mathbf{a}_c$ magnetic unit cell could be distinguished from each other, including those groups identified by our previous study of Fe_1

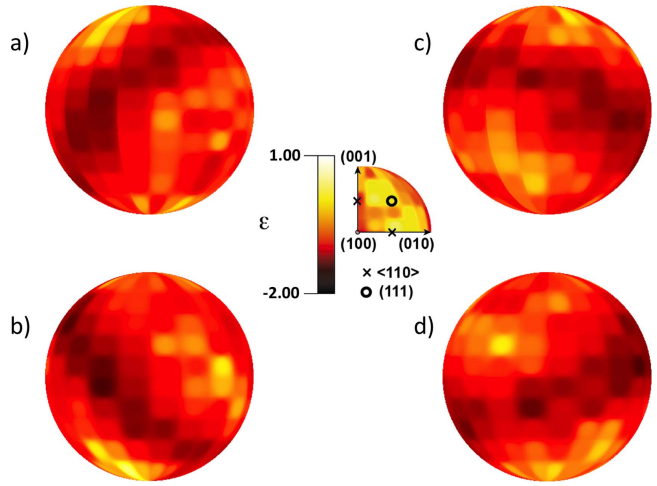


Figure 3. (a) and (b) are stereographic projections from a fully refined ordered starting configuration rotated by 180° relative to each other, around the *c*-axis; (c) and (d) represent the same for a refinement completed from a random spin configuration. The relative spin density $\varepsilon(\theta, \phi) = \ln\left[\frac{n(\theta, \phi)}{N\mathrm{d}(\cos\theta)\mathrm{d}\phi}\right]$ where $n(\theta, \phi)$ is the number of spins with orientations within the range d(cosθ), dϕ [4].

$_{-x}$O. Stereographic projections showed no particular variations in spin orientations beyond that required for the known collinear antiferromagnetic structure, however, suggesting an absence of systematic deviations of the spin orientations of different sites in NiO (see figure S4).

3.2. CoO

Rietveld fits to the neutron diffraction patterns of CoO above 289 K, in the paramagnetic phase, were well fitted by the cubic rock salt structure with $a = 4.265\ 99(4)$ Å and 4.289 03(13) Å, for 300 K and 673 K respectively. Refinement of the oxygen occupancy did not significantly improve the fit, confirming the sample is also stoichiometric with respect to oxygen content. The medium resolution of the diffractometer used in this study only reveals splitting consistent with symmetry lowering to tetragonal in the ordered phase, instead of the recently reported monoclinic structure. Fits to data at 100 K, gave $a = 3.014\ 315(9)$ Å and $c = 4.216\ 85(3)$ Å for the nuclear cell with magnetic reflections well fitted by the known $2a \times b \times 2c$ magnetic structure with spins parallel and antiparallel to $[1,1, \overline{3.60}(11)]_c$ with an overall moment of 3.864(5) μ_B (see figure S5) [17].

RMC refinements started from both ordered and disordered arrangements of spins both gave equivalent fits to the total scattering patterns obtained at 100 K, with final average χ^2 of 19.45(6) % obtained over eight refinements of each type (see figure 4). As was the case for NiO examination of the refined atomic positions did not reveal any major defects or clustering of atoms with both cobalt and oxygen atoms having a uniform distribution around their average positions (see figure S6). The average nearest neighbour distances for Co–O, Co–Co and O–O were very similar with 2.10(2) Å 2.94(2) Å and 2.991(15) Å obtained from the ordered starting

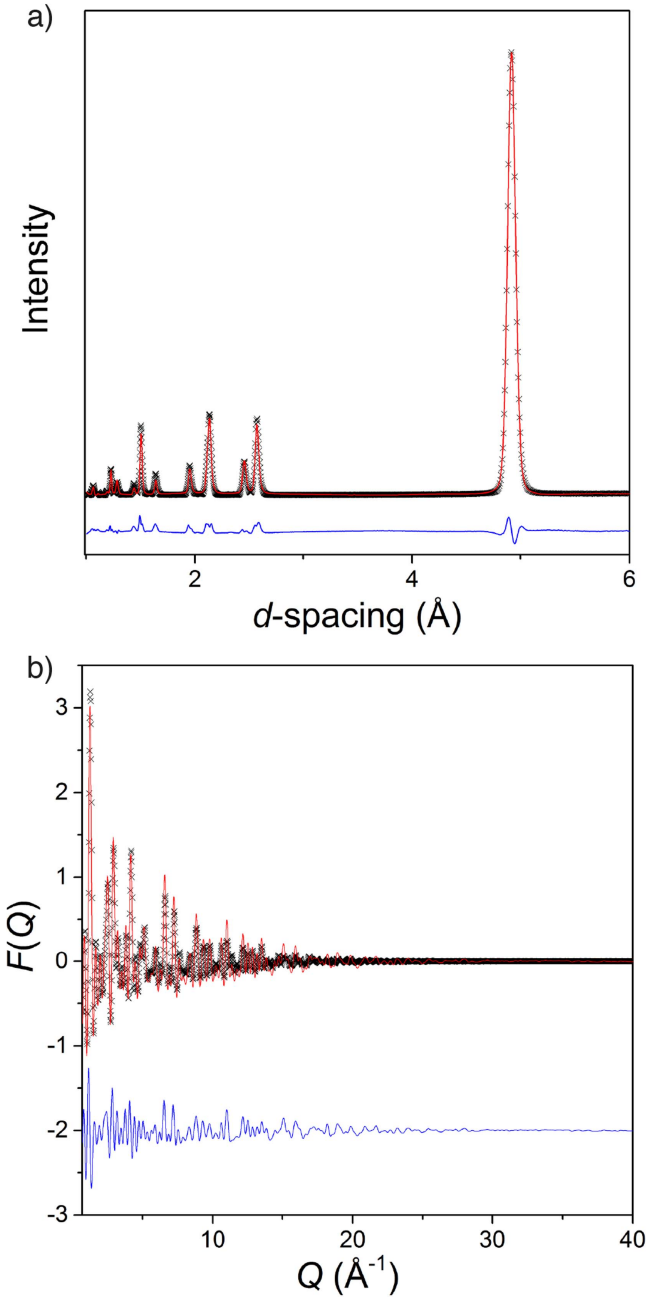


Figure 4. Representative RMC fits to (a) Bragg data from detector bank 3 of the GEM diffractometer and (b) total scattering data, respectively, for CoO. The format is the same as for figure 1. The fit shown is that obtained with a collinear model; fits obtained from non-collinear models were of visually identical quality.

configurations and 2.12(2) Å, 2.99(2) Å and 2.991(15) Å obtained from starting with random spin orientation.

Analysis of the magnetic structures obtained from RMC refinements starting from ordered spin configurations indicated they retained a similar magnetic structure, with $\{111\}_c$ ferromagnetic planes coupled antiferromagnetically to each other. In these cases the spin orientation remained close to the orientations present in the ordered starting configurations (see figures 5 and S7). Examination of the stereographic projections calculated for each site in the $2a_t \times 2a_t \times 2c_t$ magnetic unit cell for the random configurations showed that while half

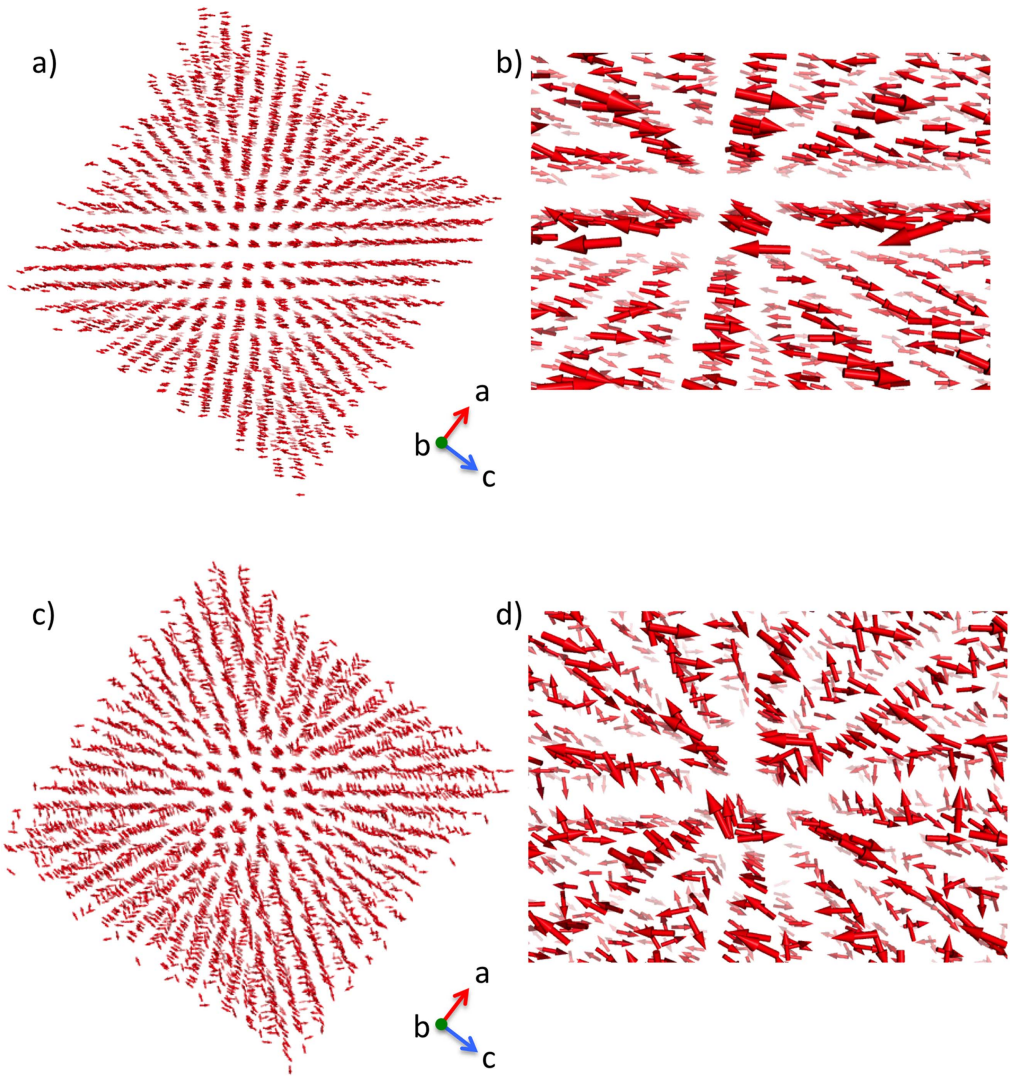


Figure 5. Spin orientations of Co in RMC refined structures with collinear, (a) and (b), and non-collinear configurations, (c) and (d). The format is the same as figure 2. (a) and (c) show the entire magnetic configuration while (b) and (d) highlight the presence and lack of {111} planes.

of the refinements starting from random spin configurations led to a similar structure the other half gave rise to a more complex structure that did not contain simple $\{111\}_c$ ferromagnetic planes or collinear magnetic moments. This structure can be described on the basis of a $2a_t \times 2a_t \times 2c_t$ magnetic unit cell (here, subscript t indicates we are referring to the tetragonal setting) but only the spins on atoms related to each other by the body-centred operation maintain the same spin direction (see figures 5 and S8). The spin orientations still remain close to the $\langle 102 \rangle_t$ directions but these are arranged in such a way that, while still satisfying the antiferromagnetic next-nearest neighbour coupling required by the dominant super-exchange, spins on nearest neighbour sites that would otherwise be ferromagnetically coupled to each other are offset by about 30° (see figure 6). Qualitatively it is very similar to the non-collinear model proposed by Van Laar, whose model also lacked {111} planes of aligned planes [16]. As found in a similar result for $Fe_{1-x}O$ this model would minimise the frustration inherent in these rock salt oxides by at least partially satisfying the desire for nearest neighbour spins to be antiferromagnetic [12]. That the non-collinear structure does not emerge from any of our refinements starting from a collinear phase again highlights the potential for configurational bias in magnetic RMC refinements. This highlights the important effect the starting model selected has on the results obtained from magnetic RMC refinements and, therefore, the need to be careful when selecting a starting model. Interestingly pairs of identical random starting spin configurations tend to lead to the emergence of either collinear or non-collinear structures. This suggests that even the precise nature of the random spin configuration influenced where collinear or non-collinear models emerged, although the number of pairs of refinements performed was relatively small so we are reluctant to draw any definitive conclusions here.

We have fitted our diffraction patterns of the antiferromagnetic phase to the non-collinear model using the Rietveld method to compare to the fit we obtain using the

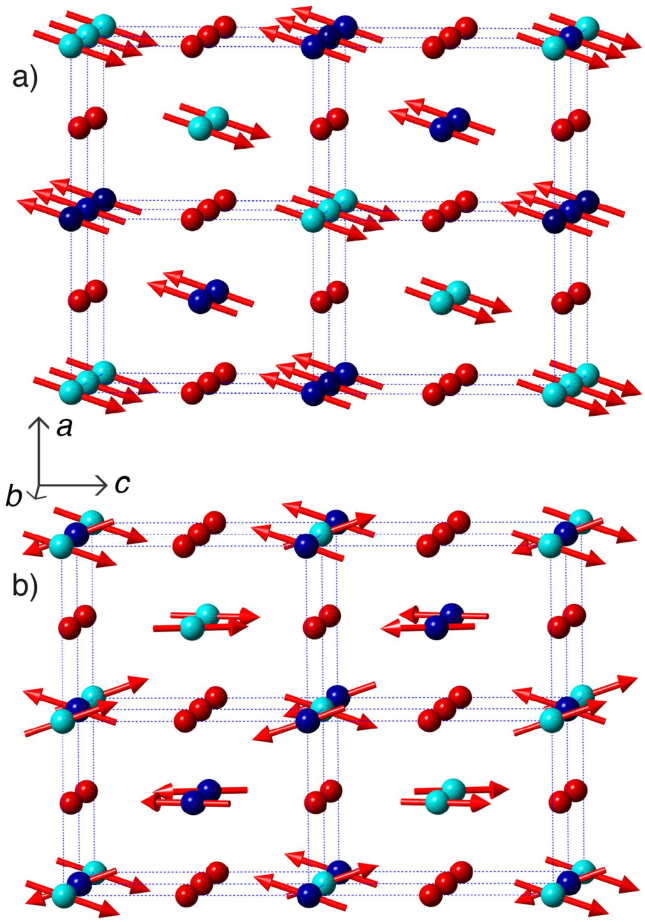


Figure 6. Average magnetic structures of the (a) collinear and (b) non-collinear magnetic structures of CoO.

collinear structure. Unfortunately, as established by the work of Van Laar [16] using low resolution data, we get almost identical fits. The non-collinear models give a fit with R_p, and R_{wp} and χ^2 of 3.50% and 3.40%, which is very similar to the values of 3.51% and 3.42% that we get from the collinear structure. The Rietveld refinements of the non-collinear model give Co magnetic moments of 3.853(6) μ_B with spins pointed along the $\langle 1.00(2), 0, 2.61(3)\rangle_t$ directions. While neither of these fits are ideal the recently reported monoclinic model [18, 19] surprisingly gave a slightly worse fit to the data with R_p, R_{wp} and χ^2 of 4.24, 4.88 and 0.633. This is not to say that the magnetic structure of CoO is not monoclinic, merely there is no direct evidence for this in our moderate resolution data.

Using the group-theoretical analysis package ISODISTORT [26] we have examined how the two magnetic structures relate to the parent $Fm\bar{3}m$ structure. The FINDSYM [26] programme in this package identifies that the non-collinear magnetic structure has I_c4_1/acd symmetry in a structure containing a single unique Co cation at the 16*e* (¾,¾,¾) position with freely refineable magnetic moments along the *c*-axis and perpendicular to it. The collinear structure, on the other hand, is in magnetic space group C_c2/c with the Co at the 4*d* (0,½,0) position, with refineable magnetic moment along the *a*- and *c*-axes. Removal of the magnetic spins from this latter structure leads to the *C2/m* crystallographic structure first proposed Jauch *et al* [18] consistent with their similar magnetic structures. The modes active for these two magnetic structures are similar, with group-theoretical analysis suggesting that a transition to either structure would involve symmetry lowering via primary distortion modes at both the Γ, (0, 0, 0), and Λ-points, (½,½,½), with the former allowing the distortion of the lattice while the latter describes the magnetic order. In the I_c4_1/acd non-collinear structure, however, there are secondary distortions allowed at the X-point, (0,1,0), which is consistent with the weak reflections observed in the work of Tomiyasu *et al* [20]. On this basis they proposed a different non-collinear model, which does not emerge in any of our RMC refinements, but we agree that such distortions would not be allowed by the C_c2/c collinear structure. We do not observe any X-point reflections in our data but, as Tomiyasu *et al* [20] suggest these have very weak intensities, ~1×10^{-3} of the order of the (001) reflection and would be in the noise of our data.

Since both the collinear and non-collinear fits to the data are equivalent, and indeed both emerge from non-configurationally biased RMC refinements starting from random spin arrangements, we are unable to distinguish between these two on the basis of our data. We suggest that in-order to distinguish clearly whether the magnetic structure of CoO is collinear or non-collinear patterns would need to be obtained that have both the extremely high resolution required to resolve the subtle monoclinic splitting of CoO [18, 19], but also have low enough background to confirm the presence of the very weak X-point reflections detected by Tomiyasu *et al* [20]. The approach used for this analysis would need to allow for the likely possibility that the symmetry of CoO will have to be lowered further than either of the models encountered in this work, to allow both these features to be accounted for. Only an approach that can confirm and then reconcile these two observations will provide a satisfying solution to the continuing debate over the magnetic structure of CoO. Furthermore, that the results obtained from these compounds are so heavily influenced by the chosen starting configurations, may suggest implications for RMC studies of other materials. It emphasises the importance of considering starting from a number of different random arrangements of spins, ideally alongside configurations of more-ordered configurations thought to be likely candidates for the magnetic structure of a material. Only when a magnetic structure appears from the vast majority of starting points for the refinement is it likely to be a trustworthy solution.

4. Conclusions

In this study we have carried out RMC refinements of the strongly magnetoelastically coupled CoO and NiO rock salt antiferromagnets. We have found that regardless of whether an ordered or disordered starting point is used for the magnetic structure of NiO, we are able to recover the known antiferromagnetic structure for this material [14], with its ferromagnetic $\{111\}_c$ planes coupled antiferromagnetically to

each other. While the spin orientations that emerge from our models remain in the $\{111\}_c$ planes we find no clear evidence that our data are sensitive to a particular orientation within them. Configurational bias from the ordered starting points, however, ensures the spins in these refinements remain along the $\langle 11\bar{2}\rangle_c$ directions. In CoO we find that both collinear and non-collinear models emerge from our RMC refinements, which give an equally good fit to our data. Evidence for configurational bias again is found as all the refinements starting with collinear models as starting points yield collinear structures at the end of their refinements. We have confirmed the magnetic symmetry of these two structures, showing that the collinear structure is C_c2/c and the non-collinear structure is I_c4_1/acd, each of which account for a different observation regarding CoO observed in recent diffraction studies [18–20]. Further studies are required to confirm and reconcile these two observations to enable the true magnetic symmetry of CoO to be uncovered.

Acknowledgments

The authors gratefully acknowledge financial support from the Glasstone Bequest (Oxford), the ERC (Grant 279705), EPSRC and the STFC. This work was made possible by access to the GEM diffractometer at ISIS.

References

[1] Halla A M *et al* 2012 *Phys. Rev.* B **86** 134431
Paddison J A M, Agrestini S, Lees M R, Fleck C L, Deen P P, Goodwin A L, Stewart J R and Petrenko O A 2014 *Phys. Rev.* B **90** 014411
Nilsen G J, Thompson C M, Ehlers G, Marjerrison C A and Greedan J E 2015 *Phys. Rev.* B **91** 054415
Paddison J A M, Jacobsen H, Petrenko O A, Fernández-Díaz M T, Deen P P and Goodwin A L 2015 *Science* **350** 179
Saines P J, Paddison J A M, Thygesen P M M and Tucker M G 2015 *Mater. Horiz.* **2** 528
Bera A K, Yusuf S M, Kumar A, Majumder M, Ghoshray K and Keller L 2016 *Phys. Rev.* B **93** 184409
[2] Keen D A, Bewley R I, Cywinski R and McGreevy R L 1996 *Phys. Rev.* B **54** 1036
Mellergård A, Mc Greevy R L, Wannberg A and Trostell B 1998 *J. Phys.: Condens. Matter* **10** 9401
Mellergård A, McGreevy R L and Eriksson S G 2000 *J. Phys.: Condens. Matter* **12** 4975
Azad A K, Mellergård A, Eriksson S-G, Ivanov S A, Eriksen J and Rundölf H 2002 *Appl. Phys.* A **74** 763
[3] McGreevy R L and Pusztai L 1988 *Mol. Simulat.* **1** 359
[4] Paddison J A M and Goodwin A L 2012 *Phys. Rev. Lett.* **108** 017204
[5] Paddison J A M, Stewart R J and Goodwin A L 2013 *J. Phys.: Condens. Matter* **25** 454220
[6] Sandlund L, Fahlander M, Cedell T, Clark A E, Restorff J B and Wun-Fogle M 1994 *J. Appl. Phys.* **75** 5656
Clark A E, Restorff J B, Wun-Fogle M, Lograsso T A and Schlagel D L 2000 *IEEE Trans. Magn.* **36** 3238
[7] Fabrèges X, Petit S, Mirebeau I, Pailhès S, Pinsard L, Forget A, Fernandez-Diaz M T and Porcher F 2009 *Phys. Rev. Lett.* **103** 067204
Park J *et al* 2011 *J. Phys. Soc. Japan.* **80** 114714
[8] Saines P J, Barton P T, Jura M, Knight K S and Cheetham A K 2014 *Mater. Horiz.* **1** 332
[9] Tucker M G, Keen D A, Dove M T, Goodwin A L and Hui Q 2007 *J. Phys.: Condens. Matter* **19** 335218
[10] Karlsson L, McGreevy R L and Wicks J D 1999 *J. Phys.: Condens. Matter* **11** 9249
[11] Goodwin A L, Tucker M G, Dove M T and Keen D A 2006 *Phys. Rev. Lett.* **96** 047209
[12] Saines P J, Tucker M G, Keen D A, Cheetham A K and Goodwin A L 2013 *Phys. Rev.* B **88** 134418
[13] Shull C G, Strauser W A and Wollan E O 1951 *Phys. Rev.* **83** 333
[14] Roth W L 1958 *Phys. Rev.* **110** 1333
[15] Yamada T, Saito S and Shimomura Y 1966 *J. Phys. Soc. Japan.* **21** 672
Baruchel J, Schlenker M, Kurosawa K and Saito S 1981 *Phil. Mag.* B **43** 853
Ressouche E, Kernavanois N, Regnault L-P and Henry J-Y 2006 *Physica* B **385–386** 394
[16] van Laar B 1965 *Phys. Rev.* **138** A584
[17] Hope D A O and Cheetham A K 1988 *J. Solid State Chem.* **72** 42
[18] Jauch W, Reehuis M, Bleif H J, Kubanek F and Pattison P 2001 *Phys. Rev.* B **64** 052102
[19] Lee S, Ishikawa Y, Miao P, Torii S, Ishigaki T and Kamiyama T 2016 *Phys. Rev.* B **93** 064429
[20] Tomiyasu K, Inami T and Ikeda N 2004 *Phys. Rev.* B **70** 184411
[21] Hannon A C 2005 *Nucl. Instrum. Methods* A **551** 88
[22] Keen D 2001 *J. Appl. Crystallogr.* **34** 172
[23] Soper A K 2011 *Technical Report* No.RAL-TR-2011-013 Rutherford Appleton Laboratory
[24] Larson A C and Dreele R B V 1994 *General Strucuture Analysis System (GSAS)* LAUR 86-748 Los Alamos National Laboratory, Los Alamos
[25] Toby B 2001 *J. Appl. Crystallogr.* **34** 210
[26] Campbell B J, Stokes H T, Tanner D E and Hatch D M 2006 *J. Appl. Crystallogr.* **39** 607

JACS
JOURNAL OF THE AMERICAN CHEMICAL SOCIETY

Communication

pubs.acs.org/JACS

Control of Multipolar and Orbital Order in Perovskite-like $[C(NH_2)_3]Cu_xCd_{1-x}(HCOO)_3$ Metal–Organic Frameworks

Nicole L. Evans,[†] Peter M. M. Thygesen,[†] Hanna L. B. Boström,[†] Emily M. Reynolds,[†] Ines E. Collings,[‡] Anthony E. Phillips,[§] and Andrew L. Goodwin*[,†]

[†]Department of Chemistry, Inorganic Chemistry Laboratory, University of Oxford, South Parks Road, Oxford OX1 3QR, U.K.
[‡]Laboratory of Crystallography, University of Bayreuth, D-95440 Bayreuth, Germany
[§]School of Physics and Astronomy, Queen Mary, University of London, 327 Mile End Road, London E1 4NS, U.K.

Supporting Information

ABSTRACT: We study the compositional dependence of molecular orientation (multipolar) and orbital (quadrupolar) order in the perovskite-like metal–organic frameworks $[C(NH_2)_3]Cu_xCd_{1-x}(HCOO)_3$. Upon increasing the fraction x of Jahn–Teller-active Cu^{2+}, we observe an orbital disorder/order transition and a multipolar reorientation transition, each occurring at distinct critical compositions x_o = 0.45(5) and x_m = 0.55(5). We attribute these transitions to a combination of size, charge distribution, and percolation effects. Our results establish the accessibility in formate perovskites of novel structural degrees of freedom beyond the familiar dipolar terms responsible for (anti)ferroelectric order. We discuss the implications of cooperative quadrupolar and multipolar states for the design of relaxor-like hybrid perovskites.

Some of the most important and interesting phenomena exhibited by conventional oxide perovskites arise from the coupling of ostensibly independent degrees of freedom.[1,2] In the colossal magnetoresistance manganites, for example, it is an interplay between charge localization, magnetic order, orbital order, and atom displacements that allows the conductivity to be switched on and off in response to external magnetic fields.[3−5] Likewise, the anomalous dielectric behavior of relaxor ferroelectrics arises from coupling of compositional variation with orbital and dipole orientations.[6]

Many of these same degrees of freedom are as relevant to metal–organic frameworks (MOFs) and hybrid inorganic/organic solids as they are to conventional oxide ceramics.[7,8] It is this realization that has fueled the quest for multiferroic MOFs, for example, where coupled magnetic spin and dipolar order would allow magnetic-field switching of bulk polarization.[9−14] The relevance to photovoltaic performance in hybrid organic perovskites is also clear: anomalous exciton lifetimes are now understood to emerge from a complex interplay between cooperative molecular tumbling, lattice vibrations, and polar displacements.[15−17]

In this context, the MOF community has focused almost exclusively on the cooperative behavior of *dipolar* degrees of freedom (e.g., molecular dipole orientations,[18−20] ion displacements,[21] and magnetic order[21−24]). However, MOFs also allow access to a variety of quadrupolar and higher-order multipolar ordering processes, the phenomenology of which is almost entirely unexplored.[25,26] For example, the charge distribution of guanidinium (point-group symmetry D_{3h}) is multipolar rather than dipolar (Figure 1a),[27] so molecular orientations in guanidinium-containing MOFs can be described by different states of multipolar order.[26] These states are conceptually related to the "hidden order" phases[28,29] of URu_2Si_2 and $Ga_3Gd_5O_{12}$ and often have no direct analogue in conventional oxide perovskites. A related phenomenon is the quadrupolar order associated with cooperative Jahn–Teller (JT) distortions

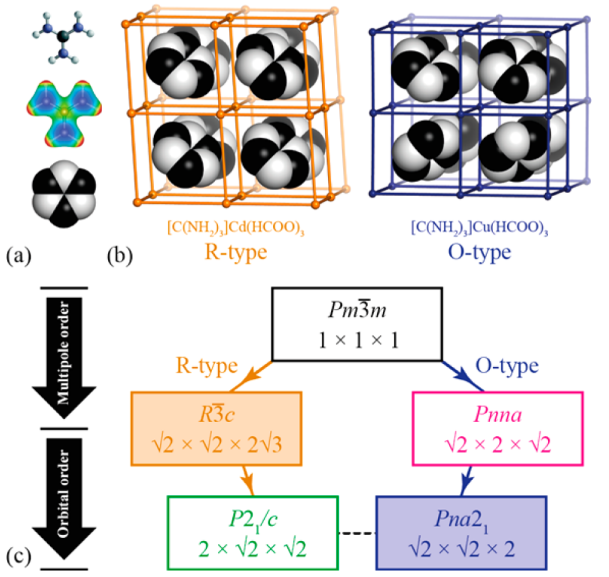


Figure 1. (a) Guanidinium ion (top), electrostatic potential (middle), and multipolar representation (bottom). (b) Multipolar order in Cd- (left) and Cu-containing (right) guanidinium formates. Metal–formate linkages are shown as straight rods. (c) Symmetry relationships between multipolar and orbital ordering processes. Arrows represent group–subgroup relationships; dashed lines represent discontinuous pathways. The space groups of the Cd (orange) and Cu (blue) formate perovskites are shaded.[30,36]

Received: May 28, 2016
Published: July 14, 2016

ACS Publications © 2016 American Chemical Society

DOI: 10.1021/jacs.6b05208
J. Am. Chem. Soc. 2016, 138, 9393−9396

in, e.g., [A]Cu(HCOO)$_3$ hybrid frameworks (A$^+$ = molecular cation).[30,31] In ref 9 it was demonstrated that this quadrupolar order could itself induce a macroscopic dipole, allowing the design of polar states in a manner similar to "tilt engineering" approaches.[32] Thus, while these more complex degrees of freedom accessible to MOFs may not be directly susceptible to manipulation by external fields, they can nevertheless couple to degrees of freedom that *are* susceptible. Hence, there is substantial unrealized potential for developing new functional MOFs based on exploiting the ordering behavior of complex degrees of freedom.

Here we study the phase behavior of the hybrid perovskite analogues [C(NH$_2$)$_3$]Cu$_x$Cd$_{1-x}$(HCOO)$_3$. Relatively few mixed-metal formates have been reported elsewhere,[33−35] and in this case only the x = 0 and 1 end members have been characterized previously.[30,36] They adopt structures with different guanidinium arrangements and thus are related to different states of multipolar order. Whereas in the Cd compound the molecular C_3 axes align along a single [111]-type direction of the underlying cubic net (we call this arrangement "R-type" as it enforces rhombohedral symmetry), in the Cu compound the alignment is along an alternating pair of ⟨111⟩ directions, giving an orthorhombic structure (hence "O-type") (Figure 1b). Both arrangements are mediated by hydrogen bonding between guanidinium cations and formate linkers.[30] In the absence of further distortions, the R and O multipole states have $R\bar{3}c$ and *Pnna* symmetry, respectively.[37] The lower symmetry of the Cu compound (*Pna*2$_1$, a polar space group) arises from coexistence of O-type multipolar order with the quadrupolar orbital order of its cooperative JT distortion.[9] Combining the same orbital arrangement with the R multipole state gives the centrosymmetric space group $P2_1/c$ [see the Supporting Information (SI)]. Hence, polarization is a nontrivial consequence of the symmetries of quadrupolar and multipolar order (Figure 1c).[9,10] By studying the Cd/Cu solid solution, we determine the extent to which the multipolar and quadrupolar order jointly responsible for bulk polarization in [C(NH$_2$)$_3$]Cu(HCOO)$_3$ might be controlled and hence exploited in future materials design.

We prepared[24,36] polycrystalline samples of [C(NH$_2$)$_3$]-Cu$_x$Cd$_{1-x}$(HCOO)$_3$ with x = 0, 0.1, 0.2, ..., 1; the compositions were verified using atomic absorption spectroscopy (see the SI). Synchrotron X-ray diffraction patterns show a progressive shift in peak positions and diffraction profiles consistent with solid-solution formation across the entire composition field (Figure 2a). Two clear transitions divide the phase field into three regions. The first occurs for the most Cu-poor samples ($0 \le x \le 0.4$): here the structure type is that of the Cd parent ($R\bar{3}c$), indicating R-type multipolar order and the expected absence of quadrupolar JT order. The second is observed for the single composition x = 0.5. Here the diffraction pattern can be explained by a single phase of symmetry $P2_1/c$, indicating a combination of R multipolar order and quadrupolar JT order. A monoclinic distortion is clearly evident in the splitting of relevant reflections (see the inset of Figure 2a); this splitting is not convincingly explained by a two-phase ($R\bar{3}c$ + *Pna*2$_1$) model (see the SI). The third and final region occurs for $0.6 \le x \le 1$, where the *Pna*2$_1$ phase of the Cu end member is stable. The symmetry of this phase is consistent with the same combination of O-type multipolar order and quadrupolar orbital order as in the Cu end member itself. We found no evidence for cation ordering; the crystal symmetries of each phase are consistent only with a single Cd/Cu crystallographic site. Consequently, we attribute the transitions at x_o = 0.45(5) and x_m = 0.55(5) to orbital order and multipole reorientation transitions, respectively. To the best of our knowledge, this is the first identification of these classes of transitions in a MOF/hybrid system.

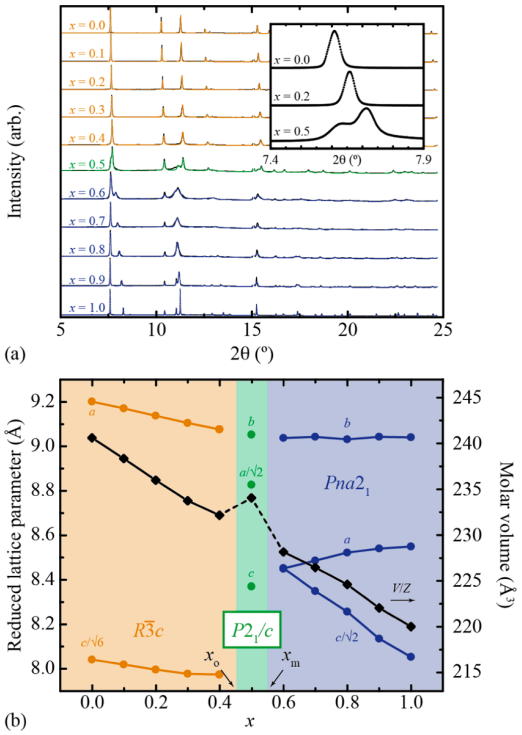


Figure 2. (a) Synchrotron X-ray diffraction patterns (λ = 0.82599(1) Å) for [C(NH$_2$)$_3$]Cu$_x$Cd$_{1-x}$(HCOO)$_3$. Data are shown as black points, and Pawley fits as colored lines. The inset shows the splitting of a single reflection upon transition from $R\bar{3}c$ ($x \le 0.4$) to $P2_1/c$ (x = 0.5). (b) Corresponding lattice parameters.

The effect of composition on the lattice parameters was determined using Pawley refinement (Figure 2b) (see the SI). Within a given phase the variation is smooth, consistent with the formation of a genuine solid solution. However, both transitions appear discontinuous and are accompanied by volume anomalies. A volume *increase* with orbital order at x_o reflects the behavior of LaMnO$_3$.[38,39] The different signs of ΔV for orbital and multipolar ordering suggests that pressure may be used to manipulate these transitions independently of one another.

How might we understand the microscopic mechanisms responsible for transitions at x_o and x_m? We suggest that increasing Cu composition has three key effects.

The first effect is that of size: the difference in the Cu−O and Cd−O bond lengths (2.1 and 2.3 Å, respectively[30,36]) means that the edge length of the cubic perovskite net is shorter in [C(NH$_2$)$_3$]Cu(HCOO)$_3$ than in [C(NH$_2$)$_3$]Cd(HCOO)$_3$ (6.03 vs 6.24 Å). This comparison holds for all of the first-row transition metals; that the analogous framework for each of these systems adopts the same O multipole state[30] suggests that this particular arrangement of guanidinium cations reflects a more efficient packing. In other words, the volume decrease upon Cu doping (Figure 2b) may drive the multipole transition in order to pack guanidinium ions more efficiently.

DOI: 10.1021/jacs.6b05208
J. Am. Chem. Soc. 2016, 138, 9393−9396

A second factor is the variation in hydrogen-bond strength between guanidinium and the framework induced as the transition metal is varied.[36,40−42] R and O multipole states should support different cation−framework interaction strengths,[41,42] suggesting that a change in charge density may also explain the transition at x_m.

The final effect we consider is that of introducing JT-active ions into a JT-inactive matrix. On one level, it is perhaps surprising that even in flexible MOFs the strains associated with JT distortions are sufficient to enforce coupling between orbital orientations of neighboring cations. However, orbital order is indisputably present in $[C(NH_2)_3]Cu(HCOO)_3$ itself.[30] For small x, the JT axes of isolated Cu^{2+} ions are uncorrelated since most are surrounded by a JT-inactive matrix of Cd^{2+}. As x increases, however, the fraction of Cu^{2+} ions with Cu^{2+} neighbors quickly increases, and strain effects enforce local coupling between orbital orientations. At some critical Cu composition these correlations become long-range, resulting in an orbital disorder/order transition; on the basis of symmetry arguments we identify this as the transition at x_o. We used a Monte Carlo simulation to identify the composition at which this transition might be anticipated (see the SI). Our toy Hamiltonian considers the effect of random-site percolation on a cubic lattice using only nearest-neighbor interactions. For this model, we find that the orbital order transition occurs at $x_o \approx 0.6$. That orbital order occurs experimentally at a lower value of x suggests that (i) there exists short-range cation order and/or (ii) JT strain fields extend beyond nearest neighbors.[43]

We investigated the temperature dependence of x_o and x_m (there is none, consistent with percolative mechanisms;[44] see the SI) and also established the corresponding phase behavior of the solid solution $[C(NH_2)_3]Mn_xCd_{1-x}(HCOO)_3$. In this JT-inactive system we observe a single temperature-dependent multipole transition from $R\bar{3}c$ directly to *Pnna* (Figure 1c) (see the SI) that occurs at a higher doping level, $x_m(Mn) = 0.75(5)$ Å, consistent with our size arguments.[45]

Therefore, we have demonstrated for a family of perovskite-like MOFs that multipolar and orbital degrees of freedom undergo independent ordering processes as a result of compositional variation. The particular system studied here has a readily identifiable signature of orbital order; however, one expects similar phenomena in, e.g., $[C(NH_2)_3]Cu_xMn_{1-x}(HCOO)_3$, where systematic absence violations would identify a progression from disordered (*Pnna*) to ordered ($Pna2_1$) states. Compositions in the vicinity of this transition may prove especially interesting since the symmetry arguments of ref 9 guarantee that critical fluctuations in orbital order must couple to fluctuations in the polarization to give polar nanodomains, as in the Pb-containing perovskite relaxors PZN/PMN.[46] Not only do our results suggest an avenue for the design of lead-free relaxors, but the inclusion of magnetic transition metals allows in principle for coupling to magnetic order. Moreover, since different organic cations have different multipolar charge distributions, substitution[47,48] is an obvious means of exploring a large variety of multipolar states. In all cases both the statistical mechanics and the symmetry implications of correlated multipolar, quadrupolar, and dipolar order will prove crucial in exploiting the degrees of freedom accessible to MOFs.

■ ASSOCIATED CONTENT

Supporting Information

The Supporting Information is available free of charge on the ACS Publications website at DOI: 10.1021/jacs.6b05208.

Experimental methods; powder diffraction refinement details; lattice parameters; Monte Carlo simulation description; symmetry discussion (PDF)

■ AUTHOR INFORMATION

Corresponding Author

*andrew.goodwin@chem.ox.ac.uk

Notes

The authors declare no competing financial interest.

■ ACKNOWLEDGMENTS

The authors gratefully acknowledge useful discussions with J. A. Hill (Oxford). The synchrotron diffraction measurements were carried out at the Diamond Light Source (I11 Beamline). We are extremely grateful for the award of a Block Allocation Grant, which made this work possible, and for the assistance in data collection provided by M. S. Senn (Oxford) and the I11 beamline staff. P.M.M.T. and A.L.G. gratefully acknowledge funding through the European Research Council (Grant 279705). I.E.C. thanks the Alexander von Humboldt Foundation for a Postdoctoral Fellowship. This project received funding from the European Union (EU) Horizon 2020 Research and Innovation Programme under Marie Sklodowska-Curie Grant Agreement 641887 (project acronym DEFNET).

■ REFERENCES

(1) Lee, J. H.; Fang, L.; Vlahos, E.; Ke, X.; Jung, Y. W.; Kourkoutis, L. F.; Kim, J.-W.; Ryan, P. J.; Heeg, T.; Roeckerath, M.; Goian, V.; Bernhagen, M.; Uecker, R.; Hammel, P. C.; Rabe, K. M.; Kamba, S.; Schubert, J.; Freeland, J. W.; Muller, D. A.; Fennie, C. J.; Schiffer, P.; Gopalan, V.; Johnston-Halperin, E.; Schlom, D. G. *Nature* **2010**, *466*, 954−959.

(2) Millis, A. J. *Nature* **1998**, *392*, 147−150.

(3) Jin, S.; Tiefel, T. H.; McCormack, M.; Fastnacht, R. A.; Ramesh, R.; Chen, L. H. *Science* **1994**, *264*, 413−415.

(4) Goodenough, J. B. *Phys. Rev.* **1955**, *100*, 564−573.

(5) Adams, C. P.; Lynn, J. W.; Mukovskii, Y. M.; Arsenov, A. A.; Shulyatev, D. A. *Phys. Rev. Lett.* **2000**, *85*, 3954−3957.

(6) Xu, G.; Zhong, Z.; Bing, Y.; Ye, Z.-G.; Shirane, G. *Nat. Mater.* **2006**, *5*, 134−140.

(7) Jain, P.; Dalal, N. S.; Toby, B. H.; Kroto, H. W.; Cheetham, A. K. *J. Am. Chem. Soc.* **2008**, *130*, 10450−10451.

(8) Rogez, G.; Viart, N.; Drillon, M. *Angew. Chem., Int. Ed.* **2010**, *49*, 1921−1923.

(9) Stroppa, A.; Jain, P.; Barone, P.; Marsman, M.; Perez-Mato, J. M.; Cheetham, A. K.; Kroto, H. W.; Picozzi, S. *Angew. Chem., Int. Ed.* **2011**, *50*, 5847−5850.

(10) Stroppa, A.; Barone, P.; Jain, P.; Perez-Mato, J. M.; Picozzi, S. *Adv. Mater.* **2013**, *25*, 2284−2290.

(11) Wang, W.; Yan, L.-Q.; Cong, J.-Z.; Zhao, Y.-L.; Wang, F.; Shen, S.-P.; Zou, T.; Zhang, D.; Wang, S.-G.; Han, X.-F.; Sun, Y. *Sci. Rep.* **2013**, *3*, 2024.

(12) Tian, Y.; Stroppa, A.; Chai, Y.; Yan, L.; Wang, S.; Barone, P.; Picozzi, S.; Sun, Y. *Sci. Rep.* **2014**, *4*, 6062.

(13) Jain, P.; Ramachandran, V.; Clark, R. J.; Zhou, H. D.; Toby, B. H.; Dalal, N. S.; Kroto, H. W.; Cheetham, A. K. *J. Am. Chem. Soc.* **2009**, *131*, 13625−13627.

(14) Gómez-Aguirre, L. C.; Pato-Doldán, B.; Mira, J.; Castro-García, S.; Señaris-Rodríguez, M. A.; Sánchez-Andújar, M.; Singleton, J.; Zapf, V. S. *J. Am. Chem. Soc.* **2016**, *138*, 1122−1125.

DOI: 10.1021/jacs.6b05208
J. Am. Chem. Soc. 2016, 138, 9393−9396

(15) Lee, J.-H.; Bristowe, N. C.; Bristowe, P. D.; Cheetham, A. K. *Chem. Commun.* **2015**, *51*, 6434−6437.
(16) Frost, J. M.; Walsh, A. *Acc. Chem. Res.* **2016**, *49*, 528−535.
(17) Leguy, A. M. A.; Frost, J. M.; McMahon, A. P.; Sakai, V. G.; Kockelmann, W.; Law, C.; Li, X.; Foglia, F.; Walsh, A.; O'Regan, B. C.; Nelson, J.; Cabral, J. T.; Barnes, P. R. F. *Nat. Commun.* **2015**, *6*, 7124.
(18) Sánchez-Andújar, M.; Presedo, S.; Yáñez-Vilar, S.; Castro-García, S.; Shamir, J.; Señarís-Rodríguez, M. A. *Inorg. Chem.* **2010**, *49*, 1510−1516.
(19) Besara, T.; Jain, P.; Dalal, N. S.; Kuhns, P. L.; Reyes, A. P.; Kroto, H. W.; Cheetham, A. K. *Proc. Natl. Acad. Sci. U. S. A.* **2011**, *108*, 6828−6832.
(20) Mączka, M.; Costa, N. L. M.; Gągor, A.; Paraguassu, W.; Sieradzki, A.; Hanuza, J. *Phys. Chem. Chem. Phys.* **2016**, *18*, 13993−14000.
(21) Xu, G.-C.; Zhang, W.; Ma, X.-M.; Chen, Y.-H.; Zhang, L.; Cai, H.-L.; Wang, Z.-M.; Xiong, R.-G.; Gao, S. *J. Am. Chem. Soc.* **2011**, *133*, 14948−14951.
(22) Saines, P. J.; Tan, J.-C.; Yeung, H. H.-M.; Barton, P. T.; Cheetham, A. K. *Dalton Trans.* **2012**, *41*, 8585−8593.
(23) Saines, P. J.; Paddison, J. A. M.; Thygesen, P. M. M.; Tucker, M. G. *Mater. Horiz.* **2015**, *2*, 528−535.
(24) Wang, Z.; Zhang, B.; Otsuka, T.; Inoue, K.; Kobayashi, H.; Kurmoo, M. *Dalton Trans.* **2004**, 2209−2216.
(25) Li, W.; Zhang, Z.; Bithell, E. G.; Batsanov, A. S.; Barton, P. T.; Saines, P. J.; Jain, P.; Howard, C. J.; Carpenter, M. A.; Cheetham, A. K. *Acta Mater.* **2013**, *61*, 4928−4938.
(26) Hill, J. A.; Thompson, A. L.; Goodwin, A. L. *J. Am. Chem. Soc.* **2016**, *138*, 5886−5896.
(27) Davis, M. R.; Dougherty, D. A. *Phys. Chem. Chem. Phys.* **2015**, *17*, 29262−29270.
(28) Mydosh, J. A.; Oppeneer, P. M. *Rev. Mod. Phys.* **2011**, *83*, 1301−1322.
(29) Paddison, J. A. M.; Jacobsen, H.; Petrenko, O. A.; Fernández-Díaz, M. T.; Deen, P. P.; Goodwin, A. L. *Science* **2015**, *350*, 179−181.
(30) Hu, K.-L.; Kurmoo, M.; Wang, Z.; Gao, S. *Chem. - Eur. J.* **2009**, *15*, 12050−12064.
(31) Wang, B.-Q.; Yan, H.-B.; Huang, Z.-Q.; Zhang, Z. *Acta Crystallogr., Sect. C: Cryst. Struct. Commun.* **2013**, *69*, 616−619.
(32) Pitcher, M. J.; Mandal, P.; Dyer, M. S.; Alaria, J.; Borisov, P.; Niu, H.; Claridge, J. B.; Rosseinsky, M. J. *Science* **2015**, *347*, 420−424.
(33) Shang, R.; Sun, X.; Wang, Z.-M.; Gao, S. *Chem. - Asian J.* **2012**, *7*, 1697−1707.
(34) Mączka, M.; Sieradzki, A.; Bondzior, B.; Deren, P.; Hanuza, J.; Hermanowicz, K. *J. Mater. Chem. C* **2015**, *3*, 9337−9345.
(35) Mączka, M.; Gagor, A.; Hermanowicz, K.; Sieradzki, A.; Macalik, L.; Pikul, A. *J. Solid State Chem.* **2016**, *237*, 150−158.
(36) Collings, I. E.; Hill, J. A.; Cairns, A. B.; Cooper, R. I.; Thompson, A. L.; Parker, J. E.; Tang, C. C.; Goodwin, A. L. *Dalton Trans.* **2016**, *45*, 4169−4178.
(37) We note that the tilt systems active in both compounds correspond to symmetries that are supergroups of the symmetries arising from multipolar order, allowing multipole−tilt coupling.
(38) Chatterji, T.; Fauth, F.; Ouladdiaf, B.; Mandal, P.; Ghosh, B. *Phys. Rev. B: Condens. Matter Mater. Phys.* **2003**, *68*, 052406.
(39) Ahmed, M. R.; Gehring, G. A. *Phys. Rev. B: Condens. Matter Mater. Phys.* **2009**, *79*, 174106.
(40) Li, W.; Thirumurugan, A.; Barton, P. T.; Lin, Z.; Henke, S.; Yeung, H. H.-M.; Wharmby, M. T.; Bithell, E. G.; Howard, C. J.; Cheetham, A. K. *J. Am. Chem. Soc.* **2014**, *136*, 7801−8704.
(41) Di Sante, D.; Stroppa, A.; Jain, P.; Picozzi, S. *J. Am. Chem. Soc.* **2013**, *135*, 18126−18130.
(42) Shang, R.; Xu, G.-C.; Wang, Z.-M.; Gao, S. *Chem. - Eur. J.* **2014**, *20*, 1146−1158.
(43) There is clear evidence of significant strain broadening in the diffraction patterns shown in Figure 2a that appears to be more significant for $0.6 \leq x \leq 1$ (Cd^{2+} embedded in a Cu^{2+} matrix) than for $0 \leq x \leq 0.4$ (Cu^{2+} embedded in a Cd^{2+} matrix).
(44) Whereas in conventional orbital order/disorder systems (e.g., $La_{1-x}Ca_xMnO_3$) thermally induced orbital reorganization is permitted via charge redistribution,[49] here it is likely that the distribution of JT-active cations is fixed during synthesis, resulting in the temperature independence of x_o.
(45) Shannon, R. D. *Acta Crystallogr., Sect. A: Cryst. Phys., Diffr., Theor. Gen. Crystallogr.* **1976**, *32*, 751−767.
(46) Paściak, M.; Welberry, T. R.; Kulda, J.; Kempa, M.; Hlinka, J. *Phys. Rev. B: Condens. Matter Mater. Phys.* **2012**, *85*, 224109.
(47) Kieslich, G.; Kumagai, S.; Forse, A. C.; Sun, S.; Henke, S.; Yamashita, M.; Grey, C. P.; Cheetham, A. K. *Chem. Sci.* **2016**, DOI: 10.1039/C6SC01247G.
(48) Chen, S.; Shang, R.; Wang, B.-W.; Wang, Z.-M.; Gao, S. *Angew. Chem., Int. Ed.* **2015**, *54*, 11093−11096.
(49) Rao, C. N. R.; Cheetham, A. K. *Science* **1996**, *272*, 369−370.

DOI: 10.1021/jacs.6b05208
J. Am. Chem. Soc. 2016, 138, 9393−9396

Materials Horizons

COMMUNICATION

View Article Online
View Journal | View Issue

Cite this: *Mater. Horiz.*, 2015, 2, 528

Received 22nd June 2015,
Accepted 21st July 2015

DOI: 10.1039/c5mh00113g

www.rsc.li/materials-horizons

Published on 21 July 2015. Downloaded on 23/05/2017 16:26:33.

Searching beyond Gd for magnetocaloric frameworks: magnetic properties and interactions of the $Ln(HCO_2)_3$ series†

Paul J. Saines,*[a] Joseph A. M. Paddison,[ab] Peter M. M. Thygesen[a] and Matthew G. Tucker[b]

This study probes the magnetic properties and interactions of the $Ln(HCO_2)_3$ (Ln = Tb^{3+}–Er^{3+}) frameworks. We show that the magnetocaloric effect of $Tb(HCO_2)_3$ is significantly higher above 4 K in moderate magnetic fields compared to the promising $Gd(HCO_2)_3$. While the peak performance of $Tb(HCO_2)_3$ is lower than $Gd(HCO_2)_3$, we also find that the Gd-rich members of the solid solution $Gd_{1-x}Tb_x(HCO_2)_3$ blend the advantages of both end-members. Using neutron diffraction experiments, $Tb(HCO_2)_3$ is found to be antiferromagnetic below 1.7 K with ferromagnetic face-sharing chains and antiferromagnetic coupling between them. Analysis of magnetic diffuse scattering of the paramagnetic phase indicates that ferromagnetic coupling is retained, and it is likely that this plays a role in improving its magnetocaloric performance in low fields.

Conceptual insights

Alternate coolants are needed to replace the use of increasingly scarce liquid helium to reach ultra-low temperatures, required, for example, to cool superconductors used in medical resonance imaging to below 10 K. Paramagnetic magnetocalorics, which posses entropically driven cooling when in a cycled magnetic field, are one such replacement. Recently gadolinium-based coordination frameworks that have amongst the largest magnetocaloric effects have been developed; the cooling power of these materials, however, peaks below 2 K, below the temperatures required for many applications of liquid helium. This work shows that the incorporation of heavier lanthanides, in particular terbium, into a magnetocaloric framework can lead to a significant increase in their performance at higher temperatures—particularly in applied fields reachable using permanent magnets, the most practical for functional cooling devices. The detailed magnetic interactions in terbium formate have also been examined, the first study of the magnetic correlations in a paramagnetic coordination framework, which reveals that Ising-like one-dimensional ferromagnetic coupling is present in the paramagnetic phase. These interactions are likely to play a role in its excellent magnetocaloric performance by increasing its ease of magnetisation.

1. Introduction

Functional magnets have great potential to underpin the development of new technologies for a wide range of applications.[1,2] Coordination frameworks have attracted particular attention in this regard, because their unusual architectures allow them to exhibit uniquely-modified magnetic properties not found in conventional ionic solids.[2–4] Recently, frameworks have been created that exhibit the paramagnetic magnetocaloric effect (MCE),[2,5,6] an entropically-driven cooling process that occurs when paramagnets are in a cycled magnetic field. Several frameworks, including $Gd(HCO_2)_3$, have recently been reported whose MCEs are comparable or superior to $Gd_3Ga_5O_{12}$, the benchmark compound for MCE cooling below 10 K.[5,6] These materials have possible applications as ultra-low-temperature coolants, potentially replacing increasingly expensive and scarce liquid helium.[2,7] The current focus of the development of MCE frameworks lies in achieving higher maximum entropy changes – typically for temperatures below 2 K and applied magnetic fields greater than 5 T. Such materials are used as a second stage in an adiabatic demagnetisation refrigerator (ADR), with liquid helium or a cryocooler, cooling the system down to 4 K before magnetic cooling enables the sample environment to be cooled below 1 K, typically for scientific observation. Given the increasing scarcity of liquid helium and complexity and reliability issues of multistage cryocoolers, which are necessary to reach 4 K, the development of magnetocaloric compounds that operate more efficiently at moderately higher temperatures may be useful when combined with a single stage cryocooler capable of reaching 10–20 K.[8] Ideally, this would be accompanied by having as large an MCE as possible in lower applied fields, particularly below the typical 2 T field limits of permanent magnets.[5,9] This could allow more economical devices to be created for many applications requiring cooling in the 4–10 K range, *e.g.* cooling the niobium superconducting magnets used in medical resonance imaging and nuclear magnetic resonance facilities.[10]

Very little is known regarding how the paramagnetic interactions in magnetocalorics relate to their fascinating properties.

[a] *Department of Chemistry, University of Oxford, Inorganic Chemistry Laboratory, South Parks Road, Oxford, OX1 3QR, UK. E-mail: paul.saines@chem.ox.ac.uk*
[b] *ISIS Facility, Rutherford Appleton Laboratory, Harwell Oxford, Didcot, OX1 3QR, UK*

† Electronic supplementary information (ESI) available. See DOI: 10.1039/c5mh00113g

This journal is © The Royal Society of Chemistry 2015

Published on 21 July 2015. Downloaded on 23/05/2017 16:26:33.

Neutron scattering is the method of choice for probing magnetic interactions and has recently begun to be applied to study magnetically-ordered frameworks;[4,11] its application, however, to magnetocalorics and other low dimensional and frustrated frameworks is very limited.[12] This is because sufficiently large single crystals of coordination frameworks are seldom available, and it has long been considered that little information about the paramagnetic state can be extracted using neutron powder diffraction. While the very large neutron-absorption cross section of Gd also typically restricts studying many magnetocalorics, recent studies have shown that this problem is surmountable.[13] Our research on frustrated and disordered magnets has shown that significantly more information can be obtained from powder magnetic diffuse scattering than has traditionally been anticipated.[14,15] Applying such techniques to frameworks would enable a much deeper understanding of their low dimensional or frustrated behaviour.

Here we present a survey of the magnetic properties of the $Ln(HCO_2)_3$ (Ln = Tb^{3+}, Dy^{3+}, Ho^{3+} and Er^{3+}) frameworks. Unexpectedly, we reveal that $Tb(HCO_2)_3$ has a larger MCE than $Gd(HCO_2)_3$ for temperatures between 4 and 10 K and applied fields below 2 T. Doping across the $Gd_{1-x}Tb_x(HCO_2)_3$ solid solution series is found to further optimize the MCE properties of this family. Encouraged by the properties of $Tb(HCO_2)_3$, we also investigated its magnetic interactions using neutron diffraction, characterising both its long-range magnetic order present below 1.7 K and the short-range order in its paramagnetic phase—the first time that such a study has been completed on a coordination framework. We show that ferromagnetic coupling within the TbO_9 chains in $Tb(HCO_2)_3$ is the dominant interaction in the paramagnetic phase, which may play a role in its interesting magnetocaloric properties.

2. Experimental

Samples were synthesised by slowly adding 1 g of the appropriate $Ln(NO_3)_3{\cdot}xH_2O$ (99.9%, x = 6 for Ln = Gd^{3+} or Tb^{3+}, Sigma-Aldrich, and x = 5 for Ln = Dy^{3+}, Ho^{3+} and Er^{3+}, Alfa Aesar) to 5 mL of formic acid (Sigma-Aldrich, 95% reagent grade) in a 30 mL tall glass vial. This was stirred overnight and the product filtered off, washing with ethanol. $Gd_{1-x}Tb_x(HCO_2)_3$ was made by reactions carried out with finely ground stoichiometric mixtures of $Gd(NO_3)_3$ and $Tb(NO_3)_3$. The 5 g sample of $Tb(DCO_2)_3$ used for neutron diffraction was made using the same method but was a combination of three batches made using 4 g of $Tb(NO_3)_3{\cdot}6H_2O$ and perdeuterated formic acid (Sigma-Aldrich 95% in D_2O, 98% D). Sample purity was examined by powder X-ray diffraction, using a Bragg–Brentano PANalytical Empyrean diffractometer equipped with Cu-Kα_1 radiation and a PIXcel detector. Dc magnetisation data were collected using a Quantum Design MPMS 5 XL SQUID magnetometer with powder samples contained in gel caps and held in a straw with a uniform diamagnetic background.

Time-of-flight neutron powder diffraction patterns were recorded using the GEM diffractometer at the ISIS neutron facility, Rutherford Appleton Laboratories, UK.[16] Data covered a reciprocal-space range $0.25 < Q < 25$ Å^{-1} and were measured at temperatures between 1.4 K and 300 K for 30 μAh (900 μAh at 3 K). The sample was cooled in an 8 mm V can in an Oxford Instruments Variox Cryostat. Data were fitted using the GSAS Rietveld refinement package using the EXPGUI interface.[17] Refinements were carried out with a profile function featuring a convolution of back-to-back exponentials with a pseudo-Voigt model, with backgrounds fitted using shifted Chebyschev polynomials. Refinement of the D fractional occupancy showed that the sample is perdeuterated.

Likely magnetic structures for the ordered phase were determined using the ISODISTORT software suite[18] by exploring the magnetic distortion modes and symmetries consistent with the observed magnetic propagation vector, **k**, and the parent crystal structure. In order to characterise short-range spin correlations in the paramagnetic state, magnetic diffuse scattering data were obtained from the lowest-Q detector bank (bank 1) on GEM. Bragg scattering, as determined from Rietveld refinements, and experimentally measured background contributions, including from the sample environment, were subtracted. The resulting magnetic diffuse-scattering data were fitted using the Spinvert Reverse Monte Carlo (RMC) refinement package.[15] In RMC refinement, spin orientations in a periodic supercell are fitted to diffuse-scattering data using a Metropolis Monte Carlo algorithm. We used a 5 × 3 × 13 size metrically-orthorhombic supercell related to the trigonal cell by a basis vector of [(1, 0, 0),(1/3, 2/3, 0),(0, 0, 1)]. The magnetic form factor of Tb^{3+} was obtained from tabulated coefficients.[19] The phase scale and a flat background term were also refined.

3. Results and discussion

3.1 Magnetic properties of the $Ln(HCO_2)_3$ frameworks

Rietveld fits to X-ray diffraction data confirmed that all samples used in this study were phase pure and adopt the known rhombohedral *R3m* structure under ambient conditions (see Fig. S1–S5, ESI†).[5] In this structure the LnO_9 polyhedra are connected into face-sharing chains down the *c*-axis with these chains interconnected *via* the formate ligand into a triangular arrangement (see Fig. 1). There are two different oxygen cations in the structure, bonding to one and two Ln^{3+} cations, respectively, with the latter anion connecting the Ln^{3+} cations in a chain. The triangle connections of the Ln^{3+} cation are not equilateral but instead feature two short bonds and one long bond, which rotate between adjacent layers along the *c*-axis.

Field cooled (FC) and zero-field cooled (ZFC) magnetic susceptibility data of the $Ln(HCO_2)_3$ frameworks (Ln = Gd^{3+}, Tb^{3+}, Dy^{3+}, Ho^{3+} and Er^{3+}) were measured in a 100 Oe field from 2 K to 300 K and did not show any indication of long range magnetic order. These data were well fitted using the Curie–Weiss law (see Fig. S6–S10, ESI†) with Curie–Weiss temperatures of −0.6 K, −0.9 K, −6.1 K, −10.3 K and −16.0 K, for Gd^{3+}–Er^{3+}. $Gd(HCO_2)_3$, therefore, has antiferromagnetic interactions but the significant orbital moment of the other lanthanides

Published on 21 July 2015. Downloaded on 23/05/2017 16:26:33.

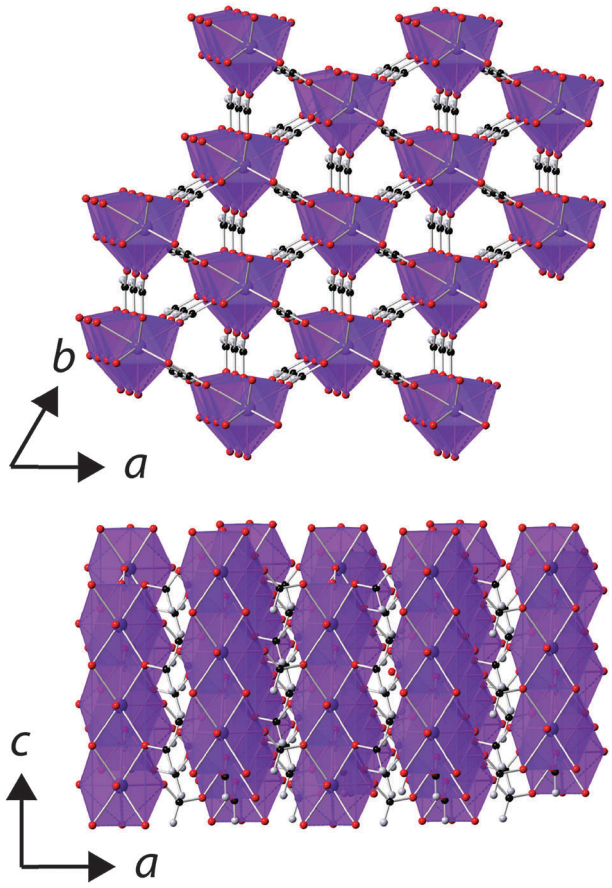


Fig. 1 The structure of the $Ln(HCO_2)_3$ frameworks. The Ln^{3+}, oxygen, carbon and hydrogen atoms are represented in purple, red, black and grey, respectively.

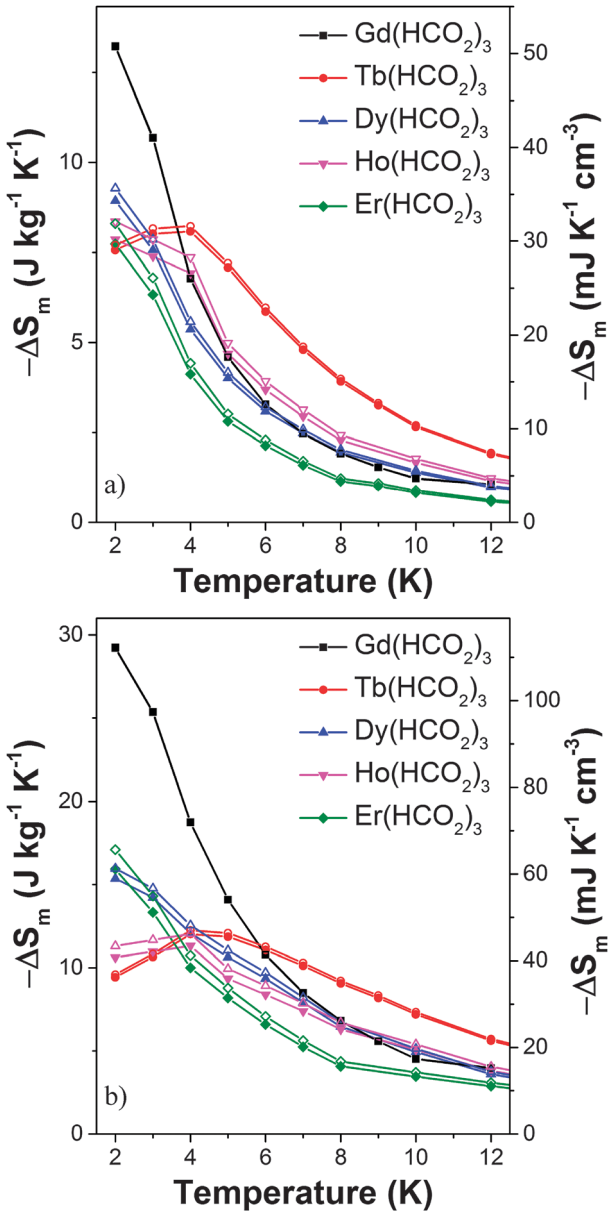


Fig. 2 Magnetic entropy change for the $Ln(HCO_2)_3$ frameworks for (a) ΔB = 1–0 T and (b) ΔB = 2–0 T. The filled and hollow symbols mark mass and volumetric units, respectively.

means their Curie–Weiss temperatures are a sum of any magnetic interactions and the effect of depopulation of the Stark levels so a similar analysis cannot be made. Effective magnetic moments were found to be broadly consistent with the values expected for these trivalent lanthanides according to the Russell–Saunders coupling scheme, with values of 7.86, 9.62, 10.00, 10.48 and 9.68 μ_B obtained. Magnetisation measurements exhibit paramagnetic behaviour and appear close to saturation under an applied field of 5 T (see Fig. S11–S16, ESI†). Interestingly, $Tb(HCO_2)_3$ appears close to saturation at 1 T, a much lower field than its Gd^{3+} analogue despite its higher magnetic anisotropy (discussed below); this greater ease of magnetisation increases further with increasing temperature.

Magnetic entropy change, ΔS_m, was calculated from the Maxwell relation $\Delta S_m(T) = \int[\partial M(T,B)/\partial T]_B dB$ from 2 K to 12 K for ΔB = 5–0 T. This gave $-\Delta S_m^{max}$ of 15.7, 20.8, 14.7 and 19.2 J kg^{-1} K^{-1} for Tb^{3+}, Dy^{3+}, Ho^{3+} and Er^{3+}, with T_{max} of 7, 6, 4 and 2 K, corresponding to volumetric values of $-\Delta S_m^{max}$ of 61.3, 82.9, 60.1 and 79.1 mJ cm^{-3} K^{-1} (see Fig. S17, ESI†). These $-\Delta S_m$ values are all significantly lower than the 190.4 mJ cm^{-3} K^{-1} we obtain for $Gd(HCO_2)_3$ with T_{max} = 2 K for ΔB = 5–0 T, which is close to the value found in a previous study.[5] The higher T_{max} temperatures of the other lanthanides, particularly Tb^{3+}, attracted our attention. Indeed, for ΔB = 1–0 T the $-\Delta S_m$ of $Tb(HCO_2)_3$ is significantly higher than that of $Gd(HCO_2)_3$ above 4 K. The same is true for $Ho(HCO_2)_3$, albeit to a very small extent (see Fig. 2a). A greater $-\Delta S_m$ is also observed for $Tb(HCO_2)_3$ for ΔB = 2–0 T above 6 K, although the differences in the values achieved compared to the Gd^{3+} compound are smaller (see Fig. 2b). This result highlights that the incorporation of Tb^{3+} cations into coordination frameworks allows their MCE properties to be optimised at higher temperatures and in lower applied fields, compared to the corresponding Gd^{3+} compound. Previous studies of $Gd_{1-x}Tb_xGa_5O_{12}$ showed the same effect, but by a much smaller margin.[20] This is significant as many of the applications of liquid helium do not require

 This journal is © The Royal Society of Chemistry 2015

Published on 21 July 2015. Downloaded on 23/05/2017 16:26:33.

cooling below 4 K, which most paramagnetic MCE materials are optimised for. It should be noted here that the magnetocaloric effect can be probed directly from heat capacity measurements, which is desirable particularly when determining the specific heat transfer, ΔQ.[21] Recent work on $Gd(HCO_2)_3$ and $GdOH(CO_3)$, however, have shown that for similar frameworks excellent agreement is usually obtained between the direct determination of $-\Delta S_m$ and the indirect method presented in this work.

Since the incorporation of Tb^{3+} yielded improved MCE properties at higher temperatures compared to $Gd(HCO_2)_3$ but lower $-\Delta S_m^{max}$, the magnetic properties of the $Gd_{1-x}Tb_x(HCO_2)_3$ (x = 0.2, 0.4, 0.6 and 0.8) solid solution were investigated. High-resolution X-ray diffraction indicate these compounds are pure single phases, although there was some evidence of peak broadening, suggesting that they exhibit a degree of strain or cation inhomogeneity (see Fig. S18, ESI†). Magnetic susceptibilities were well fitted by Curie–Weiss law, yielding effective magnetic moments consistent with stoichiometries of x = 0.19, 0.40, 0.57 and 0.76 across the series, close to the expected nominal stoichiometries. The Curie–Weiss temperatures were −0.9 K for the whole series except for $Gd_{0.4}Tb_{0.6}(HCO_2)_3$, which had a value of −1.3 K. Only $Gd_{0.4}Tb_{0.6}(HCO_2)_3$ varied from mean-field behaviour, with an antiferromagnetic cusp present in ZFC measurements at 3 K that is not observed in FC data (see Fig. S19, ESI†); magnetization measurements at 2 K are consistent with paramagnetic behaviour suggesting $Gd_{0.4}Tb_{0.6}(HCO_2)_3$ is not a simple antiferromagnet.

For the x = 0.2 and 0.4 members of the $Gd_{1-x}Tb_x(HCO_2)_3$ series the $-\Delta S_m$ for ΔB = 1–0 T are significantly higher than would be expected for a physical mix of the two end-member phases. This is particularly significant for $Gd_{0.8}Tb_{0.2}(HCO_2)_3$ as at 2 K, the lowest temperature probed its $-\Delta S_m$ for a ΔB = 1–0 T is equal to that of $Gd(HCO_2)_3$. It decreases more slowly than for the pure Gd phase, such that for temperatures above 5 K its $-\Delta S_m$ is between 10–15% higher (see Fig. 3 and Fig. S20–S23 for magnetisation data, ESI†). Similarly, while the $-\Delta S_m^{max}$ for $Gd_{0.6}Tb_{0.4}(HCO_2)_3$ is about 10% lower than $Gd(HCO_2)_3$ for a ΔB = 1–0 T above 5 K, its $-\Delta S_m$ is between 14 to 24% higher. The performance of both doped compounds also exceeds that of $Gd(HCO_2)_3$ at higher temperatures for a ΔB = 2–0 T, although this is only above 6 and 7 K for x = 0.2 and x = 0.4, respectively, and the difference remains less than 10%. To the best of our knowledge this is the first study of the magnetocaloric properties of a framework solid solution and has shown the potential advantages of such an approach to optimise the physical properties of such materials – namely, retaining most of the performance of $Gd(HCO_2)_3$ in low fields, while improving on its MCE at moderately higher temperatures.

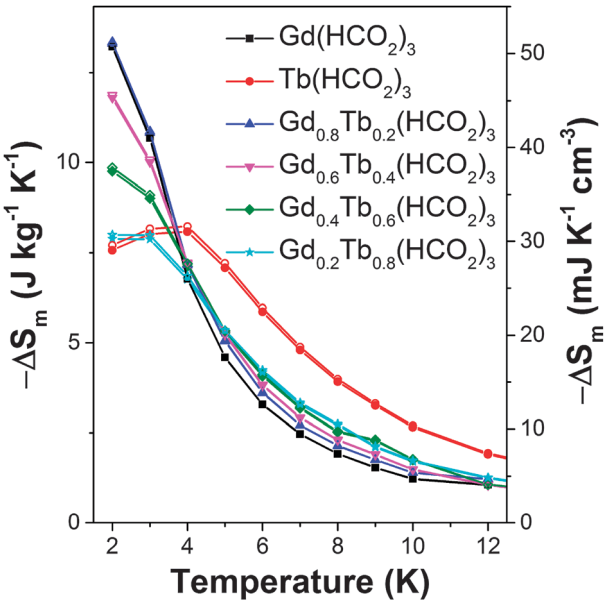


Fig. 3 Magnetic entropy change for the $Gd_{1-x}Tb_x(HCO_2)_3$ series for ΔB = 1–0 T. The filled and hollow symbols mark mass and volumetric units, respectively.

3.2 Magneto-structural characterisation of $Tb(DCO_2)_3$

The interesting properties of $Tb(HCO_2)_3$ encouraged further investigation of its structure and magnetic interactions using neutron diffraction, particularly in the paramagnetic phase. Past studies of the $Ln(HCO_2)_3$ frameworks have suggested a subtle structural transition occurs below 150 K due to a very small reduction ($\approx$0.05%) of the c-axis in $Tm(DCO_2)_3$[22] and features observed in Raman spectra of $Pr(HCO_2)_3$.[23] The proposed transition is from the ambient temperature $R3m$ rhombohedral structure to $R3$ symmetry and involves a rotation of the formate groups.[23] Neutron diffraction should be particularly sensitive to such a transition, as it will involve a significant movement of the deuterium atoms. We find a similar minute change in the lattice parameters of $Tb(DCO_2)_3$ below 80 K (see Fig. S24, ESI†), but Rietveld refinements to the data collected at 3 K using both possible space groups give equivalent excellent fits: for $R3$, R_p = 1.60% and R_{wp} = 2.26%, and for $R3m$, R_p = 1.67% and R_{wp} = 2.30%. Moreover, the maximum displacement of each atom in the $R3$ structure is within 0.1 Å of the position required by $R3m$ symmetry. We therefore conclude that $R3m$ symmetry is retained to 3 K (see Tables S1–S4 for crystallographic details and selected bond distances and angles determined at 3 and 300 K, ESI†). There are no significant changes observed that indicate the cause of the subtle change in the c-axis length. There is also no indication of diffuse scattering appearing above 10 K, so it is unlikely to be related to structural disorder.

A neutron diffraction pattern obtained from $Tb(DCO_2)_3$ at 1.4 K revealed the presence of additional reflections, especially at high d-spacing (see Fig. 4), consistent with the emergence of magnetic order. These were found to index on the parent cell but violated the rhombohedral centering conditions. This is consistent with the magnetic structure of $Tb(DCO_2)_3$ belonging to the **k**-vector Λ, (0, 0, g), which is allowed to be incommensurate but here appears to have locked into a commensurate value of g = 1. Of the possible magnetic structures suggested by ISODISTORT only those belonging to the magnetic space group $P3m'1$ fitted the data. There were two possible magnetic structures of this type, each of which have ferromagnetic face-sharing chains, with spins found to align along the c-axis. One possible structure has three ferromagnetic chains with

Published on 21 July 2015. Downloaded on 23/05/2017 16:26:33.

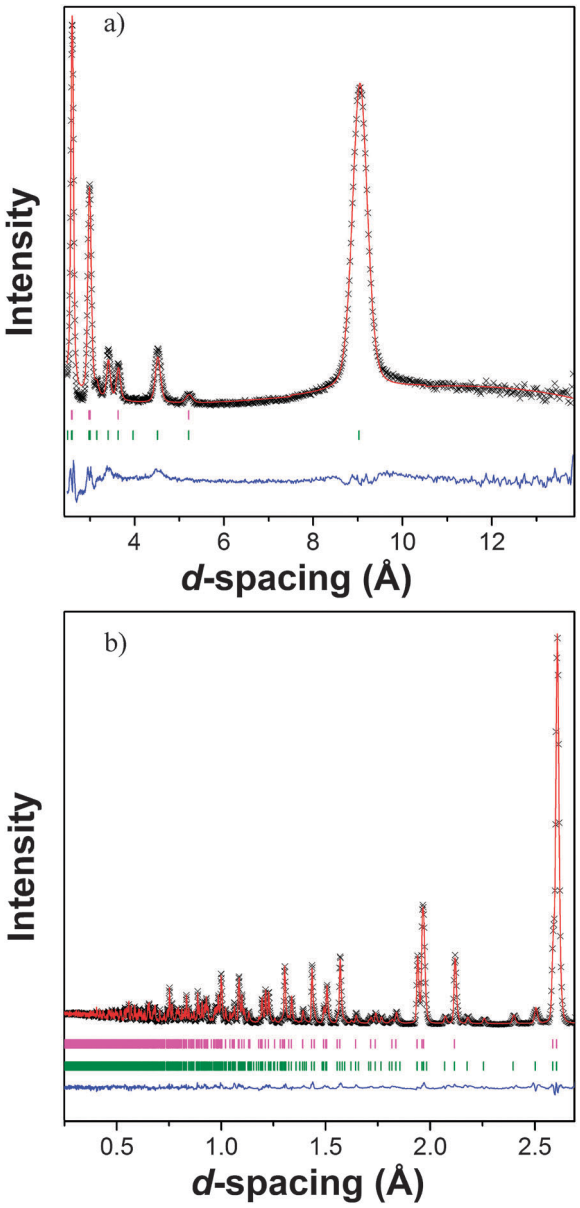


Fig. 4 Neutron diffraction pattern collected from $Tb(DCO_2)_3$ at 1.4 K using (a) bank 2 and (b) bank 5 of the GEM diffractometer fitted using the Rietveld method. The crosses, upper and lower lines indicate the observed and calculated intensities and the differences between these. The upper and lower sets of vertical markers indicate those allowed by the nuclear and magnetic structures.

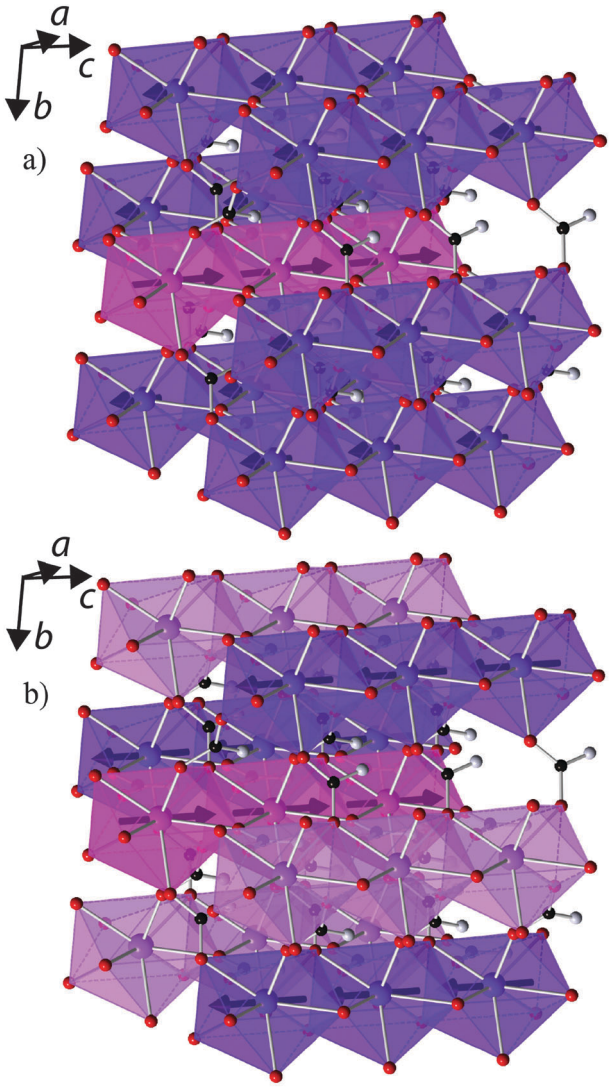


Fig. 5 The two possible magnetic structures of $Tb(DCO_2)_3$. The distinct Tb^{3+} cations are shown in different colours with the ordered spin direction indicated by the arrows pointing through them. All other colours are the same as in Fig. 1.

one chain having twice the magnetic moment of the others and coupled antiferromagnetically to them (see Fig. 5a). This model is consistent with that proposed in a previous study of Kurbakov *et al.*,[24] who briefly analysed the magnetic structure of $Tb(DCO_2)_3$ using a basis vector approach. The other structure has the spins in two ferromagnetic chains coupled antiferromagnetically to each other with the remaining chain being disordered (see Fig. 5b), a so-called spin-idle structure. The fits of these two structures to the 1.4 K data are equivalent (R_p = 1.94% for both models and R_{wp} = 2.09% and 2.10% for the spin-idle and unequal spin structure, respectively). The largest magnetic moment is 5.91 μ_B and 6.80 μ_B for the spin-idle and unequal-spin structure, respectively. These values are well below the expected magnetic moment of 9.72 μ_B for isotropic Tb^{3+} moments, consistent with the observation of magnetic diffuse scattering, which persists more weakly up to 10 K. Magnetic reflections appear between 1.65 and 1.72 K, indicating the onset of magnetic order (see Fig. S25 for the evolution of the magnetic moments, ESI†). The square of the observed magnetic moment is proportional to the Landau order parameter, Q; a good linear fit to the square of the ordered magnetic moment is obtained, confirming that the magnetic-ordering transition is second order and occurs at 1.72(12) K.

Both possible magnetic structures of $Tb(DCO_2)_3$ indicate that the dominant intra-chain coupling is ferromagnetic, consistent with the small Tb–O2–Tb bond angle of 105.79(4)°. As the intra-chain super-exchange distances are much smaller than those

 This journal is © The Royal Society of Chemistry 2015

Published on 21 July 2015. Downloaded on 23/05/2017 16:26:33.

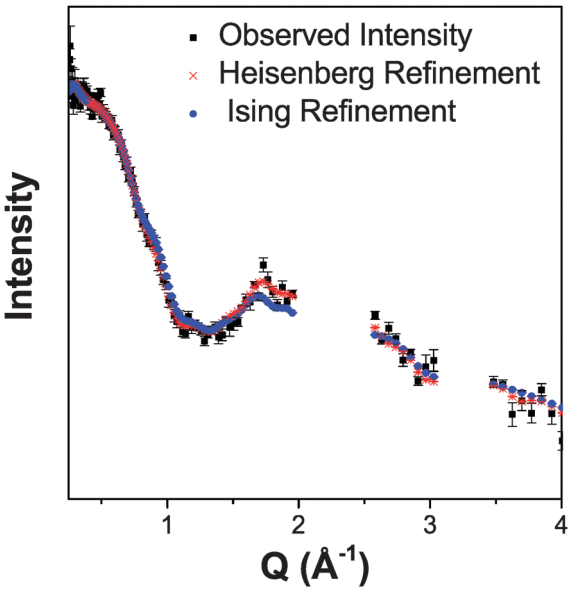


Fig. 6 Comparison of the Heisenberg-like and Ising-like RMC fits to the neutron diffuse scattering of $Tb(DCO_2)_3$ at 3 K. The results are averaged over ten refinements.

between chains (*cf.* 4.98 Å to 7.42 Å), it would be expected that this compound will resemble a one-dimensional system above its long-range ordering temperature. Fits to the diffuse magnetic scattering observed at 3 K using RMC refinement confirm that this is the case (see Fig. 6 for the quality of fit). Initially, unconstrained refinements were performed in which the spins were allowed to point in any direction, in a Heisenberg-like fashion. A plot of $\langle S_0 \cdot S_r \rangle$ averaged over ten such refinements show that the dominant spin correlations in this material are ferromagnetic within the chains (see Fig. 7a), with a correlation length of 9.2(1.3) Å. The inter-chain correlations are much weaker and antiferromagnetic, with $\langle S_0 \cdot S_r \rangle$ correlations of −0.082(2) and −0.044(3) observed for Tb^{3+} cations separated by the shorter, 6.16 Å and longer, 6.57 Å distances found in the triangles, respectively.

Stereographic projections of the refined spin orientations indicate that even well above the magnetic ordering temperatures the spins are preferentially aligned along the *c*-axis (see Fig. 7b), indicating an Ising-like magnetic anisotropy. Attempts were therefore made to fit the diffuse scattering data with Ising spins constrained to point along the *c*-axis. The Ising refinements also yielded a reasonable fit, though of somewhat lower quality than the unconstrained refinement (*cf.* χ^2 of 290 and 414 for ten averaged Heisenberg and Ising fits, respectively), which would be expected as the Ising refinement is more highly constrained. This result suggests that the spins have a strong, although probably not purely, Ising character. To the best of our knowledge this is the first RMC study of the magnetic interactions in the paramagnetic phase of a coordination framework.

The significant ferromagnetic intra-chain interactions in the paramagnetic phase of $Tb(HCO_2)_3$ explain the relative ease of its magnetization compared to $Gd(HCO_2)_3$, whose negative Curie–Weiss temperature indicates predominantly antiferromagnetic

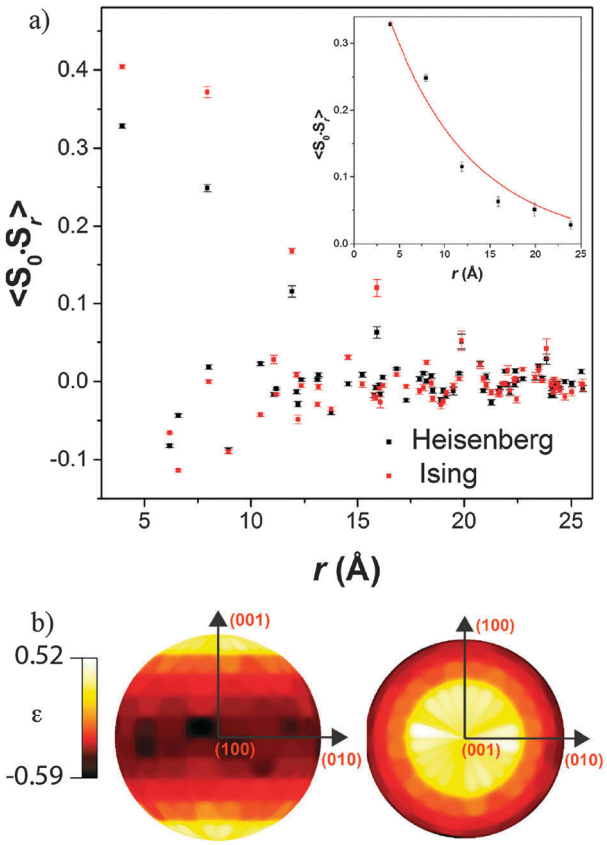


Fig. 7 Depictions of (a) $\langle S_0 \cdot S_r \rangle$ correlations averaged over ten RMC refinements with an inset showing a exponential correlation length fit to the ferromagnetic intra-chain interactions and (b) stereographic projections of the spin orientations averaged over 100 RMC Heisenberg-like fits to diffuse neutron scattering data from $Tb(DCO_2)_3$ at 3 K. The relative spin density, $\varepsilon(\theta, \phi)$, is defined as $\varepsilon(\theta, \phi) = \ln\left[\frac{n(\theta, \phi)}{N \mathrm{d}(\cos\theta)\mathrm{d}\phi}\right]$, where $n(\theta, \phi)$ is the number of spins with orientations within the range $\mathrm{d}(\cos\theta)$, $\mathrm{d}\phi$.

interactions. It can be envisaged that the strong ferromagnetic intra-chain interactions, present on a local scale of about 10 Å, will lead to the Tb^{3+} spins aligning readily with an applied magnetic field, easily overcoming the much weaker inter-chain antiferromagnetic coupling. Bulk measurements show that this greater ease of magnetization is retained to higher temperature, leading to a higher peak temperature for $-\Delta S_m^{max}$ than found in $Gd(HCO_2)_3$, which may make $Tb(HCO_2)_3$ suitable for cooling applications at moderately higher temperatures. The trade-off for this is a lower $-\Delta S_m^{max}$ compared to $Gd(HCO_2)_3$, due to a combination of its lower magnetic moment and a more gradual change of magnetisation with temperature. In the $Gd_{1-x}Tb_x(HCO_2)_3$ solid solution a mixture of these two cations leads to a retention of most of the peak performance of the $Gd(HCO_2)_3$ but a slower reduction in $-\Delta S_m$ with temperature in low applied fields. While to date the development of magnetocaloric frameworks has focused on Gd^{3+} containing-compounds, this study highlights the benefits of incorporating heavier lanthanides into framework structures known to have excellent magnetocaloric properties. By combining a deeper understanding of their magnetic interactions with judicious choices of doping in

Published on 21 July 2015. Downloaded on 23/05/2017 16:26:33.

solid solutions, it should be possible to expand the palate of available magnetocaloric frameworks and optimize their application.

4. Conclusion

In this work we have reported the MCE of the $Ln(HCO_2)_3$ (Ln = Tb^{3+}, Dy^{3+}, Ho^{3+} and Er^{3+}) frameworks for the first time and compared them to the properties of the related $Gd(HCO_2)_3$, which is already proven to be an excellent candidate as a magnetocaloric material.[5] We have shown that, although the peak performance of the other lanthanide formates is not as great as for $Gd(HCO_2)_3$, the temperature at which their performance peaks is significantly higher. This is particularly important in the case of the Tb^{3+} compound, which significantly outperforms $Gd(HCO_2)_3$ above 4 K in fields below 2 T, the maximum field typically achievable with permanent magnets. Moreover, we show that the Gd^{3+}-rich end-members of the solid solution $Gd_{1-x}Tb_x(HCO_2)_3$ retain much or all of the peak performance of $Gd(HCO_2)_3$ but also exhibit a slower decline in their $-\Delta S_m$, leading to better performance. The magnetic order of $Tb(DCO_2)_3$ in both its antiferromagnetic and paramagnetic phases has also been examined. We find that the Tb^{3+} spins in the edge-sharing chains order ferromagnetically below 1.7 K into an arrangement featuring antiferromagnetic triangles. Only partial order occurs, indicating the inherent frustration in this system, and significant magnetic diffuse scattering therefore remains. Fitting magnetic diffuse scattering in the paramagnetic phase, suggests that the compound resembles a one-dimensional ferromagnetic chain with magnetic moments oriented along the *c*-axis as in the ordered phase, which increases its ease of magnetisation and thereby magnetocaloric properties.

Acknowledgements

Experiments at the ISIS Pulsed Neutron Source were supported by a beamtime allocation from the Science and Technology Facilities Council. PJS would like to thank the Glasstone Bequest for financial support through the provision of a Glasstone Fellowship and Professor Andrew Goodwin for helpful discussions.

References

1 (*a*) J. Glanz, *Science*, 1998, **279**, 2045; (*b*) G. J. Halder, C. J. Kepert, B. Moubaraki, K. S. Murray and J. D. Cashion, *Science*, 2002, **298**, 1762–1765; (*c*) D. Maspoch, D. Ruiz-Molina, K. Wurst, N. Domingo, M. Cavallini, F. Biscarini, J. Tejada, C. Rovira and J. Veciana, *Nat. Mater.*, 2003, **2**, 190–195; (*d*) W. Eerenstein, N. D. Mathur and J. F. Scott, *Nature*, 2006, **442**, 759–765.

2 Y.-Z. Zheng, G.-J. Zhou, Z. Zheng and R. E. P. Winpenny, *Chem. Soc. Rev.*, 2014, **43**, 1462–1475.

3 (*a*) M. Kurmoo, H. Kumagai, K. W. Chapman and C. J. Kepert, *Chem. Commun.*, 2005, 3012–3014; (*b*) M. Kurmoo, *Chem. Soc. Rev.*, 2009, **38**, 1353–1379; (*c*) G. Rogez, N. Viart and M. Drillon, *Angew. Chem., Int. Ed.*, 2010, **49**, 1921–1923; (*d*) Z. Wang, K. Hu, S. Gao and H. Kobayashi, *Adv. Mater.*, 2010, **22**, 1526–1533; (*e*) P. J. Saines, M. Steinmann, J.-C. Tan, W. Li, P. T. Barton and A. K. Cheetham, *Inorg. Chem.*, 2012, **51**, 11198–11209; (*f*) P. J. Saines, P. T. Barton, P. Jain and A. K. Cheetham, *CrystEngComm*, 2012, **14**, 2711–2720.

4 P. J. Saines, P. T. Barton, M. Jura, K. S. Knight and A. K. Cheetham, *Mater. Horiz.*, 2014, **1**, 332–337.

5 G. Lorusso, J. W. Sharples, E. Palacios, O. Roubeau, E. K. Brechin, R. Sessoli, A. Rossin, F. Tuna, E. J. L. McInnes, D. Collison and M. Evangelisti, *Adv. Mater.*, 2013, **25**, 4653–4656.

6 (*a*) S. Biswas, H. S. Jena, A. Adhikary and S. Konar, *Inorg. Chem.*, 2014, **53**, 3926–3928; (*b*) Y.-C. Chen, L. Qin, Z.-S. Meng, D.-F. Yang, C. Wu, Z. Fu, Y.-Z. Zheng, J.-L. Liu, R. Tarasenko, M. Orendac, J. Prokleska, V. Sechovsky and M.-L. Tong, *J. Mater. Chem. A*, 2014, **2**, 9851–9858; (*c*) Y. Meng, Y.-C. Chen, Z.-M. Zhang, Z.-J. Lin and M.-L. Tong, *Inorg. Chem.*, 2014, **53**, 9052–9057.

7 M. Evangelisti and E. K. Brechin, *Dalton Trans.*, 2010, **39**, 4672–4676.

8 (*a*) Z. H. Gan, W. Q. Dong, L. M. Qiu, X. B. Zhang, H. Sun, Y. L. He and R. Radebaugh, *Cryogenics*, 2009, **49**, 198–201; (*b*) L. Chen, H. Jin, J. Wang, Y. Zhou, W. Zhu and Q. Zhou, *Cryogenics*, 2013, **54**, 54–58; (*c*) K. Yamada, *Cryogenics*, 2014, **63**, 110–113.

9 (*a*) K. A. GschneidnerJr, V. K. Pecharsky and A. O. Tsokol, *Rep. Prog. Phys.*, 2005, **68**, 1479; (*b*) A. Smith, C. R. H. Bahl, R. Bjørk, K. Engelbrecht, K. K. Nielsen and N. Pryds, *Adv. Energy Mater.*, 2012, **2**, 1288–1318.

10 L. Yuri, S. Ernst Wolfgang and Z. Tao, *Supercond. Sci. Technol.*, 2013, **26**, 093001.

11 (*a*) P. J. Saines, J. R. Hester and A. K. Cheetham, *Phys. Rev. B: Condens. Matter Mater. Phys.*, 2010, **82**, 144435; (*b*) O. Fabelo, L. Cañadillas-Delgado, I. Puente Orench, J. A. Rodríguez-Velamazán, J. Campo and J. Rodríguez-Carvajal, *Inorg. Chem.*, 2011, **50**, 7129–7135; (*c*) P. J. Saines, H. H. M. Yeung, J. R. Hester, A. R. Lennie and A. K. Cheetham, *Dalton Trans.*, 2011, **40**, 6401–6410; (*d*) L. Cañadillas-Delgado, O. Fabelo, J. A. Rodríguez-Velamazán, M.-H. Lemée-Cailleau, S. A. Mason, E. Pardo, F. Lloret, J.-P. Zhao, X.-H. Bu, V. Simonet, C. V. Colin and J. Rodríguez-Carvajal, *J. Am. Chem. Soc.*, 2012, **134**, 19772–19781; (*e*) R. A. Mole, M. A. Nadeem, J. A. Stride, V. K. Peterson and P. T. Wood, *Inorg. Chem.*, 2013, **52**, 13462–13468; (*f*) J. M. M. Lawler, P. Manuel, A. L. Thompson and P. J. Saines, *Dalton Trans.*, 2015, **44**, 11613–11620.

12 A. Kumar, S. M. Yusuf, L. Keller, J. V. Yakhmi, J. K. Srivastava and P. L. Paulose, *Phys. Rev. B: Condens. Matter Mater. Phys.*, 2007, **75**, 224419.

13 (*a*) O. A. Petrenko, C. Ritter, M. Yethiraj and D. McK Paul, *Phys. Rev. Lett.*, 1998, **80**, 4570–4573; (*b*) E. Reynolds, P. E. R. Blanchard, B. J. Kennedy, C. D. Ling, S. Liu, M. Avdeev, Z. Zhang, G. J. Cuello, A. Tadich and L.-Y. Jang, *Inorg. Chem.*, 2013, **52**, 8409–8415; (*c*) E. Palacios, J. A. Rodríguez-Velamazán, M. Evangelisti, G. J. McIntyre, G. Lorusso, D. Visser, L. J. de Jongh and L. A. Boatner, *Phys. Rev. B: Condens. Matter Mater. Phys.*, 2014, **90**, 214423.

14 (*a*) A. M. Hallas, J. A. M. Paddison, H. J. Silverstein, A. L. Goodwin, J. R. Stewart, A. R. Wildes, J. G. Cheng,

 This journal is © The Royal Society of Chemistry 2015

J. S. Zhou, J. B. Goodenough, E. S. Choi, G. Ehlers, J. S. Gardner, C. R. Wiebe and H. D. Zhou, *Phys. Rev. B: Condens. Matter Mater. Phys.*, 2012, **86**, 134431; (*b*) J. A. M. Paddison and A. L. Goodwin, *Phys. Rev. Lett.*, 2012, **108**, 017204; (*c*) P. J. Saines, M. G. Tucker, D. A. Keen, A. K. Cheetham and A. L. Goodwin, *Phys. Rev. B: Condens. Matter Mater. Phys.*, 2013, **88**, 134418; (*d*) J. A. M. Paddison, S. Agrestini, M. R. Lees, C. L. Fleck, P. P. Deen, A. L. Goodwin, J. R. Stewart and O. A. Petrenko, *Phys. Rev. B: Condens. Matter Mater. Phys.*, 2014, **90**, 014411.

15 J. A. M. Paddison, J. R. Stewart and A. L. Goodwin, *J. Phys.: Condens. Matter*, 2013, **25**, 454220.

16 A. C. Hannon, *Nucl. Instrum. Methods Phys. Res., Sect. A*, 2005, **551**, 88–107.

17 B. Toby, *J. Appl. Crystallogr.*, 2001, **34**, 210–213.

18 B. J. Campbell, H. T. Stokes, D. E. Tanner and D. M. Hatch, *J. Appl. Crystallogr.*, 2006, **39**, 607–614.

19 P. J. Brown, Magnetic Form Factors, http://www.ill.eu/sites/ccsl/ffacts/ffachtml.html, 2015.

20 C. P. Reshmi, S. Savitha Pillai, K. G. Suresh and M. R. Varma, *J. Magn. Magn. Mater.*, 2012, **324**, 1962–1966.

21 V. Khovaylo, *J. Alloys Compd.*, 2013, **577**, S362–S366.

22 V. Trounov, E. Tserkovnaya, S. Gavrilov and S. Vahrushev, *Physica B*, 1997, **234–236**, 679–681.

23 M. R. Moura, A. P. Ayala, J. Mendes Filho, I. Guedes, C. W. A. Paschoal, A. G. Leyva, G. Polla, D. Vega, P. K. de Perazzo and H. Lanza, *J. Raman Spectrosc.*, 2004, **35**, 159–164.

24 A. I. Kurbakov, J. Rodriguez-Carvajal, V. Trounov and N. V. Starostina, *Mater. Sci. Forum*, 2000, **321–324**, 971–975.

Published on 21 July 2015. Downloaded on 23/05/2017 16:26:33.